UCLA
UCLA Electronic Theses and Dissertations

Title
Non-Contrast Enhanced Cardiovascular Magnetic Resonance Imaging for Characterizing Chronic Myocardial Infarctions

Permalink
https://escholarship.org/uc/item/7b3097ff

Author
Kali, Avinash

Publication Date
2015

Peer reviewed|Thesis/dissertation

eScholarship.org Powered by the California Digital Library
University of California

UNIVERSITY OF CALIFORNIA

Los Angeles

Non-Contrast Enhanced Cardiovascular Magnetic Resonance Imaging for Characterizing Chronic Myocardial Infarctions

A dissertation submitted in partial satisfaction of the

requirements for the degree Doctor of Philosophy

in Biomedical Engineering

by

Avinash Kali

2015

© Copyright by

Avinash Kali

2015

ABSTRACT OF THE DISSERTATION

Non-Contrast Enhanced Cardiovascular Magnetic Resonance Imaging for Characterizing Chronic Myocardial Infarctions

by

Avinash Kali

Doctor of Philosophy in Biomedical Engineering

University of California, Los Angeles, 2015

Professor Rohan Dharmakumar, Co-chair

Professor Daniel B. Ennis, Co-chair

Myocardial infarction (MI) is the leading cause of morbidity and death globally. Non-invasive characterization of MIs is of significant clinical importance due to its association with adverse cardiac outcomes such as cardiac arrhythmias, heart failure, and sudden cardiac death. Late Gadolinium Enhancement (LGE) Magnetic Resonance Imaging (MRI) has evolved into a robust non-invasive imaging technique for characterizing MIs. However, the requisite Gadolinium administration in LGE MRI is contra-indicated in nearly 20% of the MI patients due to co-morbidity of chronic kidney disease.

In the absence of LGE MRI, acute MIs (AMIs) can still be reliably characterized using non-contrast enhanced MRI techniques based on the T_1, T_2, and T_2* properties of different pathological hallmarks of AMI such as myocardial edema, microvascular obstruction, and intramyocardial hemorrhage. However, these pathological features of AMI typically resolve in

the chronic phase of MI, and LGE imaging remains the only technique that can characterize chronic MIs (CMIs). The location, extent, and transmurality of CMIs evaluated using LGE imaging are well known prognostic indicators of adverse left-ventricular (LV) remodeling and heart failure. In addition, gray-zone identified within CMIs using LGE imaging has been long documented to be an important predictor of malignant ventricular arrhythmias (mVAs) and sudden cardiac death. CMI patients who are contra-indicated to LGE imaging due to pre-existing chronic kidney disease, therefore, cannot be adequately risk-stratified for adverse long-term outcomes. In this regard, there has been a growing interest to develop non-contrast enhanced MRI techniques for robust characterization of CMIs.

The first objective of this dissertation was to develop, test, and validate a non-contrast enhanced MRI approach that can reliably determine the location, extent, and transmurality of CMIs. Using extensive histopathological validation in a canine model of CMI, this dissertation identified native T1 mapping using MOLLI-bSSFP at 3T as a reliable technique for characterizing the morphology of CMIs with a diagnostic performance comparable to that of the gold standard LGE imaging. By definition, native T_1 mapping does not require exogenous contrast agents, and can thereby be safely used in CMI patients contra-indicated to Gadolinium. Different semi-automatic, automatic, and visual techniques for objectively characterizing the morphology of CMIs on native T_1 maps at 3T were evaluated. Threshold-based detection using Mean + 5 Standard Deviations (SD) criterion was found to be the most robust detection technique for this purpose. Using the Mean+5SD criterion, native T_1 mapping at 3T demonstrated strong diagnostic performance for characterizing chronic MIs in a pilot patient population with healed ST-elevation and non-ST-elevation MIs.

The second objective of this dissertation was to develop, test, and validate a non-contrast enhanced MRI approach for characterizing pathological markers of adverse cardiac outcomes including heart failure and malignant ventricular arrhythmias within CMIs. Using T_2*-based MRI, this dissertation has identified that acute reperfusion intramyocardial hemorrhage resolves into localized iron deposition within CMIs, and such iron deposits may evolve into potential pathological substrates of heart failure and malignant ventricular arrhythmias. Using histopathological and mass spectrometric validation, T_2*-based MRI was found to be a highly sensitive technique for characterizing acute reperfusion intramyocardial hemorrhage and the ensuing iron deposition within CMIs. Subsequently, chronic iron deposition was found to be associated with significant pro-inflammatory burden and adverse LV remodeling in the chronic phase of MI.

Ex-vivo bulk electrical impedance measurements showed that chronic iron deposition within CMIs could alter the electrical characteristics of chronic infarct tissue. Co-registration of in-vivo T_2*-weighted images with high-resolution electroanatomical maps showed that chronic iron deposition could be a potential marker of mVAs. In CMI patients undergoing ICD therapy, hypointense cores within CMI territories detected using non-contrast enhanced balanced steady state free precession (bSSFP) images were found to be independent markers of mVA risk. Subsequent validation studies in canines using T_2*-based MRI showed that these hypointense cores in bSSFP images are indicative of chronic iron deposition. Finally, persistent microvascular obstruction, with or without reperfusion hemorrhage, was also found to resolve into localized iron deposition within CMIs, which could be a potential mechanism by which microvascular obstruction exerts adverse long-term effects well after being completely resolved.

In summary, this dissertation lays extensive groundwork for the widespread adoption of native T_1 mapping at 3T, T_2*-based MRI, and bSSFP MRI as potential non-contrast enhanced MRI techniques for robustly characterizing CMI morphology and pathological substrates of adverse cardiac outcomes within CMIs.

This dissertation of Avinash Kali is approved.

Michael C. Fishbein

Michael Albert Thomas

Zhilin Qu

Daniel B. Ennis, Committee Co-chair

Rohan Dharmakumar, Committee Co-chair

University of California, Los Angeles

2015

To my parents, grandparents, and Samyukta

CONTENTS

LIST OF TABLES

LIST OF FIGURES

LIST OF SYMBOLS & ABBREVIATIONS

α	Flip angle
β	Coefficient of linear regression
γ	Gyromagnetic ratio
ε	Electrical permittivity
κ	Cohen's Kappa coefficient
σ	Electrical conductivity
φ (z,t)	Phase accumulated by a spin in time t at longitudinal location z
ω_0	Larmor frequency
ω (z,t)	Angular frequency of precession of a spin at time t and longitudinal location z
AC	**A**lternating **C**urrent
AHA	**A**merican **H**eart **A**ssociation
AMI	**A**cute **M**yocardial **I**nfarction
ANOVA	**A**nalysis **O**f **V**ariance
ATP	**A**denosine **T**ri**P**hosphate
AUC	**A**rea **U**nder the **C**urve
B_0	Static external magnetic field
bSSFP	**B**alanced **S**teady State **F**ree **P**recession
BW	**B**and**W**idth
C	Electrical capacitance
CABG	**C**oronary **A**rtery **B**ypass **G**raft
CAD	**C**oronary **A**rtery **D**isease

CARE	**C**holesterol **A**nd **R**ecurrent **E**vents
CI	**C**onfidence **I**nterval
CMI	**C**hronic **M**yocardial **I**nfarction
CNR	**C**ontrast-to-**N**oise **R**atio
CT	**C**omputed **T**omography
CV	**C**oefficient of **V**ariation
CVD	**C**ardio**V**ascular **D**isease
DSE	**D**obutamine **S**tress **E**chocardiography
EAM	**E**lectro**A**natomical **M**ap
ECG	**E**lectro**C**ardio**G**ram
ECV	**E**xtra**C**ellular **V**olume fraction
EDSI	**E**nd **D**iastolic **S**phericity **I**ndex
EDV	**E**nd **D**iastolic **V**olume
EF	**E**jection **F**raction
EGE	**E**arly **G**adolinium **E**nhancement
EGM	**E**lectro**G**ram
EMT	**E**lastin **M**asson's **T**richrome
ESV	**E**nd **S**ystolic **V**olume
FDG	**F**luorine-19 **D**eoxy **G**lucose
FLASH	**F**ast **L**ow **A**ngle **SH**ot
G	Electrical admittance
GBCA	**G**adolinium-**B**ased **C**ontrast **A**gent
GFR	**G**lomerular **F**iltration **R**ate

GISSI	**G**ruppo **I**taliano per lo **S**tudio della **S**opravvivenza nell'**I**nfarto miocardico
GRE	**G**radient **R**ecalled **E**cho
G_z	Constant magnetic field gradient along z-axis
H & E	**H**ematoxylin and **E**osin
HF	**H**eart **F**ailure
HR	**H**eart **R**ate
ICD	**I**mplantable **C**ardioverter **D**efibrillator
ICP-MS	**I**nductively **C**oupled **P**lasma - **M**ass **S**pectrometry
ILP	**I**solated **L**ate **P**otential
IQR	**I**nter-**Q**uartile **R**ange
IR	**I**nversion **R**ecovery
I-R	**I**schemia-**R**eperfusion
IRA	**I**nfarct **R**elated **A**rtery
LAD	**L**eft **A**nterior **D**escending artery
LGE	**L**ate **G**adolinium **E**nhancement
LV	**L**eft **V**entricle
M_0	Equilibrium magnetization
MCE	**M**yocardial **C**ontrast **E**chocardiography
MI	**M**yocardial **I**nfarction
MMP	**M**atrix **M**etallo-**P**rotease
MO	**M**icrovascular **O**bstruction
MOLLI	**MO**dified **L**ook-**L**ocker **I**nversion recovery
MRI	**M**agnetic **R**esonance **I**maging

MSE	**M**ulti-**S**pin **E**cho
MT	**M**agnetization **T**ransfer
M_{xy}	Transverse component of magnetization
M_z	Longitudinal component of magnetization
NSTEMI	**N**on-**ST**-**E**levation **M**yocardial **I**nfarction
NYHA	**N**ew **Y**ork **H**eart **A**ssociation
OR	**O**dds **R**atio
PCI	**P**ercutaneous **C**oronary **I**ntervention
PET	**P**ositron **E**mission **T**omography
PMO	**P**ersistent **M**icrovascular **O**bstruction
QTc	QT-interval corrected for heart rate
QTcd	QT-interval dispersion corrected for heart rate
R1	Rate of decay of longitudinal magnetization
R2	Rate of decay of transverse magnetization
R2*	Rate of decay of transverse magnetization in the presence of static magnetic field inhomogeneities
RBC	**R**ed **B**lood **C**ell
RF	**R**adio**F**requency
ROC	**R**eceiver **O**perator **C**haracteristic
ROI	**R**egion **O**f **I**nterest
SASHA	**SA**turation recovery single **SH**ot **A**cquisition
SAVE	**S**urvival **A**nd **V**entricular **E**nlargement
SCD	**S**udden **C**ardiac **D**eath

SD	**S**tandard **D**eviation
SE	**S**pin **E**cho
ShMOLLI	**Sh**ortened **MO**dified **L**ook-**L**ocker **I**nversion recovery
SI	**S**ignal **I**ntensity
SNR	Signal-to-Noise Ratio
SPECT	**S**ingle **P**hoton **E**mission **C**omputed **T**omography
SSFP	**S**teady **S**tate **F**ree **P**recession
STEMI	**ST**-**E**levation **M**yocardial **I**nfarction
STICH	**S**urgical **T**reatment for **I**schemic **H**eart **F**ailure
STIR	**S**hort $\mathbf{T_1}$ **I**nversion **R**ecovery
T_1	Longitudinal or spin-lattice relaxation time constant
$T_{1\rho}$	Spin-locked magnetization relaxation time constant
T_2	Transverse or spin-spin relaxation time constant
T_2'	Transverse relaxation time constant due to static magnetic field inhomogeneities
T_2^*	Transverse or spin-spin relaxation time constant in the presence of static magnetic field inhomogeneities
TE	Echo time
TI	Inversion time
TIMI	**T**hrombolysis **I**n **M**yocardial **I**nfarction
TNF	**T**umor **N**ecrosis **F**actor
TR	Repetition time
TSE	**T**urbo **S**pin **E**cho
TTC	**T**riphenyl **T**etrazolium **C**hloride

Y	Electrical admittance
Z	Alternating current impedance

ACKNOWLEDGEMENTS

My doctoral work was performed under the supervision of Dr. Rohan Dharmakumar at the University of California at Los Angeles, Cedars-Sinai Medical Center, and Northwestern University. I am greatly indebted to Dr. Dharmakumar for his enthusiastic guidance, without which this exciting research would have not been possible. His exemplary vision and multi-disciplinary style of solving research problems have been instrumental in publishing so many high-impact research articles in my doctoral work. I am privileged to have had Dr. Daniel Ennis, Dr. Michael Fishbein, Dr. Zhilin Qu, and Dr. Albert Thomas in my PhD advisory committee, whose invaluable guidance has helped me in improving the quality of my dissertation.

This dissertation is a product of highly multi-disciplinary collaborations among different teams with varied skill sets. I particularly acknowledge the important contributions of Dr. Ivan Cokic, Dr. Behzad Sharif, and Hsin-Jung Yang in my research. It has been my pleasure working closely with you all.

I thank Dr. Andreas Kumar from Laval University for several fruitful discussions regarding the pathophysiology of myocardial infarctions. I thank Dr. Sumeet Chugh from the Cedars-Sinai Heart Institute and Dr. Warren Jackman from the University of Oklahoma Heart Rhythm Institute for providing exceptional guidance in the electrophysiology studies. I thank Dr. James White from the London Health Sciences Center for providing the invaluable ICD patient data. I thank Dr. Hyuk-Jae Chang from the Yonsei University College of Medicine for providing access to chronic myocardial infarction patients. I also thank Dr. Xiaoming Bi and Dr. Bruce Spottiswoode from Siemens Healthcare for providing several WIP sequences used in this dissertation in a timely fashion. I thank Dr. Sotirios Tsaftaris from IMT Institute of Advanced

Studies, Lucca and Dr. Mourad Tighiouart from the Cedars-Sinai Medical Center for teaching me several biostatistical methods that have been extensively used in this research.

I sincerely thank the Biomedical Imaging Research Institute at Cedars-Sinai Medical Center for providing a conducive research environment and invaluable resources for my doctoral work. Many thanks to Dr. Debiao Li and his research team at the Cedars-Sinai Medical Center for their vital research guidance during the weekly seminars and periodic research presentations. I sincerely acknowledge my colleagues Dr. Zhaoyang Fan, Dr. Jianing Pang, Dr. David Chen, Dr. Christopher Nguyen, and Dr. Yibin Xie for the fruitful project discussions. I also acknowledge the research support that I have received from the American Heart Association in the form of predoctoral fellowship.

I thank Dr. Richard Tang and Adrian Glenn for the complex animal surgeries, and Laura Smith for teaching me the nuances of cardiac MRI scanning techniques. I thank Dr. Xiangzhi Zhou, Dr. Veronica Rundell, Dr. Ying Liu, and Swati Gupta for their research assistance during my doctoral work at Northwestern University.

Above all, I thank my parents, Padmavathi and Surya Prakash, my grandparents, Venugopala Rao, Swarna Kumari, Ramakrishna, and Subashini, and my brother, Harish for their unwavering love and support. This dissertation, as well as the various awards and fellowships that I have received during my doctoral research, stand as a testimony to the sacrifices my parents had to make to provide me excellent education. I would also like to thank my fiancée Samyukta, who always stood by me in good and tough times. Her steadfast patience and constant appreciation of my hard work have played an inspiring role in my research career. She has been a true companion in all my endeavors and no word can justify my gratitude towards her.

BIOGRAPHICAL SKETCH

Education

Master of Science in Biomedical Engineering, Northwestern University, Evanston, IL 2009

Bachelor of Engineering in Biotechnology, Birla Institute of Technology, Ranchi, India 2008

Peer-Reviewed Journal Publications

1. **Kali A***, Kumar A*, Cokic I*, Tang R L, Tsaftaris SA, Friedrich MG, Dharmakumar R. Chronic Manifestation of Post-Reperfusion Intramyocardial Hemorrhage as Regional Iron Deposition – A Cardiovascular MR Study with Ex-vivo Validation. Circulation: Cardiovascular Imaging, 2013, 6(2): 218-228. (*equal contribution)
2. **Kali A**, Kumar A, Tang RL, Min J, Dharmakumar R. Detecting Acute Reperfusion Myocardial Hemorrhage with CMR: T_2 vs. T_2*. Radiology, 2013, 269(2): 387-395.
3. **Kali A***, Cokic I*, Wang X, Tang RL, Yang HJ, Thajudeen A, Shehata M, Amorn AM, Enzhao L, Stewart B, Bennett N, Harlev D, Tsaftaris SA, Jackman WM, Chugh SS, Dharmakumar R. Iron Deposition Following Chronic Myocardial Infarction as a Substrate for Cardiac Electrical Anomalies: Initial Findings in a Canine Model. PLoS One, 2013, 8(9): e73193 (*equal contribution)
4. **Kali A**, Cokic I, Tang RL, Yang HJ, Sharif B, Marban E, Li D, Berman D, Dharmakumar R. Determination of Location, Size and Transmurality of Chronic Myocardial Infarction without Exogenous Contrast Media Using Cardiac Magnetic Resonance Imaging at 3T. Circulation: Cardiovascular Imaging, 2014, 7(3): 471-481.
5. Yang HJ, Tang RL, Cokic I, Klein M, **Kali A**, Sharif B, Smith L, Tang J, Tsaftaris S, Li D, Conte AH, Fisher J, Yumul R, Dharmakumar R. Assessment of Myocardial Reactivity to

Controlled Hypercapnia with Free-Breathing T_2-Prepared Cardiac Blood-Oxygen-Level-Dependent MR. Radiology, 2014, 272(2): 397-406.

6. Yang HJ, Sharif B, Pang J, **Kali A**, Bi X, Cokic I, Li D, Conte AH, Dharmakumar R. Free-Breathing, Motion-Corrected, Highly-Efficient Whole-Heart T_2 Mapping at 3T with Hybrid Radial-Cartesian Trajectory. Magnetic Resonance in Medicine, 2015 (*Published Online Before Print*).
7. Thajudeen A, Jackman WM, Stewart B, Cokic I, Nakagawa H, Shehata M, Amorn AM, **Kali A**, Liu E, Harlev D, Bennett N, Dharmakumar R, Chugh SS, Wang X. Correlation of Scar in Cardiac MRI and High-Resolution Contact Mapping of Left Ventricle in a Chronic Infarct Model. Pacing and Clinical Electrophysiology, 2015, doi: 10.1111/pace.12581 (*Published Online Before Print*).
8. **Kali A***, Choi EY*, Sharif B, Kim YJ, Bi X, Spottiswoode B, Cokic I, Yang HJ, Tighiouart M, Li D, Berman DS, Choi BW, Chang HJ, Dharmakumar R. Native T_1 Mapping at 3T can Characterize Chronic Myocardial Infarctions in Patients. JACC Cardiovascular Imaging, 2015 (*In Press,* *equal contribution).
9. **Kali A***, Cokic I*, Yang HJ*, Yee R, Tang RL, Tighiouart M, Wang X, Jackman WM, Chugh SS, White JA, Dharmakumar R. Malignant Ventricular Arrhythmias in Patients with Chronic Myocardial Infarction and Predictive Value of Iron-Sensitive Cardiac Magnetic Resonance Imaging. Circulation: Cardiovascular Imaging, 2015 (*In Review,* *equal contribution).
10. **Kali A**, Yang HJ, Cokic I, Tang RL, Sharif B, Dharmakumar R. Robustness of Native Myocardial T_1 Maps at 3T for Chronic Infarct Characterization. Journal of Cardiovascular Magnetic Resonance, 2015 (*In Review*).

CHAPTER 1

Myocardial Infarction

Cardiovascular disease (CVD) is the leading cause of morbidity and mortality in the world accounting for 17.3 million deaths a year, representing nearly 30% of all the deaths worldwide (1). The prevalence and incidence of CVD is steadily rising and is expected to reach 23.6 million by 2030. Globally, the annual direct and indirect costs associated with CVD, which includes healthcare expenditures and lost productivity, amounts to a staggering $320 billion. In the United States alone, CVD kills 780,000 people every year, which is equivalent to a death every 40 seconds.

Coronary artery disease (CAD) is the most prevalent form of CVD globally, killing over 375,000 people annually in the United States. Significant narrowing of coronary arteries due to atherosclerotic disease or acute embolic obstruction, which impedes blood flow and oxygen to the myocardium, can result in acute myocardial infarction (AMI), commonly referred to as heart attack (2). Nearly 735,000 people have a heart attack every year in the United States of which 120,000 succumb to it immediately. Nearly 300,000 patients, who survive a heart attack, suffer a recurrent heart attack in their lifetime.

1.1. Pathophysiology of Myocardial Infarction

The occlusion of a coronary artery results in ischemia of the myocardial bed downstream of the infarct-related artery (IRA), which demarcates the area at risk of permanent damage if the IRA remains permanently occluded. The biochemical changes in cardiomyocytes during the ischemia

are well studied. A decreased ATP availability due to loss of oxygen drives the cells into anaerobic metabolism (3-7). This results in intracellular acidosis due to excessive accumulation of H^+ and lactate. Under these conditions, glycolysis and mitochondrial fatty acid metabolism are further hampered. The declined ATP availability also inhibits the transmembrane Na^+-K^+ ATPase pump leading to the efflux of K^+ and influx of Na^+, Cl^{-+}, and water (intracellular edema). Cytosolic Ca^{2+} increases due to the weakened sarcolemma and sarcoplasmic reticulum. This activates a number of intracellular proteases that degrade the myofibrillar structures and impair contractility. Also, elevated Ca^{2+} activates phopholipases that degrade the phospholipid cell membrane and release free fatty acids. The mitochondrial fatty acid metabolism is disrupted as well, and together with the long-chain acyl-CoA and acyl carnitine, the released free fatty acids incorporate into cell membranes and impair function. After a prolonged ischemia, typically around 20 minutes, cardiomyocyte death begins as a wavefront that originates in the endocardium and spreads to the epicardium within the ischemic territory (8). The spread of the necrosis wavefront depends on several factors such as the duration of occlusion, collateral circulation, the rate of oxygen consumption, and any ischemic preconditioning (8-10).

The most obvious and commonly used therapeutic strategy for patients suffering from an AMI is to reopen the occluded coronary artery and re-establish the normal blood flow to the myocardium. Early reperfusion of the infarct-related artery (IRA) using thrombolytics or percutaneous coronary intervention (PCI) is well known to reduce the morbidity and mortality in patients suffering from ST-elevation myocardial infarction (STEMI) (8,11-16). Although the benefits of early reperfusion are well established, the notion that reperfusion itself can cause more myocardial injury (termed as ischemia-reperfusion (I-R) injury) is well accepted in both experimental and clinical settings (17-25). I-R injury manifests in several forms including spate

of ventricular arrhythmias immediately after the reperfusion procedure (26,27), reversible contractile dysfunction (myocardial stunning) (21), inability to fully reperfuse the ischemic bed even after reopening the IRA (known as microvascular obstruction (MO)) (20), and reperfusion-induced cardiomyocyte death (23). Several biochemical factors acting in concert have been implicated in I-R injury, the most prominent of which include sudden burst of oxidative stress post-reperfusion (28,29), intracellular and mitochondrial Ca^{2+} overload (30,31), rapid restoration of physiological pH (32), massive infiltration of inflammatory cells into the infarcted myocardium (33), and rapid opening of the mitochondrial permeability transition pore (34).

The acute phase of myocardial infarction (MI) is characterized by the loss of myocytes and the extracellular connective tissue matrix (35,36). A host of inflammatory cells infiltrate the infarcted myocardium, which is necessary for the clearance of necrotic debris and wound healing (36). Myofibroblasts infiltrate the infarcted territories for the reconstruction of collagen network (35). In the chronic phase of MI (CMI; several weeks post-MI), the entire infarcted territory is replaced by a solid collagenous scar with little cellularity. The left-ventricle (LV) undergoes gross morphological, histological, and molecular changes in both infarcted and viable myocardium that leads to LV remodeling. Long-term LV remodeling in MI patients is characterized by LV chamber enlargement and significant reduction in LV ejection fraction (EF). LV remodeling post-MI is a strong predictor of heart failure (HF), arrhythmias, and sudden cardiac death (SCD) after MI (37).

1.2. Heart Failure and Sudden Cardiac Death in Myocardial Infarction

The improved therapeutic interventions in MI patients have resulted in a 70% decline in deaths in CAD patients (38-41). Alarmingly, there has been a concomitant increase in the incidence of

heart failure (HF) in CAD patients (42). Heart failure (HF) is a common fatal complication in patients with healed MI. The loss of ventricular function in healed MIs can worsen over time, which can reach a point when the heart is unable to pump enough blood to supports the body's demands. This can eventually lead to sudden cardiac death (SCD), which is defined as sudden and unexpected death caused by loss of heart function.

In the United States, nearly 5.1 million patients are currently suffering from HF, with more than 650,000 new cases reported every year (43). HF is the primary or contributory cause of death in nearly 300,000 patients annually, with 1 out of 2 patients succumbing to HF within 5 years of diagnosis (44,45). Heart failure management, which includes hospitalization, physician office-visit and drugs, costs $40 billion annually (46). CAD is the leading cause of HF (47), with a population attributable risk reportedly as high as 62% (48,49). Other studies have shown that CAD was the primary diagnosis in 40-70% of the HF patients (50-57). A range of incidence rates of HF in MI patients has been reported by a number of studies. A study from the Survival and Ventricular Enlargement (SAVE) trial showed that 17% of 412 post-MI patients developed HF at 2 years follow-up (58). Lavine et al showed that 29% of 109 post-MI patients diagnosed between 1988 and 1992 developed HF (59). Patients diagnosed with MI between 1979 and 1988 showed a 41% incidence of HF at a mean of 6.6 years (60,61). The Cholesterol and Recurrent Events (CARE) study of 3860 patients reported a 6.3% incidence of HF at 5 years from the onset of MI (62). Suleiman et al have reported an incidence rate of 10.7% of HF at 23 months following MI in their study of 1044 patients (63). Alarmingly, evaluation of Framingham Heart Study participants showed that the incidence of HF at both 30 days and 5 years HF following MI increased in the recent decades (42).

SCD is the most common cause of mortality in HF patients with an incidence of 300,000 to 400,000 annually in the United States (64). Approximately 80% of patients dying of SCD have underlying coronary heart disease and CMIs are present in more than 75% of all victims. In the majority of cases, SCD is triggered by the onset of ventricular tachyarrhythmia (VA), an abnormally rapid heart rate originating in the ventricle. If undetected and untreated, this can degenerate into asystole leading to hemodynamic impairment causing death (65-67).

1.3. Pathological Features of Myocardial Infarctions

Characterizing pathological features of AMIs and CMIs is of critical importance to evaluate an MI patient's risk to develop adverse cardiac outcomes such as HF and SCD, and to develop evidence-based therapeutic strategies for treating the patients. LV remodeling is the most straightforward measure of cardiac dysfunction and a strong predictor of mortality post-MI. Several studies have shown the prognostic significance of LV end-diastolic volume (EDV), end-systolic volume (ESV), and ejection fraction (EF) for predicting mortality in MI patients (68-70).

Before the advent of non-invasive imaging techniques, characterizing MI tissue was performed exclusively during post-mortem examination by pathologists. Therefore, the clinical significance of MI characteristics and their relevance in developing new treatments was largely unexplored for a long time. Over the past three decades, widespread use of non-invasive imaging in clinical decision-making has revealed a number of MI characteristics with significant additive utility in predicting short-term and long-term outcomes. The most prominent features including myocardial viability, edema, MO, and intramyocardial hemorrhage are discussed below.

1.3.1. Myocardial Viability

The success of reperfusion strategies in MI patients is determined by the extent to which the spread of myocardial necrosis wavefront is limited, and the amount of myocardium that is potentially salvaged. In this setting, differentiation of viable myocardium from infarcted myocardium is essential to understand whether the reperfusion strategy would be able to salvage any ischemic myocardium.

Evaluating myocardial viability is also important in the setting of myocardial hibernation and stunning, two common pathophysiological features observed in MIs. Hibernating myocardium refers to ischemic, but viable, myocardial segments with depressed contractile function, which recovers to normal upon reperfusion (71-77). Myocardial hibernation is a mechanism by which ischemic myocardial segments down-regulate energy utilization to survive ischemia at the expense of contractile function (78-80). Myocardial stunning is a form I-R injury in which ischemic myocardial segments that have not been irreversibly damaged demonstrate severe contractile dysfunction for a long period even after complete restoration of blood flow through reperfusion (21,81-83). As mentioned, myocardial stunning is a form of I-R injury caused by sudden burst of oxidative stress (28,29) and increased intracellular Ca^{2+} overload (30,31) following reperfusion. The contractile function in stunned myocardium and the electrocardiographic (ECG) pattern are restored after several hours to weeks post-reperfusion. Understanding myocardial viability is also critical in CAD patients who demonstrate significant akinetic or hypokinetic myocardial segments, as such patients may still be candidates from reperfusion rather than heart transplantation (84).

Several studies have investigated the prognostic value of myocardial viability in AMI patients. Meta-analyses of 24 non-randomized studies in MI survivors with EF$\leq$ 40% have

shown that myocardial viability is an independent predictor of survival rate in MI patients with LV dysfunction (46,85). Interestingly, these studies have shown that reperfusion of ischemic myocardium offers no benefits in terms of survival when there is no significant viability. A similar analysis of the same non-randomized studies has shown that in the absence of myocardial viability, there is no difference between different reperfusion strategies in terms of survival benefits (86). In a prospective cohort of 167 MI patients, Desideri et al have reported that myocardial viability, evaluated using FDG-PET, is an independent predictor of survival rate only if the extent of viable myocardium exceeds 20% of the entire LV (87). In contrast, the Surgical Treatment for Ischemic Heart Failure (STICH) trial has shown that myocardial viability, evaluated using SPECT and/or Dobutamine Stress Echocardiogram, is not clinically useful in determining which patients would benefit from reperfusion compared to medical therapy alone (88). Recently, Gerber et al have demonstrated in 144 patients that myocardial viability, evaluated using Late Gadolinium Enhancement (LGE) Magnetic Resonance Imaging (MRI), is an independent predictor of adverse LV remodeling and mortality before reperfusion (89). Other studies using LGE MRI have shown that the location and size of infarct are important predictors of post-MI LV remodeling, LV dysfunction, and death (90-92).

In patients with healed MIs and symptomatic HF, assessment of myocardial viability was also shown to have significant prognostic significance. The presence of scar in MI patients with significantly low EF has shown to be a prognostic indicator of survival (93). Using LGE MRI, Lonborg et al have shown that infarct size measured in 309 STEMI patients at 3 months post-MI was a significant and independent predictor of all-cause mortality and HF hospitalization (94). The same study has also shown that infarct size in healed MIs has additive prognostic value in combination with EF and LV volumes for prediction of adverse cardiac events. Analysis of the

Gruppo Italiano per lo Studio della Sopravvivenza nell'Infarto Miocardico (GISSI) trial has shown that infarct size measured on the basis of number of ECG leads with ST-segment elevation is an independent predictor of in-hospital outcome (95). Klem et al have shown that the scar size is an independent predictor of malignant ventricular arrhythmias (mVA) in MI patients implanted with cardioverter defibrillators (96). Several studies have also investigated the prognostic significance of infarct location and transmurality with adverse LV remodeling and adverse outcomes (14,97-101). Anterior MIs have been shown to cause more adverse LV remodeling, and thereby worse prognosis compared to patients with non-anterior MIs (102-106). Orn et al have shown that infarct size is the strongest predictor of long-term EF and LV volumes independent of infarct location and transmurality (107).

1.3.2. Myocardial Edema

Myocardial edema is the first and foremost pathophysiological phenomenon observed during myocardial ischemia. The altered ion transport systems and myocyte permeability to ions during ischemia results in increased intracellular osmolarity and influx of water into the cells, leading to moderate intracellular edema. The myocyte sarcolemma also loses its mechanical resistance due to protein digestion by the Ca^{2+} activated proteases. During reperfusion, the extracellular osmotic pressure is rapidly normalized and this leads to greater cell swelling. Together with the mechanical stress of myocytes contraction, the weakened sarcolemma is easily disrupted leading to cell necrosis and lethal reperfusion injury (23,108). These mechanisms are further corroborated by the observations that highly osmotic reperfusion reduces the myocytes swelling and the mechanical stress, thereby limiting myocardial necrosis (109-112).

Severe ischemia disturbs the myocardial fluid homeostasis, which leads accumulation of water in the myocardial interstitium. Fluid enters the interstitium through the microvascular exchange bed, while it leaves through the myocardial lymphatic system. In a healthy myocardium, the flux with which the fluid enters the cardiac interstitium is balanced by the flux with which it leaves the interstitium (113). During I-R injury, the fluid entry through microvascular exchange rapidly increases due to endothelial injury and increase in capillary permeability (108). The flux of fluid into the lymphatic system from the interstitium is significantly reduced due to impaired LV contractility (114). This imbalance results in excessive accumulation of the fluid in the interstitium, leading to interstitial edema.

Various studies have shown that the area of myocardial edema is consistently larger than the area of irreversible injury (115,116). A plausible explanation is that the area of irreversible injury (necrotic myocardium) is surrounded by an area of salvageable reversible injury that is edematous (area-at-risk). It is now believed that, similar to myocardial necrosis, myocardial edema also spreads as a wavefront from the subendocardium to epicardium, and this wavefront precedes that of the myocardial necrosis (117). Using Magnetic Resonance Imaging (MRI), Abdel-Aty et al. have shown that edema occurs even before the onset of myocardial necrosis and can be used as an early marker of MI (117). Edema has also been shown to completely resolve within a few weeks post-MI, and can be used as a marker for differentiating AMIs from CMIs (118).

While the pathophysiological effects of myocardial edema during reperfusion injury has not been extensively studied, its role in LV dysfunction has been well studied in other clinical conditions such as pulmonary artery hypertension (119), cardiopulmonary bypass (120), coronary sinus hypertension (121), warm blood and cold blood cardioplegia (114), and blocking

of β-adrenergic receptors (122). Laine and Allen have shown that, for a given preload, a 3.5% increase in myocardial water content reduced the cardiac output by 40% (123). Myocardial edema also increases the cardiac chamber stiffness resulting in reduced LV compliance (124-128). Together with LV contraction against accumulated viscous water, reduced LV compliance increases the cardiac energy requirements in a setting where the availability of ATP is already low (129). Additionally, the interstitial edema decreases the diffusion capacity of oxygen, and increases the distances through which oxygen has to diffuse to reach the myocytes (130). This further drives the myocytes into an ischemic state. Myocardial edema has also been shown to trigger interstitial cardiac fibrosis (123,131). Recent studies using MRI have shown that myocardial salvage (difference between area-at-risk and area of myocardial necrosis) is a strong predictor of adverse LV remodeling (132-134).

1.3.3. Microvascular Obstruction

While recanalization of the occluded coronary artery is well known to reduce the morbidity and mortality of the patients suffering from ST-elevation myocardial infarction (STEMI) (8,11-16), the success of reperfusion is often diminished by a persistent post-procedural reduction of tissue perfusion on a microvascular level (20,135). This phenomenon, called microvascular obstruction (MO) and clinically reflected as “no-reflow” or “slow reflow”, has been shown to be prevalent in 30-80% of the patients with reperfused AMIs (136-149).

Numerous studies have investigated the no-reflow phenomenon. In a landmark study, Kloner and colleagues showed in dogs, that blood flow could be completely restored after 40 minutes of coronary artery occlusion, but not after 90 minutes of occlusion (20). Kloner and colleagues argued that endothelial swelling, endothelial protrusions, and intraluminal fibrin and

platelet deposits are the sources of capillary obstruction limiting blood flow. Other studies have demonstrated that the potential mechanisms of no-reflow include leukocyte plugging of microvasculature (150-155), mechanical compression of microvasculature due to myocyte swelling (156), intracoronary accumulation of fibrin/fibrinogen and platelets (157-159), extensive production of reactive oxygen species during reperfusion (160-163), and thrombi embolizing into the microvasculature (164). Kloner et al further showed that while irreversible cardiomyocyte damage is apparent at 20 minutes of ischemia, capillary damage lagged behind and was only visible after 60 minutes of coronary occlusion (165). Capillary damage could therefore be regarded as a more severe form of ischemic tissue damage. Independent studies showed that the area of MO expanded by 3-fold between 2 minutes and 3.5 hours post-reperfusion in dogs (166), and between 2 minutes and 8 hours post-reperfusion in rabbits (167). In a study using MRI, expansion of the no-reflow zone was demonstrated in dogs examined at 2, 6, and 48 hours after reperfusion (168) suggesting that MO may follow a similar time-dependent pattern as the "wave-front-phenomenon", as initially described for cell death by Reimer and Jennings (8). These findings show that MO is likely caused by severe and/or prolonged ischemic damage and follows myocyte necrosis.

Conflicting observations exist regarding the changes in the MO size during the acute and subacute phases post-reperfusion with some studies showing no changes in MO size between 2 days and 9-10 days post-reperfusion (148,169), and other studies showing decrease in MO size at 1 week post-reperfusion (143,170). Differences in these observations have been attributed to the severity of MO and the structural or functional nature of MO (171,172). Several non-invasive imaging studies have shown that MO can persist up to 1-month post-reperfusion (173-175). Long-term persistence of MO has been associated with poor regional wall motion, scar thinning,

infarct expansion, and reduced capillary density (173,175). In patients, early resolution of MO has been associated with improved long-term LV function and prognosis (146,174,176,177).

The prognostic clinical outcome of MO in patients with reperfused AMIs has been evaluated in a number of clinical studies (136-138,140,142,145-147,149,178-180). MO measured by CMR in the first week post-reperfusion has been associated with larger infarct size, reduced myocardial salvage, larger LV volumes and reduced LV EF. MO was also shown to be an independent predictor of long-term major adverse cardiovascular events such as cardiovascular death, reinfarction, congestive heart failure, stroke and unstable angina (141). More recently, the percentage of infarcted myocardium that has MO was shown to be a more powerful predictor of major adverse cardiovascular events . Experimental animal studies have shown that MO was associated with thinner infarcts, infarct expansion, reduced longitudinal myocardial stretching, reduced radial thickening, and reduced first principal strain (169,175). These results suggested that increased myocardial stiffness and reduced elasticity possibly lead to poor LV remodeling. Also, impediment of blood flow in MO may not allow inflammatory cells to reach the MO core for infarct healing, and limit collateral blood flow to the core (181).

1.3.4. Intramyocardial Hemorrhage

Intramyocardial hemorrhage is a consequence of severe microvascular injury post-reperfusion and is closely related to MO. Hemorrhage is characterized by rapid disruption of severely injured microvasculature and extravastion of blood into the myocardial interstitium. Hemorrhage has been widely reported to be associated with larger MIs and MO in animal models (182-187), as well as in humans after PCI (173,188,189), coronary artery bypass graft (CABG) surgery (190) and thrombolytic therapies (189,191,192).

Intramyocardial hemorrhage is a common, but not a mandatory consequence of MO. Using canines, Kloner *et al* demonstrated that after 2 hours of coronary artery occlusion and subsequent reperfusion, gross hemorrhage can be observed within the AMI zones (193). The hemorrhagic zone was consistently located in the subendocardium, covered on average 40% of the necrotic tissue, and was surrounded by a rim of necrotic, but non-hemorrhagic myocardium. In a complementary study in swine, Capone and Most demonstrated that short-term ischemia followed by reperfusion does not result in hemorrhage, but prolonged ischemia followed by reperfusion results in significant intramyocardial hemorrhage (183). Higginson and colleagues observed in dogs, that hemorrhage occurs in 75% of reperfused MIs, but never in MIs with permanent coronary occlusions (194). In another study, it was shown that hemorrhage expands as a second wave within the more rapidly evolving MO zone (167). Fishbein et al have shown that hemorrhage is confined to the zone of MO and thus may be a consequence of pre-existing ischemic microvascular injury (184). Hence, hemorrhage is a consequence of severe microvascular ischemic damage, occurring as a complication of reperfusion, and it may occur in a similar pattern to that of myocyte injury, originating in the subendocardium and becoming transmural over time.

It has been suggested that reperfusion hemorrhage may lead to infarct expansion and delayed infarct healing. Lie et al showed that hemorrhagic MIs were substantially larger, affecting more than 50% of left ventricular muscle, than non-hemorrhagic MIs in patients (190). They demonstrated that the hemorrhagic zones seemed to form “intramural dissecting tracts” beyond the area of MI, with myocardial necrosis at the border zone, and the formation of granulation tissue was delayed in hemorrhagic versus non-hemorrhagic MIs. Bresnahan *et al*, using canines, showed that when hemorrhage was present, the infarct was nearly 70% larger than

if there were no hemorrhage (182). Roberts *et al*, also using a canine model, found that in reperfused hemorrhagic MIs, as opposed to in non-reperfused MIs, polymorphonuclear granulocyte infiltration is significantly reduced at day 3, suggesting adverse effects on LV remodeling (195). More recently, several studies have shown that patients with hemorrhagic MIs have increased LV EDV and ESV, lower EF and lower systolic wall thickening at 3-4 month follow-up than patients with non-hemorrhagic MIs (196-199). Eitel *et al* have shown that hemorrhage is an independent predictor of death, re-infarction and congestive heart failure at 6 months post-reperfusion (141).

Although the mechanism by which intramyocardial hemorrhage leads to adverse LV remodeling is not fully understood, results from recent studies can be used to shed light on hemorrhage-mediated infarct expansion. Hemorrhage, a byproduct of intravascular hemolysis, is expected to exasperate infarct expansion by furthering ischemic damage through efficient scavenging of nitric oxide, a vasodilator actively produced by the endothelial cells lining the capillaries. As the nitric oxide is removed, reactive hyperemic responses that increase vascular O_2 through "fight-or-flight" mechanisms are diminished, leading to a negative feed-back loop that sustains ischemic conditions that propel infarct expansion (200).

1.4. Detection and Quantification of Pathological Features in Myocardial Infarction

A number of invasive and non-invasive techniques have been investigated for detecting and quantifying different pathological features in MI patients. The following is a brief summary of

the different techniques for detection and quantification of myocardial viability, edema, MO, and intramyocardial hemorrhage.

1.4.1. Detection and Quantification of Myocardial Viability

Electrocardiography (ECG) markers such as ST-segment elevation under stress (201,202), reciprocal ST-segment depression (203), ST-segment elevation with pseudonormalization of negative T waves (204), and low QT dispersion (205) were shown to indicate myocardial viability. However, the sensitivity and specificity of ECG markers are modest relative to other non-invasive imaging modalities. Moreover, ECG markers are only indirect measures of myocardial viability.

Non-invasive imaging of myocardial viability using Single-Photon Emission Computed Tomography (SPECT) has been shown to be a significant predictor of LV function recovery post-reperfusion (206), event-free survival post-CABG (207), and short-term (208) and long-term adverse cardiac events (209). Major limitations of SPECT imaging include poor spatial resolution and use of harmful ionizing radiation. Due to its limited resolution, it cannot effectively defect subendocardial infarcts. A meta-analysis of thallium and Technetium-99m–tetrofosmin studies has shown high sensitivity, but moderate specificity (210), likely due to its inability to detect subendocardial infarcts (211).

Fluorine-19 Deoxy Glucose (FDG) Positron Emission Tomography (PET) is a commonly used imaging technique for evaluating myocardial viability. The strength of PET lies in a plethora of radioactive tracers available for studying different pathologies and better spatial resolution than SPECT (212-214). However, the spatial resolution is still not adequate to detect subendocardial infarcts. Similar to SPECT, PET requires the use of harmful ionizing radiation.

As with SPECT, PET has high sensitivity, but moderate specificity for predicting LV function recovery post-reperfusion on the basis of viability imaging (215-217).

Dobutamine Stress Echocardiography (DSE) has also been shown to detect viable but dysfunctional myocardium (218). However, Pagano et al have show that the technique fails when the regional LV dysfunction is severe (216). Pooled meta-analyses have shown that, relative to SPECT, the technique has good specificity but poor sensitivity (219). Major drawbacks of DSE include poor contrast-to-noise ratio (CNR), poor spatial resolution, highly subjective interpretation of DSE data (220), poor acoustic window for imaging lateral wall (221), and poor endocardial delineation (214). Myocardial contrast echocardiography (MCE) based evaluation of myocardial perfusion post-reperfusion has been shown to be a strong predictor of subsequent functional recovery (222). In combination with DSE, MCE-based microvascular perfusion patterns have been shown to indicate myocardial viability (176). However, the technique has low predictive value when used alone (223,224).

Late Gadolinium Enhancement (LGE) MRI, has superior resolution compared to PET and SPECT, and thereby can detect very small infarcts. In combination with cine MRI and perfusion MRI, LGE has been shown to predict LV function recovery post-reperfusion in several studies (225-228). LGE MRI has shown comparable diagnostic performance to DSE, SPECT, and PET (211,229,230). The concept, utility, and limitations of LGE MRI are discussed in significant detail in chapter 2.

1.4.2. Detection and Quantification of Myocardial Edema

The most direct approach to quantify myocardial water content in experimental studies is the gravimetric method in which the wet and dry weight calculations of the tissue are used

(119,121,123,130). Due to the invasive nature of this method, it cannot be applied to clinical settings. As a result, non-invasive methods have become reliable tools to assess myocardial edema. Myocardial edema results in a 10% increase in LV wall thickness. Given that the normal adult LV wall thickness is about 10-12mm, a robust non-invasive imaging method should reliably detect a 1mm change in wall-thickness. Computed tomography (CT) has been proposed for sequential quantification of myocardial edema (231). However, CT is limited by the use of ionizing radiation and inadequate spatial resolution to detect 1mm change in wall thickness. Echocardiography has been proposed as a simple tool for assessing myocardial edema (120,128,232), but it also suffers from inadequate spatial resolution for detecting minute changes in wall thickness. MRI has become an increasingly valuable tool as it not only relies on the increase in wall thickness to detect edema, but it is also sensitive to change in the water content in the tissue of interest. Myocardial segments affected by edema appear bright on T_2-weighted MRI due to the long T_2 relaxation of free water bound protons (233-237). Myocardial edema detected on the basis of T_2-based MRI has been shown to be a significant predictor of major adverse cardiovascular events (134).

1.4.3. Detection and Quantification of Microvascular Obstruction

Early studies using coronary angiography to assess the success of reperfusion therapy defined a Thrombolysis in Myocardial Infarction (TIMI) flow grade ≤ 2 post-reperfusion in the absence of a residual obstructive lesion as "angiographic no-reflow" (238). However, angiographic definition of MO is subjective in nature. Objective angiographic methods such as corrected TIMI frame count have been developed (239). Nevertheless, angiography only measures perfusion in the epicardial artery that may not be necessarily synonymous with microcirculation (240,241).

Myocardial blush grade evaluates myocardial perfusion at the capillary level on the basis myocardial contrast density post-reperfusion. However, it is also suspected to not directly reflect microcirculation as the wash-in and wash-out kinetics of contrast dye are significantly influenced by capillary permeability, capillary resistance and interstitial edema.

ECG markers such as absence of complete ST-segment recovery post-reperfusion in patients despite having a patent culprit artery and TIMI flow grade 3 has been associated with microvascular dysfunction (145,242-250). However, a standard definition of ST-segment recovery does not exist, and different studies used varied criteria for this measurement (251-253). A patent infarct-related artery with terminal T-wave inversion has also been associated with MO (254-256). ECG-based markers are, however, only indicative of patent culprit artery and have not been well validated to depict MO. Moreover, these measurements are limited by low diagnostic accuracy, operator dependency, and temporal variability (249,257).

Few studies have also demonstrated the feasibility to detect MO using Thallium-201 and Techentium-99m-pyrophosphate SPECT (258,259). As mentioned earlier, this modality is significantly limited by poor spatial resolution and use of ionizing radiation. More recently, the utility of contrast-enhanced multidetector CT for detecting microvascular obstruction has been evaluated (260-262). However, multidetector CT is primarily limited by low CNR and use of ionizing radiation.

Changes in coronary blood flow velocity patterns measured using contrast-enhanced echocardiography (222,263-269) and Doppler guide-wire assessment (263,264,268,269) have been associated with MO, poor LV function, and long-term adverse cardiac events in patients with reperfused MIs. Angiographic and coronary blood flow velocity methods for determining microcirculation are primarily performed within hours after recanalization of the culprit artery at

which point microcirculation is known to be hyperemic and microvascular damage is known to be dynamic and still evolving. Therefore, echocardiography techniques are not suited for evaluating stable MO, which evolves after a few days post-reperfusion. MCE using intracoronary or intravenous infusion of microbubbles has been previously used to determine myocardial perfusion and MO post-reperfusion (241,270-273). However, the technique is limited by poor CNR, poor spatial resolution, subjective interpretation of the images, and inability to visualize lateral wall (270,272).

MRI techniques have been increasingly used for the temporal assessment of myocardial perfusion following the advent of Gadolinium-based contrast agents (GBCAs) (274,275). Early studies using experimental animal models have shown that the myocardial region that remained hypoenhanced following 2 minutes of Gadolinium bolus correlated closely with the anatomical no-reflow determined using thioflavin-S administration (276-278). Thereafter, first-pass perfusion CMR techniques have been developed in which the Gadolinium arrival and distribution kinetics were measured over the first minute immediately following contrast delivery (146,149,279-282). MO observed using the first-pass perfusion technique, also known as "early MO", has been shown to correlate well with histopathological observations (148,277). However, early MO may be an overestimate of the true microvascular dysfunction as the presence of any significant epicardial stenoses may delay the downstream contrast delivery (171). First-pass perfusion techniques also suffer from poor spatial resolution, incomplete LV coverage, and low signal-to-noise ration (SNR).

More recently, Early Gadolinium Enhancement (EGE) and LGE techniques are being increasingly used to detect MO (136-138,142,145-147,178-180). MO is detected as hypointense core within hyperintense infarcted territories at ~2-5 minutes following contrast administration

on EGE images, and at ~10-15 minutes following contrast administration on LGE images. These techniques offer full LV coverage at high spatial resolution and SNR. Since Gadolinium is an extravascular agent, increasing amounts of contrast medium can extravasate into the initially hypoenhanced region with time. Therefore, LGE images are less sensitive to smaller MO and may underestimate MO size relative to first-pass perfusion images (144,279,282). MO seen on LGE images is referred to as "late" or "persistent" MO, and its size has been shown to be temporally less variable than early MO (144). Late MO was also shown to be more powerful predictor of LV function recovery in reperfused AMI patients and major adverse cardiovascular events than early MO (138,140,142,145-147,179). These results suggested that late MO reflects a more severe form of microvascular injury, while early MO may depict regions with reduced residual blood flow.

1.4.4. Detection and Quantification of Intramyocardial Hemorrhage

Until recently, non-invasive imaging methods for detecting reperfusion intramyocardial hemorrhage in-vivo were not available. Therefore, studies of reperfusion hemorrhage solely relied on autopsy data, were primarily observational descriptions, and limited in size (190-192,283,284). Recently, both T_2-weighted and T_2*-weighted MRI have been shown to non-invasively discriminate between hemorrhagic and non-hemorrhagic MIs. When red blood cells are extravasated into the myocardial interstitium in hemorrhage, oxyhemoglobin is reduced to deoxyhemoglobin in <48 hours (285). Deoxyhemoglobin is paramagnetic, and therefore causes local magnetic field inhomogeneities that appear as signal losses in both T_2-weighted and T_2*-weighted MRI (286). Early ex-vivo studies have shown that both T_2-weighted and T_2*-weighted MRI signal changes are well correlated with the occurrence of hemorrhage (287,288). However,

ex-vivo studies by Lotan et al have shown that the high intrinsic sensitivity of T_2-weighted MRI to post-reperfusion myocardial edema, which appears as bright territories on T_2-weighted images, may reduce the conspicuity of hemorrhage (289).

Over time, different research groups have advocated the use of either T_2-weighted or T_2*-weighted MRI for in-vivo detection of myocardial hemorrhage. Payne et al have shown that T_2-weighted signal losses in reperfused AMI has high diagnostic accuracy for hemorrhage (290), while Eitel et al have shown that the same signal losses are important predictors of major adverse cardiovascular events (141). Studies by Ochiai et al (291), O'Regan et al (199,292) and Kumar et al (293) have shown the feasibility of T_2*-weighted MRI for detecting intramyocardial hemorrhage. Importantly, O'Regan et al have shown that extensive edema in reperfused AMI can completely mask out small hemorrhages in T_2-weighted images (199). While no consensus exists regarding the optimal technique for characterizing intramyocardial hemorrhage, T_2*-weighted MRI is considered to be the gold standard technique to detect hemorrhage in the brain (285,294,295).

CHAPTER 2

Magnetic Resonance Imaging: Principles and Applications in Myocardial Infarction Imaging

In this chapter, a brief overview of the physics and principles of magnetic resonance imaging (MRI) are provided. The primary focus of this chapter is the interaction of hydrogen nuclei with strong static magnetic fields and radio-frequency (RF) pulses. The chapter further discusses different nuclear relaxation techniques and their applications in detecting and characterizing MIs. The chapter discusses the current state-of-art MRI techniques for characterizing MIs, with special emphasis on Late Gadolinium Enhancement (LGE) Imaging. Unless specifically mentioned, most of the sections here were distilled from well-known texts in MRI (296-300).

2.1 Interactions of Hydrogen Nuclei with External Magnetic Fields

Nearly 65% of the human body is composed of water molecules, which contain two hydrogen atoms and an oxygen atom each (301). In the nucleus of an atom, the protons or neutrons tend to form pairs of opposite spin angular momentum, thereby balancing out the net angular momentum of the nucleus to zero. In a nucleus with both even number of protons and neutrons, all protons and neutrons have pairs with opposite angular momentum, which cancel out the net angular momentum. If a nucleus contains odd number of protons and/or neutrons, there is a net non-zero angular momentum due to the last unpaired proton and/or neutron. Examples of naturally occurring atomic nuclei with net non-zero magnetic moment include ^{1}H, ^{23}Na, and ^{31}P.

Each nucleus with a non-zero magnetic moment (spin) can have either of two quantum energy states, +1/2 (up-state) and -1/2 (down-state). In the absence of an external magnetic field and under thermal equilibrium, the number of spins in each of these states is equal. Moreover, each spin is oriented along random directions, and the net magnetic moment of all the spins in a given voxel average out to zero. In the presence of a strong static external magnetic field, nuclei with net non-zero magnetic moment (spins) precess about the direction of the external magnetic field (referred to as longitudinal direction) like a spinning top (Figure 2.1). The angular frequency (ω_0, known as Larmor frequency) with which the spins precess about the external magnetic field is determined by the gyromagnetic magnetic ratio (γ) and strength of the external magnetic field (B_0) according to the below equation.

$$\omega_0 = \gamma B_0 \qquad (2.1)$$

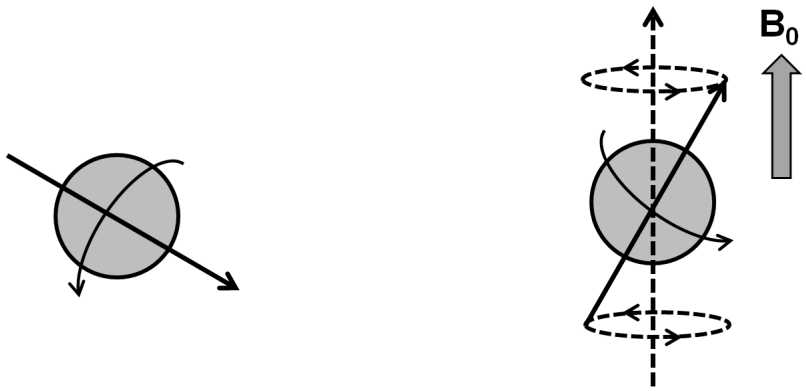

Figure 2.1: *Interaction of a hydrogen nucleus (spin) with external static magnetic field.* In the absence of an external static magnetic field, a spin is oriented randomly in space. When a strong external magnetic field B0 is applied, the spin precesses about the direction of the external magnetic field like a spinning top.

The gyromagnetic ratio for ^{1}H nucleus in water is 42.6 MHz/T. At an external magnetic field strength of 1.5T, the spins precess at an angular frequency of 63.9 MHz.

Depending on the energy state of a given spin, the spin aligns either parallel to or anti-parallel to the longitudinal direction. Under the influence of B_0, a non-zero thermal equilibrium is reached and the number of spins in the up-state is slightly larger than that in the down-state. This difference in the spin population between two energy states results in a net magnetization (M_0) in the longitudinal direction. The excess number of spins between the two energy states is only a millionth fraction of the total number of spins. However, there is Avogadro number (6.022×10^{23}) of water molecules in a single unit volume, which collectively give a measurable M_0 that is detected as MRI signal. Moreover, M_0 increases proportionally with the strength of the external static magnetic field. Therefore, higher magnetic field strengths are preferred to increase the magnitude of the detected signal, albeit at the expense of incurring several other technical limitations.

2.2. Nuclear Magnetic Relaxation

To detect the M_0, the magnetization is manipulated by a series of RF pulses operating at the Larmor frequency in a direction perpendicular to the longitudinal direction. For illustration purposes, two frames of reference are defined to simplify the visualization of the M_0's interaction with the RF pulses. In the standard laboratory frame of reference, M_0 precesses freely about the longitudinal axis of B_0 at the Larmor frequency ω_0. Assume a second frame of reference, which is rotating about the longitudinal axis of B_0 at the Larmor frequency ω_0. In the rotating frame of reference, M_0 can be considered to be a static vector pointing in the longitudinal direction. In this frame of reference, any RF pulse applied in a direction perpendicular to the longitudinal creates a resonance condition, and M_0 can be tipped by arbitrary angles (referred to as flip angle (α)) depending upon the strength and the duration of the RF pulses.

2.2.1. Spin-Lattice Relaxation

Once the RF pulse has been applied, M_0 recovers back to the equilibrium position at a rate determined by the time constant T_1. This relaxation of M_0 to the longitudinal direction is known as spin-lattice relaxation. The tipping of M_0 away from the longitudinal direction, and its relaxation back to the longitudinal direction are illustrated in Figure 2.2.

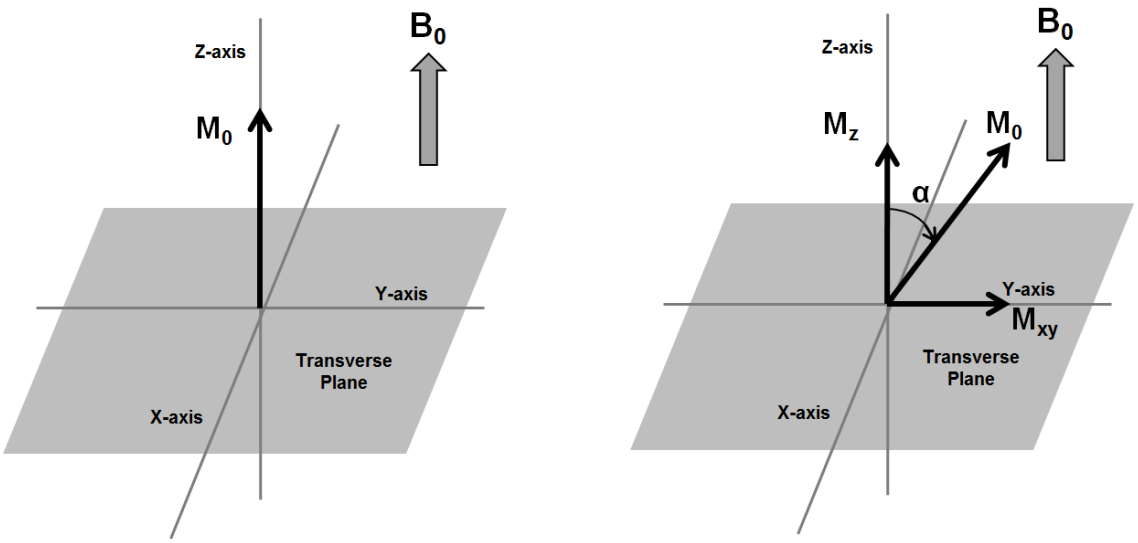

Figure 2.2: *Spin-lattice relaxation.* At equilibrium, the net magnetization M0 is oriented along the direction of the external magnetic field B0 (z-axis). When an RF pulse is applied perpendicular to the z-axis, M0 can be tipped away from z-axis towards the transverse x-y plane. The M0 can be resolved into two orthogonal components - Mz, the longitudinal component, and Mxy, the transverse component. When the RF pulse is turned off, M0 relaxes back to its original equilibrium position, which is known as spin-lattice relaxation.

When M_0 is tipped away from the longitudinal axis (z-axis) and towards the transverse plane (x-y plane) by an angle α, the magnetization vector can be resolved into two orthogonal components – the longitudinal component (M_z) and the transverse component (M_{xy}). The longitudinal component at a given time t is then determined by the following equation.

$$\frac{dM_z}{dt} = \frac{1}{T_1}(M_0\text{-}M_z) \qquad (2.2)$$

When the magnetization is completely tipped to the transverse plane, the longitudinal component at a given time t is given by the following equation.

$$M_z(t) = M_0.\exp(1 - t/T_1) \qquad (2.3)$$

The spin-lattice relaxation occurs by two independent mechanisms known as spontaneous and stimulated emission. In spontaneous emission, which is a very slow process with $T_1 \approx 10^{15}$ s, an individual hydrogen nucleus relaxes to equilibrium without any interaction with the surrounding lattice. In stimulated emission, which is much faster than the spontaneous emission with $T_1 \approx 1$ s, a spin experiences rapid vibrational and translational motions. This creates a fluctuating magnetic field that dissipates the energy from the spin into the surrounding lattice.

2.2.2. Spin-Spin Relaxation

In the transverse plane, the spins experience a different type of relaxation called the spin-spin relaxation, which is independent of the spin-lattice relaxation. Spin-spin relaxation is a mechanism by which the transverse magnetization component M_{xy} gradually decays to zero. The spin-spin relaxation in transverse plane is illustrated in Figure 2.3. In equilibrium, the longitudinal magnetization M_0 consists of an ensemble of spins each with its own net magnetic moment. Suppose the spins are tipped completely into transverse plane about the x-axis. Immediately after tipping, all spins are in phase and precessing with the same frequency in the x-y plane. However, due to rapid vibrational motions experienced by a spin, each spin experiences a slightly different local magnetic field variations. This in turn slightly perturbs the frequency with which the spins are precessing and causes the spins to accumulate different phase. The loss

of phase coherence (known as dephasing) among the spins causes the net transverse magnetization to decay depending upon the extent to which different spins accumulate phase. The rate at which the transverse magnetization decays is determined by the time constant T_2. The longitudinal component at a given time t is then determined by the following equation.

$$\frac{dM_{xy}}{dt} = -\frac{1}{T_2}(M_{xy}) \quad (2.4)$$

When the magnetization is completed tipped to the transverse plane, the transverse component at a given time t is given by the following equation.

$$M_{xy}(t) = M_0 . \exp(-t/T_2) \quad (2.5)$$

2.2.3. Relaxation Mechanisms

As mentioned earlier, the natural mechanism by which spin-lattice and spin-spin relaxations occurs is dipole-dipole coupling in which spins interact with internally generated magnetic field variations. The time-varying magnetic fields are generated by rapid molecular motions typically on the order of picoseconds. Typically these motions are generated by rapid vibrations and rotations along the covalent bonds in a water molecule, as well as rapid rotation of the water molecules (known as "tumbling"). These rapid motions lead to time-varying magnetic fields exerted by one spin on the other, and collectively cause nuclear relaxation. In free water, the natural motional frequencies of water molecules are much higher than the Larmor frequency due to which the dipole-dipole coupling is weak and the T_1 relaxation is inefficient. This manifests as long time required by free water to recover the longitudinal magnetization once it is perturbed from equilibrium, and hence the long T_1. A similar statement can be made regarding the long T_2 of free water. When the water is bound to larger moieties such as the charged groups of proteins,

the molecular motion is slowed down, which leads to greater dipole-dipole coupling and faster nuclear relaxation. For this reason, T_1 and T_2 of proteinaceous solutions are much shorter than those of free water.

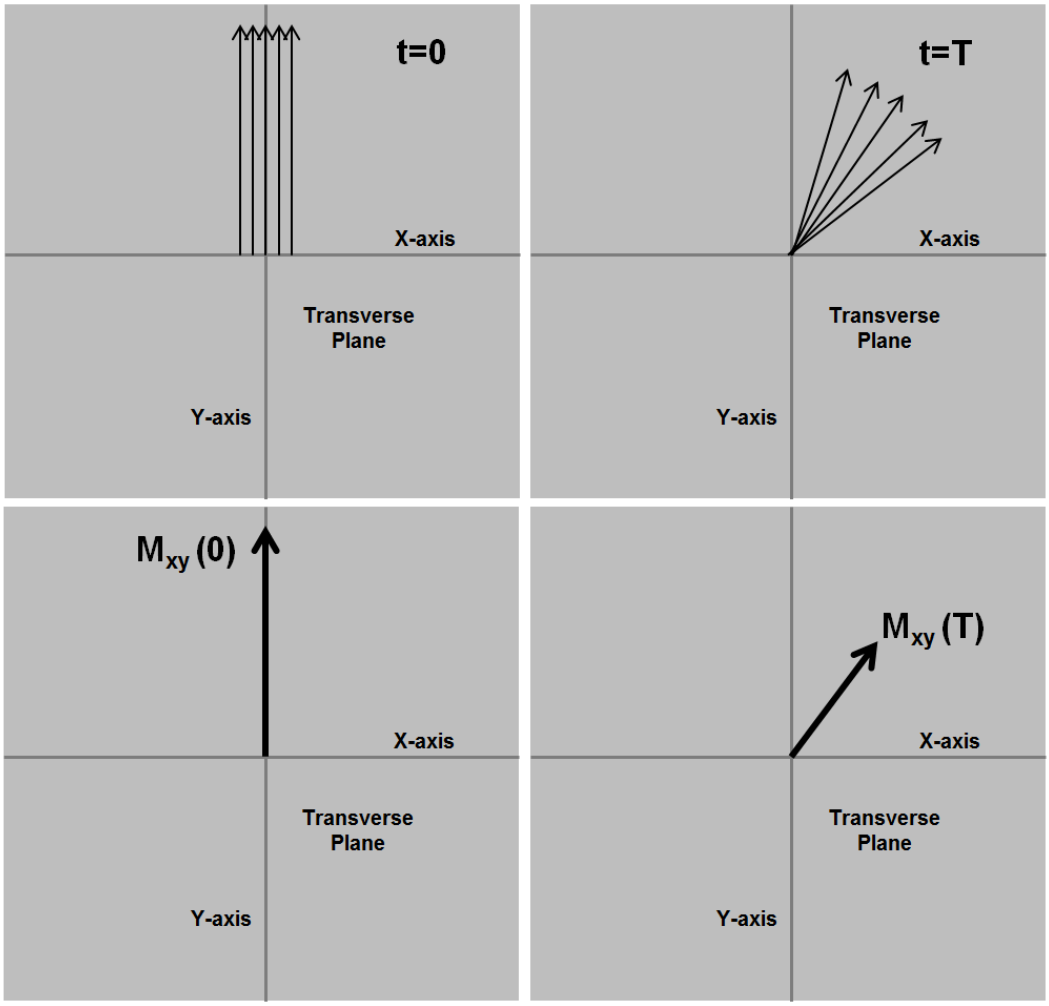

Figure 2.3: *Spin-spin relaxation.* When the spins are tipped completely into the transverse plane by an RF pulse at t=0, all spins are phase and the net transverse magnetization is equal to the equilibrium longitudinal magnetization M0. By the time t=T, each individual spin accumulates a different phase due to the time-varying fluctuations in the local magnetic field experienced by each spin. This results in a loss of phase coherence, and at time t=T, the net transverse magnetization Mxy(T) is smaller than the initial magnetization M0. This decay of the transverse magnetization is known as spin-spin relaxation.

A second form of nuclear relaxation arises when the spins diffuse through spatially varying static magnetic fields. Such spatially varying magnetic fields arise when there is a bulk magnetic susceptibility difference between the water molecules and their environment. When a spin diffuses through spatially varying magnetic field, it experiences random magnetic field variations, and thereby loses phase coherence with neighboring spins. This mechanism particularly accelerates the decay of transverse magnetization and thereby reduces T_2. In the presence of such static magnetic field inhomogeneities, the T_2 is replaced by T_2* to account for the field inhomogeneity-induced loss of phase coherence. The relationship between T_2 (transverse relaxation in the absence of magnetic field inhomogeneities) and T_2* (transverse relaxation in the presence of magnetic field inhomogeneities) is given by the following equation.

$$\frac{1}{T_2^*} = \frac{1}{T_2} + \frac{1}{T_2'} \tag{2.6}$$

The T_2' component in the above equation accounts for the additional transverse magnetization decay due to magnetic field inhomogeneities.

Static spatially varying magnetic fields can be induced by magnetically active substances such as paramagnetic substances. Paramagnetic substances have a small positive magnetic susceptibility to external magnetic fields. In the presence of strong external magnetic fields, paramagnetic substances can induce small local magnetic fields, which can alter the otherwise homogenous external magnetic fields experienced by the spins. Any diffusion of spins across the paramagnetic substances can therefore accelerate relaxation. Typically paramagnetic substances have unpaired electrons that make them magnetically active in the presence of external magnetic field. A well-known paramagnetic substance naturally occurring in the human body is deoxyhemoglobin in which the iron atom has two unpaired electrons.

Paramagnetic substances can also induce significant shortening of T_1, mainly due to dipole-dipole coupling. To achieve significant T_1 shortening, hydrogen nuclei should be able to approach the paramagnetic center by at least 3Å (302). For this reason, deoxyhemoglobin does not have significant T_1 shortening capability as the iron center is shielded from hydrogen nuclei by an extensive protein network. A more popular paramagnetic substance for T_1 shortening is Gadolinium. Gadolinium, which has 7 unpaired electrons, is widely used as T_1 shortening agent for myocardial viability imaging.

2.3. Spin Manipulation Techniques

This section provides a brief overview of the basic spin manipulation techniques including free-induction, spin-echo, gradient-echo, and inversion-recovery, which are commonly used for measuring different MR relaxation parameters.

2.3.1. Free-Induction Decay

Free-induction decay (FID) is the simplest technique for acquiring an MRI signal. In this technique, the longitudinal magnetization is tipped into the transverse plane and the MRI signal is collected from the resulting emission. The tipped spins precess freely to generate a net transverse magnetization. The precession generates a magnetic flux that can be detected as an electrical voltage in any RF coil placed perpendicular to the transverse plane. In the absence of any static magnetic field inhomogeneities, the transverse magnetization undergoes monoexponential decay according to the equation 2.5. However, in the presence of static magnetic field inhomogeneities, the decay is no longer monoexponential. In such a case, the

decay is complex and the rate of decay is determined by the geometry and the spatial distribution of the source of the magnetic field inhomogeneity.

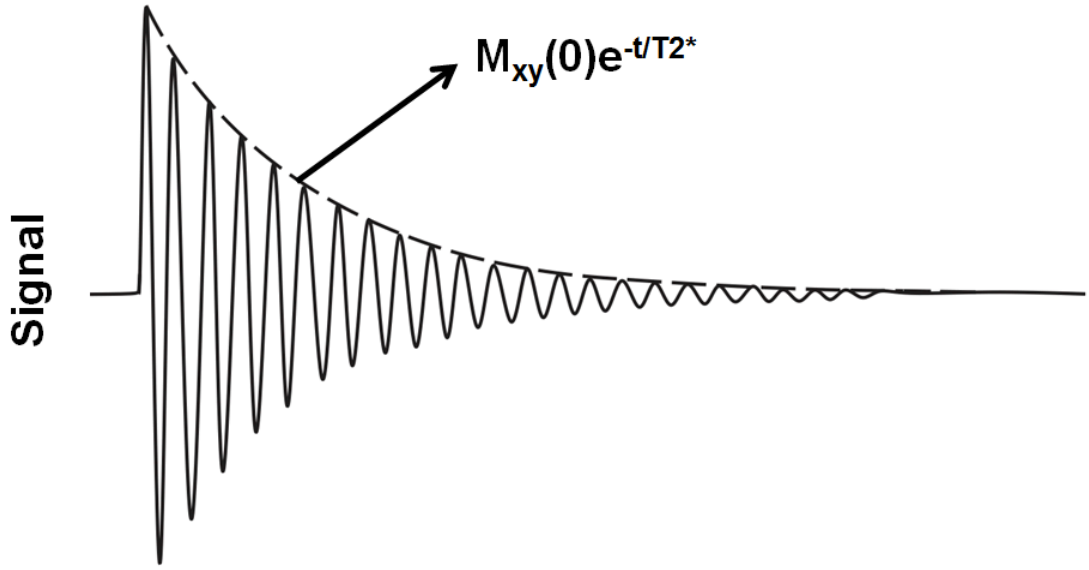

Figure 2.4: *Free-induction decay*. When the longitudinal magnetization is tipped into the transverse plane, it undergoes monoexponential decay due to transverse relaxation in the absence of any static field inhomogeneities. The transverse magnetization can be detected as an electrical voltage induced in any RF coil place perpendicular to the transverse plane.

2.3.2. Spin-Echo

The presence of static magnetic field inhomogeneities will accelerate the rate of transverse magnetization decay. However, the additional dephasing caused by the magnetic field inhomogeneities can be recovered using spin-echo (SE) pulses. The SE technique is illustrated in Figure 2.5. In this technique, the longitudinal magnetization is initially tipped into the transverse plane using a 90° RF pulse about the x-axis (denoted as $(\pi/2)_x$).

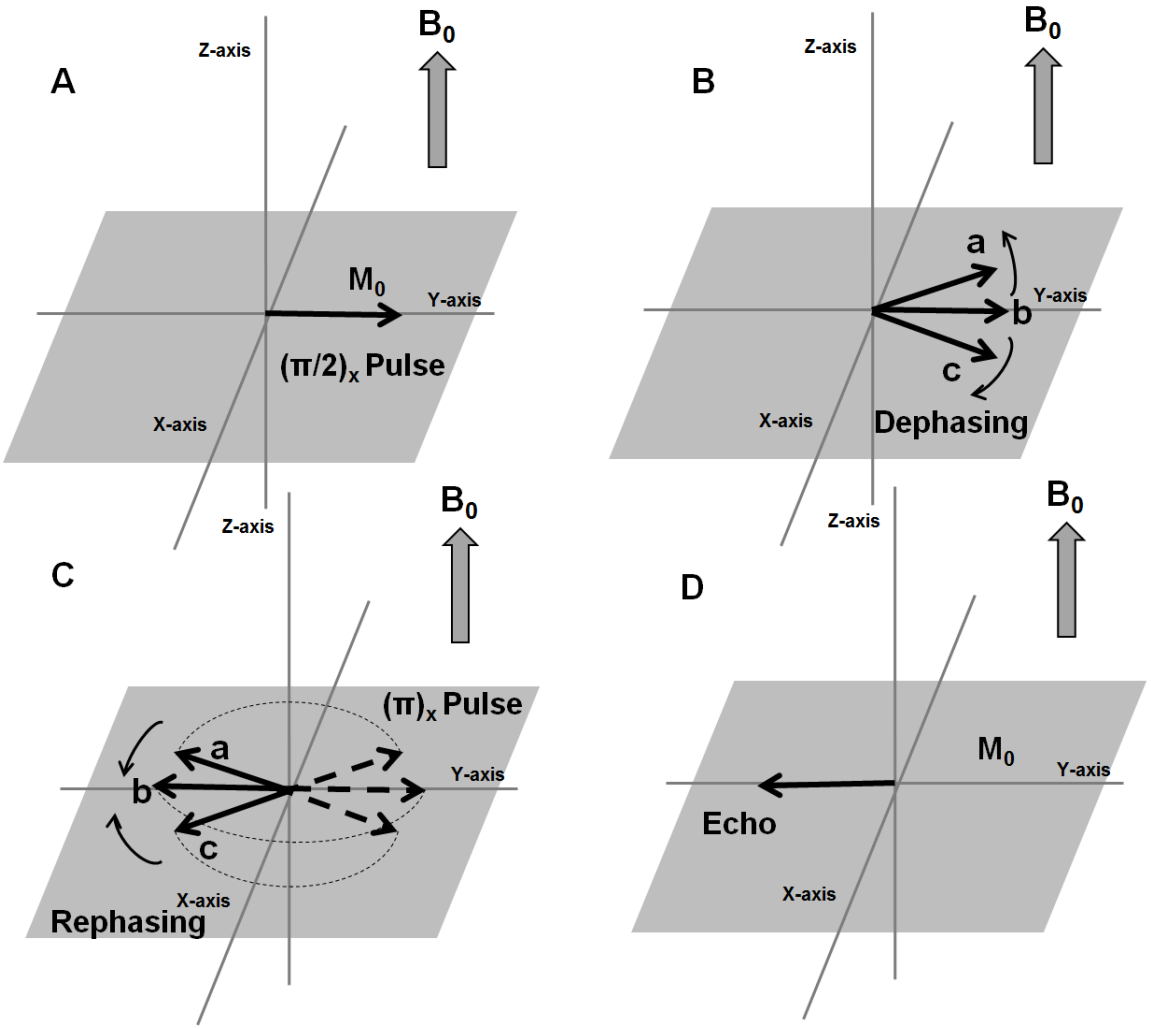

Figure 2.5: *Spin-Echo*. In spin-echo technique, the equilibrium longitudinal magnetization is tipped into the transverse plane using a π/2 pulse. The spins undergo accumulate different phases over a time depending upon the local magnetic field variations and lose phase coherence. The spins are inverted by a π pulse back into the transverse plane upon which the dephasing spins start rephasing. After a finite time, the spins refocus to generate an echo.

Immediately after this tipping (t = 0), all spins are in coherence and the net transverse magnetization is M_0 (panel A). At time t = T, the spins are dephased due to the differences in the local external magnetic field experienced by each individual spin. The dephasing causes the net transverse magnetization to decrease. For illustration purposes, Figure 2.5 shows three spins labeled ‘a’, ‘b’, and ‘c’. In a rotating frame of reference, assume that spin ‘b’ is on resonance due

to which it stays fixed on the positive y-axis (the right side of y-axis in the illustration). Spin 'a' accumulates a phase due to which it drifts away from the spin 'b' with time in the counter-clockwise direction. Spin 'c', on the other hand accumulates a phase due to which it drifts away from the spin 'b' with time in the clockwise direction. At time t = T, a 180° RF pulse (denoted as $(\pi)_x$) is applied about the x-axis, due to which the spins 'a', 'b', and 'c' are inverted about the x-axis on to the negative side of the y-axis (the left side of the y-axis in the illustration). At this moment, the spins 'a' and 'c' can be observed to be rephasing towards the spin 'b'. At time t = 2T, all the three spins refocus on the negative y-axis to yield M_0. This is referred to as an echo in MRI literature and the time from initial $(\pi/2)_x$ pulse to the echo (t = 2T) is known as the echo time (TE).

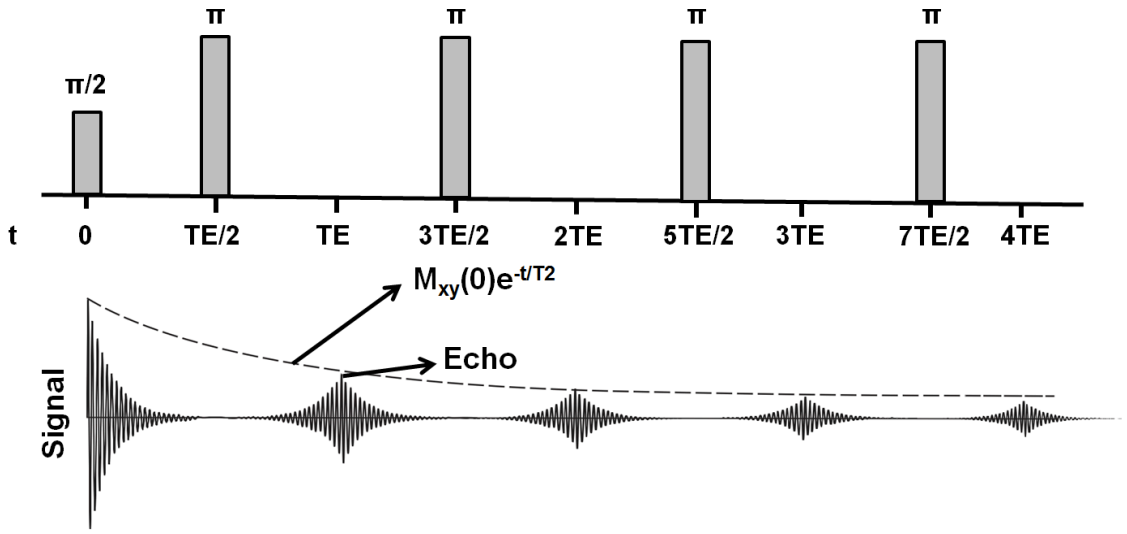

Figure 2.6: *Signal evolution in spin-echo technique*. The longitudinal magnetization is tipped into the transverse plane by a π/2 pulse at t = 0. At t = TE/2, a π pulse is applied which inverts the dephasing spins in the transverse plane. The spins refocus at t = TE to generate an echo. A train of π pulses separated by TE following the initial π/2 tipping pulse generates multiple echoes without allowing the magnetization to reach thermal equilibrium. The amplitude of the echoes, however, decays monoexpoentially due to the independent transverse relaxation.

In a simple SE experiment the initial π/2 pulse is followed by a single π pulse to give a single echo. The multi-spin echo (MSE) technique is a more efficient way of repeatedly refocusing the spins in the transverse plane to yield multiple echoes. In this technique, the initial π/2 pulse is followed by a train of π pulses each separated by a time TE. An illustration of the MRI signal evolution in the spin-echo technique is provided in Figure 2.6. The refocusing effect of the π pulses removes the additional dephasing due to static field inhomogeneities. However, it should be noted that the intrinsic spin-spin relaxation still occurs independent of the echoes. Therefore the magnitude of each subsequent echo is smaller than the one preceding it by a factor determined by the transverse relaxation time constant T_2.

The SE experiment is commonly used to measure the transverse relaxation time constant T_2. To determine the T_2 of a sample, the MSE technique is applied to measure the signal from multiple echoes at different TEs. The signal from the successive echoes are then fitted to a monoexponential decay function to determine the transverse relaxation time constant T_2. For example, for an MSE experiment with two echoes at TE_1 and TE_2, the corresponding echo signals S_1 and S_2 are measured. The T_2 of the tissue of interest is then determined according to the following equation.

$$T_2 = \frac{TE_2 - TE_1}{\ln\left(\frac{S_1}{S_2}\right)} \tag{2.7}$$

It should also be noted that in the MSE technique, the longitudinal magnetization recovers to thermal equilibrium independent of the transverse relaxation. The longitudinal magnetization tipped only once into the transverse plane is commonly not enough to completely measure all the echoes. In a single tipping (known as excitation), each echo is often partially

measured, or only a single echo is measured before the transverse relaxation complete decays. To measure all the echoes, the longitudinal magnetization is repeatedly tipped into the transverse plane, and the data measured during each excitation is pieced together to get the complete data. Repeated excitation is also necessary when the data is measured multiple times and averaged to improve the SNR. The time between two successive excitations is referred to as repetition time, TR. Since the magnitude of transverse magnetization that is available immediately after an excitation is determined by the magnitude of the longitudinal magnetization immediately preceding the excitation, the choice of TR is very important to optimize the desired contrast. If the successive excitations are not spaced far enough (TR is too short), enough time is not allowed for the longitudinal magnetization to fully recover, and the transverse magnetization in the subsequent excitation becomes saturated. If the TR is too long, it takes longer time to acquire the data and is inefficient. The choice of TR, therefore, determines the type of contrast achieved.

2.3.3. Gradient Recalled Echo

In the SE technique, after the initial $\pi/2$ pulse that tips the magnetization into the transverse plane, the spins are refocused using a train of RF pulses. In the gradient recalled echo (GRE) technique, after the initial $\pi/2$ pulse, the spins are refocused using spatially varying magnetic fields known as gradients. Suppose a linear gradient G_z (t) is applied along the z-axis (the direction of external magnetic field B_0). Then the external magnetic field experienced by a spin at a location z along the longitudinal axis (z-axis) is given by the following equation,

$$B(z,t) = B_0 + z.G_z(t) \qquad (2.8)$$

where Gz is defined as

$$G_z = \frac{\partial B(z)}{\partial z} \tag{2.9}$$

Since the spins at a given longitudinal location experience an external magnetic field that is dependent on the local gradient, the angular frequency at which these spins precess is given by the following equation.

$$\omega(z,t) = \omega_0 + \gamma z G_z(t) \tag{2.10}$$

As a result, spins at a given longitudinal location z accumulate additional phase φ(z,t) at time t due to the gradient according to the following equation.

$$\varphi(z,t) = -\gamma z \int_0^t G_z(t)dt \tag{2.11}$$

Suppose a constant positive gradient G is applied along the z-axis for a time interval (t_1, t_2). The phase accumulated in this time interval by a spin at location z is given by the following equation.

$$\varphi_1(z,t) = -\gamma z G(t_2 - t_1) \tag{2.12}$$

At time $t = t_2$, if the gradient is reversed to –G, the phase accumulated by the same spins in the time interval (t_2, t_3) is given by the following equation.

$$\varphi_2(z,t) = +\gamma z G(t_3 - t_2) \tag{2.13}$$

The total phase accumulated the spins in the time interval (t_1, t_3) is then given by the following equation.

$$\varphi(z,t) = -\gamma z G(t_2 - t_1) + \gamma z G(t_3 - t_2) \tag{2.14}$$

If the time interval (t_1, t_2) is equal to the time interval (t_2, t_3), the total phase accumulated by the spins is equal to zero, which results in an echo. The general condition for a GRE is given by the following equation.

$$\int G(t)dt = 0 \tag{2.15}$$

As mentioned earlier, there are no refocusing RF pulses used in the GRE technique. Due to this reason, any additional dephasing caused by the presence of local static magnetic field variations are not compensated in this technique. The GRE technique is, therefore, commonly used to measure the relaxation time constant T_2*.

2.3.4. Inversion-Recovery

Inversion-recovery (IR) is a commonly used spin manipulation technique for measuring T_1. In this technique, the longitudinal magnetization is inverted along the longitudinal direction and the relaxation of the longitudinal magnetization to equilibrium is sampled at different time points along the recovery to measure T_1. Suppose the longitudinal magnetization at equilibrium M_0 is oriented along the z-axis as shown in Figure 2.2. In the IR technique, M_0 is completely inverted using a π pulse on to the negative z-axis. The longitudinal magnetization M_z immediately after the π pulse is equal to $-M_0$. The magnitude of M_z at any given time thereafter is determined by the longitudinal relaxation time constant T_1 according to the following equation.

$$M_z(t) = -M_0 e^{-\frac{t}{T_1}} + M_0\left(1 - e^{-\frac{t}{T_1}}\right) = M_0\left(1 - 2e^{-\frac{t}{T_1}}\right),\ 0 < t < TI \qquad (2.16)$$

At time t = TI (known as inversion time), the longitudinal magnetization is tipped into the transverse plane to measure the signal. The evolution of the transverse magnetization M_{xy} thereafter is given by the following equation.

$$M_{xy}(t) = \left|M_0\left(1 - 2e^{-\frac{TI}{T_1}}\right)\right| e^{-\frac{t-TI}{T_2^*}},\ t > TI \qquad (2.17)$$

An illustration of the evolution of M_z in the IR experiment is provided in Figure 2.7. Signals measured at different TIs, can be fit to this monoexponential growth equation to determine the T_1 value of a tissue of interest. When $TI = T_1\ln(2)$, the signal is zero. This is

known as the null time, which is commonly used to enhance the contrast between two different tissues with different intrinsic T_1 values. The utility of this concept for LGE imaging is further explained in section 2.5 in this chapter.

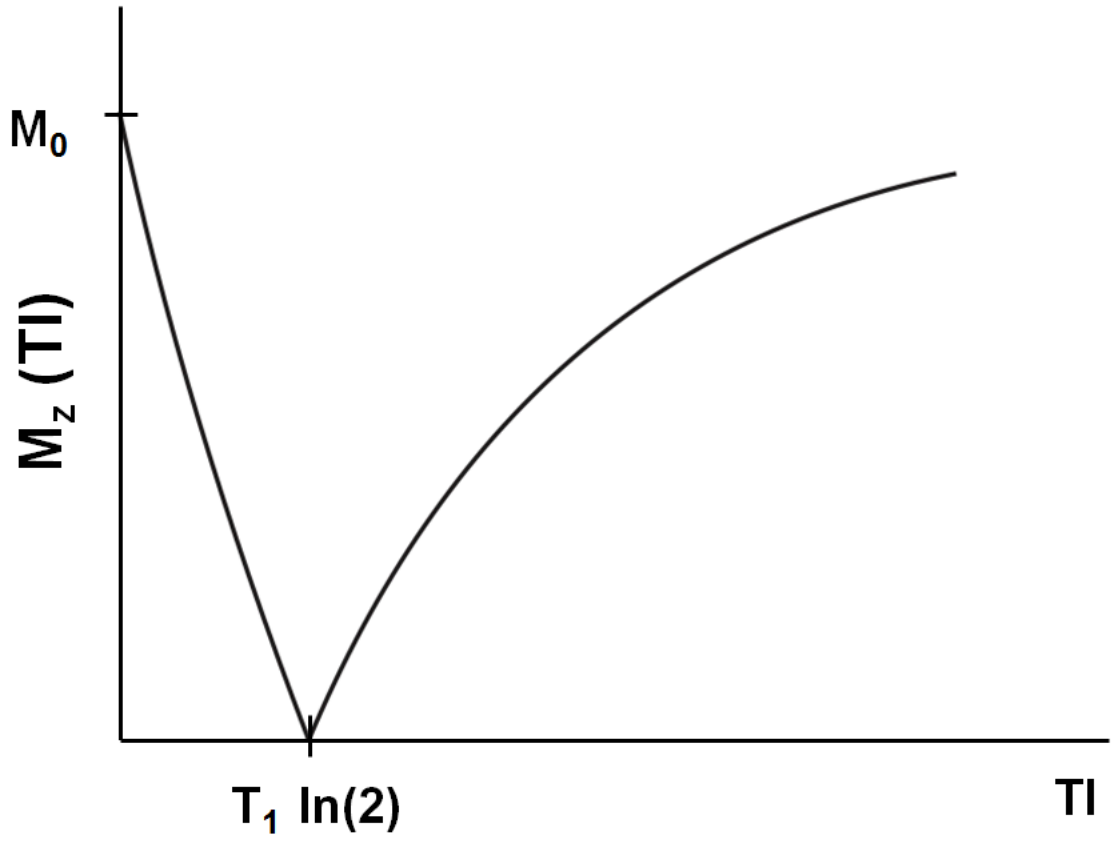

Figure 2.7: *Longitudinal magnetization in inversion-recovery technique*. The magnitude of the longitudinal magnetization in the inversion-recovery technique is shown as function of TI. At the null time TI = T_1ln(2), the signal is zero.

2.4. MRI Contrast Mechanisms and Applications in Myocardial Infarct Characterization

This section provides a brief overview of the basic contrast mechanisms in MRI based on the T_1, T_2, and T_2* relaxation properties of the tissue of interest. As mentioned earlier, different spin manipulation techniques and the choice of TR and TE can optimize the desired contrast. This can in turn facilitate the visualization of different myocardial infarct tissue pathologies. This section lays special emphasis on LGE imaging, its application to myocardial infarct characterization, and its limitations.

2.4.1. T_1-Weighted Imaging and T_1 Mapping

T_1-weighted imaging generates contrast on the basis of the difference in intrinsic T_1 relaxation properties of hydrogen nuclei in different tissues. A T_1-weighted image is typically a GRE image acquired using TE<<T_2* and TR on the order of T_1. The short TE ensures minimal T_2* effects. Since the TR is on the order of T_1, the longitudinal magnetization is not fully recovered between successive excitations. However, the flip angle α allows sufficient recovery of the longitudinal magnetization. After several repetitions, the equilibrium magnetization reaches a steady state, whose intensity is determined the ratio of TR/T_1 and the flip angle α. To achieve optimal T_1 contrast, the flip angle can be set to the Ernst angle, which is given by the following equation.

$$\alpha = \cos^{-1} e^{-TR/T_1} \tag{2.18}$$

Basic GRE imaging is limited by the need for long TR, which is unfavorable particularly in cardiac imaging applications. For this purpose, spoiled GRE imaging is typically used to quickly decay the transverse magnetization after readout. In spoiled GRE, the TR can be kept sufficiently

short (typically $<T_2$), and any T_2 contributions are minimized using spoiler gradients. A commonly used spoiled GRE technique is the Fast Low Angle SHot (FLASH) technique.

T_1-weighted imaging has been previously shown to detect myocardial edema (303-306) and reperfusion hemorrhage (307) in AMIs. The elevated tissue water content in the acutely infarcted myocardium due to tissue edema increases the T_1 value of the infarct relative to viable myocardium. In myocardial hemorrhage, the paramagnetic effect of deoxyhemoglobin in the externalized red blood cells (RBCs) decreases the T_1 value. The foremost application of T_1-weighted imaging, however, remains the LGE imaging for evaluating the extent of myocardial viability in AMI and CMI patients (226,308,309). LGE imaging generates T_1 contrast between infarcted and viable myocardium on the basis of differential GBCA kinetics in the two tissues. The details of LGE imaging are separately provided in section 2.5.

While T_1-weighted imaging is useful for visualizing different pathologies in the setting of MI, the technique is qualitative in nature in which signal measurements depend on the choice of MRI parameters used. Moreover, the use of phased array coils for signal acquisition can cause signal variation across the field-of-view. For this reason, measuring the intrinsic T_1 values rather than the T_1-weighted signal is often desired. As mentioned earlier, T_1 values are traditionally measured using an IR-prepared sequence in which the signal is sampled at different T_I times and fitting to a monoexponential growth function. Unfortunately, traditional IR-prepared sequences require a long acquisition time because the longitudinal magnetization needs to be adequately recovered between successive excitations. This is highly undesirable in cardiac imaging applications, as multiple breath-holds are required to acquire the T_1 map of a single myocardial slice. The widespread use of T_1 mapping for cardiac imaging applications began with the introduction of the MOdified Look-Locker Inversion recovery sequence by Messroghli et al

(310). In this technique, the IR curve is sampled at multiple TIs during the recovery using a single-shot SSFP readouts spaced at heart beat intervals. However, the T_1 measurements using MOLLI are dependent on heart rate variations (311) and intrinsic T_2 values (312). A shortened version of MOLLI (ShMOLLI) with heart rate independence was proposed by Piechnik et al (313). To minimize the T_1 measurement errors in IR-prepared T_1 mapping techniques, saturation recovery (SR)-based T_1 mapping techniques such as Saturation recovery single SHot Acquisition (SASHA) has been proposed (314). In this technique, SR preparation is used instead of the traditional IR preparation. Due to this reason, the longitudinal magnetization between successive excitations is independent of each other. However, this technique suffers from smaller dynamic range compared to the IR methods.

Native T_1 mapping has been successfully used in the assessment of myocardial edema in AMIs (315-318). Quantitative T_1 mapping following GBCA administration has been proposed as a reliable alternative for LGE imaging for evaluating myocardial viability (319). Unlike LGE imaging, T_1 mapping is quantitative nature and does not suffer from surface-coil bias. However, similar to LGE imaging, the infarct-to-remote myocardium contrast still is dependent on GBCA kinetics in post-contrast T_1 maps. Therefore, for optimal contrast, the acquisition of post-contrast T_1 maps should be accurately timed following GBCA administration. To overcome this limitation, extracellular volume fraction (ECV) measurements, which combine the pre-contrast and post-contrast T_1 maps has been proposed (319). ECV measurements have been shown to be stable for up to 30 minutes following GBCA administration, and acquisition of post-contrast T_1 maps need not be accurately timed (320). The ability of native T_1 maps to detect CMIs was shown to be rather poor at 1.5T (317).

2.4.2. T_2-Weighted Imaging and T_2 Mapping

T_2-weighted imaging generates contrast on the basis of the difference in intrinsic T_2 relaxation properties of the hydrogen nuclei in different tissues. As mentioned earlier, MSE techniques such as Turbo SE (TSE) are commonly used for acquiring T_2-weighted images. T_2-weighted images are typically acquired with $TR>>T_1$ (to minimize T_1 effects) and TE on the order of T_2 values. T_2-weighted images have been traditionally used to evaluate myocardial edema in AMIs (115,116,133,134,304,321-329). The elevated tissue water content in the acutely infarcted myocardium due to tissue edema increases the T_2 value of the infarct relative to viable myocardium. Since myocardial edema is a feature of AMIs, but not CMIs, T_2-weighted imaging is commonly used in conjunction with LGE imaging to differentiate AMIs and CMIs (118). T_2-weighted imaging has also been used for evaluating reperfusion hemorrhage in AMIs (132,141,188,196,198,289,330). Deoxyhemoglobin and degradation products of externalized blood in hemorrhage are paramagnetic in nature, and induce a decrease in T_2. Therefore, hemorrhage appears as hypointense cores within the hyperintense edematous territories in T_2-weighted images.

IR pulses are commonly are commonly used in T_2-weighted imaging such as T_2-STIR (Short T_1 Inversion Recovery) to suppress the signal from the blood and fat, and to improve the sensitivity to the edematous tissue (331). However, this technique suffers from slow-flow artifacts adjacent to LV wall with poor contractility, and loss of signal due to through-plane motion in the posterior wall. To overcome these limitations, a bright-blood T_2-prepared technique with single-shot Steady State Free Precession (SSFP) readout was proposed (332,333). For the reasons outlined in the T_1 mapping section, T_2 mapping is often desired for quantitative characterization of an MI. Giri et al, subsequently, have proposed a bright blood T_2 mapping

technique using T_2-prepared SSFP readouts (334). Quantitative T_2 mapping has been shown to be a more robust technique than T_2-weighted imaging for characterizing myocardial edema and reperfusion hemorrhage in AMIs (170,335).

2.4.3. T_2*-Weighted Imaging and T_2* Mapping

T_2*-weighted imaging generates contrast between different tissues on the basis of the differences in their intrinsic T_2* values. As mentioned earlier, GRE technique which is sensitive to static magnetic field inhomogeneities is commonly used to acquire T_2*-weighted images. For this purpose, the TR is chosen to be very short ($TR<<T_1$), and the TE is chosen on the order of the T_2* values. Low flip angle ensures sufficient magnetization recovery between successive excitations. The sensitivity of T_2*-weighted images to detect static magnetic field inhomogeneities increases with the increase in TE. However, T_2*-weighted images are also sensitive to off-resonance artifacts at longer TEs. Particularly in cardiac imaging applications, the off-resonance artifacts are prominent at the infero-lateral LV wall due to the magnetic susceptibility differences between the myocardial tissue and the air in the lung. Therefore, an optimal TE is chosen such that it is sensitive enough to the static magnetic field inhomogeneities, but not too sensitive to the off-resonance artifacts. T_2*-weighted imaging is commonly used to evaluate reperfusion hemorrhage in AMIs. The static field inhomogeneities induced by deoxyhemoglobin and degradation products of externalized blood in hemorrhage detected as hypointense territories on T_2*-weighted images (291,293).

Similar to T_1 and T_2 mapping, T_2* mapping is commonly performed for quantitative assessment of reperfusion hemorrhage (292). The relationship between R_2* ($1/T_2$*) and liver iron concentration is well known in the setting of hepatic iron overloading (336). Recently, T_2*-

weighted imaging and T_2* mapping are being increasingly used for evaluating myocardial iron overloading in non-ischemic cardiomyopathies such as hemosiderosis and β-thalassemia (337-342). These studies highlight the potential role of T_2*-based MRI for accurate quantitative characterization of reperfusion hemorrhage in the setting of MI.

2.5. Late Gadolinium Enhancement Imaging

This section provides a comprehensive overview of the LGE imaging technique including its implementation, utility, and limitations.

2.5.1. The Concept of Late Gadolinium Enhancement

LGE imaging is an extensively validated imaging technique for detecting AMIs and CMIs (225,226,245,278,280,308,343-351). In LGE imaging, the subject is administered an intravenous bolus of GBCAs such as gadoversetamide, gadopentetate, and gadobutrol. GBCAs used in LGE imaging are extravascular contrast agents that rapidly distribute in the extracellular space of myocardium. The loss of myocardial membrane integrity in the infarcted myocardium provides ~4-times higher fractional distribution volume to GBCA in the infarcted myocardium relative to viable myocardium (also known as remote myocardium) (352-354). Therefore, the amount of GBCA accumulating within the infarcted myocardium is much higher than that in the viable myocardium. Moreover, the wash-in and wash-out kinetics of GBCA are altered in the infarcted myocardium due to which the contrast agent retention in the infarcted myocardium is prolonged relative to that in the remote myocardium (355). Due to this concentration difference, the T_1 value of the infarcted myocardium is much shorter than that of the remote myocardium.

Image acquisition is typically performed 10-15 minutes following GBCA administration at which point the GBCA concentration difference between the infarcted and remote myocardium is near maximum (355). An IR-prepared GRE sequence is typically used in which the TI is chosen to null the remote myocardium (356). The evolution of the longitudinal magnetization M_z as a function of TI is shown in Figure 2.8. At the null time of remote myocardium, the infarcted myocardium appears hyperintense due to its shorter T_1, and faster recovery of the longitudinal magnetization.

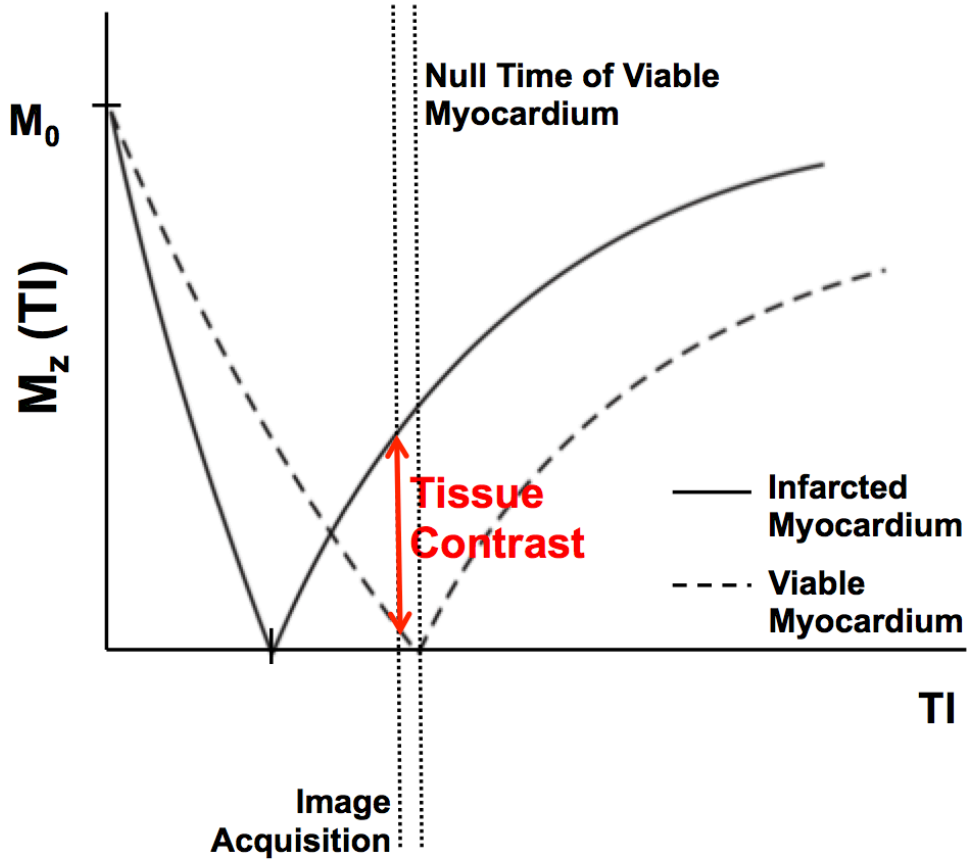

Figure 2.8: *Longitudinal magnetization in Late Gadolinium Enhancement.* The magnitude of the longitudinal magnetization in the inversion-recovery technique is shown as function of TI. Image acquisition is performed with a TI close to the null time of remote myocardium, at which point the infarct-to-viable myocardium contrast is near maximum (shown by the red arrow).

2.5.2. Utility of Late Gadolinium Enhancement Imaging

The utility of LGE imaging for detection of infarct and predicting adverse long-term cardiac outcomes has been repeatedly demonstrated. LGE imaging has shown a strong diagnostic performance for detecting both AMIs and CMIs in a large multi-center randomized trial (357). The technique has been also shown to detect minute infarctions even in the absence of ECG Q waves (211,358,359). The diagnostic performance of this technique has been shown to be equivalent to the gold standard SPECT for detecting AMIs (211,346). Several studies have shown the prognostic significance of LGE imaging for predicting long-term LV function in MI patients (225,226,280,344,346-348,360). The transmural extent of LGE in AMI patients, measured both before and after reperfusion, has been found to predict the long-term recovery of LV function (225,226). As discussed in chapter 1, MO detected on LGE imaging in AMI patients is a strong predictor of long-term adverse cardiac outcomes (138,140,142,145-147,179). LGE imaging has shown strong diagnostic performance for detecting LV segments with flow metabolism defects detected using PET imaging in CMI patients (229,361).

In relation to CMIs alone, LGE imaging has found applications in monitoring myocardial regenerative therapies and risk-stratifying patients for malignant ventricular arrhythmias (mVA). LGE imaging has played a major role in validating the efficacy of stem cell based regeneration of scarred myocardium (362,363). Klem et al have shown that the scar size is an important predictor of implantable cardioverter defibrillator (ICD) discharge in CMI patients (96). Gray-zones detected on the basis of LGE imaging has been shown to be a strong predictor for inducible mVA than EF and mortality (364-367).

2.5.3. Limitations of Late Gadolinium Enhancement Imaging

Over the past decade, LGE imaging has evolved into a robust and indispensable technique for MRI-based characterization of AMIs and CMIs. The most important limitation of LGE imaging is that it requires administration of GBCAs, which are contraindicated in patients with chronic end-stage kidney disease (368), a rising epidemic (369). Several studies have reported the incidence of renal failure (370-376) and nephrogenic systemic fibrosis (377-382) in patients with renal insufficiency who received GBCAs at doses varying from 0.1-0.4 mmol/kg. A patient prescribed for LGE imaging typically receives 0.1-0.15 mmol/kg of GBCA. Moreover, LGE imaging is often preceded by other contrast-based techniques such as perfusion imaging, which can further increase the total GBCA administered to the patient. For this reason, LGE imaging is contraindicated in patients with a glomerular filtration rate <45 mL/min/1.73m^2. This is a serious limitation in MI patients due to the high co-morbidity of chronic kidney disease in these patients. According to the Unites States Renal Data System, the fraction of patients with cardiovascular disease, who have chronic kidney disease is >40% (383). Recent studies have shown that approximately 20% of AMI (STEMI and NSTEMI) patients suffer from late stage chronic kidney disease (GFR <45 mL/min/1.73m^2), in whom LGE is expected to be contraindicated (384,385).

Gadolinium in free ionic form is highly toxic. For this reason, Gadolinium in contrast agents is typically chelated by non-toxic substances. Besides mitigating the harmful effects of Gadolinium, the chelators also facilitate its clearance from the body primarily by the kidneys through urine (386-388). In patients with prior kidney disease, the clearance of Gadolinium is significantly prolonged (389-392). When Gadolinium chelates persist in the body for prolonged periods, the Gadolinium cation (Gd^{3+}) in the chelated complex can be replaced by circulating

cations (Zn^{2+}, Mg^{2+}, Ca^{2+}, Cu^{2+}, Fe^{2+}/Fe^{3+}) in a process known as transmetallation. The free Gadolinium ions can thereby cause deleterious effects (393-397). Alarmingly, recent studies in patients with normal kidney function who underwent repeated GBCA-enhanced brain MRI scans have reported Gadolinium deposition in the neural tissues several years after the scans (398-401). Although the biological effects of Gadolinium deposits remain to be explored, these studies are raising new questions about the safety of GBCA-based MRI scans.

The use of GBCAs for LGE imaging also imposes workflow limitations in an MRI examination. Since GBCAs take at least 30 minutes to be cleared from the tissue of a subject with normal renal function, LGE imaging is typically performed at the end of the MRI examination so that the presence of Gadolinium will not affect the magnetization relaxation properties of the subsequent scans. The dependence of LGE imaging on wash-in and wash-out kinetics of GBCAs through the infarcted and remote myocardium require that the images be acquired in a tight time window following GBCA administration for optimal contrast (355,402,403). Accurate infarct detection and characterization using LGE imaging is further dependent on the effective nulling of the remote myocardium (309). Therefore, there is significant degree of operator dependency for achieving good quality LGE images.

2.6. Current Need: Non-Contrast MRI Techniques for Characterizing Chronic Myocardial Infarctions

As discussed in the preceding sections, LGE imaging is central to characterizing MIs. Due to the co-morbidity of chronic kidney disease, ~20% of MI patients are contraindicated to LGE imaging. This is not a serious limitation for characterizing AMIs as surrogates of infarcted

myocardium such as myocardial edema, MO, and hemorrhage can be well-characterized in the acute phase using non-contrast approaches based on T_1, T_2, and T_2* properties of the infarcted tissue. The problem arises when patients with CMIs are the subjects of interest. As previously discussed in chapter 1, determining the extent, transmurality, location of CMI based on LGE imaging is of significant clinical interest due to its association with adverse long-term outcomes (92,96,107) and monitoring the efficacy of regenerative stem cell therapies (362,363). LGE imaging has also been the central technique for identifying pathological substrates of mVAs in CMIs such as the gray-zone (364-367). In the chronic phase of MI, myocardial edema (118,143,404) and MO (143,170) have been shown to resolve completely, while the fate of intramyocardial hemorrhage is not well studied. As a result, LGE imaging currently remains the only technique for risk-stratification of patients with CMIs. In the absence of LGE imaging for characterizing CMIs in patients with chronic kidney disease, there is no MRI technique that can be used for risk-stratifying these patients.

The pressing need, therefore, is to develop MRI techniques that can characterize CMIs without the need for exogenous contrast agents. Apart from determining the infarct characteristics such as size, location, and transmurality, the new non-contrast enhanced MRI techniques also need to characterize pathological substrates of mVAs and HF, which are major determinants of SCD.

2.7. Working Objectives

1. To develop, test, and validate a non-contrast based MRI approach for characterizing the size, location, and transmurality of CMIs.

2. To develop, test, and validate a non-contrast based MRI approach for characterizing pathological substrates of malignant ventricular arrhythmias and heart failure.

2.8. Outline of the Thesis

Chapter 3 demonstrates the feasibility of using native T_1 mapping at 3T as an alternative to LGE imaging for characterizing CMIs. Using threshold-based detection, chapter 3 shows that native T_1 mapping acquired at 3T can detect the location, size, and transmurality of CMI with high diagnostic performance comparable to LGE imaging. Chapter 4 examines different automatic, semi-automatic, and visual methods for detecting CMI on native T_1 maps at 3T. The use of Mean + 5 Standard Deviations thresholding is shown to be the most reliable technique for detecting CMIs on native T_1 maps at 3T. Chapter 5 demonstrates the feasibility of using the Mean + 5 Standard Deviations thresholding technique for characterizing CMIs using native T_1 maps at 3T in both STEMI and NSTEMI patients with high diagnostic accuracy.

Using T_2*-based MRI, chapters 6-10 demonstrate that acute reperfusion hemorrhage can persist in the form of localized iron deposits for prolonged periods in CMIs, and such iron deposits may evolve into important pathological substrates for mVAs. Chapter 6 demonstrates the superiority of T_2* mapping to both T_2 mapping and T_2-weighted MRI for detecting reperfusion hemorrhage in AMIs. Using T_2*-mapping Chapter 7 demonstrates the link between reperfusion hemorrhage in AMIs and iron deposition in CMIs. This chapter further validates the utility of T_2* mapping for detecting chronic iron deposits using extensive histopathology and mass spectrometry analysis.

Using high-resolution electroanatomical maps of the LV endocardial wall with CMIs co-registered with in-vivo T_2*-weighted images, Chapter 8 demonstrates the chronic iron deposits detected using T_2*-based MRI may evolve as pathological substrates for mVAs. Chapter 9 further demonstrates that bSSFP imaging can detect chronic iron deposits within CMIs as hypointense cores within MI territories, and such hypointense cores have incremental prognostic significance for predicting mVAs in patients implanted with ICDs. Using T_2*-weighted imaging, chapter 10 demonstrates that iron deposition within CMIs can also evolve as fingerprint of acute MO, with or without reperfusion hemorrhage, and such iron deposition is an independent predictor of LV remodeling. Chapter 11 concludes the thesis and provides an insight into future directions for the improvements and widespread adoption of non-contrast enhanced MRI techniques for characterizing CMIs.

CHAPTER 3

Native T_1 Mapping at 3T for Characterizing Chronic Myocardial Infarctions: Feasibility Study in Canines

3.1. Abstract

LGE MRI is a powerful method for characterizing MI, but the requisite Gadolinium infusion is contraindicated in ~20% of MI patients due to end-stage chronic kidney disease. The purpose of this study is to investigate whether native T_1-based cardiac MRI obtained without contrast agents at 3T could be an alternative to LGE imaging for characterizing CMIs using a canine model of MI. Canines (n = 29) underwent MRI at 7 days (acute, AMI) and 4 months (chronic, CMI) post-MI. Infarct location, size and transmurality measured using native T_1 maps and LGE images at 1.5T and 3T were compared. Resolution of edema between AMI and CMI was examined with T_2 maps. T_1 maps overestimated infarct size and transmurality relative to LGE images in AMI ($p = 0.016$ and $p = 0.007$, respectively), which was not observed in CMI ($p = 0.49$ and $p = 0.81$, respectively), at 3T. T_1 maps underestimated infarct size and transmurality relative to LGE images in AMI and CMI ($p<0.001$), at 1.5T. Relative to the remote territories, T_1 of the infarcted myocardium was increased in CMI and AMI ($p<0.05$); and T_2 of the infarcted myocardium was increased in AMI ($p<0.001$), but not in CMI ($p >0.20$) at both field strengths. Histology showed extensive replacement fibrosis within the CMI territories. CMI detection sensitivity and specificity of T_1 maps at 3T were 95% and 97%, respectively. In summary, native T_1 maps at 3T can determine the location, size and transmurality of CMI with high diagnostic accuracy. Patient studies are necessary for clinical translation.

3.2. Introduction

As mentioned in chapters 1 and 2, the prognostic outcome in patients with MI is significantly determined by the location, size and transmurality of the MI (92,107,405-407). Over the past decade, LGE MRI has evolved into a robust non-invasive imaging technique for detecting AMIs and CMIs with excellent diagnostic accuracy and prognostic significance (226,308,408). However, accurate infarct sizing using LGE imaging is limited by the Gadolinium kinetics (355,402,403), effective nulling of the remote myocardium (309), and its qualitative nature. Contrast-enhanced T_1 mapping has been proposed as a potential alternative as it is quantitative in nature, and does not require nulling of the remote myocardium (317,319). Nevertheless, like LGE imaging, the T_1 value of infarcted myocardium in contrast-enhanced T_1 mapping depends on the Gadolinium kinetics (312). Moreover, once contrast-enhanced imaging is deemed necessary for assessment of myocardial viability, all other imaging sequences are typically required to be prescribed ahead of LGE imaging, which could impose practical limitations on the execution of the imaging exam, especially when rapid assessment of viability is all that may be necessary. Finally, perhaps most importantly, contrast-enhanced imaging requires administration of a Gadolinium chelate, which is contraindicated in patients with chronic end-stage kidney disease (368), which is a rising epidemic (369). In fact, according to the Unites States Renal Data System, the fraction of patient with cardiovascular disease, who have chronic kidney disease is >40% (383). Recent studies have shown that approximately 20% of AMI (STEMI and NSTEMI) patients suffer from late stage chronic kidney disease (GFR <45 mL/min/1.73m^2), in whom LGE is expected to be contraindicated (384,385).

By definition, native T_1 mapping does not require exogenous contrast media. Hence in addition to the patients with renal insufficiency, the technique can be safely used in significant

fraction of patients for whom LGE imaging or contrast-enhanced T_1 mapping is warranted but are contraindicated for Gadolinium. Recent studies have shown that native T_1 mapping can reliably detect AMI at both 1.5T and 3T (313,315,317,409). In contrast, the diagnostic performance of native T_1 mapping to detect CMI has been shown to be poor at 1.5T (317). Preliminary studies in non-ischemic cardiac pathologies in animals and humans have noted intrinsic T_1 dependence on myocardial collagen content (410). Recent studies have demonstrated the tremendous potential of native T_1 mapping at 3T to reliably detect and quantify diffuse myocardial fibrosis in non-ischemic settings, such as aortic stenosis (411), hypertrophic cardiomyopathy (412,413), and dilated cardiomyopathy (412,413).

This study hypothesizes that magnetic field dependent T_1 elongations permit native T_1 mapping to reliably detect and quantify replacement myocardial fibrosis associated with CMI at 3T. To test this hypothesis, the native T_1 characteristics of CMIS was studied against LGE features at both 1.5T and 3T using canine models of AMI and CMI.

3.3. Methods

3.3.1. Animal Model

Canines (n = 33; 20-25 kg body weight) were studied according to the protocols approved by Institutional Animal Care and Use Committees. MI was created by ligating the left anterior descending (LAD) artery for 3 hours followed by reperfusion. Animals were allowed to recover for 7 days before the MRI studies.

Imaging Method	Cine		Native T_1 map		Native T_2 map		LGE	
Field Strength	3T	1.5T	3T	1.5T	3T	1.5T	3T	1.5T
Sequence	Balanced SSFP		Modified Look-Locker Inversion Recovery		T_2 – prepared SSFP		IR – prepared GRE	
TR (ms)	3.2	3.5	2.2	2.4	2.8	2.2	3.0	3.5
TE (ms)	1.6	1.75	1.1	1.2	1.4	1.1	1.5	1.75
Flip Angle (α)	50°	70°	35°		50°	70°	25°	40°
Bandwidth (Hz/pixel)	1371	930	1042	1002	1371	1002	586	1002
In-plane Resolution	1.3 x 1.3 mm^2							
Slice Thickness	6 mm							
Other Parameters	25-30 cardiac phases		8 TIs; 2 inversion blocks of 3+5 images; minimum TI = 110 ms; TI increment = 80 ms		T_2-preparation times of 0, 24 and 55 ms		Optimal TI to null the remote myocardium	

Table 3.1: Typical imaging parameters used to acquire different CMR images at 1.5T and 3T

3.3.2. Cardiac Magnetic Resonance Imaging Studies

Four canines died during the first few hours of reperfusion despite resuscitation efforts. The remaining 29 canines underwent MRI studies at 7 days (acute) and 4 months (chronic) following reperfusion. Nineteen of the 29 canines were scanned on a 3T clinical MRI system (MAGNETOM Verio®, Siemens Healthcare, Erlangen, Germany), while the remaining ten canines were scanned on a 1.5T clinical MRI system (MAGNETOM Espree®, Siemens Healthcare, Erlangen, Germany). ECG-triggered breath-held cine-SSFP, native T_1-weighted and T_2-weighted images of contiguous slices covering the entire LV were acquired along the short-axis views at both 3T and 1.5T. All imaging studies were completed with the acquisition of LGE

images 8-10 minutes following intravenous administration of 0.2 mmol/kg gadopentate dimeglumine (Magnevist, Bayer Healthcare Pharmaceuticals Inc., Wayne, NJ). Imaging sequences and measurement parameters used to acquire the various images are summarized in Table 3.1. To minimize surface coil bias, pre-scan normalization was applied for each scan.

3.3.3. Histopathology

All animals were euthanized following the 4-month MRI study and their hearts were excised. Ex-vivo triphenyl tetrazolium chloride (TTC) staining and Elastin Masson's Trichrome (EMT) staining were performed.

3.3.4. Image Analyses

T_1 and T_2 maps were constructed from the native T_1-weighted and T_2-weighted images, respectively. All image analyses were performed on cvi42 image analysis software (Circle Cardiovascular Imaging Inc., Calgary, AB, Canada). Remote (viable) myocardium was identified on LGE images as the region showing no hyperintensity and a reference region-of-interest (ROI) was drawn in it. Infarcted myocardium was identified on the LGE image as the region with mean signal intensity (SI) >5 standard deviations (SDs) than that of reference ROI (414-416). Hypointense cores of MO that were not detected as infarcted myocardium on LGE images by the thresholding criterion were manually included in the final analysis for infarct size and transmurality. The reference ROI drawn on LGE image was copied on to the corresponding T_1 map. Infarcted myocardium was then identified on the T_1 map using the mean+5SD criterion. Hypointense cores of acute hemorrhage or chronic iron deposition (307) that were not detected

as infarcted myocardium on T_1 maps by the thresholding criterion were manually included in the final analysis for infarct size and transmurality.

Infarct sizes from both LGE images and T_1 maps were measured as the percentage of total left-ventricular (LV) volume, as well as on the basis of standard American Heart Association (AHA) 17-segment model. Measurements from the 17^{th} segment were excluded from the final analysis to discount the partial volume effects at the apical cap. Infarct transmurality was determined as the percentage extent of the infarct along 100 equally spaced chords on each slice. Mean transmurality was obtained by averaging the infarct transmurality across all the chords that have at least 1% scar extent.

T_1 and T_2 values of the remote and infarcted myocardium (as identified on LGE images using mean+5SD criterion) were measured from T_1 and T_2 maps respectively. Hypointense cores within infarcted myocardium were excluded from this analysis to eliminate the confounding effects of acute hemorrhage or chronic iron deposition on acute myocardial edema or chronic replacement fibrosis.

3.3.5. Statistical Analyses

Statistical analyses were performed using IBM SPSS Statistics (version 21.0, IBM Corporation, Armonk, NY). Normality of the data was tested using the Shapiro-Wilk test and quantile-quantile plots. Depending on the normality of the data, percentage infarct size and mean transmurality measured over the entire LV were compared between LGE images and T_1 maps using either paired t-test or Wilcoxon signed-rank test. Additionally, mixed-model Analysis of Variance (ANOVA) was used to compare percentage segmental infarct size measured from the two techniques. Bland-Altman analysis was performed to estimate the agreement between the

two techniques. Simple linear regression was performed to estimate the correlation between the two techniques with respect to infarct size and transmurality measurements. Measurements from the native T_1 maps and LGE images were chosen as the dependent and explanatory variables respectively. The slope and the intercept of the best-fit line were tested to be equal to 1 and 0 respectively. Using LGE images as the gold standard, sensitivity and specificity of native T_1 maps to detect infarcted myocardium at the segmental level were measured. Receiver operating characteristic (ROC) analysis was performed to measure area under the curve (AUC). The predictor variable used to generate the ROC curves was the infarct size measured on a segmental basis from the T_1 maps.

T_1 and T_2 values of the remote and infarcted myocardium were compared using mixed-model ANOVA. Similarly, percentage change in the LGE-SI of infarcted myocardium relative to remote myocardium was compared to the percentage change in T_1. Statistical significance was set at $p<0.05$ for all analyses.

3.4. Results

3.4.1. Detection of Acute Myocardial Infarction at 3T

All canines sustained MIs as verified by the presence of Gadolinium hyperenhancement on LGE images acquired at 7 days post-reperfusion. Representative LGE images and T_1 maps acquired at 7 days post-MI from a canine scanned at 3T are shown in Figure 3.1. Bulls-eye plots depicting the infarct extent on 17-segment model and transmurality are also shown for both LGE images and T_1 maps in Figure 3.1. Infarct location and spatial extent were visually well correlated between LGE images and T_1 maps. In AMI at 3T, T_1 maps modestly overestimated infarct size (13.3±8.4% vs. 11.6±6.8%, $p = 0.007$) and transmurality (64±19% vs. 56±17%, $p = 0.007$)

relative to LGE images. Mean segmental infarct size measured using T_1 maps was also greater than that

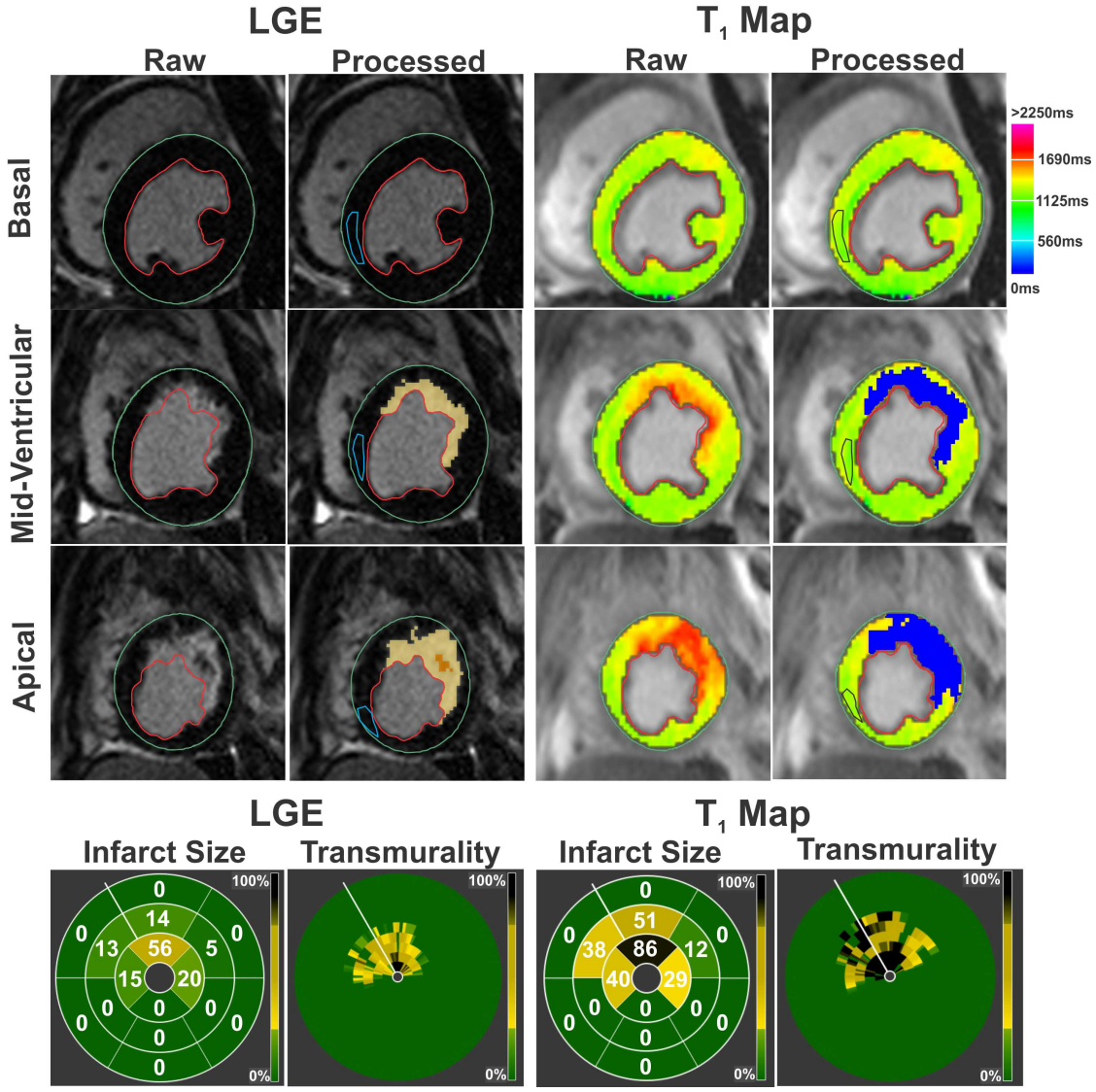

Figure 3.1: *Detecting acute myocardial infarction at 3T*. Representative LGE images and T_1 maps of basal, mid-ventricular and apical slices acquired at 7 days post MI from a canine scanned at 3T are shown. Infarcted myocardium (highlighted blue pixels in the processed images) was identified on both LGE images and T_1 maps using the mean+5SD criterion with respect to the reference ROI drawn in remote myocardium (blue contour). Bulls-eye plots depicting the extent and transmurality of the infarcted myocardium are also shown for both LGE images and T_1 maps. The number within each segment indicates the percentage volume of that segment that was detected as infarcted myocardium by the mean+5SD criterion. For transmurality, each slice was divided into 100 equally spaced

chords with the first chord placed at the anterior insertion of the RV into the LV. Each concentric ring on the Bulls-eye plot represents each short-axis slice with the most basal slice represented by the outermost ring.

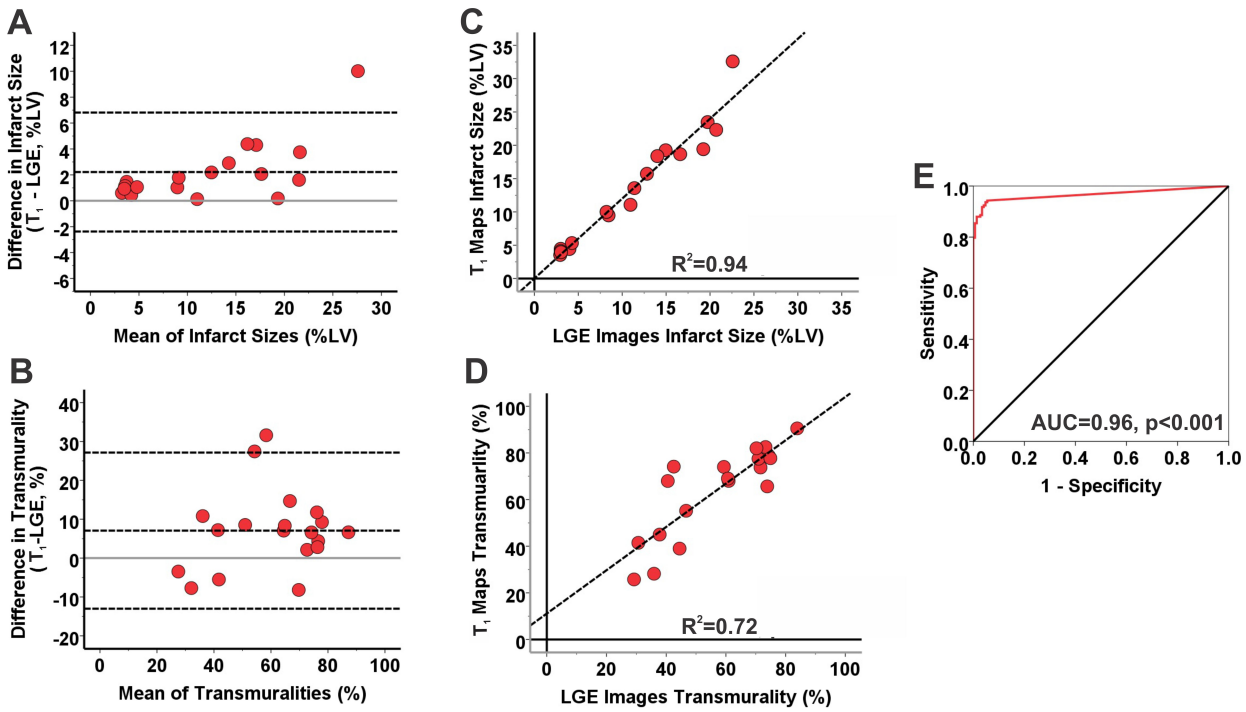

Figure 3.2: *Diagnostic performance of native T_1 maps for detecting acute myocardial infarction at 3T.* Bland-Altman analysis showed good agreement between LGE images and T_1 maps for measuring infarct size (panel A) and transmurality (panel B) in AMI at 3T. T_1 maps modestly overestimated infarct size and transmurality compared to LGE images. There were also strong correlations between LGE images and T_1 maps for measuring infarct size (R^2 = 0.94, panel C) and transmurality (R^2 = 0.72, panel D). ROC analysis showed that area under the curve was 0.96 (panel E) indicating a strong diagnostic performance of native T_1 maps for detecting AMI at 3T.

measured using LGE images (p = 0.016). Bland-Altman analysis showed good agreement between LGE images and T_1 maps for measuring infarct size (Bias = 2.22±2.34%; Figure 3.2A) and transmurality (Bias = 7.07±10.25%; Figure 3.2B). Strong correlations were observed between LGE images and T_1 maps for measuring infarct size (R^2 = 0.94; Slope = 1.20, p = 0.011; Intercept = 0.01, p = 0.98; Figure 3.2C) and transmurality (R^2 = 0.72; Slope = 0.93, p = 0.62;

Intercept = 11.14; p = 0.20; Figure 3.2D). At 3T, T_1 maps detected AMI in 149 of 158 segments that were positive for MI on LGE images (94% sensitivity; 95% confidence interval (CI): 90-98%). T_1 maps were negative for AMI in 138 of 146 segments (94% specificity; 95% CI: 91-98%). ROC analysis showed that the AUC was 0.96 (Figure 3.2E).

3.4.2. Detection of Chronic Myocardial Infarction at 3T

Representative LGE images and T_1 maps, along with the bulls-eye plots for infarct extent and transmurality, acquired from a canine scanned at 3T at 4 months post MI are shown in Figure 3.3. Infarct locations and its spatial extent were visually identical on LGE images and T_1 maps in CMI. There was no significant difference between the LGE images and T_1 maps for measuring infarct size (5.6±3.7% vs. 5.5±3.7%; p = 0.61) and transmurality (44±15% vs. 46±15%; p = 0.81). Mean segmental infarct size, measured using T_1 maps, was not different compared to that measured using LGE images (p = 0.49). Bland-Altman analysis showed excellent agreement between LGE images and T_1 maps for measuring infarct size (Bias = -0.08±0.68%; Figure 3.4A) and transmurality (Bias = 0.45±8.14%; Figure 3.4B). Excellent correlations were observed between LGE images and T_1 maps for measuring infarct size (R^2 = 0.97; Slope = 0.98, p = 0.68; Intercept = 0.02, p = 0.94; Figure 3.4C) and transmurality (R^2 = 0.75; Slope = 0.84, p = 0.18; Intercept = 8.11, p = 0.18; Figure 3.4D). At 3T, T_1 maps detected CMI in 135 of 142 segments that were positive for MI on LGE images (95% sensitivity; 95% CI: 92-99%). T_1 maps were negative for CMI in 158 of 162 segments (97% specificity; 95% CI: 95-100%). ROC analysis showed that the area under the curve was 0.99 (Figure 3.4E).

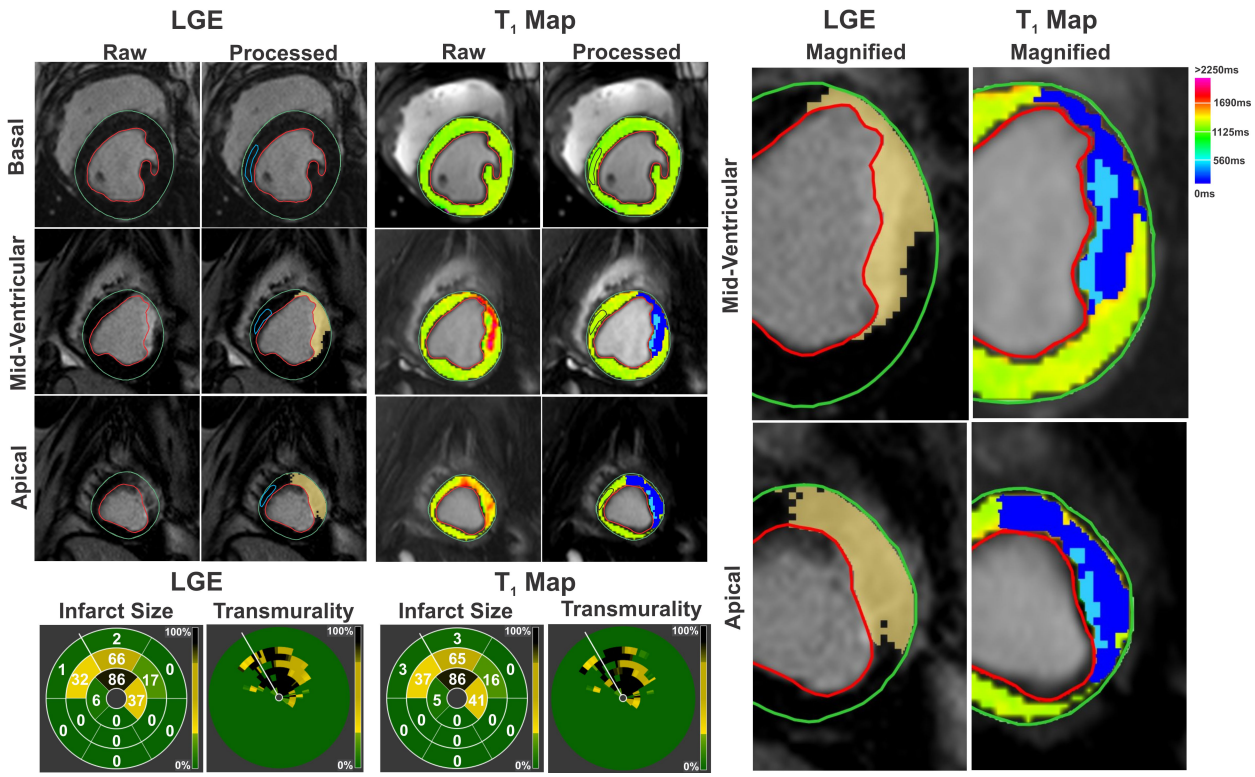

Figure 3.3: *Detecting chronic myocardial infarction at 3T*. Representative LGE images and T_1 maps of basal, mid-ventricular and apical slices acquired at 4 months post MI from a canine scanned at 3T are shown. Infarcted myocardium (highlighted dark blue pixels in the processed images) was identified on both LGE images and T_1 as in Figure 3.1. Hypointense core of chronic iron deposition within the hyperintense infarcted myocardium was not detected as infarcted myocardium by the mean+5SD criterion, and was manually included in the final analysis (highlighted light blue pixels in the processed images). Bulls-eye plots depicting the extent and transmurality of the infarcted myocardium are also shown for both LGE images and T_1 maps. Excellent correlations were observed between LGE images and T_1 maps in terms of the location, spatial extent and transmurality of the infarcted myocardium. Magnified views (on the right) of the infarcted myocardium detected on the mid-ventricular and apical slices clearly show the concordance between LGE images and T_1 maps.

3.4.3. Detecting Acute Myocardial Infarction at 1.5T

Representative LGE images and T_1 maps, along with bulls-eye plots (obtained using the mean+5SD criterion), acquired from a canine scanned at 1.5T at 7 days post MI are shown in 3.

3.5. Infarct location was visually well correlated between LGE images and T_1 maps at 1.5T. However, using the mean+5SD criterion at 1.5T, T_1 maps significantly underestimated the infarct size (9.4±5.6% vs. 15.5±9.4%, respectively, $p<0.001$) and transmurality (59±5% vs. 76±6%, respectively, $p<0.001$) in AMI relative to LGE images. Segmental comparison of infarct

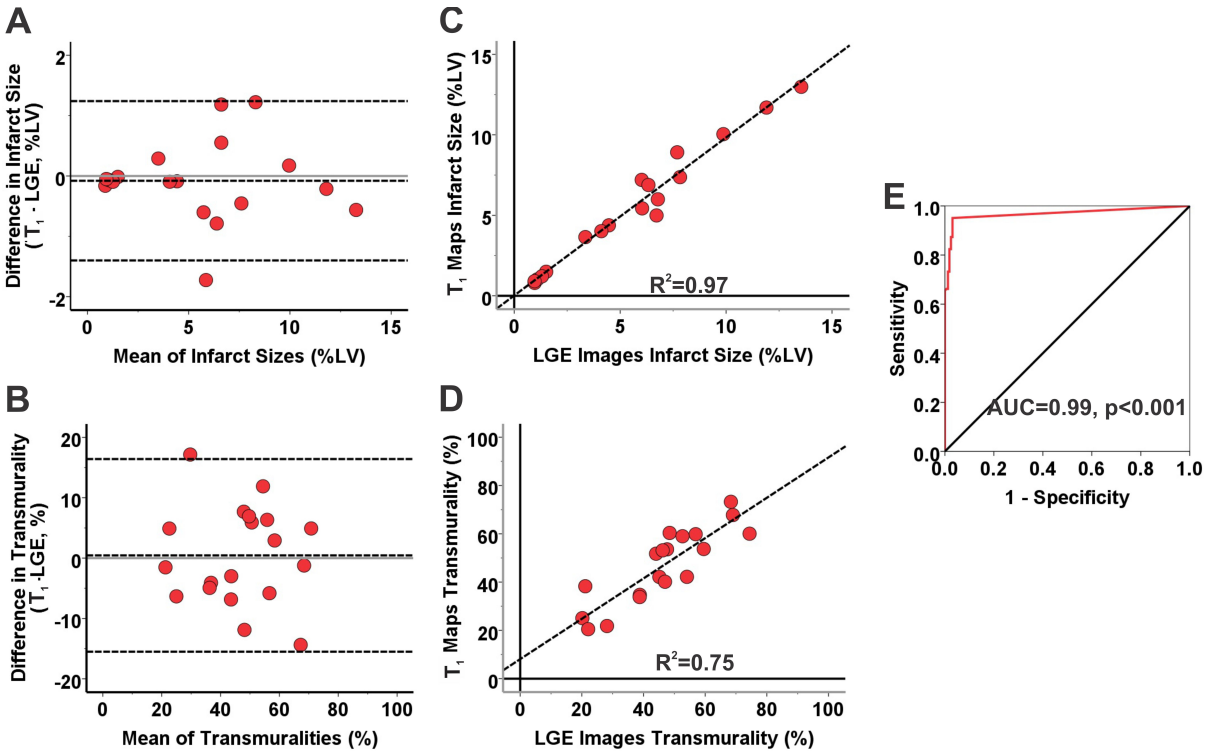

Figure 3.4: *Diagnostic performance of native T_1 maps for detecting chronic myocardial infarction at 3T.* Bland-Altman analysis showed excellent agreement between LGE images and T_1 maps for measuring infarct size (panel A) and transmurality (panel B) during the chronic phase at 3T. Excellent correlations were observed between LGE images and T_1 maps for measuring infarct size ($R^2 = 0.97$; panel C) and transmurality ($R^2 = 0.75$; panel D). ROC analysis showed that the area under the curve was 0.99 (panel E).

sizes also showed significant underestimation by T_1 maps compared to LGE images ($p<0.001$). Bland-Altman analysis showed moderate agreement between LGE images and T_1 maps for measuring infarct size (Bias = -8.07±4.6%; Figure 3.6A) and transmurality (Bias = -17.61

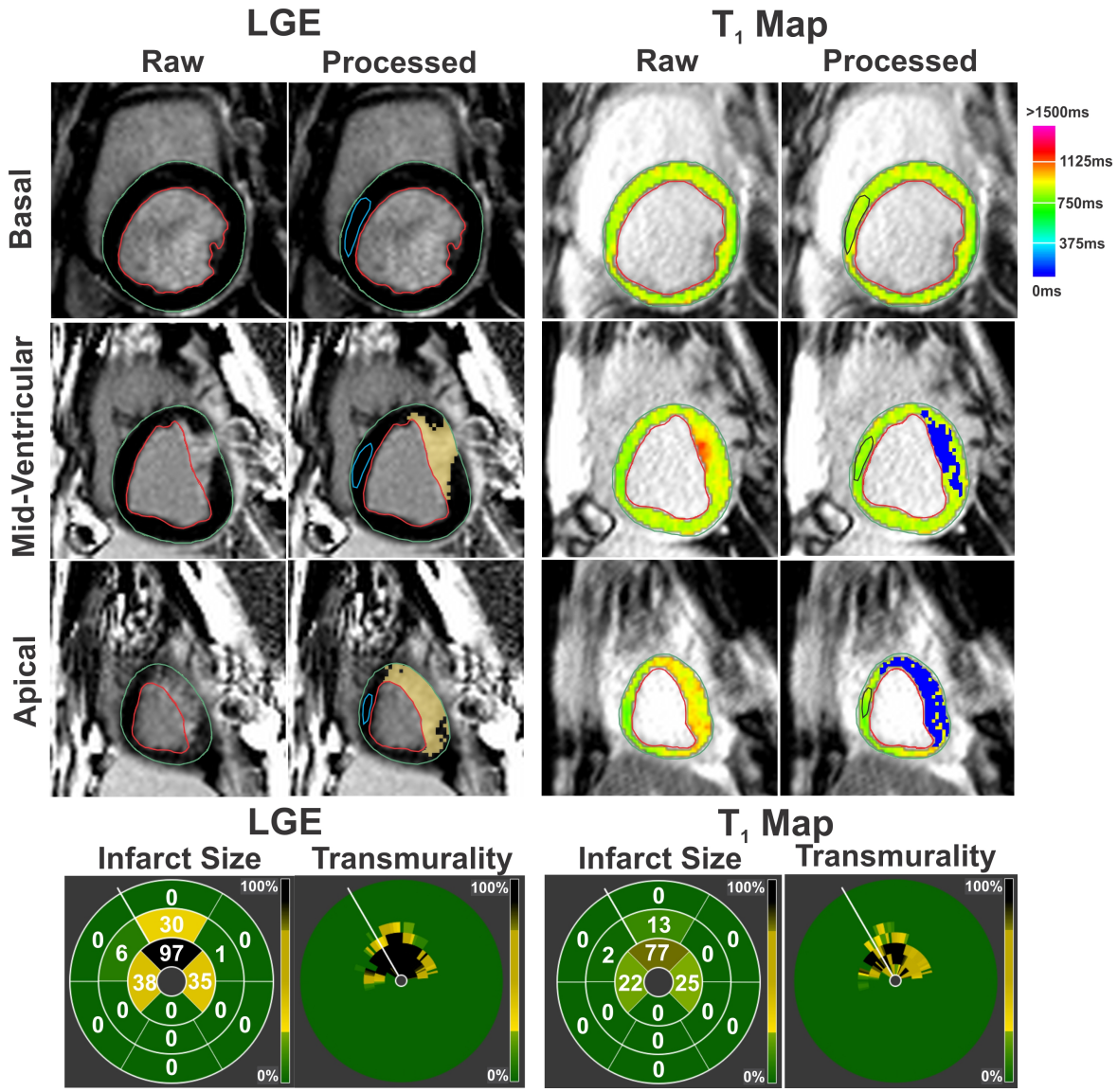

Figure 3.5: *Detecting acute myocardial infarction at 1.5T.* Representative LGE images and T_1 maps of basal, mid-ventricular and apical slices acquired at 7 days post reperfusion from a canine scanned at 1.5T are shown. Infarcted myocardium was identified as in Figure 3.1. Good correlation was observed between LGE images and the T_1 maps in terms of location of the infarcted myocardium.

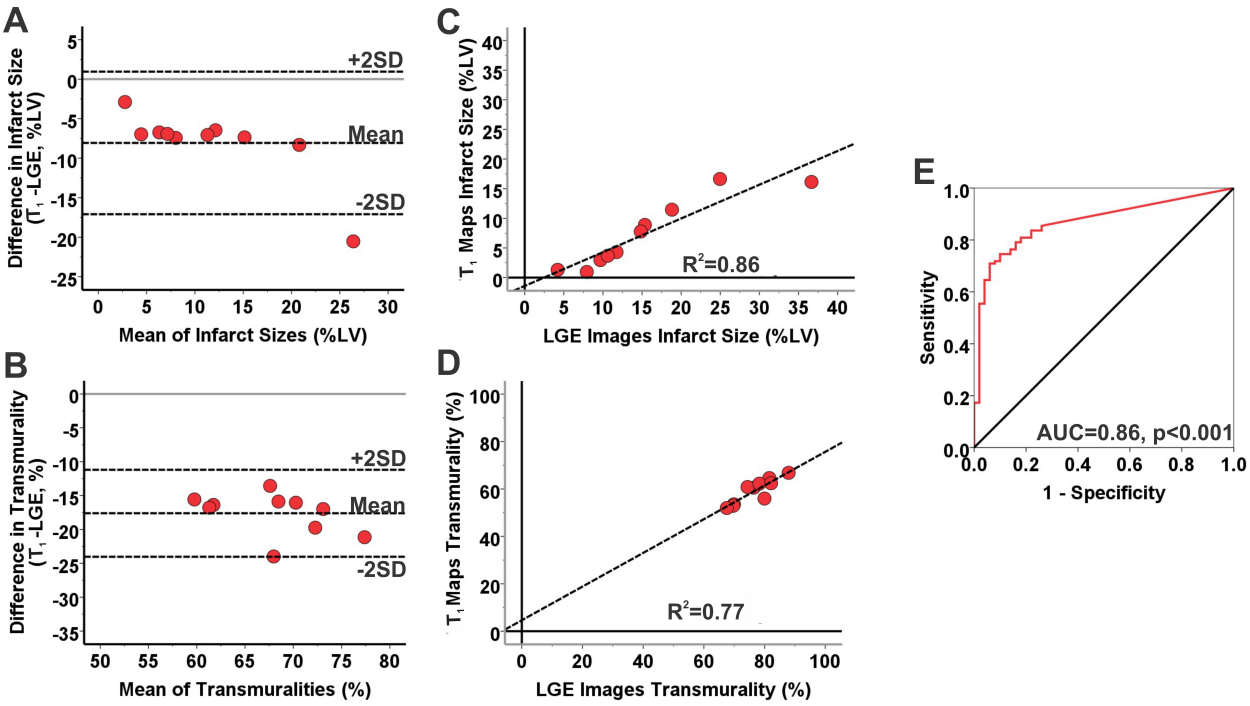

Figure 3.6: *Diagnostic performance of native T_1 maps for detecting acute myocardial infarction at 1.5T.* Bland-Altman analysis showed moderate agreement between LGE images and T_1 maps for measuring infarct size (panel A) and transmurality (panel B) using the mean + 5SD criterion at 1.5T in AMI. T_1 maps significantly underestimated infarct size and transmurality compared to LGE images. However, strong correlations were observed between LGE images and T_1 maps for measuring acute infarct size ($R^2 = 0.86$; panel C) and transmurality ($R^2 = 0.77$; panel D). ROC analysis showed that area under the curve was 0.86 (panel E).

±3.27%; Figure 3.6B) measured using the mean+5SD criterion. However, strong correlations were observed between LGE images and T_1 maps for measuring acute infarct size ($R^2 = 0.86$; Slope = 0.57, p<0.001; Intercept = –1.40, p = 0.36; Figure 3.6C) and transmurality ($R^2 = 0.77$; Slope = 0.71, p = 0.06; Intercept = 4.63, p = 0.66; Figure 3.6D). At 1.5T, T_1 maps were positive for AMI in 92 of 110 segments (84% sensitivity; 95% CI: 77-91%), and negative for AMI in 37 of 50 segments (74% specificity; 95% CI: 62-86%). ROC analysis showed that the area under the curve was 0.86 (Figure 3.6E). Using the previously reported mean+3SD criterion (317) for

detecting AMI on T_1 maps at 1.5T, infarct size (16.4±8.2%) and transmurality (81±9%) measured using T_1 maps were not significantly different from those measured using the mean+5SD criterion on LGE images (p = 0.28 for infarct size and p = 0.18 for transmurality).

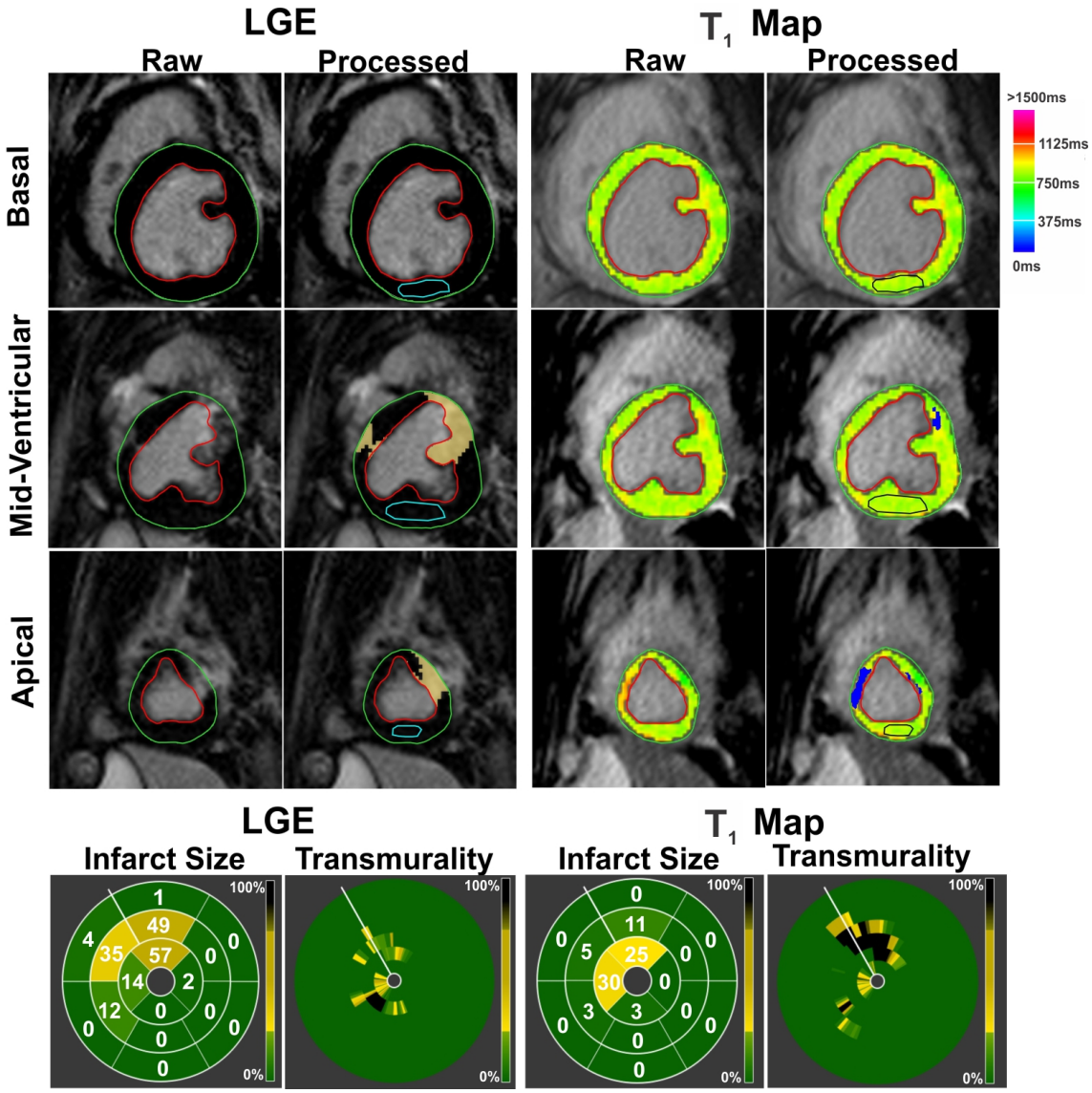

Figure 3.7: *Detecting chronic myocardial infarction at 1.5T*. Representative LGE images and T_1 maps of basal, mid-ventricular and apical slices acquired at 4 months post reperfusion from a canine scanned at 1.5T are shown. The LGE image and T_1 map were poorly correlated with respect to the spatial extent and location of the infarcted myocardium. Note that in the apical slice, there is a complete mismatch in the infarcted myocardium detected by the

LGE image and the T_1 map. T_1 hyperintensity observed in the apical slice was possibly due to partial volume effects. Bulls-eye plots showed significant underestimation of infarct size and transmurality on T_1 maps relative to LGE images ($p<0.001$ for both cases).

3.4.4. Detecting Chronic Myocardial Infarction at 1.5T

Representative LGE images and T_1 maps, along with bulls-eye plots (obtained using the mean+5SD criterion), acquired from a canine scanned at 1.5T at 4 months post-MI are shown in Figure 3.7. Mean infarct size (2.1±1.2% vs. 4.8±1.8%, $p<0.001$) and transmurality (47±7% vs. 66±9%, $p<0.001$) measured on T_1 maps using the mean+5SD criterion in CMI were significantly lower than those measured on LGE images. Segmental comparison of infarct sizes in CMI showed significant underestimation by T_1 maps compared to LGE images ($p<0.001$). Bland-Altman analysis showed poor agreement between LGE images and T_1 maps for measuring infarct size (Bias = –2.74±1.31%; Figure 3.8A) and transmurality (Bias = –19.67±6.70%; Figure 3.8B). Moderate correlations were observed between LGE images and T_1 maps for measuring infarct size ($R^2 = 0.44$; Slope = 0.43, $p = 0.004$; Intercept = –0.03, $p = 0.97$; Figure 3.8C) and transmurality ($R^2 = 0.51$; Slope = 0.61, $p = 0.10$; Intercept = 6.60, $p = 0.65$; Figure 3.8D). At 1.5T, T_1 maps were positive for CMI in 52 of 90 segments (58% sensitivity; 95% CI: 48-68%), and negative for CMI in 55 of 70 segments (78% specificity; 95% CI: 69-88%). ROC analysis showed that area under the curve was 0.79 (Figure 3.8E). Using the less stringent mean+3SD criterion for detecting CMI on T_1 maps at 1.5T, T_1 maps still significantly underestimated the infarct size and transmurality relative to those measured using mean+5SD criterion on LGE images (infarct size from T_1 map: 3.4±1.6%, $p<0.001$; transmurality from T_1 map: 52±20%, $p<0.001$).

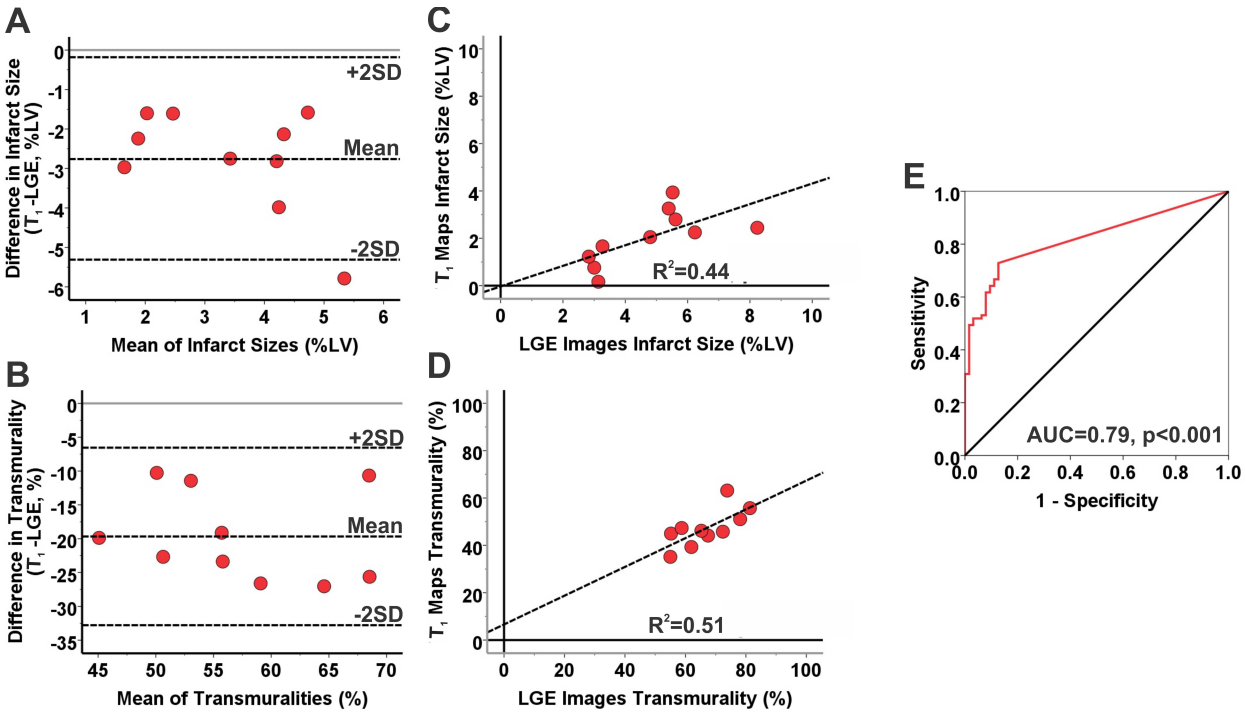

Figure 3.8: *Diagnostic performance of native T_1 maps for detecting chronic myocardial infarction at 1.5T.* Bland-Altman analysis showed poor agreement between LGE images and T_1 maps for measuring infarct size (panel A) and transmurality (panel B) during the chronic phase at 1.5T. T_1 maps greatly underestimated infarct size and transmurality compared to LGE images. Moderate correlations were observed between LGE images and T_1 maps for measuring infarct size ($R^2 = 0.44$; panel C) and transmurality ($R^2 = 0.51$; panel D). ROC analysis showed that area under the curve was 0.79 (panel E).

3.4.5. T_1, T_2 and LGE Characteristics of Infarcted Myocardium at 3T and 1.5T in Acute and Chronic Myocardial Infarctions

Table 3.2 summarizes the T_1, T_2 and LGE-SI characteristics of infarcted and remote myocardium at 3T and 1.5T at 7 days and 4 months post-MI. Representative LGE images, T_1 maps and T_2 maps acquired from four different canines at 3T and 1.5T during the acute and chronic phases of MI are shown in Figure 3.9.

Compared to remote myocardium, mean T_1 and T_2 of the infarcted myocardium were increased by 329±119 ms and 18±6 ms respectively in AMI at 3T ($p<0.001$ for both cases). In terms of infarcted to remote myocardium contrast, percentage change in LGE-SI was nearly 28-fold higher than percentage change in T_1 ($p<0.001$). However, the coefficient of variation (CV) of the percentage change in LGE-SI was two-fold higher than percentage change in T_1 (0.66 vs. 0.30) indicating a greater variability in LGE versus T_1 image contrast.

Field Strength	3T				1.5T			
Time post-MI	Day 7		Month 4		Day 7		Month 4	
Tissue Type	Remote	Infarcted	Remote	Infarcted	Remote	Infarcted	Remote	Infarcted
Native T_1 (ms)	1230±63	1563±154	1257±138	1485±139	924±72	1104±108	976±80	1060±116
Native ΔT_1 between Remote and Infarcted Myocardium (ms)	329±119		239±104		184±77		89±38	
T_2 (ms)	46±4	64±9	44±4	46±3	50±4	69±5	49±5	51±6
ΔT_2 between Remote and Infarcted Myocardium (ms)	18±6		2±3		19±7		2±5	
%Change in Native T_1 with respect to Remote	26±8		19±7		14±8		12±6	
%Change in LGE signal intensity with respect to Remote	728±484		790±513		376±192		409±163	
Sensitivity of Native T_1 Maps	94%		95%		84%		58%	
Specificity of Native T_1 Maps	94%		97%		74%		78%	

Table 3.2: T_1, T_2 and LGE signal intensity characteristics of acute and chronic myocardial infarction at 1.5T and 3T

In CMI, significant T_1 increase was still visually evident within infarcted myocardium at 3T, while edema within the infarcted myocardium, typically visualized via T_2 images, appeared to have resolved. Mean T_1 of infarcted myocardium in CMI at 3T was increased by 239±104 ms with respect to remote myocardium ($p<0.001$), while mean difference in T_2 values of infarcted and remote myocardium in CMI at 3T was not statistically significant (2±3 ms; $p = 0.19$). Mean T_1 of the infarcted myocardium in CMI was significantly lower than that in AMI ($p<0.001$). However, no significant difference was observed between mean T_1 values of remote myocardium measured during the acute and chronic phases ($p = 0.21$). Consistent with the acute studies, percentage change in LGE-SI was nearly 40-fold higher than percentage change in T_1 ($p<0.001$). However, the CV of percentage change in LGE-SI was 1.5-fold higher (0.65) compared to percentage change in T_1 (0.42), again indicating a higher degree of variability in LGE versus T_1 image contrast.

In AMIs at 1.5T, significant T_2 increase was visually evident within infarcted myocardium, while moderate T_1 increase was visible in infarcted myocardium. Mean T_1 of infarcted myocardium at 1.5T in AMI was 184±77 ms higher than that of remote myocardium ($p<0.001$), while mean T_2 of infarcted myocardium was 20±7 ms higher than that of remote myocardium ($p<0.001$). Percentage change in the LGE-SI was nearly 26-fold higher than percentage change in T_1 at 1.5T ($p<0.001$). Compared to 1.5T, infarcted to remote myocardium T_1 contrast in AMI was nearly 2-fold higher at 3T.

After 4 months post-MI, neither T_1 nor T_2 increase was visually evident within infarcted myocardium at 1.5T. Mean T_1 value of infarcted myocardium at 1.5T in CMI was mildly higher by 89±38 ms than that of remote myocardium ($p = 0.04$). Mean difference in T_2 values of infarcted and remote myocardium was not statistically different from 0 (2±5 ms; $p = 0.55$). Mean

T_1 of the infarcted myocardium in CMI was significantly lower than that in AMI ($p<0.001$). No significant difference was observed between the mean T_1 values of the remote myocardium during the acute and chronic period of MI ($p = 0.23$). Percentage change in the LGE-SI was 34-fold higher than percentage change in T_1 at 1.5T ($p<0.001$). Compared to 1.5T, infarcted to remote myocardium T_1 contrast in CMI was nearly 50% higher at 3T.

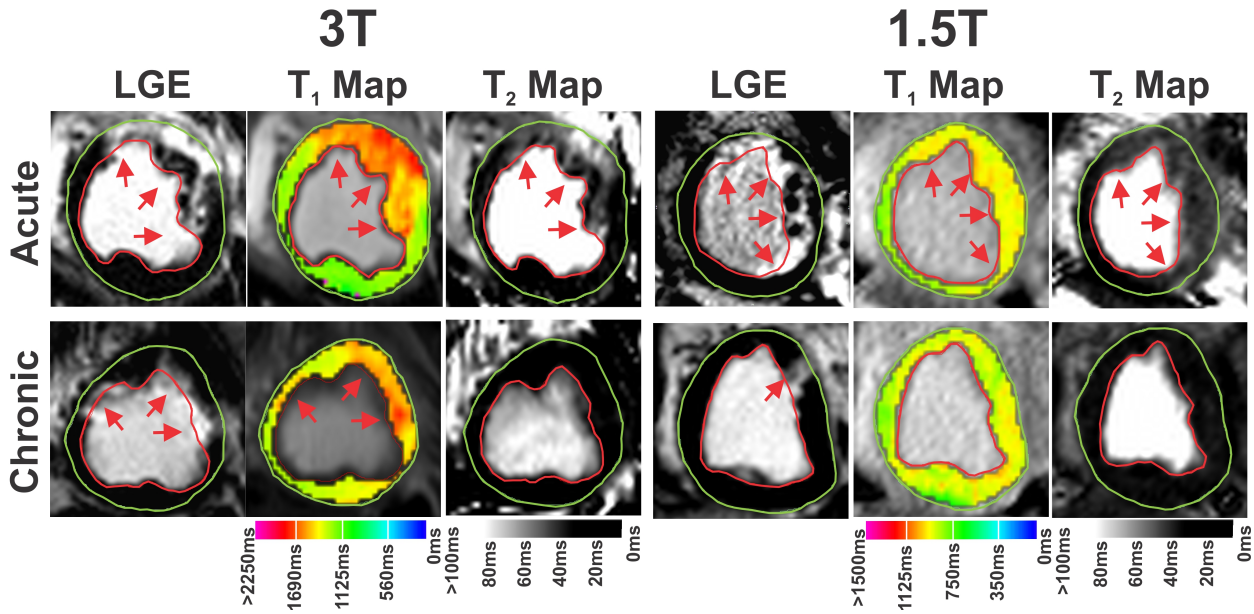

Figure 3.9: *T_1 and T_2 characteristics of infarcted myocardium at 1.5T and 3T during acute and chronic phases of infarction*. Representative LGE images, T_1 maps and T_2 maps acquired at 1.5T and 3T from four different canines at 7 days and 4 months post MI are shown. Arrows point to the hyperintense sites of LGE, T_1 and T_2. Significant T_1 and T_2 increases were visually evident within the infarcted territories in AMI at 3T. While T_1 elevations persisted at 4 months post MI at 3T, T_2 of the infarcted myocardium returned to baseline levels. At 1.5T, T_1 and T_2 of infarcted myocardium were significantly increased in AMI. However, both T_1 and T_2 values of the infarcted myocardium were not visually different from those of remote myocardium in CMI at 1.5T.

3.4.6. Histopathological Validation of Replacement Fibrosis in Chronic Myocardial Infarctions

Figure 3.10 shows representative LGE images and T_1 maps acquired at 3T from three different canines at 4 months post-reperfusion along with slice-matched ex-vivo TTC and EMT staining images. Both LGE images and T_1 maps agreed well with ex-vivo TTC images in terms of the spatial location of the MI. EMT staining showed extensive replacement fibrosis within infarcted myocardium, which validated that T_1 hyperintensity in the CMI predominantly arose from fibrosis. Similar evidence was observed in the other animals.

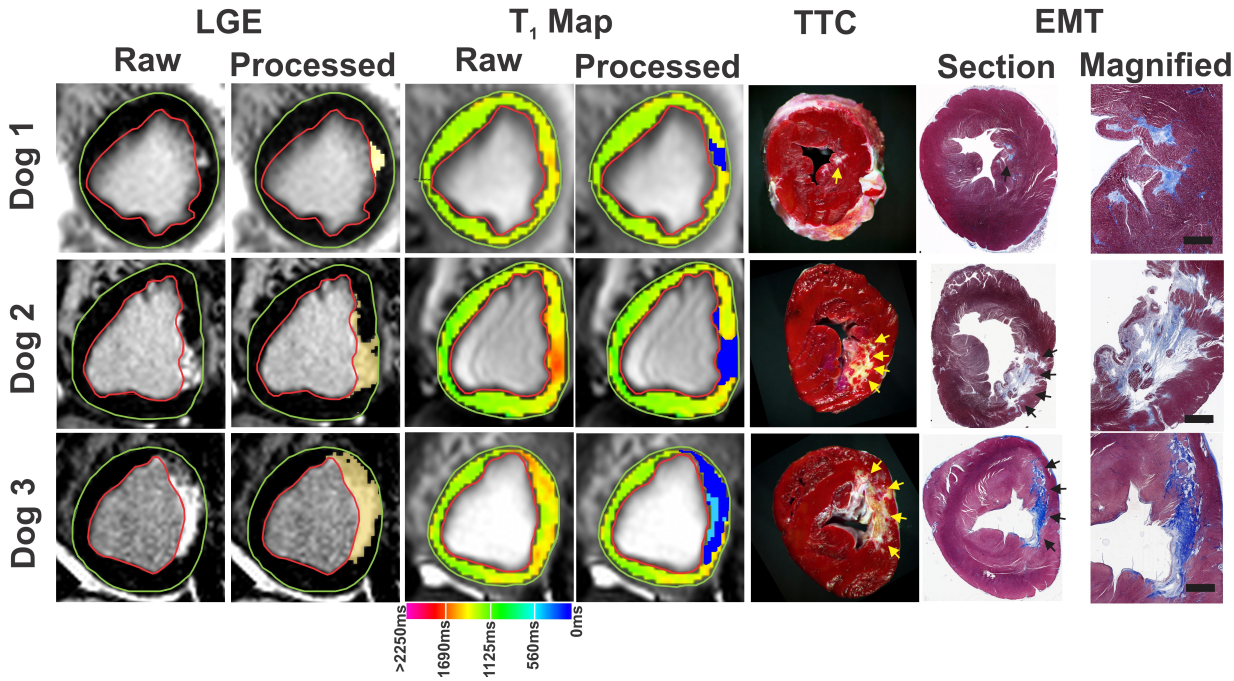

Figure 3.10: *Histopathological validation of replacement fibrosis detected on LGE images and native T_1 maps during the chronic phase of MI at 3T*. Representative LGE images and T_1 maps acquired from three different canines scanned at 3T at 4 months post MI are shown along with the corresponding ex-vivo slice-matched TTC and EMT-stained images. Highlighted blue pixels on the processed images show the site of infarction on LGE images and T_1 maps, while arrows point to the site of infarction in TTC and EMT images. Both LGE images and T_1 maps agreed well with ex-vivo TTC images in terms of spatial location of the infarcted myocardium. T_1 maps could reliably detect infarctions ranging in size from 1.2% of the total LV (Dog 1) to 12.9% of the total LV (Dog 3).

Highlighted light blue pixels on the processed T_1 map from dog 3 point to the presence of chronic iron deposition. Corresponding to the chronic iron deposition seen on T_1 map, TTC image shows a yellow-brown discoloration in the necrotic core indicating the presence of iron. Additional histological validation using EMT staining confirmed extensive replacement fibrosis within the infarcted regions indicating that T_1 hyperintensity in the chronic phase of infarction at 3T predominantly arose from fibrosis. Scale bars on the magnified views of EMT images measure 2 mm.

3.5. Discussion

Characterizing CMIs using MRI has immense clinical importance for predicting long-term LV function (92,107), assessing the efficacy of therapeutic regeneration (362,363) and risk stratifying patients for cardiac defibrillator implantation (349). However, the utility of LGE imaging for this purpose is partly limited by the contra-indication of Gadolinium infusion in nearly 20% of the patients with AMI with chronic end-stage kidney disease (368,369,384,385). Non-contrast approaches for viability imaging can, therefore, be of significant value for the clinical and therapeutic management of patients with MI.

This study confirms the hypothesis that native T_1 mapping at 3T can reliably characterize CMIs with high specificity and sensitivity. Using a canine model of MIs and threshold-based detection of infarcted myocardium, native T_1 maps at 3T have been shown to accurately determine location, size and transmurality of CMI just as well as LGE imaging. However, the same threshold-based criterion applied to native T_1 maps at 1.5T has been found to significantly underestimate infarct size and transmurality obtained from LGE images in both AMI and CMI. The less stringent mean+3SD criterion, which was previously tested by Messroghli et al (317), has significantly improved the diagnostic performance of T_1 mapping at 1.5T. Consistent with the previously reported observations, these results have indicated that T_1 maps at 1.5T can

reliably determine infarct size using the mean+3SD criterion in AMI (317), but significantly underestimates infarct size at 1.5T in the CMI despite the less stringent criteria. The ability to reliably detect infarcted myocardium at 3T compared to 1.5T is further explained by the findings that infarcted to remote myocardium T_1 contrast is 2-fold higher at 3T relative to 1.5T in AMI, and 1.5-fold higher in CMI. These results have suggested that native T_1 mapping at 3T can be a reliable alternative to LGE for characterizing CMI with the potential for clinical translation. In addition, the results are consistent with previously reported observations that myocardial edema, as detected using T_2-based imaging, resolves in the chronic phase of MI (143,404), and T_2-based imaging in conjunction with LGE imaging can be used to differentiate between AMIs and CMIs (118). Hence, together with T_2 and T_1 maps it may be possible to reliably discriminate CMI in much the same way T_2 imaging is used for discriminating CMI when LGE is available.

LGE imaging and contrast-enhanced T_1 mapping are primarily limited by the association of Gadolinium use to nephrogenic systemic fibrosis in patients with late-stage chronic kidney disease (378,382). Further, as observed from the high CV in the LGE contrast in this study, Gadolinium kinetics in infarcted and remote myocardium lead to dynamic changes in LGE-SI values and contrast-enhanced T_1 values which may be irreproducible across different imaging sessions. These limitations may be overcome by the application of contrast-free techniques for assessing MIs. Recently, $T_{1\rho}$ imaging has been proposed as a potential contrast-free MRI technique for detecting AMI (417) and CMI (418). However, this technique is limited by its high specific absorption rate (SAR), which can further limit the contrast between infarcted and remote myocardium. Native T_1 mapping overcomes many of the limitations faced by other techniques and opens the door to unique opportunities. First, it enables infarct characterization in patients with poor renal function, and is not SAR-limited. Second, it can improve the work flow demands

during imaging exams: (a) allows for infarct characterization typically performed with LGE to be executed in any order within the imaging session, (b) eliminates the need to determine the inversion time, which continually changes as a function of the wash-out kinetics of the GBCA, and (c) removes the waiting period between contrast administration and LGE acquisitions. Third, since pixel intensities of T_1 maps provide intrinsic T_1 values, it makes the approach inherently quantitative, which permits reliable serial examinations of infarct healing and remodeling, especially when prescribed with a T_1 mapping approach that is less sensitive to heart rate variations (313). Finally, it can render significant cost savings since contrast infusions and venous cannulations would become unnecessary and the length of the imaging exam may be reduced.

Previous studies have reported that myocardial edema associated with AMI can be accurately detected and sized using T_1-weighted imaging (306) and native T_1 maps at both 1.5T and 3T (313,315,317,409). Consistently, this study has shown that T_1 elevation in AMI is accompanied by T_2 elevation, indicating that the ability of T_1 mapping to reliably detect AMI predominantly arose from increased free water content in infarcted myocardium (118,315). Although the clinical value of native T_1 maps for detecting AMI has been well studied, its potential for assessing CMI has not been fully explored to date. Messroghli et al (317) and Bauner et al (319) have shown that, at 1.5T, CMIs are associated with significant increase in native T_1. However, the diagnostic performance of native T_1 maps at 1.5T to detect CMI has been reported to be poor. Recently, Dall'Armellina and colleagues have reported preliminary case studies at 3T in which T_1 hyperenhancement could be observed even in CMI without any concomitant T_2 increase (419). However, the nature of such T_1 hyperenhancement was not fully elucidated. This study has shown that that the extensive replacement fibrosis associated with

CMI might be responsible for the observed T_1 elevations in chronic phase of MI. The reversion of T_2 values of infarcted myocardium to baseline levels, which indicates complete resolution of edema (118), additionally support the notion that the apparent T_1 elevations in CMI may be predominantly due to fibrosis. This is consistent with previous reports showing significant T_1 elevations associated with diffuse myocardial fibrosis in non-ischemic cardiomyopathies such as aortic stenosis (411), hypertrophic cardiomyopathy (412,413) and idiopathic dilated cardiomyopathy (412,413).

This study has shown that one of the primary reasons that CMIs are more reliably characterized at 3T is due to the biophysical differences in T_1 relaxation of remote myocardium and infarcted myocardium at 3T and 1.5T. As the field strength is increased from 1.5T to 3T, the T_1 values of the non-infarcted (remote) myocardium and the infarcted (fibrotic) myocardium have been found to increase by ~29% and ~40% (Table 3.2), respectively. This is consistent with previous studies, which have rigorously shown that T_1 of a given tissue can increase between ~10% to ~70% at 3T compared to 1.5T, and that the extent of the increase is dependent on the type of tissue (420). Although the mechanistic underpinnings of native T_1 elongation in CMIs are not entirely clear, there are a few possible explanations. One potential mechanism is that the apparent diffusion coefficient in CMIs is higher than that of remote myocardium (421-424), which implies greater diffusivity of water molecules, lower viscosity, lower correlation times of molecular motion and hence longer T_1 values (425). In addition, another possibility is the potential bias in T_1 values measured using MOLLI sequences with SSFP readouts which may be subject to magnetization transfer (MT) effects. Robson et al have shown that MT effects can lead to T_1 underestimation by MOLLI (426). Scholz et al (427) and Weber et al (428) have shown that the MT effects are reduced in AMIs and CMIs, which could potentially lead to longer

apparent T_1 values within infarcted myocardium. Nevertheless, further studies are necessary to fully elucidate the mechanisms and their relative contributions to the underlying T_1 elongations observed in CMIs.

This study has shown that LGE images have a nearly 30-fold higher infarcted to remote myocardium contrast relative to the proposed native T_1 maps at 3T. While the high image contrast of infarcted myocardium in LGE images is attributable to the use GBCA, the imposed nulling of remote myocardium by IR preparation is another significant contributor to the observed contrast. In this context, it should be noted that as in LGE imaging, IR preparation could also be introduced to significantly improve image contrast between infarcted and remote myocardium in native T_1-weighted techniques as well. Based on the T_1 values of remote myocardium (1250 ms) and CMIs (1490 ms) at 3T, an IR preparation that nulls remote myocardium gives a 12% equilibrium magnetization available for readout from infarcted myocardium. Similarly, assuming that the contrast-enhanced T_1 values (10 minutes post-Gadolinium injection) of remote and infarcted myocardium at 3T are 400 ms and 230 ms respectively, an IR-prepared sequence that nulls remote myocardium (such as conventional LGE imaging) gives a 40% equilibrium magnetization available for readout from infarcted myocardium. This suggests that, if employed, IR preparation can potentially increase the image contrast between infarcted and remote myocardium by 900% compared to the current levels. Experimental studies are necessary to confirm these theoretical estimations. Nevertheless, while this is expected to improve the visualization of CMI, the current T_1 mapping approach evaluated here still provides excellent diagnostic accuracy.

Together with previous studies, this study has shown that native T_1 mapping has great potential for widespread clinical applicability in the setting CMI. While a few studies have

assessed the prognostic significance of T_1 hyperenhancement in AMI (315,316), future studies that elucidate the relationship of T_1 hyperenhancement in the CMI to long-term LV function, collagen metabolism and extracellular matrix remodeling are necessary.

3.5.1. Study Limitations

First, the sample size used in this study is relatively small, but comparable to those used in previous studies in patients with MIs (315-317,319). Second, this study relied on identifying the remote territory on the basis of LGE. Additional studies are necessary to examine whether remote territories can be reliably identified solely on the basis of native T_1 maps. Third, the proposed approach has not been evaluated in a clinical setting. Hence, additional studies are required to determine the diagnostic performance of native T_1 maps in patients with CMI. Third, this study has only used the mean+5SD thresholding as this criterion has been shown to be robust for delineating infarcted myocardium in LGE imaging (414-416). Nevertheless, a comprehensive study comparing the different thresholding criteria to ex-vivo histology-based infarct sizing may be necessary for further validation. However, such a study needs to take into account potential changes in T_1 following animal sacrifice and registration between MR images and ex-vivo standard. Finally, this study was limited to LAD MIs. Additional studies are needed to extend the findings from this study to MIs in other coronary territories.

3.6. Conclusion

Native T_1 mapping at 3T can reliably determine infarct location, size, and transmurality of CMI with high diagnostic accuracy that is comparable to conventional LGE imaging. Given its non-reliance on exogenous contrast media, potential efficiency improvements associated with

workflow during imaging sessions, and quantitative nature, native T_1 mapping provides an appealing alternative for viability imaging when LGE imaging is contraindicated. Patient studies are necessary for clinical translation.

CHAPTER 4

Robustness of Native T_1 maps at 3T for Characterizing Chronic Myocardial Infarctions

4.1. Abstract

In the previous chapter, native T_1 maps at 3T have been shown to be able to CMIs without the need for exogenous contrast agents. The purpose of this study is to establish the sensitivity and specificity of different automatic, semi-automatic, and visual methods for characterizing CMIs on native T_1 maps at 3T. Native T_1 maps and LGE images were acquired at 3T in canines (n = 23) at 4 months following MI. Infarct size and transmurality determined from T_1 maps using Mean+2SD, Mean+3SD, Mean+4SD, Mean+5SD, Mean+6SD, Otsu's, Full Width at Half Maximum (FWHM), and visual delineation methods were compared against the gold-standard LGE measurements, and their diagnostic performance was evaluated. Relative to LGE images, mean infarct size and transmurality measured from native T_1 maps were significantly over-estimated by Mean+2SD, Mean+3SD, Mean+4SD, and FWHM methods ($p<0.001$, for all cases). Mean+6SD criterion and visual delineation significantly underestimated infarct size ($p<0.001$ for both cases) and transmurality (Mean+6SD: $p = 0.01$; Visual: $p<0.001$) on T_1 maps. Otsu's method showed no difference for measuring infarct size on T_1 maps compared to LGE images ($p = 0.06$), but it over-estimated the infarct transmurality ($p<0.001$). Mean+5SD criterion showed no difference for measuring either infarct size ($p=0.98$) or transmurality ($p = 0.57$) on T_1 maps relative to LGE images. Mean+5SD criterion for detecting CMIs on T_1 maps at 3T showed the

strongest diagnostic performance (AUC = 0.981, $p<0.001$), while visual delineation showed the weakest diagnostic performance (AUC = 0.886, $p<0.001$).

4.2. Introduction

In chapter 3, native T_1 mapping based on MOLLI with SSFP readout at 3T has been shown to be a potential alternative to LGE imaging for characterizing CMIs. However, the optimal approach for determining the size and transmurality of MIs from native T_1 maps relative to LGE remains to be systematically investigated. The purpose of this study is to (a) establish the sensitivity and specificity of automatic, semi-automatic and visual methods; and (b) identify the optimal approach for characterizing CMIs on the basis of native T_1 maps at 3T. This was investigated in canines subjected to CMIs and imaged with LGE and native T_1-based MRI.

4.3. Methods

4.3.1. Animal Preparation and Imaging Protocol

Twenty-three canines were studied according to the protocols approved by the Institutional Animal Care and Use Committee. Canines were subjected to 3 hours of total LAD occlusion followed by reperfusion. MRI exams were performed at 4 months following MI on a 3T clinical MRI system (MAGNETOM® Verio, Siemens Healthcare, Erlangen, Germany). ECG-triggered breath-held cine-bSSFP (TR/TE = 3.2/1.6 ms; $\alpha = 50°$; BW = 1371 Hz/pixel; 25-30 cardiac phases), native T_1 –weighted (MOLLI; 8 TIs with 2 Look-Locker cycles of 3+5 images (429); minimum TI = 110 ms; ΔTI = 80 ms; TR/TE = 2.2/1.1 ms; $\alpha = 35°$; BW = 1042 Hz/pixel), T_2*-weighted (for chronic iron (430); multiple gradient-echo; TR = 12 ms; 6 TEs = 2.0-9.5 ms; ΔTE

= 1.5 ms; α = 10°; BW = 930 Hz/pixel), and LGE images (IR-prepared GRE acquired 10 minutes following intravenous injection of 0.2 mmol/kg gadopentate dimeglumine (Magnevist, Bayer Healthcare Pharmaceuticals Inc., Wayne, NJ); optimal TI to null remote myocardium; TR/TE = 3.0/1.5 ms; α = 25°; BW = 586 Hz/pixel) of contiguous short-axis slices covering the entire LV were acquired. All canines were euthanized immediately following the MRI study, and ex-vivo TTC and EMT staining were performed to confirm the presence of MI and collagen deposition.

4.3.2. Image Analyses

Motion-corrected native T_1 maps were generated from the MOLLI images. All image analyses were performed using cvi[42] image processing software (Circle Cardiovascular Imaging Inc., Calgary, AB, Canada). Remote myocardium was identified on LGE images as the region showing no hyperintensity. Infarcted myocardium was identified on LGE images using the standard (Mean +5SD) criterion relative to a reference ROI drawn within the remote myocardium (415). Infarcted myocardium was identified on T_1 maps using the following methods.

- *Mean + n SD Criteria* (414) – The reference ROIs drawn on LGE images were copied onto the corresponding native T_1 maps. The mean signal intensity of all the pixels within the ROI and its SD were calculated. The detection thresholds were then set at Mean+2SD, Mean+3SD, Mean+4SD, Mean+5SD, and Mean+6SD and the infarcted myocardium was identified according to the different criteria.
- *Full Width at Half Maximum (FWHM)* – A reference ROI was manually drawn in the visually hyperintense territories on native T_1 maps. The maximum signal intensity within

the ROI was determined, and the threshold was set at >50% of the maximum signal intensity to identify the infarcted myocardium (414).

- *Otsu's Method* – Otsu's method automatically detects the infarcted myocardium without the need to pre-define any reference ROIs. The method separates the infarcted (hyperintense) and remote (hypointense) myocardium by calculating an optimal threshold that minimizes the intra-class variance among the two pixel sets (431).
- *Visual Delineation* – Two blinded reviewers, with more than 5 years of experience in analyzing MRI images, manually delineated the visually hyperintense territories on T_1 maps in consensus using cvi[42] software.

The presence of chronic iron deposition within the infarcted territories was visually confirmed on the basis of T_2* signal losses on the corresponding T_2*-weighted images. T_2* signal losses occurring due to off-resonance effects at the heart-lung interface were carefully excluded as previously described (432). For all detection methods, hypointense cores of chronic iron deposition within the infarcted territories, when present, were manually included on T_1 maps. Segments that were not interpretable on T_1 maps due to banding artifacts were excluded from the analysis. Infarct size was measured for the entire heart as the percentage of total LV volume. To compare the diagnostic performance of different detection methods on a segmental basis, infarct size was calculated for the first 16 segments on the basis of AHA 17-segment model (apical cap was discarded). Transmurality was measured using the centerline chord method as previously described (433). For this purpose, each slice was divided into 100 equally spaced chords and the extent of the infarct along the length of each chord was measured. Mean transmurality was measured by averaging the infarct transmurality across all the chords that had at least 1% of infarct extent.

4.3.3. Statistical Analyses

All statistical analyses were performed using the IBM SPSS Statistics (version 21.0, IBM Corporation, Armonk, NY). Normality of the data was tested using Shapiro-Wilk test and quantile-quantile plots. Whole-LV infarct size and transmurality measured using Mean+5SD criterion on LGE images was compared to those measured using threshold-based and visual delineation methods on native T_1 maps. For this purpose, paired Student's t-test or Wilcoxon signed rank test were used depending on the normality of the data. Bland-Altman and linear regression analyses were performed to evaluate the concordance between LGE images and native T_1 maps for measuring whole-LV infarct size and transmurality. The slope and the intercept of the lines of best fit were tested for their equality to 1 and 0, respectively. Mixed-model ANOVA was used to compare LGE images and native T_1 maps for measuring AHA-segmental infarct size. Diagnostic performance of the different detection methods applied to native T_1 maps was evaluated using ROC analysis. For this purpose, an AHA-segmental infarct size on LGE images that is at least 1% of the total segment volume was used as the ground truth and segmental infarct size as the predictor variable. Statistical significance for all analyses was set at $p<0.05$.

4.4. Results

All canines were successfully infarcted as confirmed by the presence of LGE hyperintensity and subsequent histological validation at 4 months post-MI, of which 17 had chronic iron deposition within the infarcted territories as confirmed by T_2*-weighted images. Over all, 368 AHA segments from 23 canines were analyzed, of which 152 (41%) were positive for MI as observed on LGE images, and 216 (59%) were negative for MI. Of these, 20 segments (5%) could not be interpreted on native T_1 maps due to banding artifacts predominantly in the infero-lateral wall of

the LV, and were excluded from the final analysis. All of these excluded segments were negative for MI as confirmed by LGE images. Chronic iron deposition occurred in 68 of the 152 (45%) segments positive for MI.

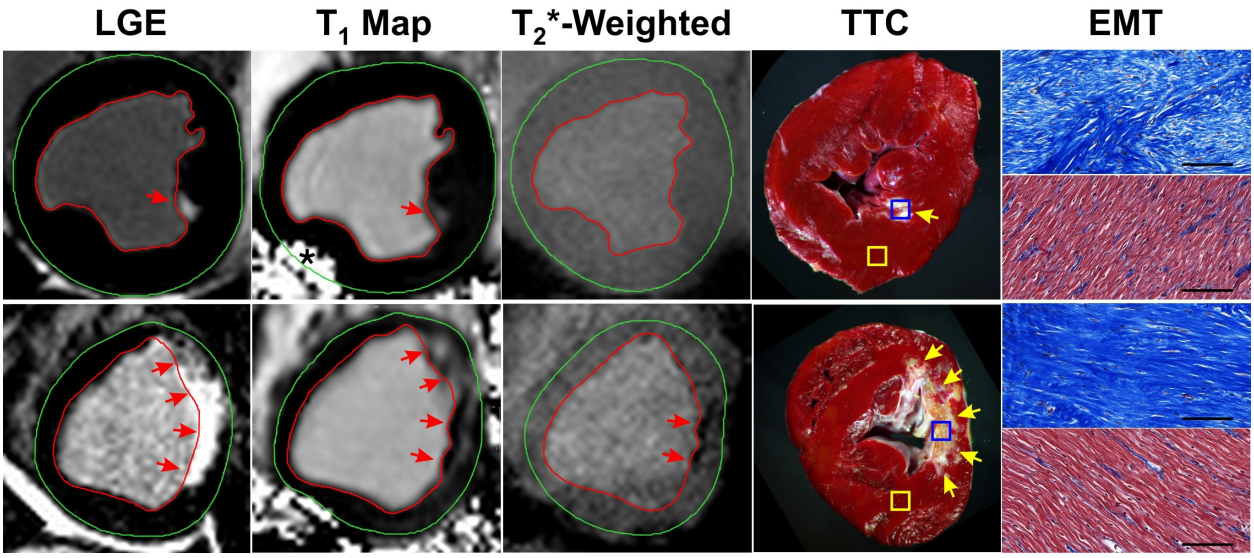

Figure 4.1: *Native T_1 maps of chronic myocardial infarctions*. Representative LGE images, native T_1 maps, and T_2*-weighted images (TE=6.5 ms) acquired from two canines, one without chronic iron deposition (top row) and one with significant chronic iron deposition (bottom row), at 4 months following MI are shown. Arrows point to the sites of MI on LGE images, native T_1 maps and ex-vivo TTC images, and chronic iron deposition on T_2*-weighted images. Significant T_1 elevations within infarcted territories (as seen on LGE images) are visually conspicuous on native T_1 maps in both cases. Hypointense core could be observed within the hyperintense infarcted territories on T_1 maps in the case with chronic iron deposition, but not in the case without chronic iron deposition. Segments affected by banding artifacts on T_1 maps (marked by asterisk) were manually excluded from the analysis. Ex-vivo TTC staining confirmed the presence of MI in both cases, while a brown discoloration within the infarcted territories indicative of chronic iron deposition is evident only in the chronic iron deposition case. Consistent with CMI, EMT staining showed significant collagen deposition within the infarcted territories (blue staining, top panel in both cases), but not in the remote myocardium (red staining, bottom panel in both cases). Scale bars correspond to 100μm.

Representative LGE image, native T_1 map, and T_2*-weighted image (TE = 6.5 ms) of a single slice acquired from two canines, one without and one with chronic iron deposition, at 4 months following MI are shown in Figure 4.1. Significant T_1 elevations within infarcted territories are visually conspicuous on native T_1 maps in both cases. Good visual agreement can be observed between the LGE image and the T_1 map in terms of the spatial location and extent of MI. In the case with chronic iron deposition, hypointense core within the infarcted territory can be observed on the T_1 map corresponding to the T_2* losses on the T_2*-weighted image. Ex-vivo TTC and EMT staining further confirmed the presence of MI and significant collagen deposition in both cases.

Figure 4.2 shows the infarcted myocardium (highlighted pixels) detected on LGE images with the standard approach, and using the different detection methods on native T_1 maps. The spatial location of MI detected using all the methods on T_1 maps generally agreed well with that detected on LGE images. Figure 4.2 also shows the infarct size measured in each of the 16 AHA segments for that canine and a bulls-eye representation of the infarct transmurality. The number within each AHA segment denotes the percentage of that segment that has been detected as infarcted by that particular detection criterion. Each concentric ring within the bulls-eye plot for transmurality represents one short-axis slice with the outermost ring representing the most basal slice, and the innermost ring representing the most apical slice. Each chord is color-coded for transmurality according to the color scale shown on the right. The AHA-segmentation models and the transmurality bulls-eye plots show that the spatial extent of the infarct seen on LGE images using the standard criterion generally agrees well with those seen on T_1 maps using different detection methods.

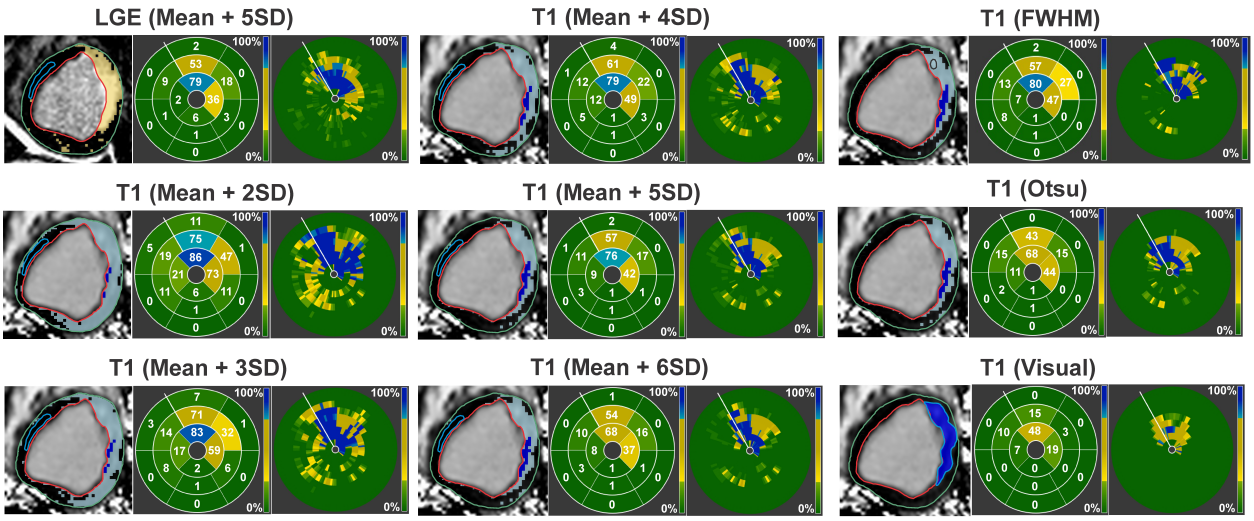

Figure 4.2: *Thresholding-based detection and visual delineation of infarcted myocardium on native T_1 maps.* Infarcted myocardium (highlighted pixels) detected using the Mean+5SD criterion on LGE images, and various (automatic, semi-automatic, and visual) methods on T_1 maps are shown. Hypointense cores of chronic iron deposition that was not detected as infarcted myocardium on T_1 maps by an automatic or semi-automatic detection method (dark blue pixels within the light blue highlighted pixels on T_1 maps) was manually included in the final analysis. Bulls-eye plots depicting the AHA-segmental infarct size and transmurality distribution are also shown for the respective methods. Infarct location and spatial extent observed on LGE images generally agreed well with those observed on native T_1 maps using the different detection methods.

4.4.1. Infarct Size Comparisons

Figure 4.3 shows a bar plot of the mean whole-LV infarct size measured from LGE images using Mean+5SD criterion, and from T_1 maps using different detection methods. Figure 4.3 also shows the Bland-Altman plots and linear regression plots for comparing the infarct size measured from LGE images to those measured from T_1 maps using different methods. Relative to LGE images, T_1 maps significantly over-estimated the infarct size when the Mean+2SD, Mean+3SD, Mean+4SD, and FWHM methods were used ($p<0.001$ for all cases). Mean+6SD criterion and

visual delineation on T_1 maps significantly under-estimated the infarct size ($p<0.001$ for both cases). However, there was no significant difference between LGE images and T_1 maps for measuring infarct size when Mean+5SD ($p = 0.98$) and Otsu's ($p = 0.06$) methods.

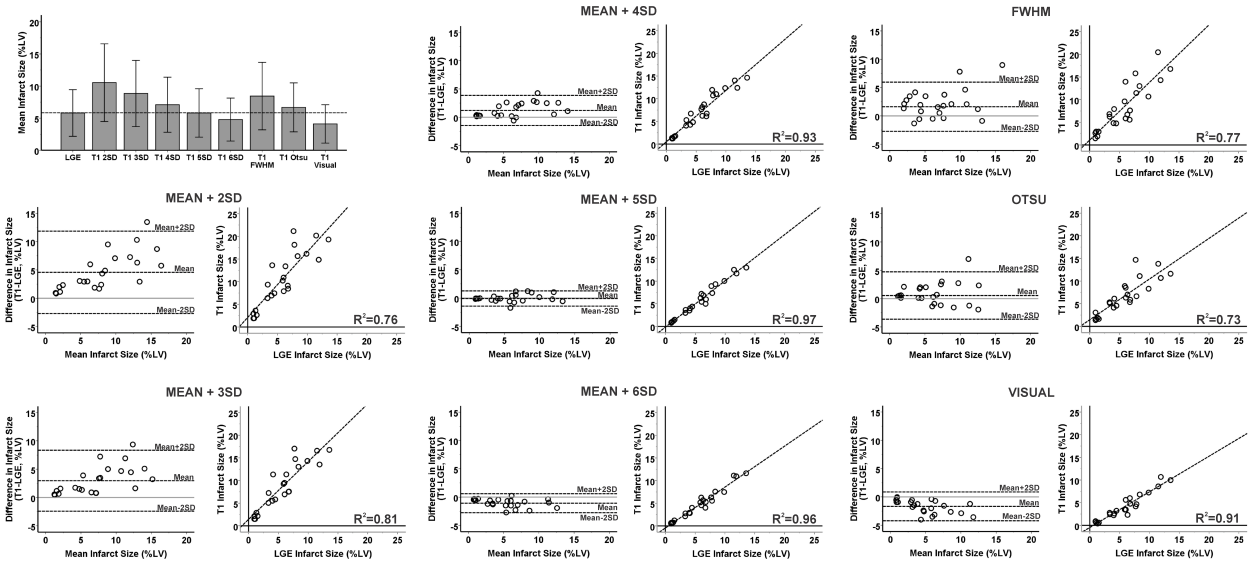

Figure 4.3: *Infarct size comparisons*. Bar plots, Bland-Altman plots, and linear regression plots, that were used to compare the infarct size measured using different methods on T_1 maps to that measured on LGE images using the standard criterion are shown. Of all the methods, infarct size measured using the Mean+5SD criterion from T_1 maps showed the best agreement to that measured using LGE images.

Table 4.1 summarizes the results from Bland-Altman and linear regression analyses for infarct size comparisons. Overall, infarct size measured using the Mean+5SD criterion on T_1 maps showed the best agreement (Bias = –0.08±0.68%) with that measured from the LGE images using the standard criterion. The strongest positive bias was observed with the Mean+2SD criterion (Bias = 4.58±3.64%), while the strongest negative bias was observed with the visual delineation method (Bias = –1.67±1.27%). Infarct size measured using the standard criterion from LGE images showed the strongest correlations with those measured using

Mean+5SD (R^2 = 0.97), Mean+6SD (R^2 = 0.96), Mean+4SD (R^2 = 0.937), and visual delineation (R^2 = 0.91) methods on T_1 maps. Weakest correlations were observed when Mean+2SD (R^2 = 0.76), FWHM (R^2 = 0.77), and Otsu's (R^2 = 0.73) methods were used on T_1 maps.

Method	Bias (% of LV)	R^2	Slope of best fit line (p-value)	Intercept of best fit line (p-value)
Mean+2SD	4.58 ± 3.64	0.76	1.45 (p = 0.02)	2.12 (p = 0.97)
Mean+3SD	2.97 ± 2.69	0.81	1.28 (p = 0.06)	1.44 (p = 0.13)
Mean+4SD	1.20 ± 1.33	0.93	1.14 (p = 0.07)	0.50 (p = 0.31)
Mean+5SD	-0.08 ± 0.68	0.97	1.02 (p = 0.62)	0.12 (p = 0.68)
Mean+6SD	-1.08 ± 0.84	0.96	0.90 (p = 0.03)	0.46 (p = 0.11)
FWHM	1.62 ± 2.17	0.77	1.27 (p = 0.09)	1.07 (p = 0.31)
Otsu	0.55 ± 2.09	0.73	0.90 (p = 0.40)	1.46 (p = 0.08)
Visual Delineation	-1.67 ± 1.27	0.91	0.79 (p<0.001)	0.46 (p = 0.22)

Table 4.1: Infarct size comparisons

Relative to the mean AHA-segmental infarct size (averaged across all the 368 segments from 23 canines) measured from LGE images (8.13±16.28%), mean AHA-segmental infarct size from T_1 maps was over-estimated by Mean+2SD (15.65±24.66%, p<0.001), Mean+3SD (13.11±22.01%, p<0.001), Mean+4SD (10.61 ± 19.10%, p<0.001), FWHM (12.81±21.79%, p<0.001), and Otsu's (9.96±17.92%, p = 0.002) methods. Mean+6SD (7.12±14.46%, p<0.001) and visual delineation (6.04±14.17%, p<0.001) methods underestimated the AHA-segmental infarct size from T_1 maps. No significant difference was observed between LGE images and T_1 maps when Mean+5SD criterion was used to measure AHA-segmental infarct size from T_1 maps (8.17±16.43%, p = 0.30).

4.4.2. Transmurality Comparisons

Figure 4.4 shows a bar plot of the mean infarct transmurality measured from LGE images using the standard criterion, and from T_1 maps using different methods. Figure 4.4 also shows the Bland-Altman plots and linear regression plots comparing transmurality measured from LGE images to those measured from T_1 maps using the different methods. Relative to LGE-based estimate, T_1 maps significantly over-estimated transmurality when the Mean+2SD, Mean+3SD, Mean+4SD, FWHM, and Otsu's methods were used ($p<0.001$, for all cases). Mean+6SD ($p = 0.01$) and visual delineation ($p<0.001$) methods significantly under-estimated infarct transmurality. However, there was no significant difference between LGE images and T_1 maps for measuring transmurality when Mean+5SD criterion ($p = 0.57$) was used.

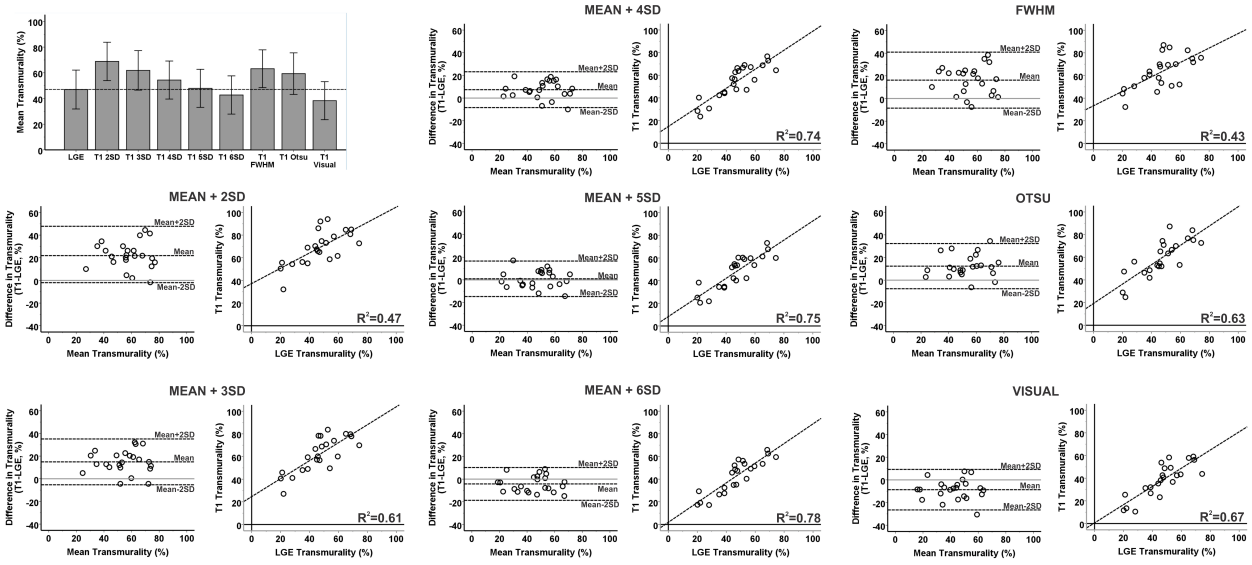

Figure 4.4: *Transmurality comparisons.* Bar plots, Bland-Altman plots, and linear regression plots that were used to compare the infarct transmurality measured using different methods on T_1 maps to that measured on LGE images using the standard criterion are shown. Of all the methods, infarct transmurality measured using the Mean+5SD criterion from T_1 maps showed the best agreement to that measured using LGE images.

Table 4.2 summarizes the results from Bland-Altman and linear regression analyses for transmurality comparisons. Overall, transmurality measured using the Mean+5SD criterion on T_1 maps showed the best agreement (Bias = 0.94 ± 7.82%) with that measured from the LGE images using the standard criterion. The strongest positive bias was observed with the Mean+2SD criterion (Bias = 21.90 ± 11.93%), while the strongest negative bias was observed with the visual delineation method (Bias = -8.66 ± 8.94%). Transmurality measured using the standard criterion applied to LGE images showed the strongest correlations with those measured using Mean+6SD (R^2 = 0.78), Mean+5SD (R^2 = 0.75), and Mean+4SD (R^2 = 0.74) criteria. Weakest correlations were observed when Mean+2SD (R^2 = 0.47) and FWHM (R^2 = 0.43) methods were used on T_1 maps.

Method	Bias (%)	R^2	Slope of best fit line (p-value)	Intercept of best fit line (p-value)
Mean+2SD	21.90 ± 11.93	0.47	0.68 (p = 0.05)	31.16 (p<0.001)
Mean+3SD	14.90 ± 10.11	0.61	0.79 (p = 0.15)	24.63 (p = 0.002)
Mean+4SD	7.40 ± 7.90	0.74	0.84 (p = 0.16)	14.81 (p = 0.01)
Mean+5SD	0.94 ± 7.82	0.75	0.84 (p = 0.16)	8.25 (p = 0.13)
Mean+6SD	-4.24 ± 7.23	0.78	0.87 (p = 0.21)	1.91 (p = 0.70)
FWHM	16.21 ± 12.36	0.43	0.64 (p = 0.03)	33.24 (p<0.001)
Otsu	12.38 ± 9.97	0.63	0.85 (p = 0.31)	19.27 (p = 0.01)
Visual Delineation	-8.66 ± 8.94	0.67	0.80 (p = 0.12)	0.58 (p = 0.93)

Table 4.2: Transmurality comparisons

4.4.3. Diagnostic Performance for the Detection Chronic Myocardial Infarction on Native T_1 Maps at 3T

Table 4.3 summarizes the diagnostic performance of the various detection methods for characterizing CMIs applied onto native T_1 maps at 3T. Figure 4.5 shows the ROC curves for the detection of CMIs using the different methods on T_1 maps. With the exception of visual delineation, all methods showed strong diagnostic performance for detecting CMIs on T_1 maps at 3T (AUC >0.90 and $p<0.001$ for all cases). Mean+5SD criterion showed the strongest diagnostic performance (AUC = 0.98, $p<0.001$). Visual delineation of CMIs on native T_1 maps had high specificity (99%), but modest sensitivity (69%). The diagnostic performance of visual delineation was weak relative to other approaches (AUC = 0.89, $p<0.001$).

Method	Mean +2SD	Mean +3SD	Mean +4SD	Mean +5SD	Mean +6SD	FWHM	Otsu	Visual
True Positives (no. of AHA segments)	149	148	148	145	136	143	140	105
True Negatives (no. of AHA segments)	164	175	177	184	185	173	181	194
False Positives (no. of AHA segments)	32	21	19	12	11	23	15	2
False Negatives (no. of AHA segments)	3	4	4	7	16	9	12	47
Sensitivity (%)	98	97	97	95	89	94	92	69
Specificity (%)	84	89	90	94	94	87	92	99
Accuracy (%)	90	92	93	95	92	91	92	86
Precision (%)	82	88	89	92	93	86	90	98
Area Under Curve	0.973*	0.971*	0.973*	0.981*	0.975*	0.966*	0.961*	0.886*

Table 4.3: Diagnostic performance of thresholding criteria and visual delineation for the detection of CMI on native T_1 maps at 3.0T. *Statistically significant ($p<0.001$)

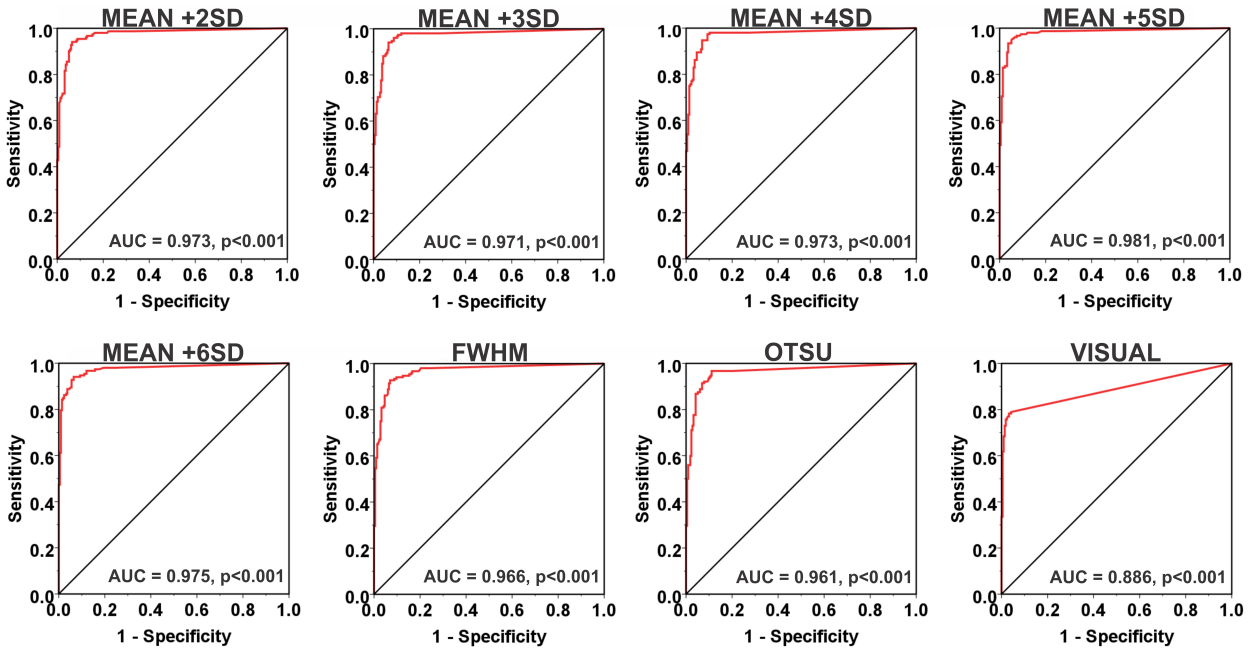

Figure 4.5: *Diagnostic performance of native T_1 maps.* ROC curves of different methods for detecting CMIs on native T_1 maps are shown. Infarction detected using the Mean+5SD criterion on LGE images (ground truth), while infarct size measured in each AHA segment was used as the predictor variable. Mean+5SD criterion on T_1 maps showed the best diagnostic performance relative to LGE images, while visual delineation showed the weakest diagnostic performance.

4.5. Discussion

In chapter 3, native T_1 mapping at 3T has been shown to be a potential alternative to LGE imaging for characterizing CMIs, but an objective technique that can accurately determine CMI location, size, and transmurality has not been fully validated to date. In this study, automatic (Otsu's), semi-automatic (SD-based thresholding and FWHM), and visual delineation methods were tested for detecting CMIs on native T_1 maps at 3T using the standard objective estimates determined from LGE images as the reference standard. All automatic and semi-automatic approaches have shown high sensitivity and specificity for detecting CMIs on native T_1 maps at

3T. Among these, Mean+5SD criterion has shown the strongest diagnostic performance. Compared to the semi-automated approaches, visual delineation of hyperintense regions on native T_1 maps has shown relatively weaker diagnostic performance with modest sensitivity but high specificity.

In this study, remote myocardium was identified first on LGE images based on which the reference ROI was drawn to perform the SD thresholding in native T_1 maps. However, for practical implementation of CMI characterization using native T_1 maps, remote myocardium needs to be solely identified on the basis of native T_1 maps. Since the specificity (i.e., the ability to identify remote myocardium) of visual delineation of CMIs on native T_1 maps in this study is 99%, the remote myocardium is expected to be reliably identified based on visual analysis, and Mean+5SD criterion can still be practically implemented for identifying CMIs.

In contrast to the SD-based thresholding methods, the FWHM method requires the visual identification of the hyperintense region of native T_1 maps followed by the manual delineation of a seed region within the hyperintense territories. While FWHM has been proposed to be a reliable method for infarct characterization on LGE images (414), the relatively modest sensitivity for visually identifying the hyperintense regions on native T_1 maps (86%) is likely a contributing factor for the weaker performance of FWHM. This potentially explains the relatively large bias and weak correlations of FWHM measurements on native T_1 maps with respect to those measured on LGE images observed in this study. The Otsu's method overcomes these limitations of the SD-based thresholding and FWHM methods, as it does not require the reader to define a reference ROI either in the remote or the infarcted myocardium. This study has shown a strong diagnostic performance of the Otsu's method for detecting CMIs on native T_1

maps (AUC = 0.961, $p<0.001$). Therefore, this method can be a promising alternative to visual identification of the remote and infarcted territories on native T_1 maps.

Owing to its relatively modest sensitivity, visual identification of CMIs may not always be feasible for practical implementation. This could be a perceived weakness of native T_1 maps for characterizing CMIs among cardiac MRI readers who solely rely on visual analysis for detection and characterization of CMI. Nevertheless, with further improvement (for e.g. via selective nulling of the remote myocardium as performed in LGE acquisitions), it may be possible to improve the diagnostic performance of visual analysis on non-contrast enhanced T_1-based images as well. However, additional studies are needed to examine this possibility..

4.5.1. Study Limitations

This study has a few limitations. To systematically test MIs of various sizes and transmuralities with adequate sample size, only LAD MIs were evaluated. The diagnostic performances of the automatic, semi-automatic, and visual delineation methods for detecting CMIs on native T_1 maps remain to be evaluated for MIs in other myocardial territories. Third, TTC planimetry as the gold standard technique for characterizing the MI; instead LGE was used as the in vivo reference standard, which has been favorably compared against TTC under ex-vivo conditions (308).

4.6. Conclusion

A semi-automated approach using Mean+5SD criterion was found to be able to characterize CMI on native T_1 maps at 3T with a sensitivity of 95% and specificity of 94% compared to the reference standard measurements from LGE images.

CHAPTER 5

Native T_1 mapping at 3T for Characterizing Chronic Myocardial Infarctions: Clinical Validity

5.1. Abstract

In chapters 3 and 4, the feasibility of detecting CMIs on native T_1 maps at 3T using the Mean+5SD thresholding method was demonstrated in a canine model. The purpose of this study is to investigate the ability of native T_1 maps at 3T to reliably characterize CMIs in patients with prior STEMI or NSTEMI. Native T_1 maps and LGE images were acquired at 3T in patients with prior STEMI (n = 13) and NSTEMI (n = 12) at a median of 13.6 years post-MI. Infarct location, size, and transmurality were measured using Mean+5SD thresholding criterion from LGE images and T_1 maps, and compared against one another. Independent reviewers assessed visual conspicuity of CMIs on LGE images and T_1 maps.

Native T_1 maps and LGE images were not different for measuring infarct size (STEMI: p = 0.46; NSTEMI: p = 0.27) and transmurality (STEMI: p = 0.13; NSTEMI: p = 0.21) using thresholding criterion. Using Mean+5SD criterion, good agreement was observed between LGE images and T_1 maps for measuring infarct size (STEMI: Bias = 0.6±3.1%; R^2 = 0.93; NSTEMI: Bias = −0.4±4.4%; R^2=0.85) and transmurality (STEMI: Bias = 2.0±4.2%; R^2 = 0.89; NSTEMI: Bias = −2.7±7.9%; R^2 = 0.68). Sensitivity and specificity of T_1 maps for detecting CMIs based on thresholding criterion were 89% and 98% respectively (STEMI); and 87% and 95% respectively (NSTEMI). Relative to LGE images, mean visual conspicuity score for detecting CMIs was significantly lower for T_1 maps ($p<0.001$ for both cases). Median infarct-to-remote

myocardium contrast-to-noise ratio was 2.5-fold higher for LGE images relative to T_1 maps ($p<0.001$). Sensitivity and specificity of T_1 maps for visual detection were: 60% and 86% (STEMI), and 64% and 91% (NSTEMI). In conclusion, CMIs in STEMI and NSTEMI patients can be reliably characterized using threshold-based detection on native T_1 maps at 3T. Visual detection of CMIs on native T_1 maps in both patient populations has high specificity, but modest sensitivity.

5.2. Introduction

Using a canine model of reperfused CMI, chapter 1 demonstrated that native T_1 mapping at 3T provides significantly greater sensitivity and specificity for characterizing CMI over native T_1 mapping at 1.5T. Chapter 2 further demonstrated that the Mean+5SD thresholding criterion is the optimal approach for characterizing CMIs using native T_1 maps at 3T. In this chapter, the clinical validity of the observations in the canine model was examined in patients with a prior history of healed STEMI or NSTEMI.

5.3. Methods

5.3.1. MRI Studies

Patients (13 STEMI and 12 NSTEMI) with prior MI were studied according to the protocols approved by the Institutional Review Board of Severance Hospital, Yonsei University Health System at a median of 13.6 years (inter-quartile range (IQR) = 7.5-18.5 years) after AMI. MRI studies were performed on a 3T clinical MR system (MAGNETOM Trio®, Siemens Healthcare, Erlangen, Germany) after obtaining informed consent. Patients were excluded from the study if

they had symptoms of chest pain, ECG changes or cardiac enzyme elevation within 1 year before the date of MRI exam, multiple MIs, or were contraindicated to an MR study (claustrophobia, metallic implants, GFR<45 mL/min/1.73m^2, etc.). The clinical features of the patients are summarized in Table 5.1. ECG-triggered breath-held 2D cine bSSFP (25-30 cardiac phases; TR/TE = 2.92/1.46 ms; α = 50°; BW = 888 Hz/pixel; voxel size = 1.3x1.3x8 mm^3), pre-contrast MOLLI (8 TIs with 2 Look-Locker cycles of 3+5 images (429); minimum TI = 120 ms; TI increment = 80 ms; α = 35°; BW = 1085 Hz/pixel; voxel size = 1.5x1.5x8 mm^3) and LGE images (IR-prepared segmented FLASH, acquired 10-12 minutes following intravenous administration of 0.2 mmol/kg of gadobutrol (Gadovist®, Bayer Schering Pharma); optimal TI for nulling the remote myocardium; TR/TE = 6.54/3.27 ms; α = 20°; BW = 460 Hz/pixel; voxel size = 1.2x1.2x8 mm^3) were acquired along the LV short-axis.

5.3.2. Image Analyses

Motion-corrected native T_1 maps were constructed from the non-rigid motion corrected pre-contrast MOLLI images as previously described (434) by the scanner's image-reconstruction system. All image analyses were performed on cvi[42] (Circle Cardiovascular Imaging Inc., Calgary, AB, Canada). LGE images and T_1 maps were randomized and independently analyzed by two blinded reviewers in consensus. The locations of remote myocardium on both techniques were identified as the regions showing no hyperintensity on the respective images and reference ROIs were drawn in the remote myocardium. In both techniques, infarct was identified using the Mean+5SD criterion relative to the respective reference ROIs (414-416,435,436). A hypointense core on T_1 maps, suggestive of chronic iron deposition (435) or fat deposition (419,437,438), that

was not detected as infarcted using the Mean+5SD criterion was manually included in the final analysis.

Parameter	STEMI (n = 13)	NSTEMI (n = 12)
Age, mean years ± SD	70.8 ± 7.2	63.0 ± 12.1
Male Sex, n (%)	10 (77)	10 (83)
Diabetes Mellitus, n (%)	3 (23)	2 (17)
Hyperlipidemia, n (%)	9 (69)	8 (67)
Hypertension, n (%)	5 (38)	4 (33)
Smoking History, n (%)	7 (54)	9 (75)
Time from symptoms to treatment, median days (IQR)	6 (1-9)	5 (3-9)
Culprit coronary artery, n (%)		
LAD	9 (69)	8 (67)
RCA	3 (23)	3 (25)
LCx	1 (8)	1 (8)
Type of treatment, n (%)		
PCI	9 (69)	5 (42)
CABG	1 (8)	4 (33)
Thrombolysis	3 (23)	1 (8)
Medical Therapy	0 (0)	2 (17)
Duration between AMI and CMR exam, median years, (IQR)	15.9 (12.6-18.5)	12.2 (4.2-18.3)

Table 5.1: Clinical features of the patients

Infarct size, as a percentage of total LV volume, was measured from both techniques. To evaluate the concordance between the two techniques for detecting infarct on a regional basis, infarct size was also measured within the first 16 segments of the AHA 17-segment model. The apical cap was excluded to avoid partial volume effects. Mean infarct transmurality was measured using the center-line chord method by calculating the extent of the scar along 100 equally placed chords drawn on each slice (433).

T_1 values of infarct and remote myocardium were measured. Percentage changes in the native T_1 value and LGE-SI of infarct relative to the remote myocardium were also measured. CNR were calculated for the two techniques as follows:

$$\mathrm{CNR_{LGE}} = \frac{\text{SI of Infarct} - \text{SI of Remote Myocardium}}{\text{SD of Noise}} \tag{5.19}$$

$$\mathrm{CNR_{T_1}} = \frac{\mathrm{T_1}\text{ of Infarct} - \mathrm{T_1}\text{ of Remote Myocardium}}{\text{SD of Remote Myocardium}} \tag{5.20}$$

5.3.3. Visualization of Chronic Myocardial Infarction

Two, blinded, independent reviewers with >5 years of experience in reading MR images scored randomized LGE images and T_1 maps for the visual conspicuity of infarct. Each reviewer was presented with basal, mid-ventricular and apical slices from every patient for both techniques. The reviewers were allowed to freely window both the LGE images and the T_1 maps to their preference. Using the AHA 17-segment model, basal and mid-ventricular slices were divided into 6 segments each, while the apical slices were divided into 4 segments. The apical cap was excluded to avoid partial volume effects. Each reviewer scored for the visual conspicuity of the MI in each segment using the following scale: 1 – absent, 2 – uncertain, and 3 – present.

5.3.4. Statistical Analyses

Statistical analyses were performed on IBM SPSS Statistics (version 21.0, IBM Corporation, New York). Shapiro-Wilk test and quantile-quantile plots were used to test the normality of the data. Whole-heart infarct size and transmurality were compared between LGE images and T_1 maps using paired Student's t-test if the data was normal or Wilcoxon signed-rank test if the data was non-normal. Infarct size measured on the basis of AHA 17-segment model was averaged for

a given AHA segment across all the canines for both the techniques. LGE images and T_1 maps were then compared for the differences in "averaged" AHA segmental infarct size. Bland-Altman and linear regression analyses were performed to determine the agreement between the two techniques. The slope of the best-fit line from linear regression was tested to be equal to 1, and the intercept was tested to be equal to 0. Sensitivity and specificity of T_1 maps for threshold-based detection of infarct were measured using LGE images as the gold standard and AHA-segmental infarct size as the predictor variable. For this purpose, an AHA-segment with an infarct size >1% by volume was considered positive for MI, while an AHA-segment with an infarct size <1% by volume was considered negative. The 1% cutoff was used to eliminate segments with spurious hyperintense pixels from being considered as infarcted. ROC analysis was performed to calculate the AUC by using the AHA-segmental infarct size on T_1 maps as the continuous variable, and the presence or absence of MI using the 1% cut-off on LGE images as the status variable. Native T_1 values of infarct and remote myocardium, percentage changes in the native T_1 value and LGE-SI of infarct relative to remote myocardium, and CNR measures were compared.

Cohen's kappa coefficient was calculated to evaluate the agreement between the two reviewers on the visual conspicuity of MI from both techniques. Mean score for each segment was calculated for both methods by averaging the scores for that segment from the two reviewers and were compared using mixed-model ANOVA. Sensitivity and specificity for visual identification of CMIs on T_1 maps were measured using LGE images as the gold standard. For this purpose, segments with a mean score >2 were considered positive for MI, segments with a mean score <2 were considered negative for MI, and segments with a mean score equal to 2 either on LGE images or T_1 maps were not included in the final analysis. Statistical significance

for all analyses was set at $p<0.05$. Normal data is expressed as Mean ± SD, while non-normal data is expressed as median with IQR.

5.4. Results

Representative LGE images and native T_1 maps of the basal, mid-ventricular and apical slices acquired from a STEMI and an NSTEMI patient are shown in Figures 5.1 and 5.2, respectively. In both cases, visually conspicuous T_1 increases could be observed within the MI territories identified on LGE images (yellow arrows in raw images in Figures 5.1 and 5.2). Semi-automatic threshold analysis using Mean+5SD criterion showed excellent visual agreement between the two techniques in terms of MI location and spatial extent in both cases (highlighted pixels in the processed images in Figures 5.1 and 5.2). Bulls-eye plots depicting infarct size and transmurality also showed good agreement between the two techniques.

5.4.1. Infarct Size Comparisons

LGE images and T_1 maps were not different for measuring whole-LV infarct size (%LV) in both STEMI (LGE: Median = 13.8%, IQR = 10.2-17.0%; T_1: Median = 14.8%, IQR = 12.8-17.9%; $p = 0.46$; Figure 5.3A) and NSTEMI (LGE: Median = 10.9%, IQR = 4.9-13.4%; T_1: Median = 12.6%, IQR = 6.2-14.7%; $p = 0.27$; Figure 5.3B) patients. In both patient pools, Bland-Altman (STEMI: Bias = 0.6±3.1%; Figure 5.3C; NSTEMI: Bias = −0.4±4.4%; Figure 5.3D) and linear regression analyses (STEMI: $R^2 = 0.93$; Slope = 0.91, $p = 0.25$; Intercept = 2.12%, $p = 0.19$; Figure 5.3E; NSTEMI: $R^2 = 0.85$; Slope = 0.62, $p = 0.001$; Intercept = 4.02%, $p = 0.009$; Figure 5.3F) showed good agreement between the two techniques for measuring infarct size. In one NSTEMI patient with infero-lateral infarct, significant under-estimations of the infarct size were

observed in T_1 maps, primarily due to banding artifacts in the inferior segment (LGE: 32.7% vs. T_1: 20.4%). Averaged segmental infarct size was not different between the two techniques in STEMI (p = 0.09) and NSTEMI (p = 0.37) patients.

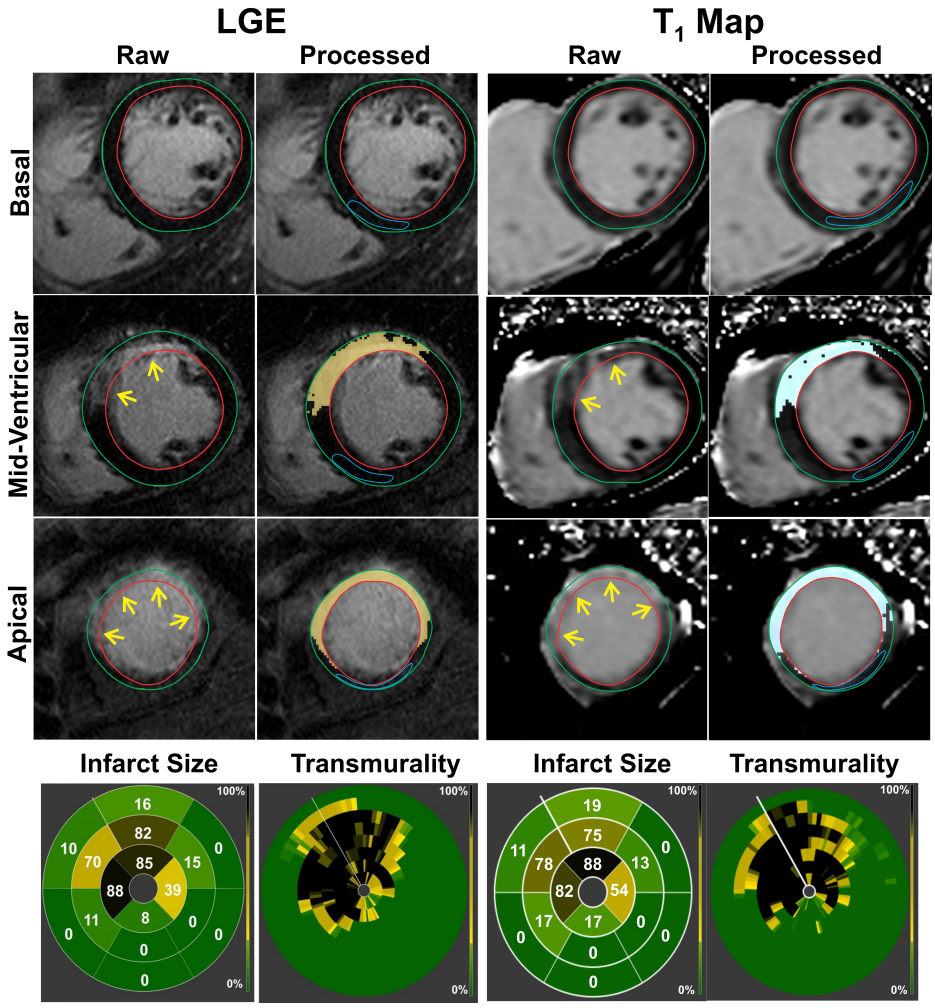

Figure 5.1: *Semi-automatic threshold analysis to detect and characterize chronic myocardial infarction at 3T in a STEMI patient*. LGE images and T_1 maps of basal, mid-ventricular and apical slices acquired from a STEMI patient (18.5 years post MI) are shown. Significant T_1 elevations could be visually observed within the infarcted regions detected on LGE images (yellow arrows, raw images). Infarct (highlighted pixels in processed images) was identified on both techniques using the Mean+5SD criterion. Infarct size was computed on the basis of AHA 17-segment model as shown in the bulls-eye plots. The number in each segment denotes the percentage volume of the segment that was detected as infarcted by the threshold analysis. Transmurality was measured as the extent of the

MI along each chord (refer to text) and color-coded accordingly as shown in the bulls-eye plots. Each concentric ring on the transmurality bulls-eye plots represents a short-axis slice with the most basal slice represented by the outermost ring. Bulls-eye plots show a close concordance between the two techniques for measuring infarct size and transmurality.

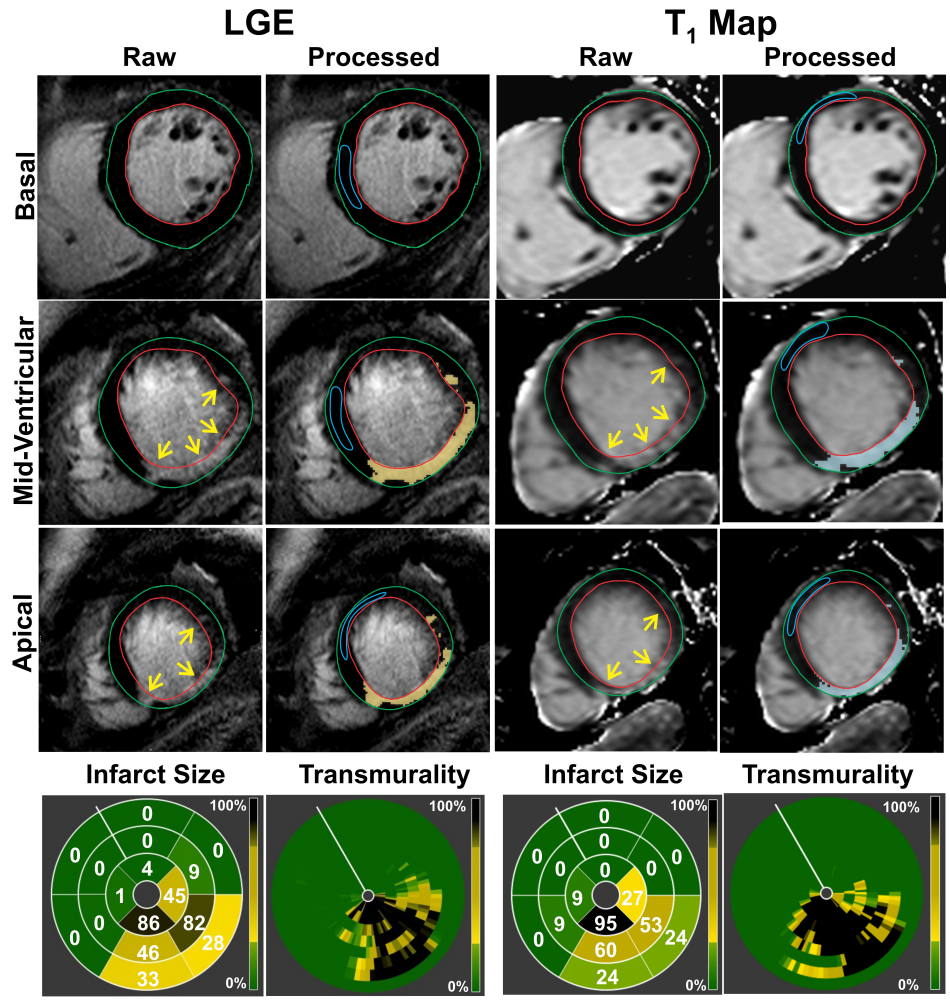

Figure 5.2: *Semi-automatic threshold analysis to detect and characterize chronic myocardial infarction at 3T in a NSTEMI patient*. LGE images and T_1 maps of basal, mid-ventricular and apical slices acquired from an NSTEMI patient (25.6 years post MI) are shown. Significant T_1 elevations could be visually observed within the infarcted regions detected on LGE images (yellow arrows, raw images). Bulls-eye plots show a close concordance between the two techniques for measuring infarct size and transmurality.

5.4.2. Transmurality Comparisons

LGE images and T_1 maps were not different for measuring transmurality in both STEMI (LGE: Median = 55.6%, IQR = 54.0-65.8%; T_1: Median = 57.3%, IQR = 53.1-69.5%; p = 0.13; Figure 5.4A) and NSTEMI (LGE: Median = 65.1%, IQR = 56.9-73.3%; T_1: Median = 59.3%, IQR = 55.9-68.8%; p = 0.21; Figure 5.4B) patients. In both patient pools, Bland-Altman (STEMI: Bias = 2.0±4.2%; Figure 5.4C; NSTEMI: Bias = −2.7±7.9%; Figure 5.4D) and linear regression analyses (STEMI: R^2 = 0.89; Slope = 0.97, p = 0.79; Intercept = 3.7%; p = 0.57. Figure 5.4E; NSTEMI: R^2 = 0.68; Slope = 0.76, p = 0.18; Intercept = 12.4%, p = 0.27; Figure 5.4F) showed good agreement between the two techniques for measuring transmurality.

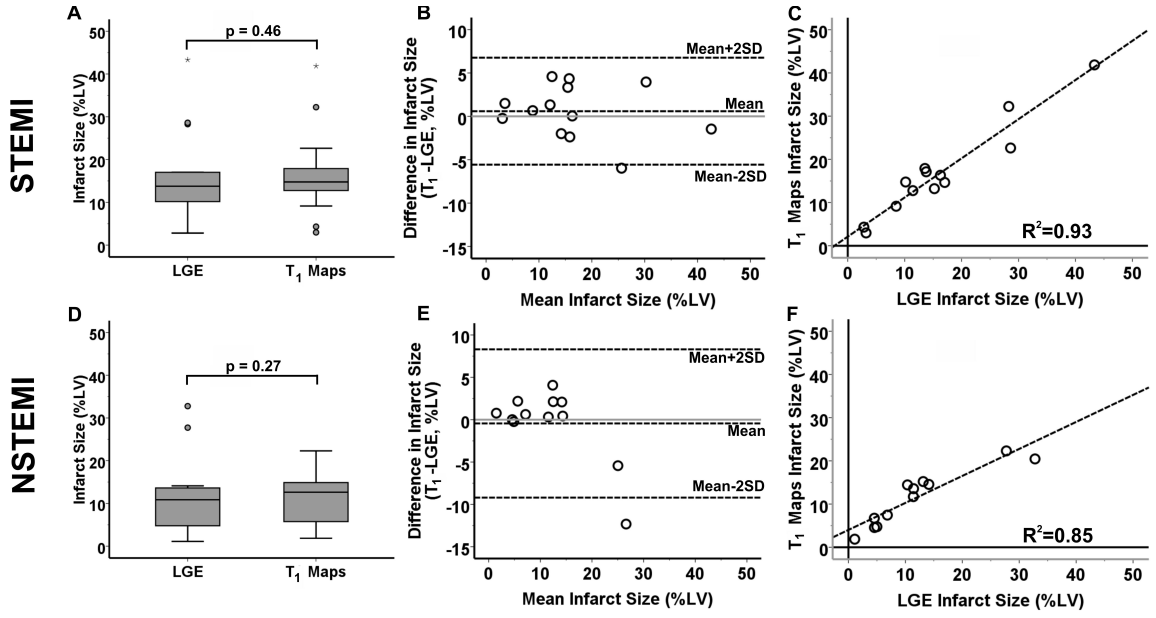

Figure 5.3: *Infarct size comparison between LGE images and native T_1 maps*. Box plots show median infarct size measured using LGE images and native T_1 maps in STEMI and NSTEMI patients (panels A and D, respectively). Circles represent outliers that do not fall within the 95% confidence interval, while asterisks represent extreme outliers that do not fall within 3 times the height of the box. LGE images and native T_1 maps were not different for measuring infarct size in both cases. Bland-Altman (panels B and E) and linear regression analyses (panels C and F)

showed good agreement between the two techniques for measuring infarct size in both patient populations. Infarct size was, however, significantly under-estimated by T_1 maps in one NSTEMI patient with infero-lateral MI due to severe banding artifacts in the inferior segments.

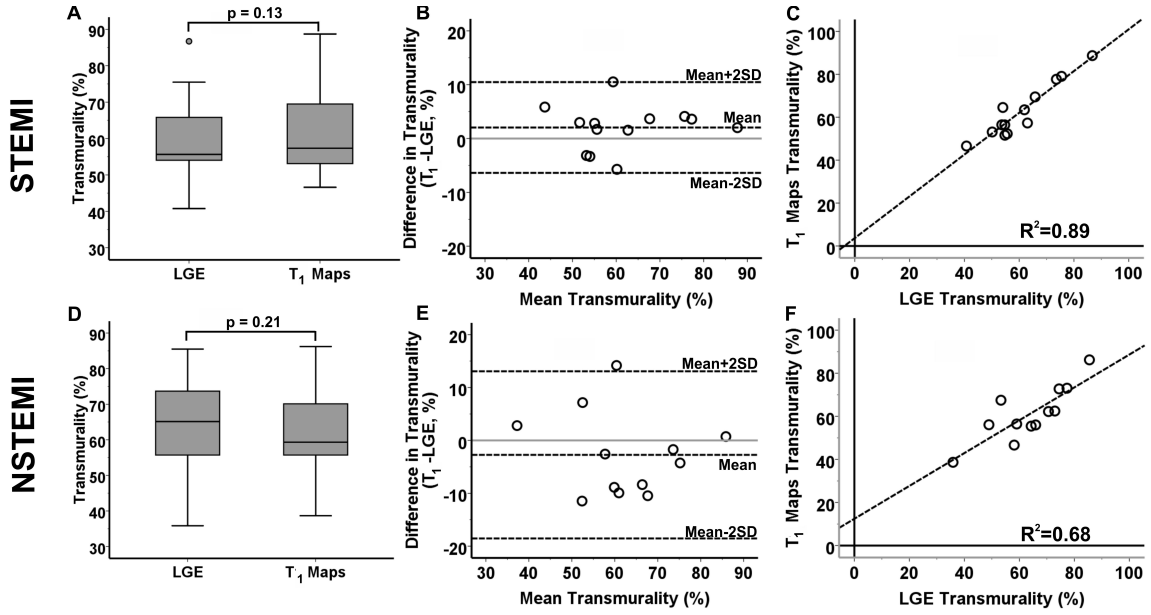

Figure 5.4: *Transmurality comparison between LGE images and native T_1 maps.* Box plots show median infarct size measured using LGE images and native T_1 maps in STEMI and NSTEMI patients (panels A and D, respectively). Circles represent outliers that do not fall within the 95% confidence interval. LGE images and native T_1 maps were not different for measuring transmurality. Bland-Altman analysis (panels B and E) and linear regression analysis (panels C and F) showed good agreement between the two techniques for measuring transmurality.

5.4.3. Diagnostic Performance of Native T_1 Maps Using Threshold-Based Detection

Approximately 5% of AHA segments (10 segments from STEMI patients and 13 segments from NSTEMI patients) were uninterpretable due to contamination from banding artifacts and were excluded from further analysis. Sensitivity and specificity of the native T_1 maps to detect chronic STEMIs on a segmental basis were 91% (108 out of 119 true positives; 95% confidence interval

(CI): 86-96%) and 97% (77 out of 79 true negatives; 95% CI: 94-100%) respectively. AUC was 0.96 ($p<0.001$; Figure 5.5A). Sensitivity and specificity of the native T_1 maps to detect chronic NSTEMIs on a segmental basis were 91% (82 out of 90 true positives; 95% confidence interval (CI): 85-97%) and 94% (84 out of 89 true negatives; 95% CI: 90-99%) respectively. AUC was 0.95 ($p<0.001$; Figure 5.5B).

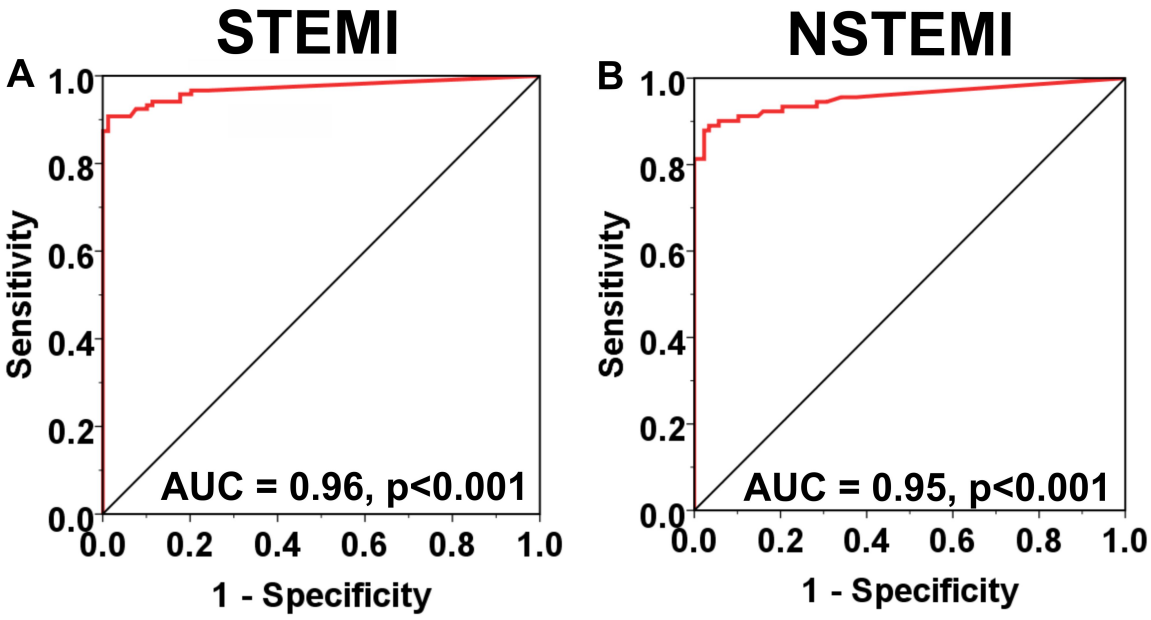

Figure 5.5: *ROC analysis for threshold-based detection of chronic myocardial infarction at 3T using native T_1 maps*. ROC analysis showed a strong diagnostic performance of T_1 maps for detecting CMIs in both STEMI and NSTEMI patients at 3T.

5.4.4. Image Contrast Characteristics between Infarct and Remote Myocardium

Relative to the remote myocardium, median T_1 of infarct was 271ms higher (IQR = 197-332ms) in STEMI patients (Infarct: Median = 1517ms, IQR = 1443-1627ms; Remote: Median = 1247ms, IQR = 1210-1302ms; $p<0.001$; Figure 5.6A), and 229ms (IQR = 190-323ms) higher in NSTEMI

patients (Infarct: Median = 1549ms, IQR = 1399-1624ms; Remote: Median = 1262ms, IQR = 1209-1326ms; $p<0.001$; Figure 5.6B). Median percentage change in LGE-SI of infarct relative to remote myocardium was significantly higher than percentage change in T_1 in both STEMI (LGE: Median = 465%, IQR = 362-629%; T_1: Median = 21%, IQR = 17-27%; $p<0.001$; Figure 5.6C) and NSTEMI (LGE: Median = 441%, IQR = 343-569%; T_1: Median = 20%, IQR = 16-25%; $p<0.001$; Figure 5.6D) patients. Median CNR of LGE images was also 2.5-fold higher relative to that of T_1 maps in both STEMI (LGE: 23.1, IQR = 15.6-39.7; T_1: 9.2, IQR = 7.0-12.3; $p<0.001$; Figure 5.6E) and NSTEMI (LGE: 25.3, IQR = 16.4-32.5; T_1: 9.7, IQR = 7.1-12.1; $p<0.001$; Figure 5.6F) patients.

5.4.5. Visual Detection of Chronic Myocardial Infarction on LGE images and Native T_1 maps at 3T

Cohen's kappa coefficient showed good inter-observer agreement for the visual conspicuity of CMIs on LGE images and T_1 maps in both STEMI ($\kappa = 0.86$, $p = 0.023$) and NSTEMI ($\kappa = 0.86$, $p = 0.024$) patients. Mean score for LGE images was significantly higher than those for T_1 maps in both cases (STEMI: 1.96±0.93 vs. 1.71±0.71, $p = 0.021$; NSTEMI: 1.83±0.93 vs. 1.66±0.89, $p = 0.024$; Figure 5.7). Less than 5% of AHA segments (8 segments from STEMI patients and 10 segments from NSTEMI patients) were uninterpretable due to contamination from banding artifacts. Fourteen segments from STEMI patients, and three segments from NSTEMI patients were excluded from the analysis, as the mean visual score was equal to 2 (indicating uncertainty for the presence of infarct) either on LGE images or T_1 maps. Sensitivity and specificity for visual detection of CMIs using native T_1 maps were 60% (54 out of 90 true positives; 95% CI: 50-70%) and 86% (89 out of 104 true negatives; 95% CI: 79-92%) respectively in STEMI

patients, and 64% (47 out of 73 true positives; 95% CI: 53-75%) and 91% (105 out of 116 true negatives; 95% CI: 87-98%) respectively in NSTEMI patients.

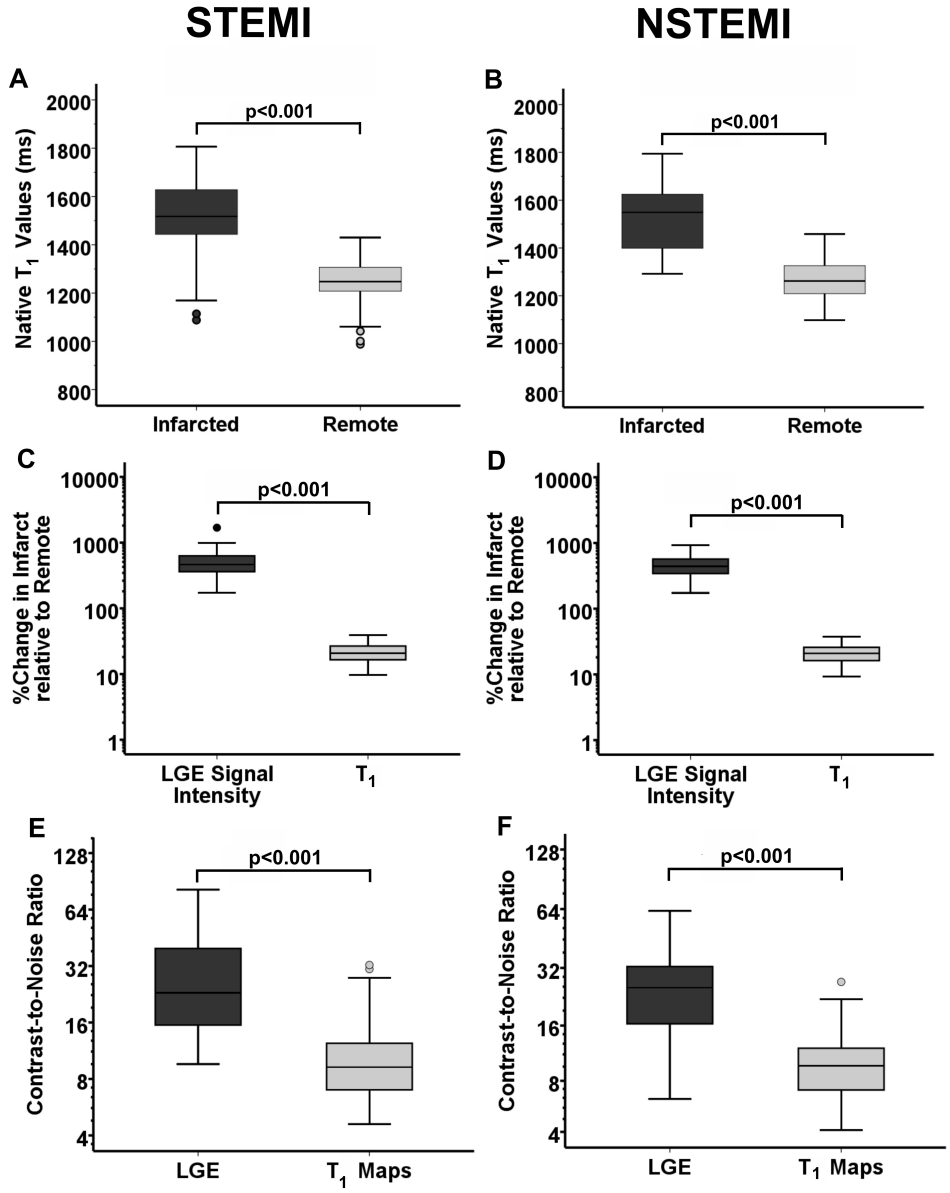

Figure 5.6: *Infarct to remote myocardium contrast in LGE images and native T_1 maps*. Box-plots show median native T_1 values of infarcted and remote myocardium (panels A and B), median percentage changes in LGE signal intensity and T_1 value of infarct relative to remote myocardium (panels C and D), and median CNR between infarct and remote myocardium for LGE images and native T_1 maps (panels E and F) in STEMI and NSTEMI patients. Median native T_1 values of infarct were higher than that of remote myocardium in both STEMI and NSTEMI

patients. Percentage change in LGE-SI was higher relative to percentage change in native T_1 values in both patient pools. Median CNR for LGE images was also higher than that of native T_1 maps in both patient pools). Note that the panels C, D, E and F are in logarithmic scale.

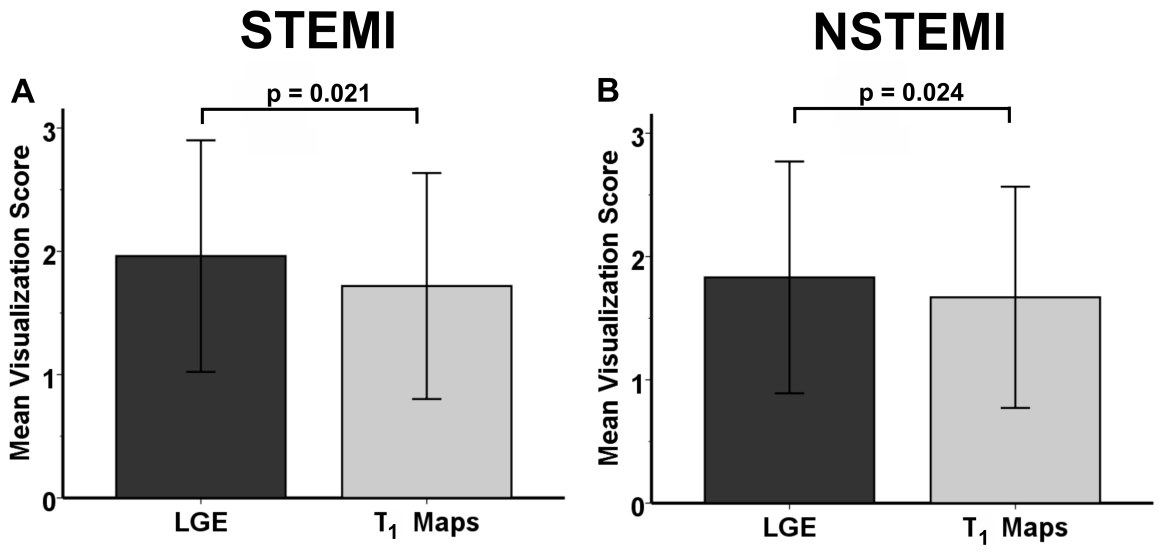

Figure 5.7: *Visual detection of chronic myocardial infarctions on LGE images and T_1 maps.* Mean scores (averaged across reviewers) for the visual conspicuity of CMIs on LGE images and T_1 maps in STEMI (panel A) and NSTEMI (panel B) patients are shown. Mean score for LGE images is significantly higher than that for T_1 maps in both cases.

5.5. Discussion

In a canine model of MI, chapters 3 and 4 have shown that native T_1 mapping at 3T can reliably characterize CMIs, and can therefore be a potential alternative to LGE MRI. In this study, the clinical validity of the canine findings was investigated in two pilot patient populations with prior STEMI and NSTEMI, respectively. Mean native T_1 value of CMIs in both patient populations was approximately 21% higher than that of remote myocardium at 3T. The threshold-based criterion applied to native T_1 maps has been found to determine the CMI location, size and transmurality with high diagnostic accuracy without contrast agents. While the

native T_1 contrast enables accurate threshold-based detection, the technique had modest sensitivity but high specificity for visual detection of CMI relative to LGE.

The feasibility of using native T_1 mapping for characterizing CMIs in patients has been previously evaluated at 1.5T (317,319). However, the low native T_1 contrast between CMIs and remote myocardium resulted in poor diagnostic accuracy of native T_1 maps. These results have been confirmed in chapters 3 and 4. The same canine studies have shown that increasing the field strength from 1.5T to 3T markedly improves native T_1 contrast for CMI detection. Hence, the observation of improved diagnostic accuracy of T_1 maps for detecting CMIs in patients compared to 1.5T in this study is consistent with animal studies.

While the biophysical mechanisms responsible for such native T_1 contrast in CMIs and its dependence on field strength remain to be elucidated, diffusion and magnetization transfer effects seem to be plausible explanations. Previous studies have shown that diffusion coefficient of protons (*D*) in CMIs is ~2-fold larger relative to remote myocardium (422) and that *D* is directly related to T_1 (425). CMIs are also known to have significantly reduced magnetization transfer (MT) effects (428). This could lead to an apparent increase in T_1 values of CMIs when an MT-sensitive T_1 mapping sequence such as MOLLI-bSSFP is used (426). The field-dependent MT-based T_1 bias (439) and T_1 elongations (420) could potentially explain the increase in native T_1 sensitivity and specificity that has been observed in this study compared to the previous study in patients at 1.5T (317).

Although native T_1 maps have high specificity, its modest sensitivity for visually detecting CMIs relative to LGE may be limiting in some patients if visual analysis is the only mode used for MI characterization. Further increases in image contrast (for e.g., through IR preparation to null the remote myocardium, analogous to IR preparation used for LGE) needs to

be investigated. Another potential difficulty with the proposed approach is image artifacts (off-resonance bands or motion). To mitigate these image artifacts, careful cardiac shimming and optimal acquisition strategies need to be used. Moreover, partial volume effects, particularly in the apical slices, may complicate accurate characterization of relatively thin and scarred myocardium. This may lead to overestimation of the true infarct size and transmurality, but this limitation also exists with LGE imaging. A more stringent thresholding criterion, and high-resolution native T_1 mapping can potentially obviate these complications.

The ability of the native T_1 maps to detect pathologies beyond those detected on LGE images also remains to be explored. A particular pathology that has been consistently observed in T_1 maps in some CMI patients is the focal decreases in T_1 values (well below the T_1 of normal myocardium and infarct) within the infarct. Based on previous studies in canines and AMI patients (430,435), this T_1 loss could be due to chronic iron deposition following acute intramyocardial hemorrhage or fat deposition in healed MIs. This is further supported by recent reports that T_1 is inversely related with both iron (440) and fat deposition (419,437,438) in MIs. Nonetheless, further studies are needed to examine the capability of native T_1 maps to consistently detect chronic iron and fat depositions within MIs.

5.5.1. Study Limitations

This study has some limitations. First, this is a single-center study with a small sample size, but comparable to previous studies that attempt to establish clinical validation (317,319). A multicenter study in a larger patient cohort is necessary to assess the reliability of the approach for clinical adoption. Second, due to imaging time constraints, native T_2 maps were not acquired

to confirm the resolution of edema. Nevertheless, the exclusion criteria of not including patients with clinically recorded symptoms for MIs within 1 year before the MRI exam ensured that the observed MI territories were indeed chronic. These observations, along with recent preclinical studies (435), support the notion that native T_1 elongations seen in CMIs in patients are likely due to replacement fibrosis. Third, to minimize imaging time, frequency-scouting scheme was not used to reduce banding artifacts (441). Finally, for calculating the sensitivity and specificity of visual analysis, segments rated as 2 were excluded due to the reader ambiguity. Nevertheless, retrospective analyses including such segments as either positive or negative for MI have shown no significant differences in sensitivities and specificities compared to those measured after the excluding the ambiguous segments.

5.6. Conclusion

CMIs in STEMI and NSTEMI patients may be accurately characterized without contrast agents using threshold-based detection on native T_1 maps. These findings justify a study in a larger patient cohort.

CHAPTER 6

Detecting Acute Reperfusion Intramyocardial Hemorrhage with MRI

6.1. Abstract

T_2-weighted and T_2*-weighted imaging techniques are commonly used to assess intramyocardial hemorrhage, but there is no general consensus regarding which of the two techniques is the more suitable approach. The purpose of this study is to evaluate T_2 and T_2* changes in acute reperfused hemorrhagic (Hemo+) and non-hemorrhagic (Hemo-) MIs, and hence determine which of the two techniques is more suitable for detecting intramyocardial hemorrhage at 1.5T. Patients (n=14; 3 women) with first STEMI underwent MRI at 3 days post-angioplasty. T_2* maps, T_2 maps, T_2-STIR and LGE images were acquired. Canines (n = 20) were subjected to I-R injury and MRI was performed 5 days post-reperfusion. T_2* maps, T_2 maps, T_2-STIR and LGE images were acquired. T_2 and T_2* changes in Hemo+ and Hemo- MIs were compared. Relative to remote myocardium, mean T_2* of Hemo+ MIs was 54±13% lower in patients (15.9±4.5 ms vs. 35.2±2.1 ms; $p<0.001$) and 40±10% in canines (23±4 ms vs. 39.3±2.5 ms; $p<0.001$). Mean T_2* of Hemo- MIs was marginally elevated by 6±2.5% in patients (37.8±2.5 ms; $p = 0.021$) and 8±5% in canines (44.6±4.8 ms; $p = 0.012$). In contrast, mean T_2-STIR signal intensities (STIR-SI) of both Hemo+ and Hemo- MIs were elevated relative to remote myocardium in both patients (Hemo+: 37±19%, $p<0.001$; Hemo-: 78±27%, $p<0.001$) and canines (Hemo+: 42±22%, $p<0.001$; Hemo-: 65±22%, $p<0.001$). Consistent with STIR-SI, mean T_2 of both Hemo+ (62±4.9 ms) and Hemo- (71.7±7.3 ms) MIs in canines were elevated relative to remote myocardium (52.1±4.8

ms) by 18±9% and 38±13% respectively ($p<0.001$ for both cases). In conclusion, T_2* MRI is a more suitable approach for detecting and characterizing acute reperfusion myocardial hemorrhage.

6.2. Introduction

Timely restoration of blood flow to ischemic myocardium can limit the extent of myocardial necrosis (19). Although the benefits of reperfusion therapy are well established, I-R injury has been shown to be associated with post-MI ventricular arrhythmias (22), myocardial stunning (21), MO (20) and lethal reperfusion injury (17). In particular, MO resulting from I-R injury has been associated with adverse outcomes and reduced event-free survival (149,265). Closely related to MO is intramyocardial hemorrhage – a condition where reperfused blood extravasates into the interstitial space. Intramyocardial hemorrhage has been widely reported to be associated with larger MIs and MO in animal models (182,184-186), as well as in humans (173,188,191) following reperfusion. Importantly, intramyocardial hemorrhage has been shown to be a significant predictor of poor LV remodeling (196,199,430,442), late arrhythmogenic risk (198) and major adverse cardiovascular events (141).

MRI based on either T_2*-weighted (199,287,291,293,430,443) or T_2-weighted imaging (134,196,198,288,290,442,444), has been shown to non-invasively discriminate between hemorrhagic and non-hemorrhagic MIs. In principle, both T_2 and T_2* approaches may be used to identify the presence of hemorrhage since both methods are sensitive to the magnetic field inhomogeneities associated with the byproducts of hemoglobin degradation (285). However, currently there is a lack of general agreement on which of the two approaches (T_2 or T_2*) is most suitable for imaging acute intramyocardial hemorrhage. Since T_2-based imaging is known to be

highly sensitive to edema, which commonly accompanies acute reperfusion hemorrhage, the appearance of hemorrhage may be masked or reduced on T_2-based imaging (289).

This study hypothesizes that T_2*-based imaging can provide a greater acuity for detecting reperfusion hemorrhage than T_2-weighted imaging. This hypothesis was tested in a cohort of individuals who underwent coronary revascularization after first STEMI and the findings were validated using an established large animal model of acute I-R injury. T_2 and T_2* changes in acute reperfused hemorrhagic (Hemo+) and non-hemorrhagic (Hemo-) MIs were evaluated to determine which of the two techniques is more suitable for detecting intramyocardial hemorrhage at 1.5T.

6.3. Methods

6.3.1. Patient Studies

Patient studies were approved by the Institutional Review Board and were HIPAA compliant. Following informed consent, patients (n = 14; 3 women; mean age = 56±9 years) with first STEMI and successful PCI (TIMI flow of 3, post-PCI) were prospectively enrolled and studied within 3 days post-PCI. Patients contraindicated for MRI were excluded from the study recruitment. ECG-triggered breath-held T_2*-weighted, T_2-weighted, and LGE images of contiguous short-axis slices covering the entire LV were acquired on a 1.5T clinical scanner (MAGNETOM Avanto®, Siemens Healthcare, Erlangen, Germany). T_2*-weighted images were acquired using a multi-echo GRE sequence (TR = 15.8 ms; 6 TEs = 2.6, 4.8, 7.0, 9.3, 11.5 and 13.7 ms; BW = 355 Hz/pixel; $\alpha = 10°$; in-plane resolution = 1.4x1.4 mm^2). T_2-weighted images were acquired using a T_2-STIR sequence (TR = 2-3 R-R intervals; TE = 61 ms; TI = 170 ms;

BW = 235 Hz/pixel; echo train length = 25; in-plane resolution = 1.4 x 1.4 mm^2). LGE images were acquired using an IR-prepared FLASH sequence (TR = 2 R-R intervals; TE = 3.32 ms; BW = 130 Hz/pixel; α = 25°; in-plane resolution = 1.5 x 1.5 mm^2) 8-10 minutes following an intravenous injection of 0.1 mmol/kg body weight of gadopentetate dimeglumine (Magnevist®, Bayer Healthcare Pharmaceuticals Inc., Wayne, NJ). Other common imaging parameters were slice thickness = 10 mm and number of averages = 1. Pre-scan normalization was applied before each scan to minimize surface-coil bias.

6.3.2. Proof-of-Concept Studies in Canines

6.3.2.1. MRI Studies

Canines (n = 25, 20-25 kg) were studied according to the protocols approved by the Institutional Animal Care and Use Committee (IACUC). Baseline MRI scans were performed on day 0. On day 2, animals were implanted with a hydraulic occluder around the LAD. On day 9, each animal was randomly assigned to one of the two experimental groups: Infarct (n = 20) and Control (n = 5). The Infarct group was subjected to 3 hours of no-flow ischemia followed by reperfusion. MRI scans were performed on the Infarct group again on day 14 post-baseline scans (5 days post I-R injury). The Control group was not subjected to the I-R protocol and MRI of these animals was performed on day 14 post-baseline scans to match the imaging time points of the Infarct group.

MRI studies were performed on a 1.5T clinical MRI system (MAGNETOM Espree®, Siemens Healthcare, Erlangen, Germany). ECG-triggered, breath-held, contiguous short-axis images covering the entire LV were acquired using T_2*-weighted, T_2-weighted, and LGE

imaging. T_2*-weighted images were acquired using multi-echo GRE sequence (TR = 21 ms; 6 TEs = 3.4, 6.4, 9.4, 12.4, 15.4 and 18.4 ms; BW = 566 Hz/pixel; $\alpha = 12°$). T_2-weighted images were acquired using both T_2-prepared SSFP (TR/TE = 2.2/1.1 ms; T_2-preparation times = 0, 24 and 55 ms; BW = 1002 Hz/pixel; $\alpha = 70°$) and T_2-STIR (TR = 2-3 R-R intervals; TE = 64 ms; echo train length = 15; BW = 235 Hz/pixel; TI = 170 ms) sequences. LGE images were acquired using a non-selective IR-prepared SSFP sequence (TR/TE = 3.75 / 1.75 ms; TI optimized to null viable myocardium; BW = 1002 Hz/pixel; $\alpha = 40°$) 8-10 minutes following an intravenous injection of 0.1 mmol/kg body weight of gadopentate dimeglumine (Magnevist, Bayer Healthcare Pharmaceuticals Inc., Wayne, NJ). Other commonly used imaging parameters were: in-plane resolution = 1.3 x 1.3 mm^2, slice thickness = 8 mm, and number of averages = 1. Pre-scan normalization was applied before each scan to minimize surface-coil bias.

6.3.2.2. Histopathology

Animals were humanely euthanized following the day 14 MRI study. The hearts were excised and cut into 8-10 mm thick short-axis slices. Infarcted areas were delineated using TTC staining. Microscopic histopathologies of the representative samples of infarcted and remote myocardium were assessed with Hematoxylin & Eosin (H&E) and Perl's stains. MIs were considered to be hemorrhagic (Hemo+) if Perl's stain showed the presence of iron and H&E stain showed the presence of extravasated RBCs within the infarcted zones. Otherwise, MIs were considered to be non-hemorrhagic (Hemo-).

6.3.3. Image Analyses

Motion-corrected inline T_2 maps were obtained using T_2-prepared SSFP images. T_2* maps were generated by fitting the multi-echo GRE images to a monoexponential decay. All image analyses were performed using cmr[42] image processing software (Circle Cardiovascular Imaging Inc., Calgary, AB, Canada). The images were evaluated in consensus by two expert reviewers with >5 years of experience in evaluating cardiac MR images. The reviewers were blinded to any other patient or canine data. Remote myocardium was identified as the region showing no hyperintensity on LGE images. Infarcted myocardium was defined using the Mean+5SD criterion relative to a reference ROI drawn in the remote myocardium (415).

In patients, MIs were considered to be Hemo+ if they contained hypointense cores on the T_2*-weighted image acquired at TE = 13.7 ms detected using the Mean-2SD criterion relative to the reference ROI. MIs were considered to be Hemo- if they were negative for hemorrhage on the T_2*-weighted images. ROIs were drawn around the Hemo+ myocardium on T_2*-weighted images and copied onto the corresponding T_2-STIR images. Mean T_2-STIR signal intensity (STIR-SI) and T_2* values were measured for remote myocardium, Hemo+ and Hemo- MIs.

Canines from the Infarct group were classified as having either Hemo+ or Hemo- MIs based on ex-vivo histopathology as explained above. In-vivo MRI images were then retrospectively analyzed based on this classification. Hemo+ myocardium was identified as hypointense cores within infarcted territories on the T_2*-weighted image acquired at TE = 15.4 ms using the Mean-2SD criterion relative to a reference ROI. ROIs were drawn around the Hemo+ myocardium on T_2*-weighted images and copied onto the corresponding T_2 maps and T_2-STIR images. For canines from the Control group, mean T_2 and T_2* values of the entire LV were measured from day 0 (baseline) and day 14 MRI studies. For the canines from the Infarct

group, mean baseline T_2 and T_2* values of the entire LV were measured from day 0 MR. For the same animals from the Infarct group, mean T_2, T_2*, and STIR-SI values for the ROIs within remote, Hemo- and Hemo+ myocardium were measured from day 14 MRI (5 days post I-R injury).

6.3.4. Statistical Analyses

Statistical analyses were performed using STATA (version 10.1, StataCorp, College Station, TX). Categorical variables were expressed as number with the percentage of animals or patients, and compared using chi-square test. Normality of continuous data was determined using Shapiro-Wilk test and quantile-quantile plots. Continuous variables with normal distribution were compared using mixed-model ANOVA with Tukey's post-hoc analysis. ROIs within each heart were entered as fixed effects, while the animals or patients were entered as random effects. Repeated measures from each heart were nested for analysis. Continuous variables with non-normal distribution were compared using non-parametric Friedman test. Pairwise comparisons for non-normal data were also performed using Mann-Whitney U test. Bonferroni corrections were used to adjust the significance level for multiple comparisons. Statistical significance was set at $p<0.05$.

6.4. Results

6.4.1. Patient Studies

Clinical features of the STEMI patients enrolled in this study are shown in Table 6.1. T_2*-weighted images, in conjunction with LGE images, showed the presence of Hemo+ MIs in 7 patients (3 lateral, 3 anteroseptal, and 1 inferior lateral), and Hemo- MIs in 7 patients (3 lateral, 2

anteroseptal, and 2 inferior lateral). Representative T_2* maps, T_2-STIR and LGE images acquired on day 3 post-PCI from a patient with Hemo+ MI and a patient with Hemo- MI are shown in Figure 6.1. Visually evident T_2* decreases and STIR-SI increases were observed within Hemo+ MIs on T_2* maps and T_2-STIR images, respectively. Hypointense cores within hyperintense edematous territories that were positive for LGE were visualized on T_2-STIR images of Hemo+ MIs. Hemorrhage was always accompanied by persistent MO on LGE images. Significant T_2* and STIR-SI increases were visualized within Hemo- MIs.

Parameter	Hemorrhagic (n=7)	Non-hemorrhagic (n=7)	p-value
Age* (years)	56 (47 – 59)	57 (56 – 66)	0.28
Male Sex, n (%)	6 (86)	3 (43)	0.09
Diabetes Mellitus, n (%)	3 (43)	2 (29)	0.58
Smoking History, n (%)	5 (71)	1 (14)	0.03*
Hypertension, n (%)	2 (29)	2 (29)	1.00
Hyperlipidemia, n (%)	2 (29)	1 (14)	0.51
Time from symptoms to reperfusion* (hours), median (range)	4.8 (3.4 – 7.3)	3.7 (3.2 – 4.0)	0.25
TIMI flow pre-PCI, n (%) **Grade 0** **Grade 1** **Grade 2**	 3 (43) 2 (29) 2 (29)	 3 (43) 1 (14) 3 (43)	 0.76
TIMI flow post-PCI, n (%) **Grade 3**	 7 (100)	 7 (100)	 –

*Data are expressed as median and interquartile range. *Statistically significant difference.

Table 6.1: Clinical features of STEMI patients

Mean T_2* values of the remote, Hemo+ and Hemo- myocardium measured from patients on day 3 post-PCI are shown in Table 6.2. Compared to the remote myocardium, mean T_2* of Hemo+ MI was 54±13% lower ($p<0.001$), while mean STIR-SI of Hemo+ myocardium was

37±19% higher ($p<0.001$). Mean T_2* of Hemo- myocardium showed a marginal increase of 6±2.5% ($p = 0.021$), while mean STIR-SI was significantly elevated by 78±27% ($p<0.001$). Mean percentage change in STIR-SI of Hemo+ MI with respect to remote myocardium was significantly lower than that of Hemo- MI ($p<0.001$). In all, 88% (38/43) of the imaging slices that were positive for hemorrhage on T_2*-weighted images showed hypointense cores within hyperintense edematous territories on the corresponding T_2-STIR images.

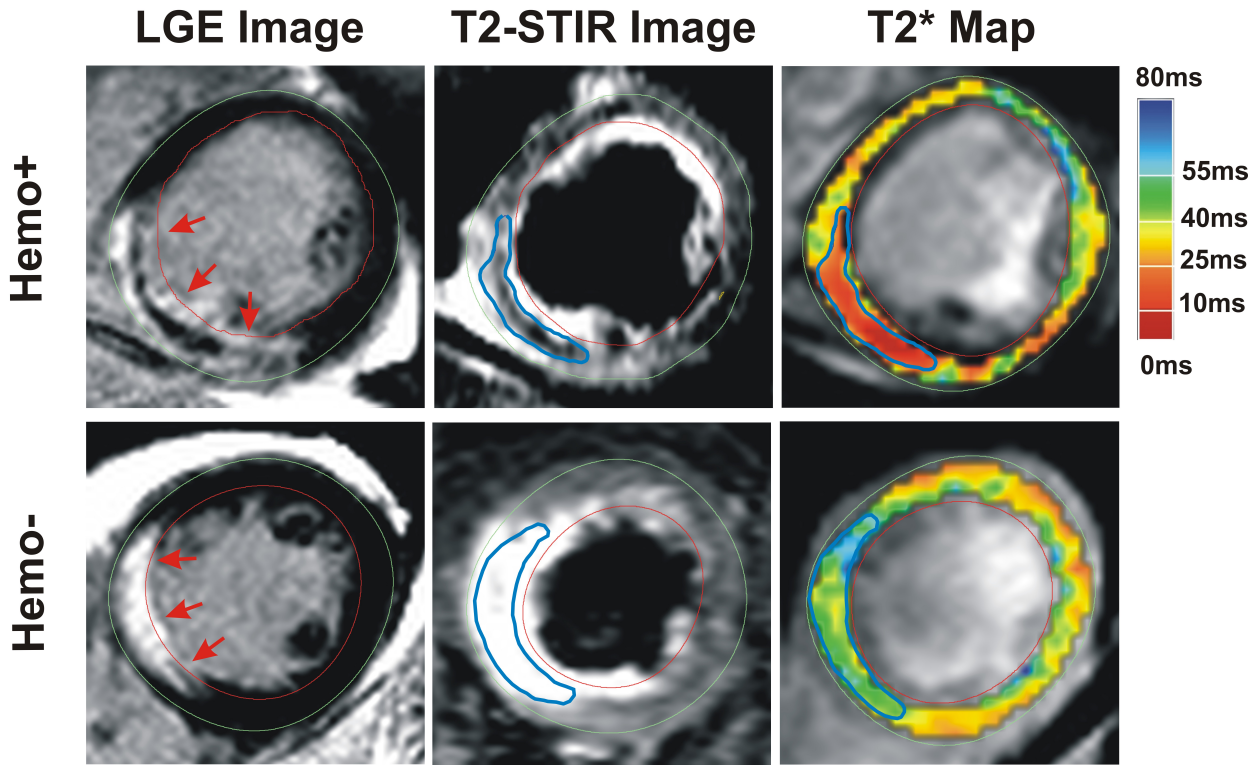

Figure 6.1: *Cardiac MRI-based detection of acute hemorrhagic and non-hemorrhagic myocardial infarctions in patients.* Representative LGE images, T_2-STIR images, and T_2* maps acquired on day 3 post-PCI from two patients with Hemo+ MI (49 years old male) and Hemo- MI (57 year old male) are shown. LGE images confirmed the presence of MI in both of the cases (arrows). Significant T_2* losses were observed within Hemo+ territories, while hypointense cores were observed within the hyperintense edematous territories on T_2-STIR images. Significant hyperintensities were observed within the Hemo- territories on both T_2* maps and T_2-STIR images.

Tissue Type	Remote	Hemorrhagic (n = 7)	Non-hemorrhagic (n = 7)
T_2* (ms)	35.2±2.1	15.9±4.5	37.8±2.5
Change in T_2* with respect to Remote (%)	–	-54.4±13.3	6±2.5
Change in T_2-STIR signal intensity with respect to Remote (%)	–	37.2±19.4	78.2±37.4

Data are expressed as mean ± SD.

Table 6.2: Mean T_2* and T_2-STIR signal intensity changes associated with acute reperfused hemorrhagic and non-hemorrhagic MIs in STEMI patients on day 3 post-PCI.

6.4.2. Animal Studies

6.4.2.1 MRI Studies

After discounting for premature death during reperfusion (n = 2) and occluder dysfunction (n = 4), a total of fourteen animals from the Infarct group were available for analysis. Nine animals from the Infarct group sustained Hemo+ MIs, while five animals sustained Hemo- MIs as verified by ex-vivo histopathology. Control animals did not sustain any MI throughout the study.

Representative T_2* map, T_2 map, T_2-STIR and LGE images acquired on day 14 MRI from the Control and Infarct (one with Hemo+ MI and one with Hemo- MI) groups are shown in Figure 6.2. Consistent with the patient studies, all canines with Hemo+ MIs showed distinct hypointense cores on at least one of the in-vivo T_2* maps, T_2 maps and T_2-STIR images acquired on day 14. The hypointense cores were always surrounded by hyperintense edematous territories on both T_2 maps and T_2-STIR images. Hemorrhage was always accompanied by persistent MO on LGE images. In contrast, canines with Hemo- MIs did not have any hypointense cores within infarcted territories on any of the in-vivo T_2* maps, T_2 maps or T_2-STIR images acquired on day

14. Marginal increase in T_2* was visually evident in Hemo- MIs, while T_2 and STIR-SI were significantly elevated.

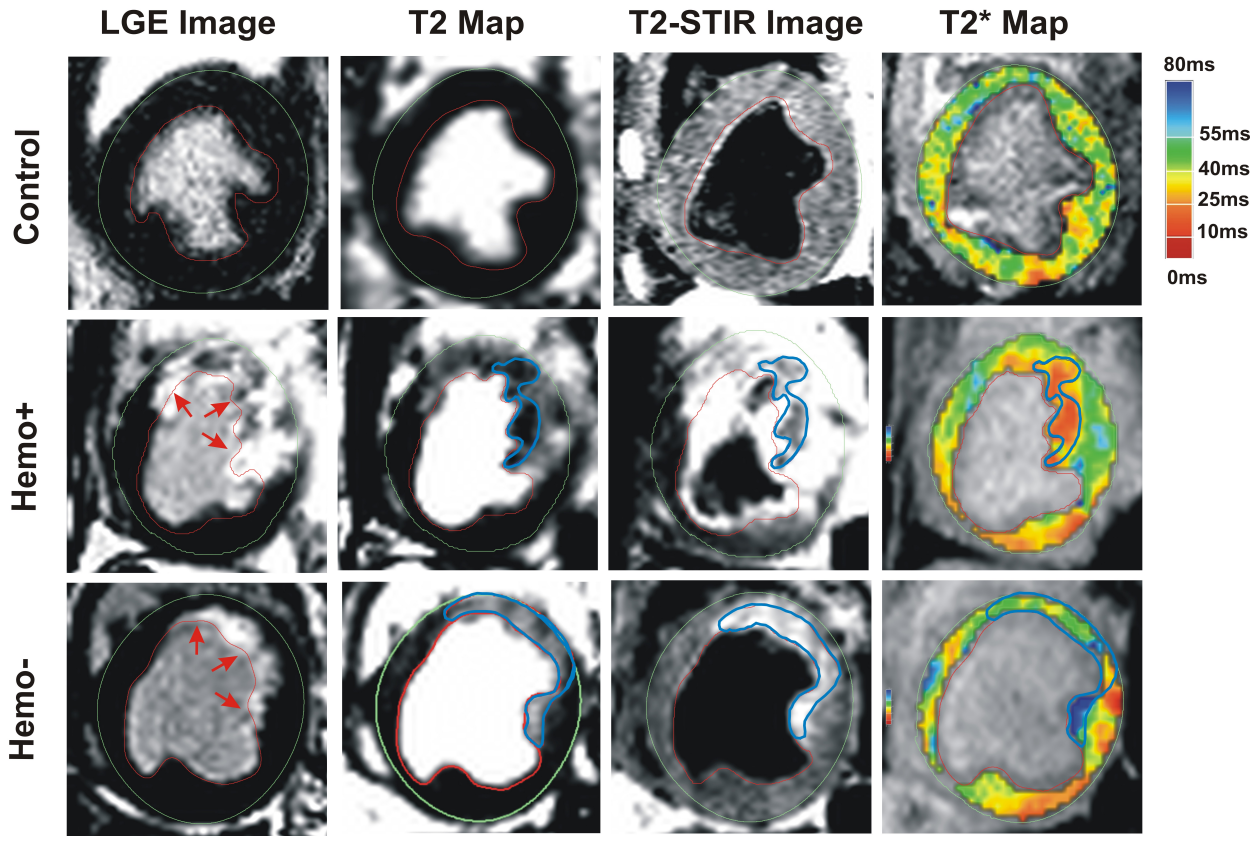

Figure 6.2: *Cardiac MRI-based detection of acute hemorrhagic and non-hemorrhagic myocardial infarctions in canines.* Representative LGE images, T_2 maps, T_2-STIR images, and T_2* maps acquired at 5 days following I-R injury are shown from a Control, and animals with Hemo+ and Hemo- MIs. Control animals did not sustain any MI as evidenced by LGE images. Corresponding T_2 map, T_2-STIR image and T_2* map did not show any distinct signal features generally observed in the presence of an AMI. LGE images confirmed the presence MIs (arrows) in animals subjected to I-R injury. Significant T_2* losses were observed within Hemo+ territories, while hypointense cores were observable within the hyperintense edematous territories on T_2 maps and T_2-STIR images. Hemo- territories showed significant hyperintensity on T_2 maps and T_2-STIR images, while marginal elevations were observed on T_2* maps.

Mean T_2 and T_2* values from the Control and Infarct groups measured on days 0 and 14 are shown in Table 6.3. Among the Controls, mean baseline T_2* and T_2 values measured from day 0 MRI were not statistically different from their respective mean values measured from day 14 MRI ($p = 0.19$). Similarly, within the Infarct group, mean baseline T_2* and T_2 values of the entire LV measured from day 0 MRI were not significantly different from the respective values of remote myocardium measured from day 14 MRI ($p = 0.18$). In contrast, mean T_2* of Hemo+ territories from day 14 MRI was significantly lower than the mean baseline T_2* of the entire LV measured prior to I-R injury ($p<0.001$), while mean T_2 of Hemo+ territories from day 14 MRI was significantly higher than the mean baseline T_2 of the entire LV prior to I-R injury ($p<0.001$). Both mean T_2* and T_2 values of Hemo- territories obtained from day 14 MRI were significantly higher than their respective baseline measures prior to I-R injury ($p<0.001$, for both cases). In all, 94% (42/45) of the imaging slices that were positive for hemorrhage on T_2*-weighted images showed hypointense cores within hyperintense edematous territories on the corresponding T_2 maps, while 91% (41/45) of the slices positive for hemorrhage showed hypointense cores on T_2-STIR images.

Across all terminal (day 14) MRI studies performed within the Infarct group, mean T_2* of Hemo+ MIs was 40±10% lower than the mean T_2* of remote myocardium ($p<0.001$). However, mean T_2 and STIR-SI of Hemo+ territories were elevated by 17±9% ($p<0.001$) and 42±22% ($p<0.001$) compared to remote myocardium, respectively. For Hemo+ MIs, mean percentage change in STIR-SI was significantly higher than the mean percentage change in T_2 ($p<0.001$). Compared to the remote myocardium, mean T_2* of Hemo- territories was elevated by a marginal 8±5% ($p = 0.012$), while T_2 and STIR-SI of Hemo- MIs were substantially elevated ($p<0.001$ for both cases). Similar to Hemo+ territories, mean percentage change of STIR-SI of Hemo-

territories was greater than mean percentage change in T_2 ($p<0.001$). Compared to Hemo- MIs, mean percentage changes in STIR-SI and T_2 were significantly lower in the presence of hemorrhage ($p<0.001$).

Group	**Control (n=5)**		**Infarct (n=9)**			
MRI Time Point	Day 0 (Baseline)	Day 14	Day 0 (Baseline)	Day 14 (5 days post I-R injury)		
Tissue Type	Whole LV	Whole LV	Whole LV	Remote	Hemorrhagic	Non-hemorrhagic
T_2 (ms)	50.9±4.7	51.4±4.7	52.1±4.8	52.2±4.7	62.0±4.9	71.7±7.3
T_2* (ms)	38.6±2.0	39.7±1.9	38.7±2.0	39.3±2.5	23.0±4.0	44.6±4.8
Change in T_2* with respect to Remote (%)	–	–	–	–	-40.1±10.0	8.0±5.0
Change in T_2 with respect to Remote (%)	–	–	–	–	17.7±9.2	38.4±12.9
Change in T_2-STIR signal intensity with respect to Remote (%)	–	–	–	–	42.2±22.9	64.5±22.4

Data are expressed as mean±SD.

Table 6.3: Mean T_2*, T_2, and T_2-STIR signal intensity changes associated with acute reperfused hemorrhagic and non-hemorrhagic MIs in canines on day 5 post I-R injury.

6.4.2.2. Histopathology

Representative histopathological images from a Control animal, and animals with Hemo+ and Hemo- MIs are shown in Figure 6.3. TTC staining confirmed the presence of MIs in animals subjected to I-R injury (Figures 6.3B and 6.3C), but not in the Controls (Figure 6.3A). Notably, TTC staining of Hemo+ territories (Figure 6.3B) showed gross bleeding within the infarct core, while no such gross bleeding was observed within TTC stained Hemo- territories (Fig. 6.3C). H&E images of both Hemo+ and Hemo- territories (Figures 6.3-B1 and C1 respectively) showed extensive myocardial damage accompanied by extensive inflammatory response. Also, H&E images of Hemo+ (but not Hemo-) territories showed the presence of eosin-stained extravasated RBCs in the interstitium. Perl's stain showed significant localized iron within Hemo+ territories (Figure 6.3-B2), but negligible or no iron within Hemo- territories (Figure 6.3-C2). Microstructural histopathologies of remote myocardium obtained from canines with Hemo+ and Hemo- MIs (Figures 6.3-B3, B4, C3 and C4) were similar to that of viable myocardium obtained from a Control animal (Figure 6.3-A1 and A2).

6.5. Discussion

Recent studies have shown that intramyocardial hemorrhage may be one of the strongest predictors of adverse outcome (141,196,198,199,430,442). This has generated substantial interest in understanding the effects of reperfusion hemorrhage on acute tissue damage and post MI remodeling. To facilitate and guide these investigations, it is imperative to ensure that the most optimal imaging strategy is employed. On the basis of patient and proof-of-concept animal studies this study has demonstrated that acute reperfusion myocardial hemorrhage is better characterized by T_2* than T_2-based MRI. This observation is consistent with previous reports,

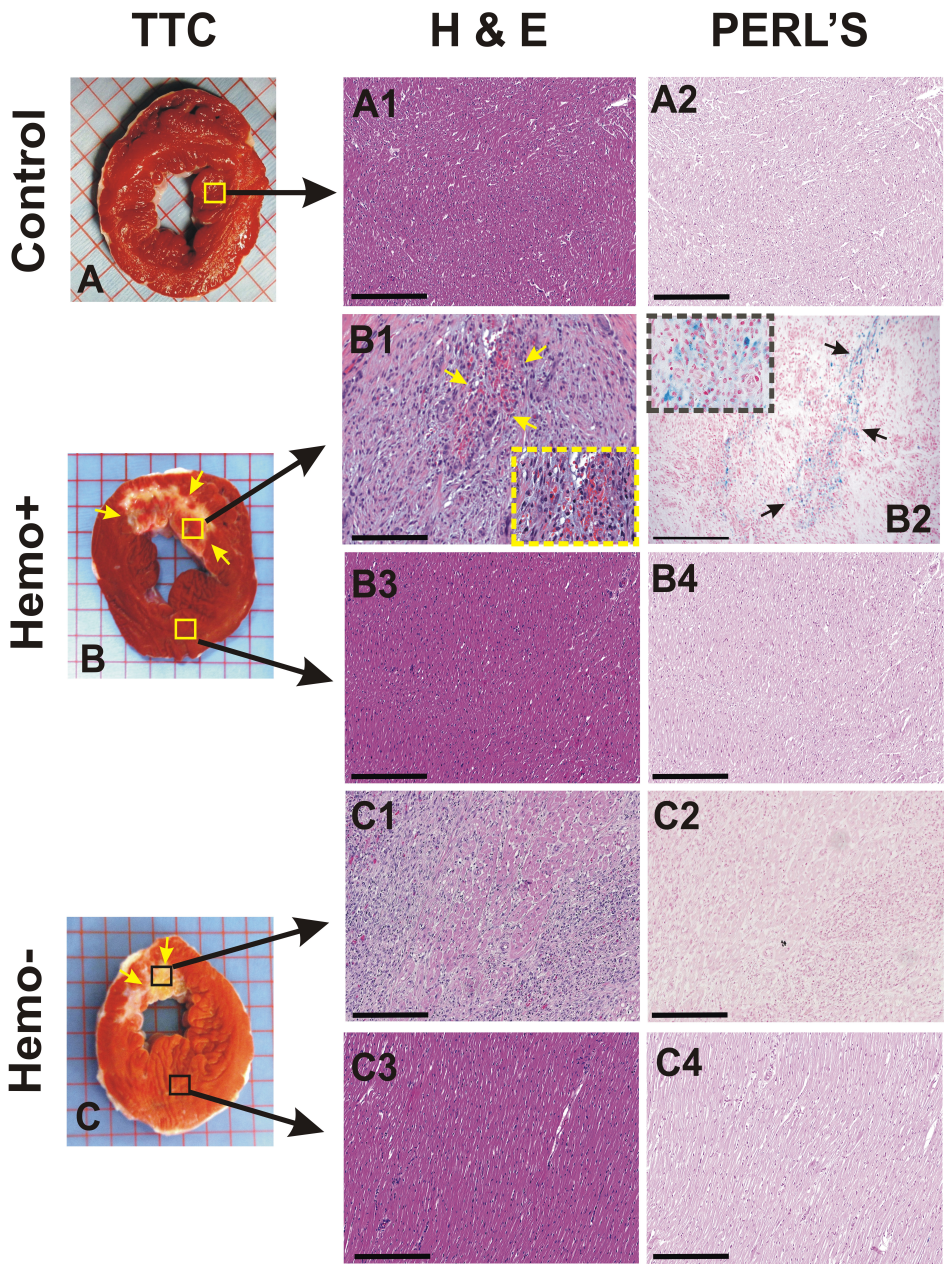

Figure 6.3: *Histopathological validation of acute hemorrhagic and non-hemorrhagic myocardial infarctions in canines.* Representative histopathological images obtained from an animal from the Control group and two animals from the Infarct group (one with Hemo+ and another with Hemo-) are shown. TTC staining confirmed the presence of MIs within the Infarct group. Corresponding H&E staining of Hemo+ and Hemo- territories showed diffuse necrosis with massive infiltration of inflammatory cells (arrows and inset). H&E staining of Hemo+ territories also showed interstitial extravasation of RBCs into the infarcted territories. Perl's stain confirmed the presence of localized iron in Hemo+ territories (arrows and inset), but not in Hemo- territories.

which have suggested that hemorrhage and edema have counter-acting influences on T_2 (and T_2-weighted) images (199,289,292). It is expected that these findings can be instrumental in furthering the understanding of the role of reperfusion hemorrhage in patients. In particular, the ability to define T_2* values can help stratify the extent of hemorrhagic tissue damage.

Degradation byproducts of hemorrhage cause local magnetic field inhomogeneities, that in turn result in signal loss on T_2- and T_2*-based images (285). In T_2-weighted imaging, refocusing RF pulses partially reverse the loss of phase coherence (or signal loss), leading to a reduced sensitivity to the presence of hemorrhage. In addition, T_2-based approaches are highly sensitive to myocardial edema, which is associated with AMI. On the contrary, the absence of refocusing RF pulses in T_2*-based imaging leads to maximal loss of phase coherence within each TE. Moreover, as shown in this study, T_2*-based MRI is relatively insensitive to edema. These biophysical underpinnings support this study's findings that, in both patients and canines, only T_2*-based MRI is capable of generating negative image contrast relative to remote/healthy myocardium; while, T_2-based approaches have a reduced sensitivity to hemorrhage. The implications are that in cases where edema is extensive, hemorrhagic volumes may be significantly underestimated or in more extreme cases, may be entirely invisible/detectable in T_2-based MRI. Moreover, partial volume effects (8-10 mm thick imaging slices) may further limit the detection of small hemorrhages with T_2-based than T_2*-based MRI.

T_2- and T_2*-weighted imaging are both limited by surface coil bias and the ensuing qualitative nature of image interpretation. Particularly, dark blood T_2-weighted techniques, such as T_2-STIR, are affected by unsuppressed slow-flowing blood signal adjacent to the infarcted myocardium and myocardial signal loss due to through-plane motion, both of which may hamper

specificity and sensitivity. T_2 mapping, being quantitative in nature, can overcome many of the issues faced by T_2-weighted imaging. However, the dependence of T_2 values on inter-echo spacing (445) and their non-monotonic relationship with the size of the paramagnetic agent (446), complicate absolute characterization of hemorrhage on the basis of T_2. Despite these limitations, this study has shown that T_2-based approaches may have adequate sensitivity to detect acute reperfusion myocardial hemorrhage. These observations are consistent with previous reports (199,290).

6.5.1. Study Limitations

This study has certain limitations. Firstly, the sample sizes in this translational study are relatively small. However, given the large T_2 and T_2* changes in Hemo+ and Hemo- MIs, retrospective analysis showed that the minimum statistical power among all the comparisons was 0.81. The sample sizes in this study are comparable to those used by other studies (290,293). Second, T_2 maps were not acquired in patients due to constraints on imaging time. However, in place of T_2 maps, T_2-STIR images were acquired. Despite this limitation, from the animal studies it appears that there is negligible difference between the characteristic changes in T_2 or T_2-weighted signal in remote/healthy myocardium and Hemo+ or Hemo- territories. Third, although validated in canines, histological validation of MIs identified to be hemorrhagic on T_2*-based MRI could not be performed in patients as all of them survived the entire study. Fourth, post-reperfusion MRI time points are slightly different in patients (day 3) and canines (day 5). This difference stemmed from the logistical difficulties of not being able to identically match the MRI studies to the post-reperfusion period of MI. Fourth, this study does not provide standard diagnostic accuracy measures for the T_2 and T_2*-based MRI primarily due to the subjective

nature of registering the in-vivo MRI images with the ex-vivo heart slices. Finally, despite the sensitivity of T_2*-based MRI for iron (337), it is also sensitive to off-resonance artifacts arising from bulk magnetic susceptibility differences at the heart-lung interface. These artifacts can particularly affect the T_2*-based diagnosis of acute hemorrhagic MIs in the infero-lateral walls of LV. Since T_2* loss from off-resonance artifacts and intramyocardial hemorrhage originate from the opposite sides of the myocardial wall (i.e., epicardial wall for off-resonance and endocardial wall for hemorrhage) and LGEs provide indication for MI, it is possible to carefully discriminate between hemorrhage and off-resonance artifacts.

6.6. Conclusion

The relative insensitivity of T_2*-based MRI to edema, but a strong sensitivity to byproducts of hemorrhage makes T_2*-based MRI a more suitable approach for characterizing acute reperfusion myocardial hemorrhage. The counteracting effects of edema and hemorrhage, as well as the refocusing effects of T_2-based MRI make hemorrhage less conspicuous in T_2 maps and T_2-weighted images.

CHAPTER 7

Localized Chronic Iron Deposition Secondary to Acute Reperfusion Intramyocardial Hemorrhage: Application of T_2*-Based MRI

7.1. Abstract

Intramyocardial hemorrhage frequently accompanies large reperfused MIs. However, its influence on the make-up and the ensuing effect on the infarcted tissue during the chronic phase remain unexplored. The purpose of this study is to investigate the long-term effects of acute reperfusion intramyocardial hemorrhage on CMI characteristics, and to evaluate the ability of T_2*-based MRI to characterize such effects. Patients (n = 15; 3 women), recruited after successful PCI for first STEMI, underwent cardiac MRI on day 3 and month 6 post-PCI. Patients with hemorrhagic (Hemo+) MIs, as determined by non-contrast enhanced T_2*-based MRI on day 3 (n = 11), showed persistent T_2* losses co-localized with scar tissue on the follow-up scans, suggesting chronic iron deposition. T_2* values of non-hemorrhagic (Hemo-) and remote territories were not significantly different from one another (p = 0.51), but were significantly higher than T_2* of Hemo+ territories (p<0.001). Canines (n = 20), subjected to I-R injury (n = 14), underwent MRI on days 3 and 56 post-reperfusion. Similarly, sham-operated animals (Shams; n = 3) were imaged using MRI at similar time points. Subsequently, hearts were explanted, imaged ex-vivo, and samples of Hemo+, Hemo-, remote and Sham myocardium were isolated and stained. The extent of iron deposition ([Fe]) within each sample was measured using mass spectrometry. Hemo+ infarcts showed significant T_2* losses compared to the other (control) groups (p<0.001), and Perl's stain confirmed localized iron deposition. Mean [Fe] of

Hemo+ was nearly an order of magnitude greater than the control groups ($p<0.001$), but no significant differences were observed among the control groups. A strong linear relationship was observed between $\log(T_2^*)$ and $-\log([Fe])$ ($R^2 = 0.7$; $p<0.001$). The monoclonal antibody Mac387 stains, along with Perl's stains, showed preferential localization of newly recruited monocytes at the site of chronic iron deposition. Multivariate regression showed that hemorrhage volumes measured during the acute phase is a significant independent predictor of the change in end-diastolic sphericity index (EDSI) between acute and chronic phases, while Fe volume was only a significant univariate predictor. In conclusion, hemorrhagic MI can lead to iron depositions within the infarct zones, which can be reliably monitored using T_2^*-based MRI. The chronic iron deposition can also be a source of adverse LV remodeling and prolonged inflammatory burden in chronic phase of MI.

7.2. Introduction

Specific pathological conditions can mediate increased tissue levels of iron in a number of organs including the brain (285,447,448), liver (449,450), and heart (451,452). In these settings, biodegradation of heme, harbored by RBCs is considered to be the most significant source of iron. In the heart, chronic deposition of iron has been known to occur predominantly in hemochromatosis (453,454), and blood transfusion therapy for thalassemia major (337,455) or sickle-cell anemia (336). Abnormal accumulation of iron in the heart has been associated with poor cardiac function (452,456-458), and conduction abnormalities (459-461).

Pathological pooling of RBCs within the heart muscle is known to take place in the setting of reperfused MI (182,183). While the endothelial cells have a higher tolerance for ischemia than cardiomyocytes, prolonged periods (more than 90 minutes) of no-flow ischemia in

myocardial tissue leads to oncosis (cell death) of the vascular endothelium and thus to a breakdown of the microvascular barrier (462). Therefore, a delayed re-institution of epicardial coronary blood flow after acute coronary occlusion may lead to the extravasation of erythrocytes (hemorrhage) with severe consequences for regional perfusion. In fact, gross bleeding within the heart muscle is a frequently encountered hallmark of large MIs (173,185-187). The observed correlate with respect to blood flow is known as "no-reflow" (20,166).

Even though the prognostic significance of large MIs with MOs has been well studied (24,145,149), interest in the clinical consequences of intramyocardial hemorrhage has been increasing only recently. Hemorrhagic MIs have been shown to be associated with adverse LV remodeling (188,196,442,463), late arrhythmogenic risk (198) and major adverse cardiovascular events (141). However, the long-term fate of acute reperfused myocardial hemorrhage and its effects on the heart remain largely unexplored. This study investigated (a) whether acute reperfusion hemorrhage specifically imparts compositional changes in chronically infarcted myocardial tissue, (b) whether such compositional changes can be detected using non-contrast enhanced T_2*-based MRI, and (c) whether such compositional differences mediate adverse LV remodeling and prolonged inflammation in the chronic phase of MI. In particular, this study hypothesized that acute reperfusion myocardial hemorrhage leads to chronic iron depositions localized within the infarcted territories in the chronic phase, which can be detected using T_2*-based MRI. We tested this hypothesis using cardiac MRI in a pilot patient population who underwent successful coronary revascularization for first STEMI. Further, using a proof-of-concept canine model subjected to I-R injury, the findings in humans were validated. Subsequently, this study tested the hypothesis whether reperfusion-induced chronic iron depositions lead to adverse LV remodeling and a prolonged inflammatory activity in the chronic

phase of MI. This hypothesis was tested from histopathological analysis of chronically infarcted canine myocardium with a history of acute reperfusion hemorrhage.

7.3. Methods

7.3.1. Patient Selection and Cardiovascular MRI Studies

Patients were enrolled following informed consent and studied according to the protocols approved by the Institutional Review Board at the Foothills Medical Center (Calgary, AB, Canada). Patients with acute STEMI (n = 15; 3 women; mean age = 58±8 years) meeting AHA diagnostic criteria were enrolled in the study only if successful percutaneous coronary intervention (TIMI flow grade 3 post-PCI) was performed within 12 hours of the onset of symptoms. Patients were excluded from the study if they had previous MIs or had contraindications for a MRI study. All enrolled patients underwent MRI 3 days after PCI and again at 6 months after initial enrollment on a clinical 1.5T MRI system (MAGNETOM Avanto, Siemens Medical Solutions, Erlangen, Germany).

Cine-SSFP (TR/TE = 3.32/1.16 ms; $\alpha = 65°$; BW = 930 Hz/pixel; 25 cardiac phases; in-plane resolution = 1.8×1.8 mm^2), T_2*-weighted (multi-echo GRE; TR = 240 ms; 6 TEs = 2.6–13.7 ms with $\Delta TE = 2.2$ ms; $\alpha = 10°$; BW = 355 Hz/pixel; in-plane resolution = 1.6×1.6 mm^2) and LGE (IR-prepared FLASH; TR =1 R-R interval; TE = 3.32 ms; BW = 235 Hz/pixel; 1.6×1.6 mm^2) images of contiguous short-axis sections of the LV along with 2, 3 and 4 chamber long-axis views of the heart were acquired. Commonly used imaging parameters were slice thickness = 10 mm and number of averages = 1.

7.3.2. Proof-of-Concept Studies in Canines

7.3.2.1. Animal Preparation and MRI Studies

Canines (n = 23, 20-25 kg) were studied according to the protocols approved by the Institutional Animal Care and Use Committee. Animals were subjected to I-R injury (Infarct group, n = 20) by fully occluding the LAD for 3 hours followed by reperfusion. MRI studies were performed on a clinical 1.5T MRI system (MAGNETOM Avanto, Siemens Medical Solutions, Erlangen, Germany) on days 3 (acute) and 56 (chronic) following I-R injury. Sham-operated animals (Sham group, n = 3) underwent MRI at similar time points. Cine-SSFP (TR/TE = 3.5/1.75 ms; α = 70°; 25-30 cardiac phases; BW = 930 Hz/pixel), T_2*-weighted (TR = 240 ms; 6 TEs = 3.4–18.4 ms with ΔTE = 3.0 ms; α = 12°; BW = 566 Hz/pixel) and LGE images (IR-prepared SSFP; TR/TE = 3.5/1.75 ms; α = 40°; BW = 1002 Hz/pixel) of contiguous short-axis sections covering the entire LV and the three long-axis views were acquired at mid-diastole. Commonly used imaging parameters were in-plane resolution = 1.3×1.3 mm^2, slice thickness = 8 mm and number of averages = 1. On day 56, animals were euthanized and their hearts were excised and cut into roughly 1 cm thick slices. Ex-vivo 2D T_2*-weighted and LGE images of each slice were acquired using the in-vivo imaging parameters.

7.3.2.2. Isolation of Tissue Samples and Histopathology

The freshly excised heart from each animal was sliced and stained with TTC to histochemically validate irreversible myocardial damage and delineate the infarcted territories from viable myocardium. Remote, hemorrhagic (Hemo+), and non-hemorrhagic (Hemo-) myocardium were identified on the basis of ex-vivo MRI and TTC staining as explained in the Image Analysis section. Hemo+ and Hemo- infarcts were cut out into 0.5-0.8 cm^3 samples from densely infarcted

areas. Similarly, from each slice, at least 2 samples of TTC-stained viable myocardium were isolated (remote). From each sham slice, at least 2 samples of TTC-stained normal myocardium were isolated. Contiguous 5 μm sections were obtained from a representative sample of each of the Hemo+, Hemo-, remote and sham groups from every animal. These sections were stained with H&E stain, Masson's Trichrome stain for fibrosis, Perl's stain for iron, and monoclonal antibody Mac387 (Dako, Carpinteria, CA) for newly recruited monocytes, and imaged at 100X and 400X magnifications.

7.3.2.3. Inductively Coupled Plasma – Mass Spectrometry (ICP-MS)

The amount of iron deposited within each myocardial sample ($[Fe]_{Sample}$ in mg per g of tissue) was measured using a quadrupole-based X Series 2 ICP-MS (Thermo-Fisher Scientific, USA) equipped with Collision Cell Technology to reduce interference from doublets. Whole-heart Fe content ($[Fe]_{Heart}$) was calculated by weight-averaging the Fe content of all the constituent samples. In all, 55 samples of remote, 20 samples of Sham, 31 samples of Hemo- and 183 samples of Hemo+ of myocardial tissue were analyzed.

7.3.3. Image Analyses

Image analyses were performed using cmr[42] (Circle Cardiovascular Imaging Inc., Calgary, AB, Canada). T_2* maps were constructed by fitting the multi-echo T_2*-weighted images to a mono-exponential decay. For the in-vivo MR images from both patients and animals, remote myocardium was defined as the region showing no hyperintensity on LGE images. A reference ROI was drawn in remote myocardium on both LGE and T_2*-weighted images. Infarcted myocardium was defined on LGE images using the Mean+5SD criterion relative to the reference

ROI(415). On the acute phase LGE images, hypointense regions of MO were manually included as part of the infarcted myocardium. Hemo+ myocardium was defined as infarcted myocardium with hypointense signal on the T_2*-weighted image acquired at the last echo (TE = 13.7 ms for patients and 18.4 ms for animals) using the Mean-2SD criterion relative to the reference ROI (199,293). Hemo- myocardium was defined as the region positive for MI on LGE images, but negative for hemorrhage on the corresponding T_2*-weighted images. For the in-vivo T_2*-weighted images, care was taken not to include infero-lateral LV segments affected by off-resonance artifacts (464) arising from the susceptibility shifts at the heart-lung interface.

For the ex-vivo MR images from animals, remote myocardium of a given slice was defined as the section of the tissue showing no hyperintensity on ex-vivo LGE images and stained brick red by TTC. Hemo+ and Hemo- myocardium were similarly identified on the basis of ex-vivo T_2*-weighted and LGE images on the basis of threshold analysis used for in-vivo image analysis. In-vivo and ex-vivo T_2* values for Hemo+, Hemo-, remote and sham groups were measured on per-slice (T_2*_{Slice}) and whole-heart (T_2*_{Heart}) basis for each animal.

LV mass, EDV, ESV, EF and end-diastolic sphericity index (EDSI) were calculated for both patients and canines from the respective cine-SSFP images. All measurements were normalized to the body surface area. Infarct volume (%Infarct) and hemorrhage volume (%Hemo) were calculated with respect to the total LV myocardial volume.

7.3.4. Statistical Analyses

Statistical analyses were performed using STATA (version 10.1, StataCorp, College Station, TX). A two-tailed p-value <0.05 was considered to be statistically significant for all statistical analyses in both patients and canines. For patients, mixed-model linear regression with

Bonferroni corrections ($p<0.001$) was used to compare in-vivo T_2*_{Slice} among the Hemo+, Hemo-, and remote groups. The null hypothesis that there was no difference in in-vivo T_2*_{Slice} among the three different groups was tested. Patients were entered as random effects, while slices from each heart were nested in the analysis to account for repeated measurements from a single heart (or myocardial slice). Changes in in-vivo T_2*_{Heart} values between day 3 and 6 months were evaluated using a paired t-test. The relationship between mean in-vivo T_2*_{Heart} from acute and chronic phase MRI studies was also evaluated.

LV mass, EDV, ESV, EF, end-diastolic sphericity index (EDSI), and %Infarct were compared between patients with Hemo+ and Hemo- MIs using two-sample t-test, as well as, between acute (day 3) and chronic (month 6) phases of MI post-PCI using paired t-test. Among the patients with Hemo+ MIs, %Hemo was compared between day 3 and month 6 post-PCI using paired t-test. Simple and multivariable regression analyses were performed to determine whether %Infarct and/or %Hemo volumes were predictors of LV remodeling parameters (EDV, EF, ESV and EDSI) in the chronic phase at 6 months post-PCI.

For animals, in-vivo T_2*_{Slice}, ex-vivo T_2*_{Slice} and $[Fe]_{Sample}$ were compared among the Hemo+, Hemo-, remote, and sham groups using mixed-model linear regression with Bonferroni corrections ($p<0.001$). The null hypothesis that there was no difference among the four different groups for each parameter of interest was tested. Canines were entered as random effects, while samples from each heart (or myocardial slice) were nested in the analysis to account for repeated measurements from a single heart (or myocardial slice). Paired t-test was used to compare in-vivo T_2*_{Heart} values obtained from MRI studies on day 3 and day 56. The relationship between in-vivo T_2*_{Heart} (from day 3 and day 56 MRI studies) and the corresponding ex-vivo T_2*_{Heart} was

evaluated. Similarly, the relationship between log(ex-vivo T_2*_{Heart}) and $-\log([Fe]_{Heart})$ was evaluated.

LV mass, EDV, ESV, EF, EDSI, %Infarct and %Hemo were compared in canines between acute (day 3) and chronic (day 56) phases post-reperfusion using paired t-test. Simple and multivariable regression analyses were performed to determine whether %Infarct and/or %Hemo were predictors of LV remodeling (EDV, ESV, EF and EDSI) at in the chronic phase (day 56) post-reperfusion.

7.4. Results

7.4.1. Chronic Iron Deposition in Humans Following Hemorrhagic Myocardial Infarction

In the acute phase (day 3), eleven patients were identified positive for hemorrhagic MI (Table 7.1; regions: 5 lateral, 3 anteroseptal, and 3 inferior lateral), while four patients had non-hemorrhagic MIs (2 lateral, 1 anteroseptal, and 1 inferior lateral). A representative set of MR images acquired on day 3 and 6 months post-PCI from a patient with hemorrhagic MI is shown in Figure 7.1A. Relative to the remote myocardium, significant T_2* decreases were observed in the acute infarct territories in eleven patients and remained reduced on the 6-month follow up images. On day 3 MRI, all the imaging slices that showed significant T_2* losses within the infarcted territories, also showed MO on the corresponding LGE images. In the four patients negative for hemorrhage on day 3, T_2* values of the infarct zones were similar to the remote territories on the 6-month follow up scans. Comparison of in-vivo T_2*_{slice} among the different groups obtained during the acute and chronic phases of MI showed that T_2* of Hemo+ (44 slices

from acute phase and 40 slices from chronic phase) was significantly lower than those of the other groups ($p<0.001$; Figure 7.1B); while T_2*_{Slice} values of remote (70 slices from acute phase

Parameter	Hemorrhagic (n=11)		Non-hemorrhagic (n=4)		p-value
Age* (years)	52±11		60±9		0.14
Male Sex, n (%)	9 (81)		3 (75)		0.02
Diabetes Mellitus, n (%)	0 (0)		2 (50)		0.005
Smoking History, n (%)	9 (81)		1 (25)		0.19
Hypertension, n (%)	0 (0)		2 (50)		0.005
Hyperlipidemia, n (%)	0 (0)		1 (25)		0.001
Time from symptoms to reperfusion (hours), median (range)	5.2 (1.9 – 11.7)		3.8 (2.1 – 5.3)		0.27
TIMI flow pre-PCI, n (%) **Grade 0** **Grade 1** **Grade 2**	 5 (46) 3 (27) 3 (27)		 2 (50) 2 (50) 0 (0)		 0.87
TIMI flow post-PCI, n (%) **Grade 3**	 11 (100)		 4 (100)		 —
LV Remodeling Index	**Day 3 post-PCI**	**Month 6 post-PCI**	**Day 3 post-PCI**	**Month 6 post-PCI**	
LV End-Diastolic Volume Index* (ml/m^2)	62.7±7.7	74.2±5.4	51.9±4.6	52.9±10.0	
LV End-Systolic Volume Index* (ml/m^2)	31.9±8.9	40.1±7.8	26.0±3.7	23±4.6	
LV Ejection Fraction* (%)	46.2±5.1	40.6±13.1	51.0±6.4	55.2±3.6	
LV End-Diastolic Sphericity Index*	0.44±0.14	0.51±0.17	0.46±0.12	0.43±0.06	
LV Mass Index* (g/m^2)	95.5±13.8	86.6±15.6	85.8±15.5	79.5±16.2	
Infarct Volume (%LV)	17.6±5.7	12.6±5.5	10.4±3.7	7.4±2.7	
Hemorrhage Volume (%LV)	5.0±3.2	2.1±1.6	0	0	

†NS – Non-significant; Data are reported as mean ± SD, except when noted otherwise.

Table 7.1: Patient clinical features and LV morphological and functional characteristics following PCI

and 64 slices from chronic phase) and Hemo- (26 slices from acute phase and 24 slices from chronic phase) tissue groups were not different ($p = 0.51$). T_2*_{Heart} values of remote, Hemo- and Hemo+ tissues did not differ significantly between acute and chronic phases (remote: $p = 0.21$;

Hemo-: p = 0.12; Hemo+: p = 0.19). On average, 40% reduction was observed in T_2* of Hemo+ regions compared to the control regions – remote and Hemo-. In-vivo T_2*_{Heart} values from these tissues on day 3 and month 6, regressed against one-another showed a strong correlation ($y = 0.79x + 5.85$, where y is T_2*_{Heart} at month 6 and x is T_2*_{Heart} on day 3; $R^2 = 0.7$; $p<0.001$; Figure 7.1C).

7.4.2. Morphological and Functional Characteristics of LV in Patients post-PCI

Compared to the patients with Hemo- MIs, patients with Hemo+ MIs had larger LV mass index, larger %Infarct volume, larger EDV, larger ESV and lower EF at both acute (day 3) and chronic (month 6) phases post-PCI (Table 7.1; $p<0.001$ for all cases). There was no significant difference between the EDSI of patients with Hemo+ and Hemo- MIs at 3 days post-PCI ($p = 0.31$). However, EDSI of patients with Hemo+ MIs was significantly higher than that of patients with Hemo- MIs at 6 months post-PCI ($p<0.001$).

Between the acute and chronic phases, LV mass index and %Infarct volume decreased in patients with both Hemo+ and Hemo- MIs ($p<0.001$ for all cases). Patients with Hemo- MIs had no significant difference in EDV between day 3 and month 6 post-PCI ($p = 0.14$), but there was a significant decrease in ESV ($p = 0.024$) and a significant increase in EF ($p = 0.013$). In contrast, patients with Hemo+ MIs ($p = 0.14$) had significant increases in EDV and ESV ($p<0.001$ for EDV and $p = 0.007$ for ESV), and a significant decrease in EF ($p = 0.01$) between the acute and chronic phases. EDSI of patients with Hemo- MIs was not significantly different between the acute and chronic phases ($p = 0.09$), but EDSI of patients with Hemo+ MIs increased significantly ($p = 0.02$). Among the patients with Hemo+ MIs, %Hemo volume decreased significantly between the acute and chronic phases ($p = 0.003$).

Multivariable regression analysis showed that both %Infarct volume and %Hemo volume measured at 3 days post-PCI were significant predictors of change in EDSI between the acute and chronic phases (%Infarct volume: $\beta = 1.59$, $p = 0.018$; %Hemo volume: $\beta = 2.02$, $p = 0.026$). Simple regression analysis showed that %Hemo volume measured at 6 months post-PCI is a significant predictor of percentage change in EDSI between the acute and chronic phases ($\beta = 3.25$, $p = 0.018$). However, a separate multivariable regression analysis showed that only %Infarct volume measured at 6 months was a significant predictor of the change in EDSI between the acute and chronic phases ($\beta = 0.87$, $p = 0.015$). However, neither %Infarct volume nor %Hemo volume measured at both 3 days and 6 months post-PCI could predict changes in other LV remodeling parameters (EDV, ESV and EF).

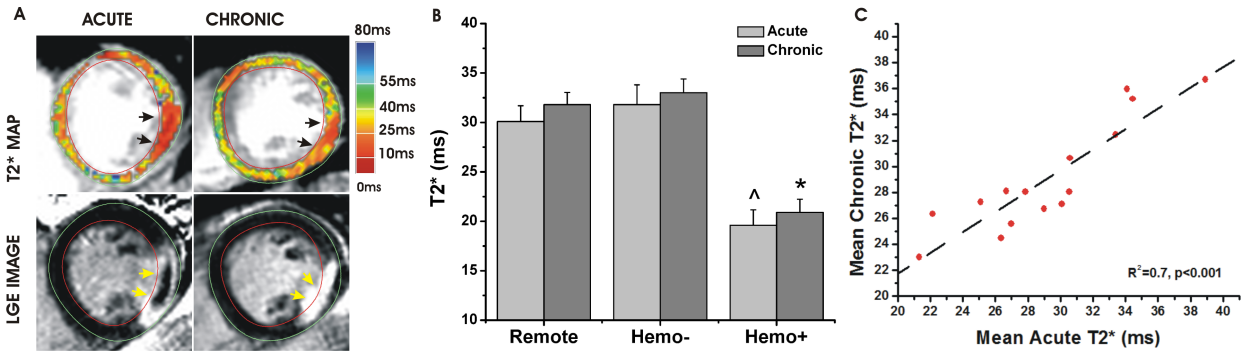

Figure 7.1: *Clinical T_2* MRI for detecting chronic iron deposition following hemorrhagic myocardial infarction in patients.* Representative MR images (acquired from a 42-year old patient following successful PCI) with significant T_2* loss (arrows) at the site of AMI and CMI (identified by LGE imaging, arrows) are shown (panel A). Mean T_2* of Hemo+ sections were significantly lower than those of remote and Hemo- sections (^,*, $p<0.001$) on both acute and chronic MRI studies (panel B). However, no difference was observed between T2* measures obtained from remote and Hemo- territories in both acute and chronic phases. No significant changes in T_2* were observed between acute and chronic phases in remote, Hemo-, and Hemo+ tissues. Linear regression analysis between T_2*_{Heart} measurements obtained on day 3 (acute) and month 6 (chronic) showed strong correlations (panel C).

7.4.3. Acute Reperfusion Hemorrhage Leads to Chronic Iron Deposition in Canine Hearts

7.4.3.1. MRI Studies

Four animals from the infarcted group died within the first two hours of establishing reperfusion despite rescue efforts. In two animals, reperfusion was not established due to occluder failure. These animals were excluded from the study. The remaining 14 animals from the infarcted group sustained acute hemorrhagic MIs as observed from the acute phase (day 3) MRI studies. Of these fourteen animals, three animals were sacrificed on day 3 for gross and histopathologic analysis of acute hemorrhagic MIs. The remaining eleven animals with I-R injury were allowed to recover into a chronic phase and underwent MRI on day 56, post reperfusion.

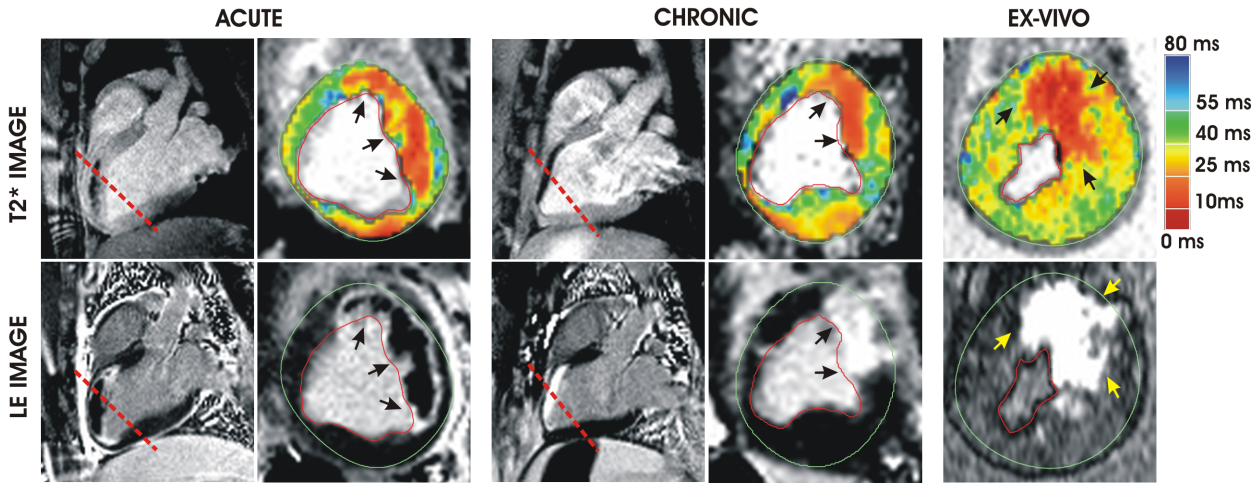

Figure 7.2: *T_2*-based MRI for detecting chronic iron deposition following hemorrhagic myocardial infarctions in a canine model*. Representative MR images (T_2* and LGE images) obtained during acute and chronic phases from a canine subjected to reperfused hemorrhagic MI along the long- and short-axis (along the dashed red line in the long-axis images), together with corresponding ex-vivo images are shown. In-vivo T_2* images (both acute and chronic phases) clearly demonstrate the evidence of signal loss in the LAD territory (arrows), where the hemorrhagic infarctions were expected to occur. Arrows in LGE images point to the site of MI. Note that the short-axis images are T_2* maps (color-coded) and the corresponding long-axis T_2* images are T_2*-weighted (TE = 18 ms).

Subsequently, the animals were sacrificed and tissue analysis was performed. The three sham animals survived the entire duration of the study and successfully underwent MRI studies on days 3 and 56, upon which the animals were sacrificed and the hearts were analyzed. All the data reported from canines in this manuscript (except the histology from acute MI) are from the Sham group and animals surviving I-R injury to day 56.

Representative T_2* maps and LGE images obtained from the acute phase (day 3), chronic phase (day 56) and ex-vivo MRI studies (post-euthanasia on day 56) are shown in Figure 7.2. Significant T_2* decreases were observable within the infarcted territories in both the acute and chronic phases. Consistent with the patient studies, all the imaging slices on day 3 MRI that showed significant T_2* losses within the infarcted territories, also showed MO on the corresponding LGE images. In-vivo T_2*_{slice} values of Hemo+ territories (33 slices from acute phase and 31 slices from chronic phase) were significantly lower than those of the control groups at acute and chronic phases ($p<0.001$ for both the cases; Figure 7.3A). In-vivo T_2*_{Slice} values between Hemo- (23 slices from acute phase and 22 slices from chronic phase), remote (56 slices from acute phase and 53 slices from chronic phase), and sham (20 slices from both acute and chronic phases) groups were not different (remote vs. sham: $p = 0.72$; remote vs. Hemo-: $p = 0.81$) during both acute and chronic phases. No significant differences in in-vivo T_2*_{Heart} of Hemo-, remote and sham territories were observed between acute and chronic phases (Hemo-: $p = 0.34$; remote: $p=0.35$; sham: $p = 0.26$); but there was a small but significant decrease in in-vivo T_2*_{Heart} of Hemo+ territories in the chronic phase at $p<0.05$ level ($p = 0.03$).

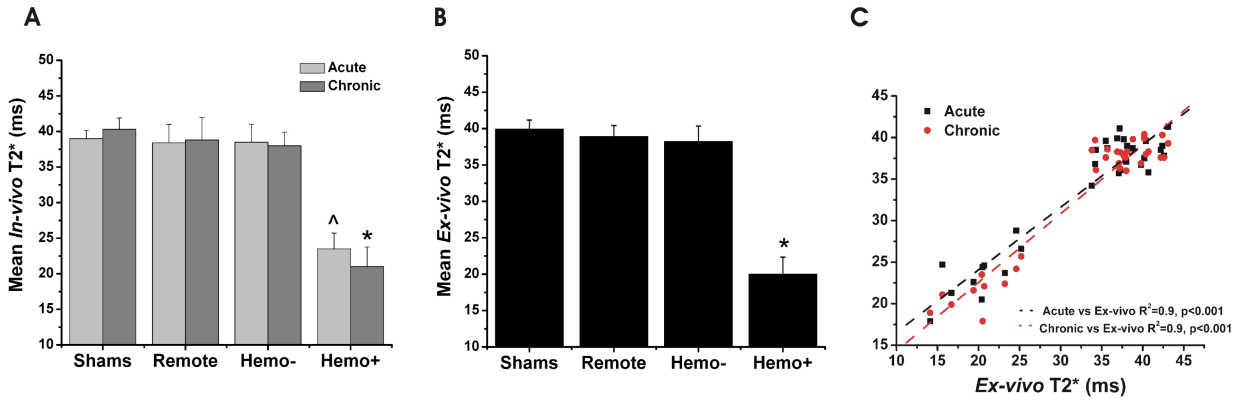

Figure 7.3: *T_2*-MRI guided characterization of regional iron deposition following hemorrhagic myocardial infarction in canine model.* Mean in-vivo T_2* of Hemo+ infarct sections was significantly lower than those of shams, remote, and Hemo- in both acute and chronic phases (^ and *, p<0.001, panel A). There was a small but significant decrease in in-vivo T_2* of Hemo+ infarct between day 3 and day 56 post-MI (p = 0.03). Mean ex-vivo T_2* of Hemo+ infarct sections was significantly lower than those of shams, remote, and Hemo- (*, p<0.001, panel B). Linear regression analysis between in-vivo T_2*_{Heart} (acute and chronic) and ex-vivo T_2*_{Heart} showed strong correlations indicating that ex-vivo T_2* provides a reasonable estimate of in-vivo T_2*_{Heart} (panel C).

Comparison of mean ex-vivo T_2*_{Slice} among the different groups showed that only Hemo+ was significantly different from the control groups (p<0.001; Figure 7.3B). In-vivo T_2*_{Heart} values from these tissues on days 3 and 56, regressed individually against ex-vivo T_2*_{Heart} estimates, showed very strong correlations ($y_1 = 0.52x + 16.18$, R^2=0.7; $y_2 = 0.56x + 14.89$, R^2=0.9, where y_1 is in-vivo T_2*_{Heart} on day 3, y_2 is in-vivo T_2*_{Heart} on day 56 and x is ex-vivo T_2*_{Heart}; p<0.001 for both cases; Figure 7.3C). Similar to patients, on average, a 40% decrease in T_2* was observed in regions of hemorrhagic MIs compared to the control groups at 1.5T.

7.4.3.2. Histopathology

Representative histopathological images of AMIs and CMIs are shown in Figure 7.4. Myocardial tissue analysis from animals sacrificed on day 3 showed that I-R injury showed large MIs evidenced by positive staining in TTC with internal bleeding at the core of the MI (Figure 7.4A). H&E stains confirmed the tissue damage and morphological alterations in regions positive for MI in TTC staining (Figure 7.4–A1). H&E stains also showed extravasation of RBCs into the interstitial space of the infarcted regions. Perl's stains confirmed a local accumulation of iron within the infarcted areas (Figure 7.4–A3). Hemorrhagic MIs in the chronic phase, on TTC staining, showed a visually evident yellowish-brown discoloration extending from the endocardial border to the core of the infarct (Figure 7.4B). H&E stains from the same tissue (Figure 7.4–B1) confirmed the presence of extensive tissue damage and Masson's Trichrome stain (Figure 7.4–B2) showed extensive collagenous tissue in the infarct zone. Perl's stain of corresponding myocardial territories showed a persistent and heterogeneous deposition of iron within the MI (Figure 7.4–B3). Iron was also found to be inter-spread among viable cells and intact blood vessels (lower inset of Figure 7.4–B3 obtained from infarct border). For a given stain, remote (non-infarcted) tissue sections were similar between acute and chronic phases, but were markedly different in infarcted tissue sections (Figures 7.4–A4 to A6, B4 to B6). The monoclonal antibody Mac387 staining of CMIs showed that newly recruited monocytes were highly co-localized with the chronic iron deposits identified on Perl's stain (Figure 7.5). Minimal/no monocyte activity was observed in the infarcted myocardial territories that were devoid of iron deposits. This suggested that there was an active and prolonged inflammatory process associated with chronic iron deposition within infarcted territories.

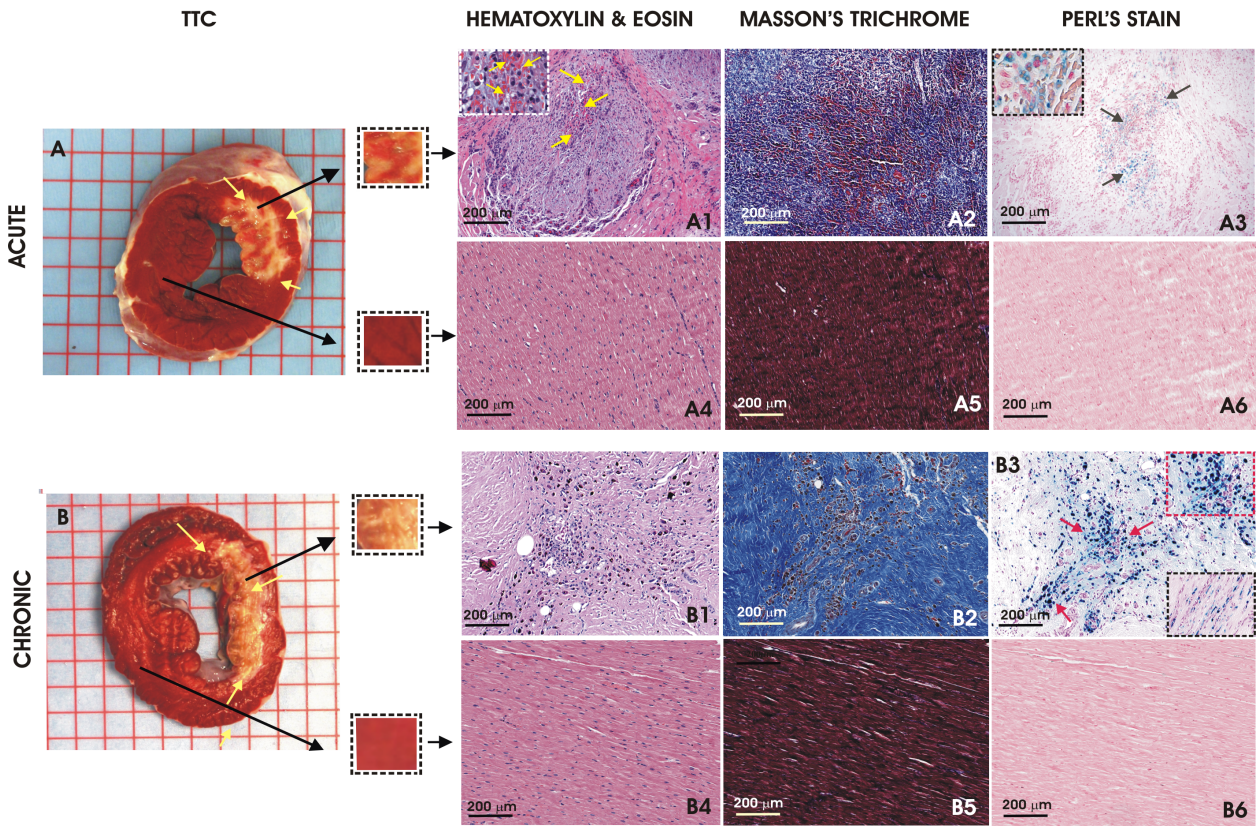

Figure 7.4: *Histological validation of chronic iron deposition in hemorrhagic myocardial infarction*. Gross histochemical staining (TTC) of short-axis sections of hearts shows the site of MI (pale color, yellow arrows) following acute (panel A) and chronic (panel B) reperfusion injury. The acute section shows blood within the necrotic tissue and the chronic section shows yellow-brown stain extending from the endocardial border to the core of the necrotic/scar tissue. Microstructural histopathology (100X magnification) of acute infarct (panels A1-A6) and corresponding remote sections show extravasation of RBCs (H&E, yellow arrows, inset), early deposition of collagen (Masson's Trichrome) and iron (Perl's stain, black arrows, inset) in the infarcted section (not observed in remote territories). Histopathology (100X magnification) of chronic infarct (panels B1-B6) and corresponding remote sections show grossly damaged myocardium (H&E), dense deposition of collagen (Masson's Trichrome) and iron (Perl's stain, black arrows, inset) in the infarcted section (not observed in remote territories). Insets show detailed views of tissue structures collected from regions indicated by arrows. Note the presence of iron mixed in with viable cells and intact blood vessels (lower inset of panel B3 obtained from infarct border).

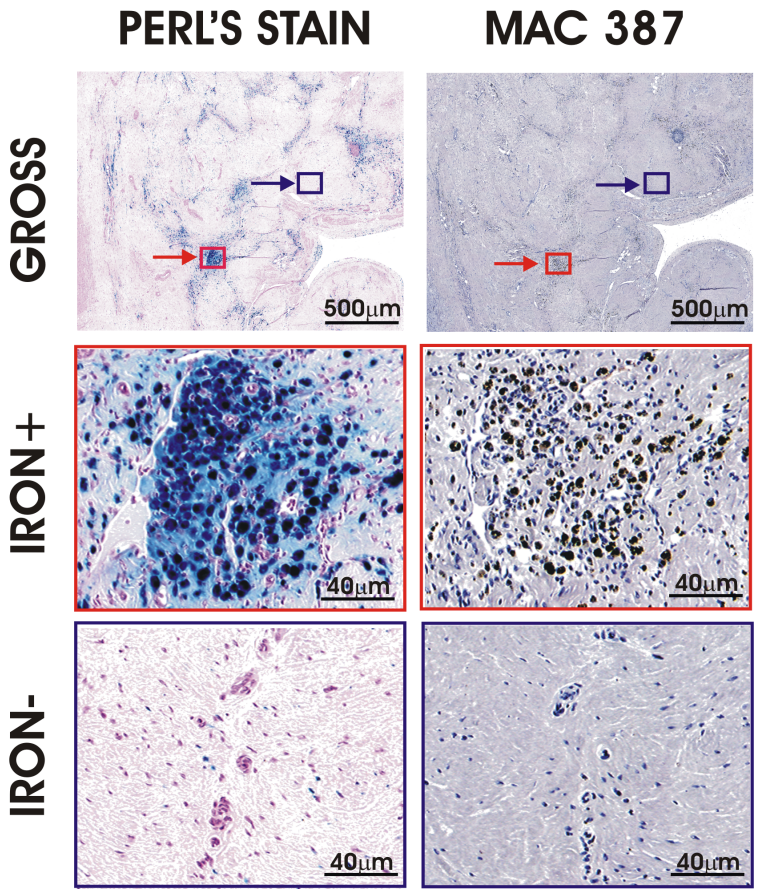

Figure 7.5: *Co-localization of newly recruited young monocytes with chronic iron deposits.* Contiguous histological sections of a chronic hemorrhagic infarction stained with Perl's stain and the monoclonal antibody Mac387 are shown. Newly recruited young monocytes are highly co-localized with the iron deposits throughout the infarct (GROSS). Magnified regions with (IRON+; red box) and without (IRON-; blue box) iron depositions show that young monocytes preferentially co-localize at the site iron depositions.

7.4.3.3. Mass Spectrometry

ICP-MS data showed that the mean iron content in Hemo+ samples ($[Fe]_{Sample}$) was significantly elevated compared to the Hemo-, remote and sham samples ($p<0.001$; Figure 7.6A). However, no significant differences in the mean iron content were observed among sham, remote and

Hemo- groups (remote vs. sham: p = 0.67; remote vs. Hemo-: p = 0.31). Regressions between ex-vivo T_2*_{Heart} estimates and tissue iron content ($[Fe]_{Heart}$) also showed a strong correlation (log (ex-vivo T_2*_{Heart}) = –0.26log ($[Fe]_{Heart}$)+1.21; R^2 = 0.7; p<0.001; Figure 7.6B).

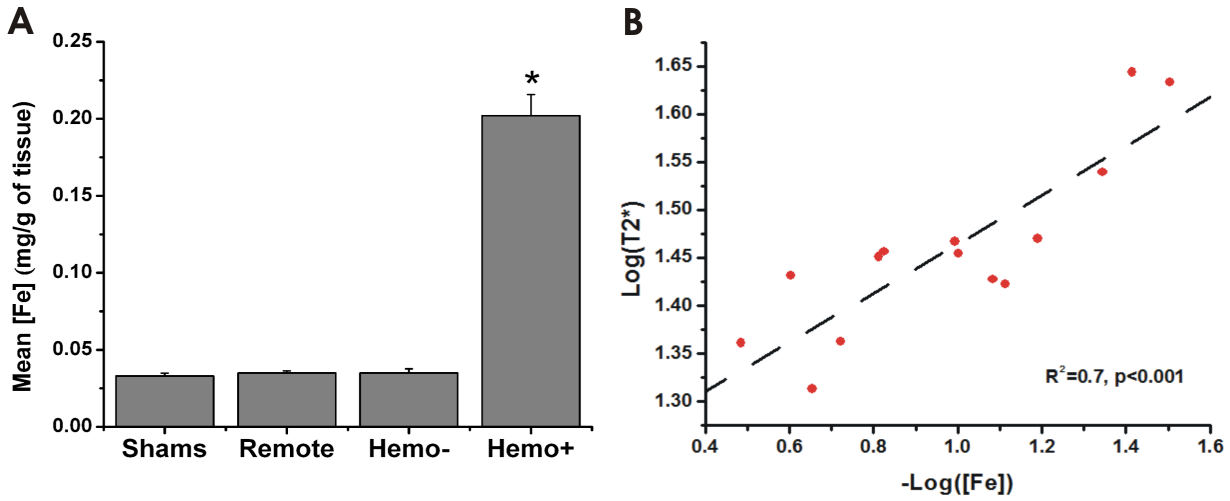

Figure 7.6: *Mass spectrometric validation of T_2*-based MRI for evaluating changes in regional myocardial iron content post reperfused infarction*. Myocardial tissue obtained from shams, remote, Hemo-, and Hemo+ sections on day 56 post reperfusion (chronic) showed significantly higher amount of iron in Hemo+ compared to all other sections (*, p<0.001, panel A). Linear regression analysis between ex-vivo log(T_2*_{Heart}) and -log($[Fe]_{Heart}$) showed a strong correlation (p<0.001, panel B).

7.4.4. Morphological and Functional Characteristics of LV in Canines Following I-R Injury

Consistent with the patient studies, LV mass index, %Infarct volume and %Hemo volume decreased significantly between acute (day 3) and chronic (day 56) phases post reperfusion (Table 7.2; p<0.001 for both cases). EDV, ESV and EDSI increased significantly between the acute and chronic phases (EDV: p = 0.034; ESV: p = 0.012; EDSI: p = 0.008), while EF decreased significantly (p = 0.021).

Parameter	Day 3 post-reperfusion* (n = 11)	Day 56 post-reperfusion* (n = 11)
LV end-diastolic volume index (ml/m^2)	64.9±10.0	68.6±9.6
LV end-systolic volume index (ml/m^2)	32.9±9.1	37.1±8.7
LV ejection fraction (%)	49.6±8.2	43.6±8.5
LV end-diastolic sphericity index	0.48±0.08	0.54±0.11
LV mass index (g/m^2)	60.6±5.1	49.5±3.2
Infarct Volume (%LV)	28.0±15.3	21.2±14.2
Hemorrhage Volume (%LV)	7.1±5.0	2.3±1.4

***Data are reported as mean ± SD

Table 7.2: Morphological and functional characteristics of LV in canines following I-R injury

Consistent with the patient studies, multivariable regression analysis showed that both %Infarct volume and %Hemo volume measured at 3 days post-reperfusion were significant predictors of percentage change in EDSI between acute and chronic phases (%Infarct volume: $\beta = 0.81$, $p = 0.014$; %Hemo volume: $\beta = 1.82$, $p = 0.034$). Simple regression analysis showed that %Hemo volume measured at 56 days post-reperfusion is a significant predictor of percentage change in EDSI between acute and chronic phases ($\beta = 2.82$, $p = 0.031$). However, a separate multivariable regression analysis showed that only %Infarct volume measured at 56 days post-reperfusion was a significant predictor of percentage change in EDSI between acute and chronic phases ($\beta = 0.76$, $p = 0.039$). However, neither %Infarct volume nor %Hemo volume measured at both 3 days and 56 days post-reperfusion could significantly predict changes in other LV remodeling parameters (EDV, ESV and EF).

7.5. Discussion

To date, the specific long-term consequence of hemorrhagic transformation of MI in humans was unknown. This study investigated whether patients suspected of having hemorrhagic MIs were disposed to regional iron depositions within the myocardial scar months after the MI, and whether such iron deposition can be reliably characterized using T_2*-based MRI. Supported by the validation studies in canines, in a pilot investigation this study has demonstrated that chronic iron deposition could take place in humans following acute hemorrhagic MIs, and such iron deposition can be characterized using T_2*-based MRI. Mass spectrometric analysis of canine myocardial tissue has shown that the mean iron content within the hemorrhagic MIs to be nearly an order of magnitude greater in a chronic phase (8 weeks) following MI compared to remote/healthy and non-hemorrhagic myocardium. In relating the mass spectrometric findings to ex-vivo MRI, the non-invasive imaging studies have shown that T_2*-based MRI can detect and quantify the extent of iron deposition within chronic hemorrhagic MIs. These observations also provided a firm basis for non-invasively characterizing chronic iron depositions following acute hemorrhagic MIs in canines in-vivo. Volumetric MRI data from both patients and canines has shown that both relative infarct and hemorrhage volume in the acute phase were significant predictors of LV remodeling on the basis of sphericity index in the chronic period following MI. In addition, immunohistological staining for newly recruited monocytes has shown an ongoing inflammatory response in the infarct tissue with iron deposits in the chronic phase of hemorrhagic MIs.

7.5.1. Detection of Regional Iron Deposition Following Hemorrhagic Myocardial Infarctions

Current knowledge of pathological iron deposition in the heart has been limited to global iron overloading in the heart due to hematological disorders such as thalassemia, hemochromatosis, and sickle-cell anemia. In a number of these settings, T_2*-based MRI has been shown to be invaluable for quantifying the global extent of iron in the heart. In particular, a recent study clearly demonstrated that the magnitude of T_2* is strongly correlated with the amount of iron deposition (measured on the basis of ICP-MS) in post-mortem hearts of deceased thalassemia patients (337). To date, however, there has been no direct evidence of significant localized deposition of iron in the heart. In this study, reperfused hemorrhagic MIs have been identified as a new etiology associated with highly localized iron deposition in the heart that can characterized on the basis of T_2*-based MRI. These findings are consistent with previous observations of the deposition of iron in other organs in the form of hemosiderin (magnetite - crystalline Fe_3O_4 particles) following the biodegradation of RBCs (285,447) that are also detected on the basis of T_2* MRI.

Both T_2*-weighted and T_2-weighted MRI techniques have been used to detect acute reperfusion intramyocardial hemorrhage (141,188,196,198,199,291,293,442,463). Following intramyocardial hemorrhage, oxyhemoglobin in the RBCs extravasated into the myocardial interstitium is slowly converted into paramagnetic forms such as deoxyhemoglobin and methemoglobin in the acute phase of MI (285). The current study has shown that, in the chronic phase of MI (ie. months after MI), iron from the extravasated RBCs is externalized and crystallized to form the highly paramagnetic hemosiderin deposits. These paramagnetic agents

induce local magnetic field inhomogeneities that appear as hypointense territories on both T_2*-weighted and T_2-weighted images (286,465).

Although T_2*-based MRI is highly sensitive to chronic myocardial iron depositions within the infarcted territories, it is also sensitive to the magnetic susceptibility differences at the heart-lung interface (off-resonance artifacts) that manifest as hypointense regions in the infero-lateral walls. Therefore, off-resonance artifacts occurring in the infero-lateral walls may be misinterpreted as hemorrhagic MIs. However, it is possible to distinguish hemorrhage from the off-resonance artifacts since hemorrhage originates in the subendocardium and is limited to the infarcted myocardium, while off-resonance artifacts originate at the epicardium (293). In this study, off-resonance artifacts were easily identified in both patients and canines, and did not limit the ability to identify hemorrhage.

7.5.2. Long-term Consequences of Regional Iron Deposition within Infarcted Myocardium

The pathological consequence of regional iron deposition in the chronic phase of the hemorrhagic MIs was also unknown prior to this study. In this study, immunohistochemical staining with Mac387 showed that infiltration of young monocytes is preferentially enhanced at the site of iron deposition within CMIs, with minimal/no monocytes within the infarcted territories without iron. The monoclonal antibody Mac387 detects the calcium-binding protein MRP14 that is selectively expressed by young monocytes newly recruited from peripheral blood, but have not matured yet into tissue macrophages (466,467). Frangogiannis et al have used Mac387 to index for active inflammatory process in the heart. They showed that Mac387+ cells extensively infiltrate the infarcted territories within 1 hour of I-R injury, but very few Mac387+ cells are found after 7 days of I-R injury (468). Hence the findings of this study suggest that

chronic iron deposition following acute reperfusion intramyocardial hemorrhage leads to an active and prolonged inflammatory process. The selective recruitment of Mac387+ cells to the zones of chronic iron deposition within infarcted territories may be one of the potential mechanisms through which hemorrhagic MIs lead to adverse LV remodeling. Nevertheless, additional studies are necessary to understand the relation between long-term inflammation in the presence of iron deposition and cardiac remodeling.

Iron deposition within infarcted myocardium has also been reported in the setting of iron-labeled regenerative cell therapies (469). It was shown that when iron-labeled stem cells are delivered to the site of MI, even after a few weeks of delivery, the iron particulates (label) continue to persist at the site of MI. However, the iron labels were co-localized within macrophages instead of the stem cells, suggesting that once the transplanted cells perished, the macrophages are drawn to the site of remnant iron particulates. The current data, along with the previous reports (469), suggests that monocytes that can potentially mature into macrophages are drawn to the site of iron regardless of its origin (endogenous or exogenous). Previous studies have also suggested that iron particulates mediate activation of microglia in the brain (470) and differentiation of blood monocytes into pro-inflammatory macrophages (471). Moreover, hemoglobin-derived iron in combination with activated macrophages has been shown to generate reactive oxygen species in chondrocytes (472). While these observations have not been extended into myocardial tissue, the highly selective recruitment of young monocytes at the site of iron deposition suggests that the mechanism of monocyte recruitment to the site of CMI may be similar. Since T_2* of hemorrhagic infarcts appears to be stable between acute and chronic phases in both animals and patients, it appears that iron depositions from hemorrhagic MIs are at best only slowly cleared by the macrophages evolving from the monocytes. Additional studies are

necessary to investigate the temporal dynamics of macrophage-based clearance of iron within infarcts. From the imaging studies in humans in this study, it appears that the clearance takes more than six months given that at the six-month follow-up, significant T_2* shortening was evident at the site of hemorrhagic MI compared to non-hemorrhagic infarct territories or remote/healthy myocardium. Since T_2* data was significantly correlated with direct measurements of iron in tissue (mass spectrometry analysis), clinical T_2*-based MRI is well positioned for the assessment of changes in iron deposition in the post-MI period.

This study has shown that in both humans and animals with hemorrhagic MI, LV remodeling (indexed on the basis of EDSI) between the acute and chronic phases of the MI was significantly impacted by %infarct and hemorrhage volume. While the effect of infarct size on LV remodeling has been well known (107,405,406), this study has shown that hemorrhage volume is a strong predictor of EDSI as well. In fact, the respective beta coefficients from multivariable regression analyses further suggest that the %hemorrhage volume in the acute phase, in both humans and canines, has a greater influence on EDSI ($\beta = 2.02$ (humans) and $\beta = 1.82$ (canines)) than infarct volume in the acute phase ($\beta = 1.59$ (humans) and $\beta = 0.8$ (canines)). Nevertheless, other LV remodeling parameters such as EF, EDV and ESV did not reach statistical significance to show dependence on %infarct or hemorrhage volume. Further studies supported by larger sample sizes are expected to be necessary to resolve these differences.

7.5.3. Study Limitations

This study has certain limitations. First, the definition of hemorrhagic myocardium as the infarcted regions with low signal intensity on T_2*-weighted images itself implies that the T_2* values of hemorrhagic myocardium is significantly lower than those of other tissues.

Nevertheless, Perl's staining and mass spectrometry clearly validated that hemorrhagic myocardium defined on the basis of low T_2* values had significantly higher iron depositions. This study has also shown that MIs with low T_2* values in the acute phase had a concomitantly low T_2* values in the chronic phase, as well. Secondly, the sample size in this study was small, which may have limited the modest differences from being detected due to insufficient power. While this could partly explain why the impact of %infarct or %hemorrhage volumes on commonly reported LV remodeling parameters such as EDV, ESV and EF could not be detected, the relationship between %infarct and %hemorrhage volume on EDSI could be still discerned. Moreover, further studies are necessary to evaluate the relative effects of MO and hemorrhage on post MI LV remodeling. Thirdly, the MI in animals was only created in the LAD territory. While we expect our results to hold independent of the territory of hemorrhagic MI, additional studies are necessary to confirm whether our findings can be extended to all territories of the myocardium. Finally, while we were able to validate our findings of iron deposition within hemorrhagic infarcts in animals on the basis of histological and mass spectrometry analysis, the evidence for iron deposition in patients with hemorrhagic MIs is only based on T_2*-based MRI. Nevertheless, since the MRI results between animals and patients were consistent, and since chronic iron deposition following hemorrhagic MIs showed significant correlation against T_2*-based MRI in animals, we anticipate that T_2*-based MRI is a reliable alternative for the assessment of iron deposition in patients. Similarly, histopathological findings of prolonged inflammation are also limited only to hemorrhagic MIs in canines. Additional histopathological and mass spectrometric analysis of human hearts with chronic hemorrhagic MIs may be necessary to rigorously extend these findings to humans.

7.6. Conclusion

Hemorrhagic MI can lead to iron depositions within the infarct zones, which can be reliably characterized using T_2*-based MRI. Such chronic iron depositions can be a source of adverse LV remodeling and prolonged inflammatory burden in the chronic phase of MI.

CHAPTER 8

Iron Deposition within Chronic Myocardial Infarctions as a Substrate for Cardiac Electrical Anomalies: Initial Findings in a Canine Model

8.1. Abstract

In the previous chapter, localized chronic iron deposition within MI territories has been shown to occur following acute reperfused intramyocardial hemorrhage, and such iron depositions can be reliably characterized using T_2*-based MRI. The purpose of this study is to investigate whether such focal iron deposition within CMI leads to electrical anomalies. Two groups of dogs (ex-vivo (n = 12) and in-vivo (n = 10) were studied at 16 weeks following I-R injury. Hearts of animals from ex-vivo group were explanted and sectioned into infarcted and non-infarcted segments. Impedance spectroscopy was used to derive electrical permittivity ($\bar{\varepsilon}$) and conductivity ($\bar{\sigma}$). Mass spectrometry was used to classify and characterize sections with (IRON+) and without (IRON-) iron. Animals from in-vivo group underwent cardiac MRI for estimation of scar volume (LGE) and iron deposition (T_2*) relative to LV volume. 24-hour ECG recordings were obtained and used to examine heart rate (HR), QT interval (QT), QT corrected for HR (QTc), and QTc dispersion (QTcd). In a fraction of these animals (n = 5), ultra-high resolution electroanatomical mapping (EAM) was performed, co-registered with LGE and T_2* MRI, and were used to characterize the spatial locations of isolated late potentials (ILPs).

Compared to IRON- sections, IRON+ sections had higher $\bar{\varepsilon}$, but no difference in $\bar{\sigma}$. A linear relationship was found between iron content and $\bar{\varepsilon}$ ($p<0.001$), but not $\bar{\sigma}$ ($p = 0.34$). Among two groups of animals (Iron(<1.5%) and Iron(>1.5%)) with similar scar volumes (7.28±1.02% (Iron(<1.5%)) vs. 8.35±2.98% (Iron(>1.5%)), $p = 0.51$) but markedly different iron volumes (1.12±0.64% (Iron(<1.5%)) vs. 2.47±0.64%(Iron(>1.5%)), $p = 0.02$), QT and QTc were elevated, and QTcd was decreased in the group with the higher iron volume during the day, night, and 24-hour period ($p<0.05$ for all cases). EAMs co-registered with MR images showed a greater tendency for isolated late potentials (ILPs) to emerge from scar regions with iron versus without iron. In conclusion, the electrical behavior of infarcted hearts with iron appears to be different from those without iron. Iron within infarcted zones may evolve as an arrhythmogenic substrate in the post-MI period.

8.2. Introduction

The electrical behavior of chronically infarcted myocardium is not well understood. Conventionally, infarcted myocardium is identified on electroanatmoical maps (EAMs) on the basis of significantly reduced bipolar voltage (< 0.5 mV) (473,474). While a significant portion of the scarred myocardium is thought to be electrically inert, the presence of non-zero voltage points within the infarct zone has been associated with surviving myocytes (475,476). However, several other studies have shown direct evidence for significant passive electrical activity within the dense scar that is free of viable myocytes (477,478). Nevertheless, the substrate mediating the electrical activity within the infarcted tissue devoid of surviving myocyte bundles remains to be explored.

Observational studies in patients with pathological iron (hemosiderin) overloading in the heart, from non-ischemic origins (hemochromatosis (453,454), thalassemia (337,455), siderosis (479), and sickle-cell anemia (336)), have long documented evidence of significant incidence of ventricular arrhythmias (459,461,480,481). Imaging studies in the same patient population have also suggested that the incidence of arrhythmias to be directly related to the extent of myocardial iron deposition (461). Moreover, carefully controlled animal studies have shown that cardiac iron overloading leads to progressively worsening electrical conductivity with increasing iron (hemosiderin) deposition, even in the absence of myocardial contractility changes (480). Notably, these studies showed that approximately 1 in 3 animals with chronic iron overloading succumbed to SCD attributable to cardiac arrhythmias. More recently, MRI based histological examination of human hearts of SCD victims have shown significant loss of T_2-weighted signals within the chronic infarcted territories, consistent with hemosiderin accumulation (482,483).

The relationship between myocardial iron deposition and electrical changes may be explored on the basis of existing biophysical findings. It has been shown that the introduction of highly conductive particulates (such as magnetite with conductivity of 2.5×10^4 S/m at the physiologic temperature (484)) into an otherwise poor dielectric medium (such as the myocardium with conductivity < 1 S/m (485)) acts to enhance the bulk electrical permittivity of the medium (486,487). Hence, the pathological elevations of iron within localized regions of the heart may be a substrate that alters the electrical milieu of myocardial regions containing iron.

The previous chapter has demonstrated in humans and animals that chronic iron overloading within the scar tissue may occur following myocardial infarctions due to pooling of blood within the MI territories. Based on biophysical principles alone, it is expected that the electrical permittivity of post-infarction scar with iron deposits can be significantly greater than

those scars without iron deposits. If such changes in the electrical features of the infarcted myocardium manifest in the same manner as in the case of iron overloading from the non-ischemic pathologies, one is expected to observe global and local electrical changes that are different between infarcted hearts with and without iron depositions.

Through controlled experiments in canine models, this study investigates whether infarcts with chronic iron deposition, identified on the basis of ICP-MS, preferentially alters the electrical features of myocardial tissue in ex-vivo preparations. In addition, it also examines whether there are differences in global and local electrical characteristics of the infarcted hearts with different levels of iron deposition, determined on the basis of T_2*-based MRI. In particular, this study explores whether the established parameters derived from surface electrocardiograms (ECG) and EAMs are altered in a manner that is dependent on the extent of iron deposition determined by T_2*-based MRI.

8.3. Methods

8.3.1. Animal Preparation and Overview of Methods

Canines were studied according to the protocols approved by the Animal Care and Use Committee. MI was created by ligating the LAD for 3 hours followed by reperfusion in 22 dogs (20-25 kg). All canines were allowed to recover for 16 weeks following I-R injury. Canines were randomly assigned to one of the two groups: Group ex-vivo (n = 12) and Group in-vivo (n = 10).

In the Group ex-vivo, 10 animals survived into the chronic phase of MI and 2 animals died during the acute phase of MI. Animals from Group ex-vivo were sacrificed and their hearts were harvested, and sectioned into 1 cm thick slices. Infarcted and non-infarcted (Remote)

segments on each slice were delineated on the basis of ex-vivo TTC staining, and 0.5-0.8cm^3 samples of tissue were isolated from the respective segments. Representative samples were selected for histological staining (Perl's and H&E stains). Samples from infarcted segments were further classified as those with and without iron deposition (IRON+ and IRON- respectively) based on ICP-MS analysis (details below). Prior to ICP-MS analysis, bulk electrical impedance spectroscopy measurements were performed on tissue samples from all the three groups (IRON+, IRON- and Remote).

The animals from Group in-vivo were fitted with a Holter monitor and ECG measurements were recorded over a 24-hour period (details below). Subsequently the animals from this group underwent MRI studies (within a week of the ECG recordings) to determine the extent of iron deposition within the MI territories (details below). Following MRI exams, 5 animals from this group underwent ultra-high resolution endocardial LV electroanatomical mapping (EAM, details below).

8.3.2. Ex-vivo Bulk Electrical Impedance Measurements

The bulk electrical impedance of each tissue sample from the Group ex-vivo animals was measured using the two-terminal electrode technique as previously described by Schwan (488). A capacitor cell, consisting of two parallel square electrodes (each of 1.5 cm^2 surface area) with variable distance between them (489), was custom built to measure bulk electrical impedance of each sample using alternating-current (AC) impedance spectroscopy (Figure 8.1).

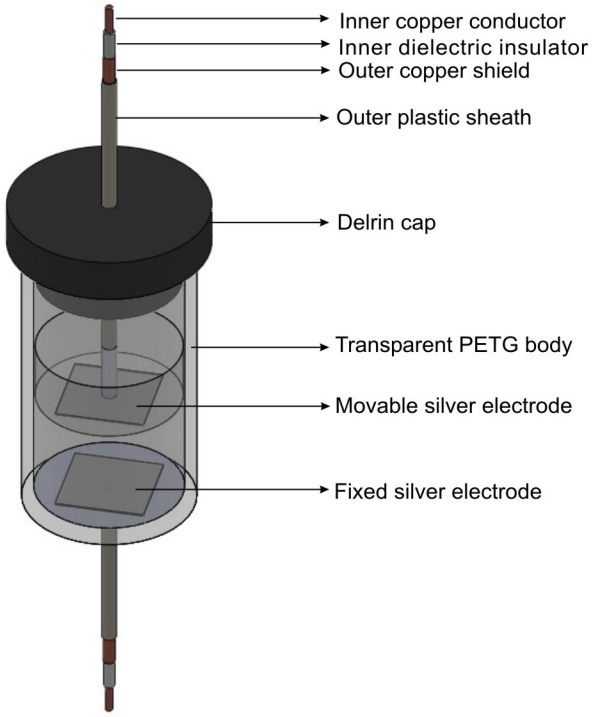

Figure 8.1: *Schematic three-dimensional drawing of a custom-made capacitor cell used for measuring bulk electrical impedance of ex-vivo tissue*. The capacitor cell consisted of a transparent tubular glycol-modified polyethylene teraphthalate body that is closed at one end and fitted with a removable Delrin cap at the other end. Two square silver electrodes, each of 1.5 cm^2 surface area, were enclosed in the tubular body. One electrode was affixed to the closed end, while the other electrode was affixed to a PETG disk that can move through the tubular body. The electrodes were soldered to the inner conductors of copper coaxial cables, which in turn were connected to the impedance analyzer. The outer conductors were connected to electrical ground.

Each sample was incubated at 37°C in phosphate buffer solution for 15 minutes prior to use. The sample was then sandwiched between the two electrodes of the capacitor cell and 10 μA of AC was passed parallel to the myocardial fibers. The voltage that developed across the sample was measured using Solartron 1260 impedance/gain-phase analyzer (Solartron Instruments,

Hampshire, UK) and acquired using ZPlot data acquisition software (version 3.3, Scribner Associates Inc., NC, USA). The induced voltage was divided by the current passed to derive the complex AC-impedance (Z in ohms) of the sample. The impedance values were measured at frequencies ranging from 100 Hz to 10 MHz with 10 measurements in each frequency decade. Stray effects in the measurements were corrected using methods described by Schwan (488). To minimize the effects of α-dispersion at lower frequencies (below 0.1 MHz) and β-dispersion (> 1 MHz) (490) from undesirable myocardial sample preparation errors (such as an partial volume effects due to samples containing both infarct region and surrounding viable myocardium), all analyses were limited to impedance data acquired at 1 MHz.

Bulk electrical permittivity and conductivity of each sample were derived from the AC-impedance measurements. Surface area (A in m^2) and distance between the electrodes (d in m) after the sample is placed between the electrodes were measured. The complex admittance Y (in siemens S) of the sample was calculated as the reciprocal of Z, which can be further expressed as follows (491).

$$Y = G + i\omega C \tag{8.1}$$

where G is the conductance (in S), C is the capacitance (in F), ω is the angular frequency (in rad/s) and i is $\sqrt{-1}$. *G* and *C* can be further expressed as follows.

$$G = \frac{A \times \sigma}{d} \tag{8.2}$$

$$C = \frac{A \times \varepsilon}{d} \tag{8.3}$$

where σ and ε are bulk conductivity (in S/m) and permittivity (in F/m) respectively. Bulk σ and ε of each sample were therefore calculated from the original complex impedance data (*Z*) as follows.

$$\sigma = \frac{\mathrm{Re}\left(\frac{1}{\overline{Z}}\right) \times d}{A} \tag{8.4}$$

$$\varepsilon = \frac{\mathrm{Im}\left(\frac{1}{\overline{Z}}\right) \times d}{A \times \omega} \tag{8.5}$$

For a given heart from an infarcted dog, mean conductivity (σ'_{Remote}) and permittivity (ε'_{Remote}) of its remote myocardium were calculated by weight-averaging the conductivities and permittivities of all of its constituent remote samples as follows.

$$\sigma'_{Remote} = \frac{\sum(\sigma_{Remote} \times W_{Remote})}{\sum W_{Remote}} \tag{8.6}$$

$$\varepsilon'_{Remote} = \frac{\sum(\varepsilon_{Remote} \times W_{Remote})}{\sum W_{Remote}} \tag{8.7}$$

where σ'_{Remote} and ε'_{Remote} are the individual conductivity and permittivity of each constituent remote sample of a heart and W_{Remote} is its corresponding sample weight. Normalized conductivity ($\bar{\sigma}_{Sample}$) and permittivity ($\bar{\varepsilon}_{Sample}$) of each IRON+, IRON- and Remote sample from the heart were then derived as follows.

$$\overline{\sigma}_{Sample} = \frac{\sigma_{Sample}}{\sigma'_{Sample}} \tag{8.8}$$

$$\overline{\varepsilon}_{Sample} = \frac{\varepsilon_{Sample}}{\varepsilon'_{Sample}} \tag{8.9}$$

Also, per-slice normalized conductivity ($\bar{\sigma}_{Slice}$) and permittivity ($\bar{\varepsilon}_{Slice}$) were calculated for the IRON+, IRON-, and Remote groups by weight averaging $\bar{\sigma}_{Sample}$ and $\bar{\varepsilon}_{Sample}$ respectively from their constituent samples.

8.3.3. Inductively Coupled Plasma – Mass Spectrometry

Iron deposition within each myocardial sample from Group ex-vivo ($[Fe]_{Sample}$ in mg per g of tissue) was measured using a quadrupole-based X Series 2 ICP-MS (Thermo-Fisher Scientific, USA). Infarcted sections with $[Fe]_{Sample} < 0.05$ mg/g of tissue were labeled as IRON- and those with $[Fe]_{Sample} \geq 0.05$ mg/g were labeled as IRON+. In all, 293 sections from a total of 11 dogs were analyzed, where 228 sections were infarcted and 67 sections were from non-infarcted sections.

8.3.4. Holter ECG Recordings and Surface ECG Analysis

24-hour Holter ECG recordings were made 16 weeks post MI in animals from Group in-vivo using a three-channel recorder (DigiTrak XT Holter Recorder, Philips Zymed Holter System, Philips Healthcare, MA, USA). The derived 12-lead ECG was recorded continuously using five adhesive leads placed (a) over the lower sternum, level with the fifth intercostal space; (b) at the level of the fifth intercostal space, on the left midaxillary line; (c) on the upper part of the sternum; (d) at the fifth intercostal space, on the right midaxillary line; and (e) on the manubrium of the sternum (reference/ground electrode).

All ECG recordings underwent automated retrospective analysis using the dedicated Holter software (DigiTrak XT Holter Recorder, Philips Zymed Holter System Philips Healthcare, MA, USA). The analyses of heart rate (HR) and repolarization parameters (QT interval and corrected QT interval) were performed after adjusting all recordings to the 24-hour clock. Only recordings with duration of 24 hours were considered for analysis. An operator blinded to the MR details of the infarct characteristics analyzed the Holter recordings. The morphology of the beats was monitored and only normal beats (sinus rhythm) were selected for

further analysis. ECG segments with excessive noise or artifact were eliminated from the analysis. The hourly mean values of each measurement were automatically calculated. QT intervals corrected for heart rate (QTc) were automatically calculated using Bazett's formula (492). QTc dispersion (QTcd) was computed as the difference between the maximum and the minimum QTc interval across the 12 derived leads.

8.3.5. MRI Studies and Image Analyses

MRI studies were performed on a clinical 3T system (MAGNETOM Verio, Siemens Medical Solutions, Erlangen, Germany). T_2*-weighted (multi-echo GRE; TR = 12 ms; 6 TEs = 2.0–9.5 ms with ΔTE = 1.5ms; α = 10°; BW = 930Hz/pixel) and LGE images (IR-prepared FLASH; TR/TE = 3.0/1.5 ms; α = 25°; BW = 586 Hz/pixel) of contiguous short-axis sections covering the entire LV and the three long-axis views were acquired at mid-diastole. Commonly used imaging parameters were: in-plane resolution = 1.3×1.3 mm^2, slice thickness = 6 mm and number of averages = 1.

Image analyses were performed using cmr[42] (version 4.0, Circle Cardiovascular Imaging Inc., Canada). Remote myocardium was defined as the region showing no hyperintensity on LGE images. A reference ROI was drawn in remote myocardium on both LGE and T_2*-weighted images. Infarcted territory was defined as the hyperintense region on LGE images using the Mean+5SD criterion relative to the reference ROI (414-416). An infarction with chronic iron deposition (IRON+) was defined as infarcted territory containing hypointense signal on the T_2*-weighted image acquired at TE of 6.5 ms using Mean-2SD criterion relative to the reference ROI (199,293). An infarction without iron deposition (IRON-) was defined as the region positive for infarction on LGE images, but negative for hypointense signal on the corresponding T_2*-

weighted images. The percentage of the infarcted myocardium (Scar Volume) and myocardium with chronic iron deposition (Iron Volume), were computed by summing up the respective slice measures and normalizing by the total LV volume.

8.3.6. Electroanatomical Mapping, Analysis, and Registration with MR Images

Electrophysiological studies were performed within 3-7 days of the MRI studies in 5 animals under general anesthesia and mechanical ventilation (protocol same as during MRI). The left femoral artery was cannulated, and a 64-electrode basket catheter (nominal diameter 18 mm) with 8 splines, each containing 8 tiny electrodes (0.4 mm^2) spaced at 2.5 mm, center-to-center (Rhythmia Mapping System, Boston Scientific, MA, USA) was introduced into the LV using the retro-transaortic approach. The catheter was used to generate ultra-high resolution endocardial contact electrograms (EGMs; within 2-3 mm spatial resolution). The surface geometry was mapped using the location of the outermost electrodes. Only EGMs recorded within 2 mm of the surface geometry were utilized. Scar areas were defined as bipolar voltage less than 1 mV (493).

At least three clinical electrophysiology experts analyzed the EAMs from each animal offline. Given the large number of data points within and surrounding the scarred myocardium, only points separated by 1.5-2 mm of one another were manually validated. The validation process included ensuring catheter contact and identifying and marking each point of interest for the presence or absence of isolated late potentials (ILPs). An ILP was defined as a voltage spike following an isoelectric interval observed after the end of the QRS complex (494-496).

The LGE and T_2* MRI data were registered with the EAMs using a custom-developed software (Rhythmia Medical, Boston Scientific, Boston, MA, USA). The registration process involved (a) manually segmenting the blood pool of both LGE and T_2* images; (b) constructing

a surface that encloses the segmented blood pool; and (c) manually registering both the LGE and T_2* blood pool surface to the EAM surface using anatomical landmarks (apex, papillary muscle grooves and aortic root). The gray scale MRI data was resampled at the vertices of the CMR blood pool mesh and displayed as a colored 3D surface with colors corresponding to signal intensity.

After registration with the EAMs, the T_2* blood pool mesh was used to manually count the number of ILPs occurring in and around the infarcted regions with and without iron. This information was used to derive values for the overall incidence of ILPs, which were computed as a percentage of ILPs from regions with and without iron relative to the total number of ILPs in the infarct territory. To examine the relationship between the number of ILPs and substrate type and extent, values normalized by the volume fraction of substrate type in each heart were computed and averaged across all animals. In particular, the following calculations were performed: (a) ILP counts from regions with iron normalized by Iron Volume; (b) ILP counts from regions without iron normalized by the percentage scar volume without iron (i.e. Scar Volume – Iron Volume); and (c) the total ILP count normalized by the percentage of total Scar Volume (with and without iron) relative to the total LV volume.

From the EAMs registered with T_2* images, number of ILPs occurring in and around the infarcted regions with and without iron were manually counted. This information was used to derive the overall incidence of ILPs, which was computed as a percentage of ILPs from regions with and without iron relative to the total number of ILPs. To examine the relationship between number of ILPs and substrate type and extent, values normalized by the volume fraction of substrate type in each heart were computed and averaged across all animals. In particular, the following calculations were performed: (a) ILP counts from regions with iron normalized by Iron

Volume; (b) ILP counts from regions without iron normalized by percentage scar without iron (i.e. Scar Volume – Iron Volume); and (c) the total ILP count normalized by Scar Volume (i.e. Scar Volume with and without iron).

8.3.7. Statistical Analyses

All statistical analyses were performed using IBM SPSS Statistics (version 21.0, IBM Corporation, Armonk, NY). A p value <0.05 was considered statistically significant. Bonferroni correction was used to adjust the significance level for multiple comparisons. Data normality was assessed using the Shapiro-Wilk test and quantile-quantile plots. Student's t-test or mixed-model ANOVA with Tukey's post-hoc analysis was used to compare data with normal distributions. For the mixed model, animals were entered as random effects, while repeated measurements from the same animal or heart were entered as fixed effects. Repeated measurements from a single animal or heart were nested. For comparing non-normal data, non-parametric Friedman's test was used. Mann-Whitney U test was used for pairwise comparisons among non-normal data.

For the canines from Group ex-vivo, $\bar{\sigma}_{\text{Sample}}$ and $\bar{\varepsilon}_{\text{Sample}}$ were compared among IRON+, IRON-, and Remote tissue sections. Mixed-model linear regressions were used to evaluate the relationships of $\bar{\sigma}_{\text{Sample}}$ and $\bar{\varepsilon}_{\text{Sample}}$ with $[\text{Fe}]_{\text{Sample}}$. A nonlinear regression analysis was used to examine the relationship between Iron Volume and Scar Volume.

In order to examine the effect of Iron Volume on the ECG parameters (HR, QT, QTc and QTcd) with minimal/no contribution from Scar Volume, animals were divided into two groups, those with Iron Volume <1.5% (denoted as Iron(<1.5%)) and those with Iron Volume >1.5% (denoted as Iron(>1.5%)). Only those animals that showed a direct relationship between Iron Volume and Scar Volume were included in the analysis (details below). Mean hourly, day (10:00

hours to 21:00 hours), night (21:00 hours to 09:00 hours) and 24-hour measurements of HR, QT, QTc, and QTcd were computed for Iron(<1.5%) and Iron(>1.5%) groups and compared, as above.

Regression analysis was used to assess the quality of the registration between MRI and EAMs on the basis of concordance between scar territories identified on LGE MRI and low voltage (<1 mV) vertices on bipolar EAMs. The incidence of ILPs was compared between scar regions with iron and without iron. The number of ILPs per volume of substrate for scars with only iron and without iron was also compared.

8.4. Results

8.4.1. Effect of Iron Deposition on the Ex-vivo Bulk Electrical Characteristics of Chronic Myocardial Infarctions

Of 228 infarcted sections, ICP-MS analysis identified 177 sections as IRON+ and the remaining 51 sections as IRON-. There was no significant difference in $[Fe]_{Sample}$ between IRON- and Remote samples ($p = 0.31$). A set of sample impedance spectra from IRON+, IRON-, and Remote sections from a canine are shown in Figure 8.2. Mean $\bar{\varepsilon}_{Sample}$ for IRON+ sections was approximately 25% higher than that of IRON- and Remote tissues ($p<0.001$), while $\bar{\varepsilon}_{Sample}$ of IRON- and Remote sections were not statistically different from 1 ($p = 0.69$; Figure 8.3A). Mean $\bar{\sigma}_{Sample}$ was not significantly different among the different tissue types (Remote vs. IRON+: $p = 0.46$; Remote vs. IRON-: $p = 0.77$; Figure 8.3B). Averaged across all studies, a mean increase in $\bar{\varepsilon}_{Sample}$ of Mixed-effects multi-linear regression analysis showed a statistically significant relation between $\bar{\varepsilon}_{Sample}$ and $[Fe]_{Sample}$ ($\bar{\varepsilon}_{Sample} = 1.34\ [Fe]_{Sample} + 0.93$; $p<0.001$; Table 8.1), but not between $\bar{\sigma}_{Sample}$ and $[Fe]_{Sample}$ ($p = 0.34$; Table 8.2)

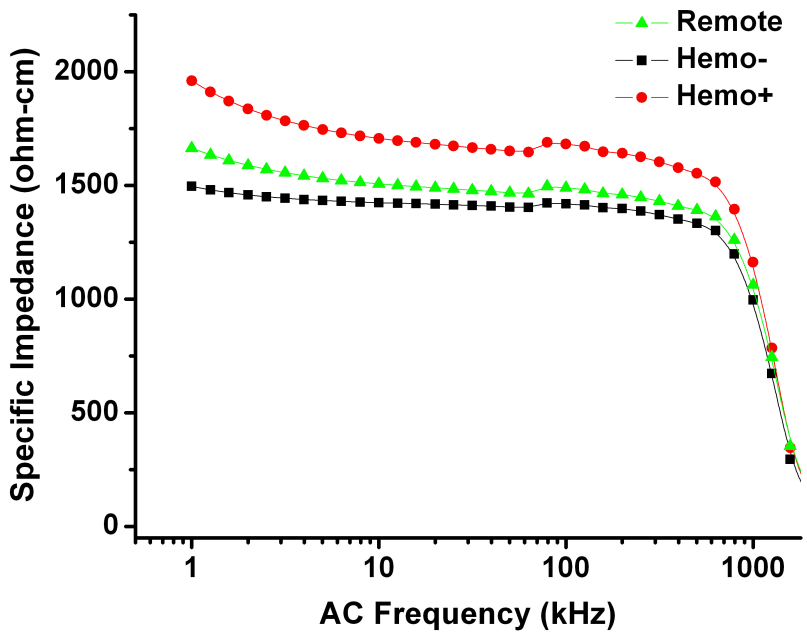

Figure 8.2: *Representative specific impedance spectra from Remote, IRON-, and IRON+ myocardial samples.* Note that for a given AC frequency, the specific impedance of IRON+ samples is higher than that of the Remote and IRON- samples.

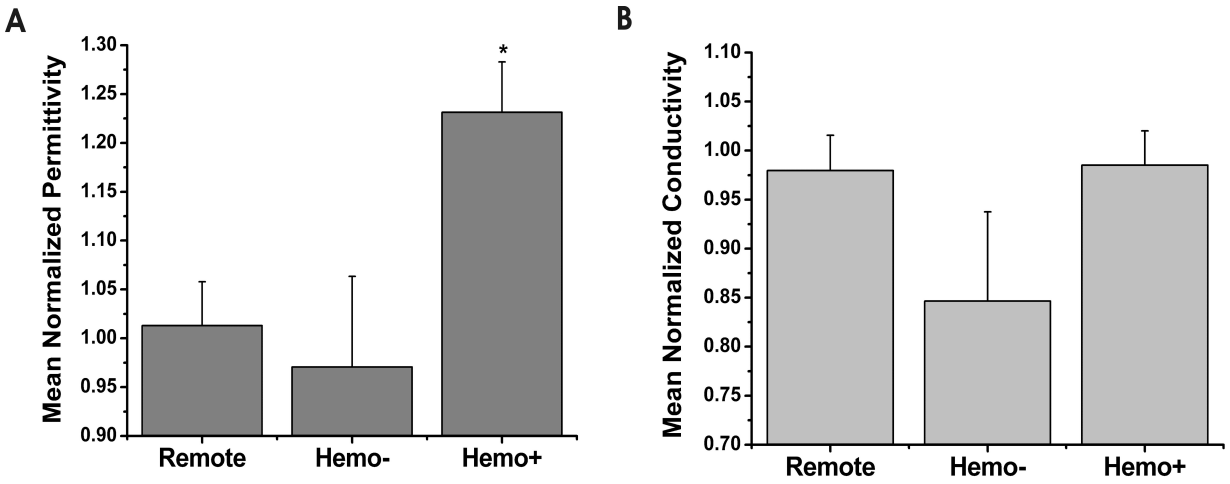

Figure 8.3: *Electrical consequences of iron deposition in ex-vivo myocardium*. Mean $\bar{\varepsilon}$ measured from Remote, IRON-, and IRON+ infarct sections showed significantly greater $\bar{\varepsilon}$ (*, $p<0.001$) in IRON+ compared to Remote and IRON- sections (panel A); however, mean $\bar{\sigma}$ measured from Remote, IRON-, and IRON+ infarct sections did not show any statistical difference in $\bar{\sigma}$ among the different sections (panel B).

Normalized Permittivity	Coefficient	Standard Error	Z	P > Z	Lower 95% CI	Upper 95% CI
[Fe] in mg/g of tissue	1.34	0.31	4.33	<0.001	0.73	1.95
Constant	0.94	0.10	9.30	<0.001	0.74	1.13

Table 8.1: Relationship between Normalized Permittivity and Iron Content

Normalized Conductivity	Coefficient	Standard Error	Z	P > Z	Lower 95% CI	Upper 95% CI
[Fe] in mg/g of tissue	0.23	0.24	0.96	0.337	-0.24	0.71
Constant	0.86	0.09	9.97	<0.001	0.69	1.02

Table 8.2: Relationship between Normalized Conductivity and Iron Content

8.4.2. In-vivo Studies

All 10 animals were positive for infarction and survived the MRI study. MRI studies showed iron depositions to be within the infarcted tissue. Specifically, the imaging studies showed that the iron deposition began at the subendocardium but did not extend beyond the mid wall. In addition regression analysis between the Scar Volume and Iron Volume showed a sigmoidal relationship ($R^2 = 0.75$, $p<0.001$, Figure 8.4), indicating that Iron Volume is small when Scar Volume is small (< 5%), rapidly increasing at intermediate levels of scar (5–12 %) and reaching a plateau with any additional increases in Scar Volume. Representative results from gross TTC staining and histological staining for iron are shown in Figure 8.5.

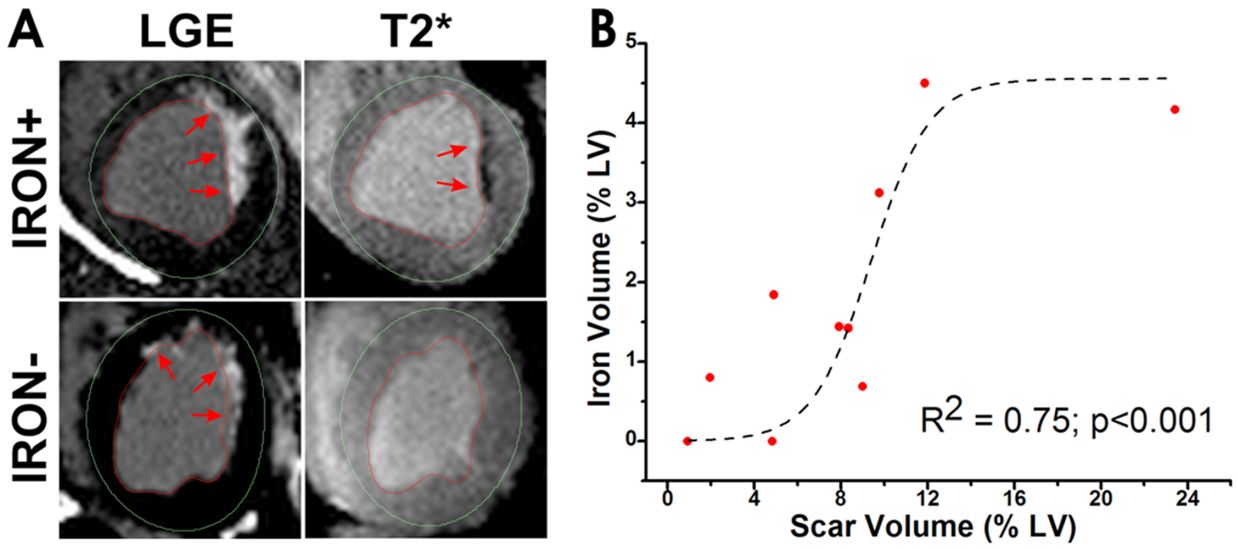

Figure 8.4: *Relation between scar features and chronic iron deposition*. Representative short-axis LGE and T_2*-weighted (TE = 6.5ms) images from two canines subjected to MI from Group in vivo – one with chronic iron deposition within the scar territory (Iron(>1.5%)) and one without chronic iron deposition (Iron(<1.5%)) are shown (panel A). Red arrows point to the site of myocardial scar on the LGE images in both the cases and to chronic iron deposition on the T_2*-weighted image. A significant sigmoidal relation was found between scar volume and iron volume (both computed as the percentage of total LV; $R^2 = 0.75$, $p<0.001$, panel B).

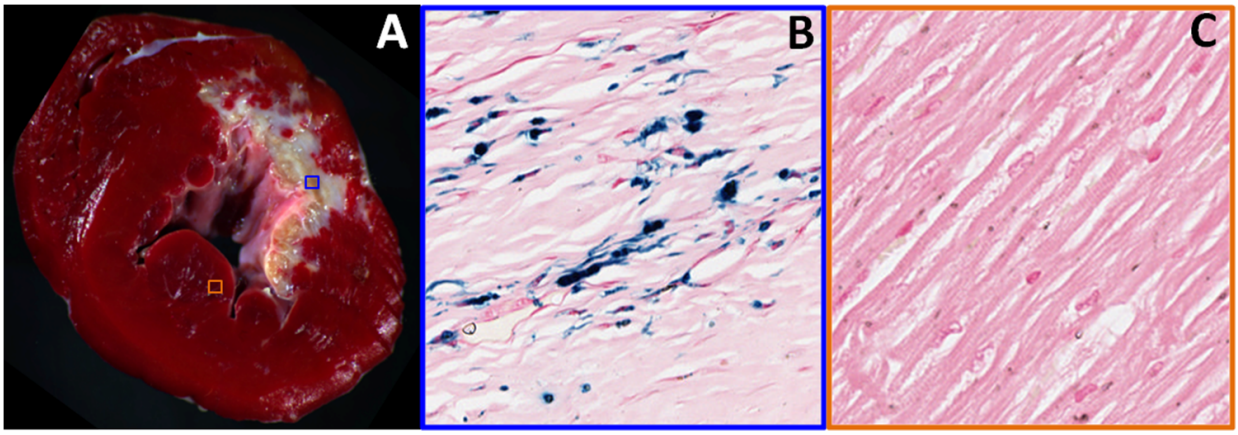

Figure 8.5: *Histological Findings*. The presence of MI in TTC stains (panel A) and iron (panel B, blue Perl's stains; black arrows) within chronic MI and its absence (panel C, Perl's stain) in remote sections are shown. Note that the iron deposits are typically found in the interstitial/extracellular space.

8.4.3. Surface ECG Recordings

To minimize the confounding effects of Scar Volume on ECG parameters (497,498), in total 7 out of the 10 animals that underwent surface ECG recordings (n = 3 in Iron (<1.5%) and n = 4 in Iron (>1.5%)). The animals with the extreme values of Scar Volume (i.e. on the plateau regions of the sigmoidal response curve, Figure 8.4) were not included as part of the analysis. The mean Iron Volume of the two groups were: 1.12±0.64% (Iron (<1.5%)) vs. 2.47±0.64% (Iron (>1.5%)), p = 0.02; and the mean Scar Volume of the two groups were: 7.28±1.02% (Iron (<1.5%)) vs. 8.35±2.98% (Iron (>1.5%)), p = 0.51. Mean HR, QT, QTc, and QTcd values obtained during day, night, and over 24 hours are shown in Figure 8.6. Mean hourly tracings of HR, QT, QTc, and QTcd over the 24-hour period are shown in Figure 8.7.

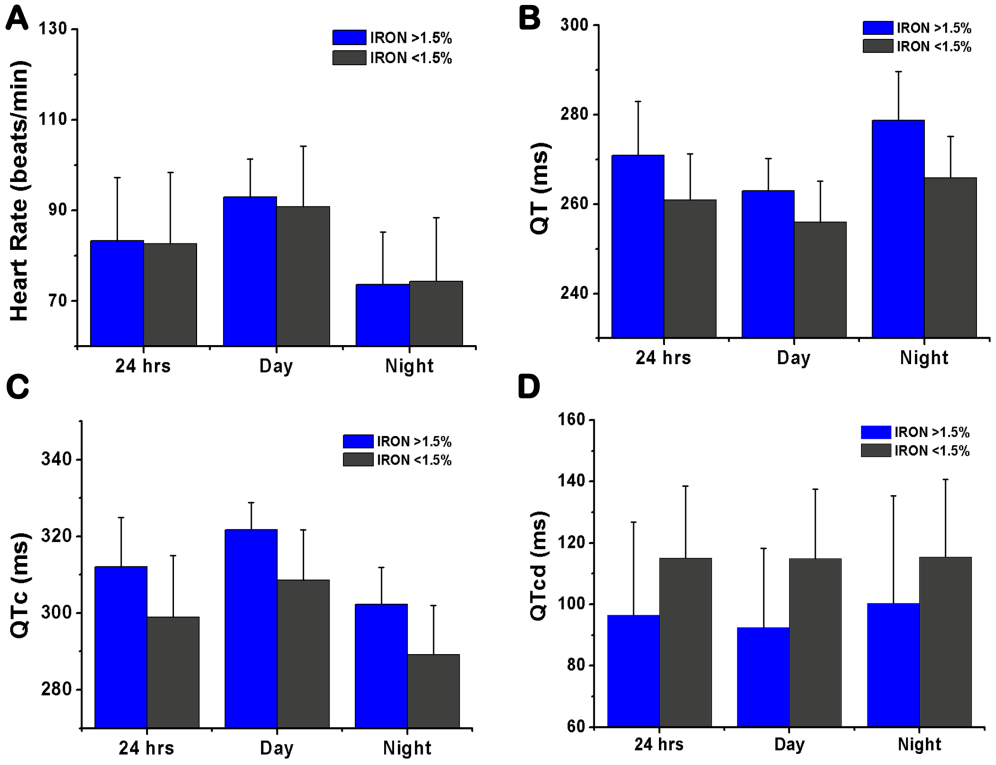

Figure 8.5: *Mean values of important surface ECG parameters over Day, Night and 24-hour periods from Iron(>1.5%) and Iron(<1.5%) dogs*. The mean values from dogs with and without iron over the period of interest for heart rate (panel A), QT (panel B), QTc (panel C) and QTcd (panel D) are shown.

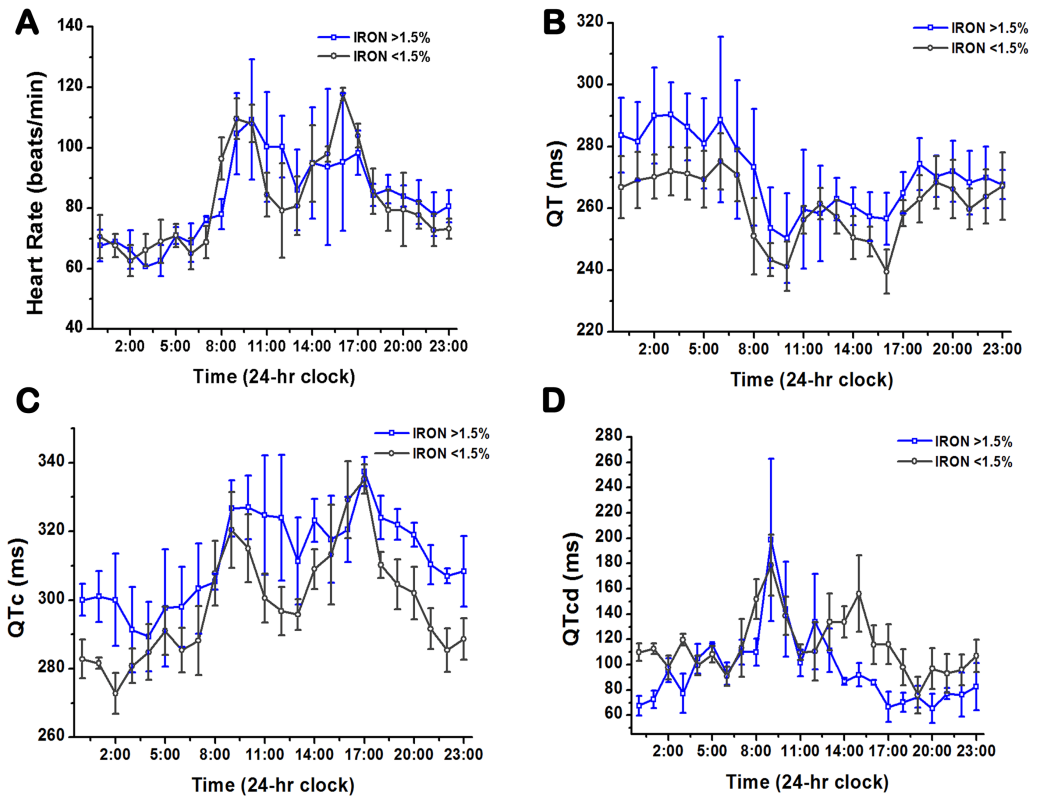

Figure 8.7: *24-hour Holter ECG recordings from Iron(>1.5%) and Iron(<1.5%) dogs*. The mean 24-hour traces showing changes in heart rate (panel A), QT (panel B), QT corrected for heart rate (panel C), and QTc dispersion (panel D) are shown for the two different groups of dogs with and without iron deposition.

QT, QTc and QTcd showed statistically significant differences between Iron(<1.5%) and Iron(>1.5%) groups. In particular, mean HR was not different between Iron(>1.5%) and Iron(<1.5%) groups during the day (77.9±17.0 beats/minute vs. 78.1±17.1 beats/minute, p = 0.51), night (88.7±7.4 beats/minute vs. 86.9±13.4 beats/minute, p = 0.73), or 24-hour period (83.3±14.0 beats/minute vs. 82.6 ± 15.8 beats/minute, p = 0.72). Mean QT interval was significantly different between Iron(>1.5%) and Iron(<1.5%) during the day (263.0±7.2 ms vs. 255.9±9.17 ms, p<0.001), night (278.8±10.9 ms vs. 265.9±9.3 ms, p<0.001), and 24-hour period (270.9±12.1 ms vs. 260.9±10.4 ms, p<0.001). Similarly, mean QTc interval was significantly

different between Iron(>1.5%) and Iron(<1.5%) during the day (321.8±7.1 ms vs. 308.9±13.1 ms, p<0.001), night (302.3±9.5 ms vs. 289.1±12.8 ms, p<0.001), and 24-hour period (312.0±12.9 ms vs. 298.9±16.1 ms, p<0.001). In addition, mean QTcd was also significantly different between Iron(>1.5%) and Iron(<1.5%) during the day (92.4±25.8 vs. 114.9±9.17 ms, p<0.01), night (100.4±35.0 ms vs. 115.4±25.3 ms, p = 0.04), and 24-hour period (96.4±30.3 ms vs. 115.1±23.5 ms, p<0.001).

8.4.4. Electroanatomical Mapping Measurements

Of the 5 animals that underwent EAMs, one animal died during the mapping procedure from spontaneous and sustained ventricular tachycardia, despite cardioversion efforts. Regression analysis of the scar size and location performed between MRI and EAM were highly correlated (R^2 = 0.77, p<0.05), indicating that the registration between the two imaging modalities was significant. Averaged across all animals, 7705 ± 2212 electrograms (EGMs) were recorded and 1577±982 EGMs were manually validated on each map in and around the scar. A representative set of EAMs (bipolar voltage, bipolar activation, and ILP maps) co-registered with MRI (LGE and T_2*) is shown in Figure 8.8. On average, a total of 158±79 ILPs were observed in each dog, and 99±58 of them were co-registered with scar regions containing iron and 59±28 were from scar regions without iron. The overall mean incidence of ILPs in scar regions containing iron was greater than that from regions without iron (Figure 8.9A), but did not reach statistical significance (p = 0.21). Similarly, the mean number of ILPs from regions containing iron, normalized by the percentage of Scar Volume containing iron, was larger than the mean number of ILPs from regions not containing iron, normalized by percentage of Scar Volume without iron; and the same observation was made for the mean number of total ILPs normalized by total

Scar Volume (Figure 8.9B). However these metrics also did not reach statistical significance (p = 0.12).

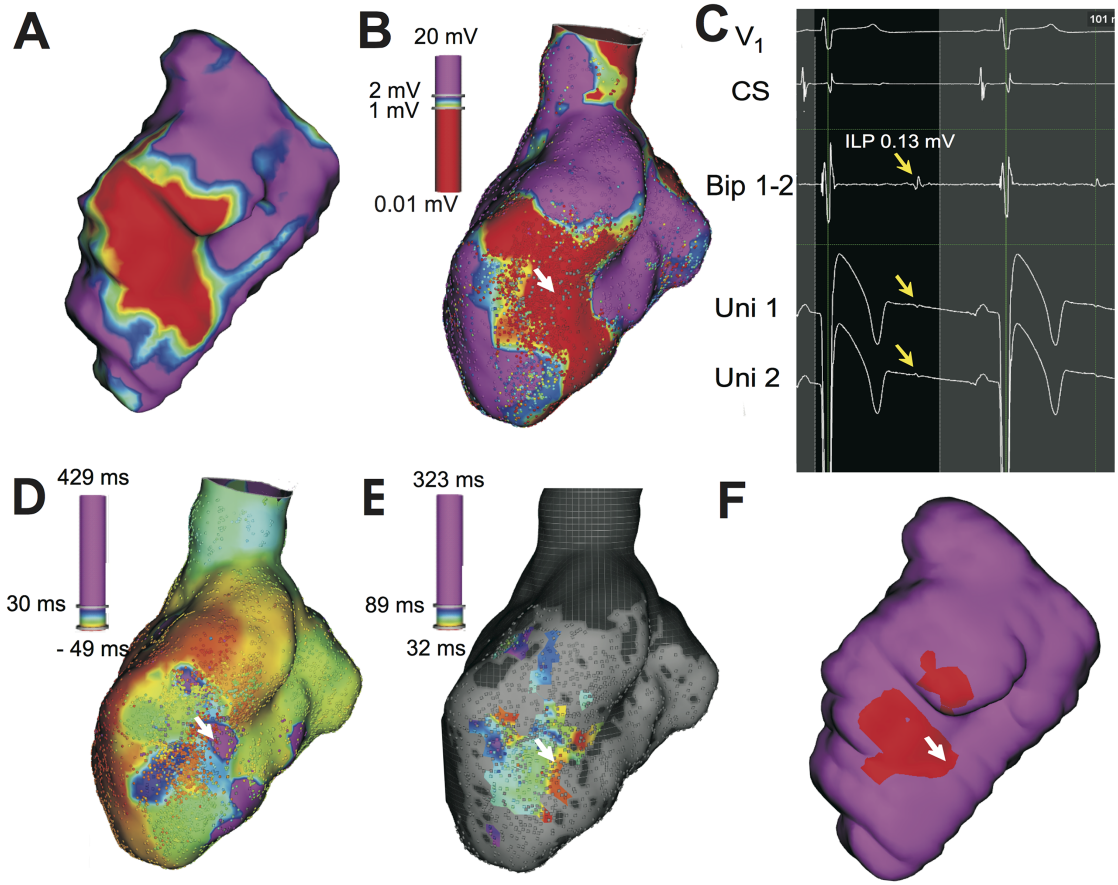

Figure 8.8: *Representative co-registered MR images and EAMs showing the association between ILPs and iron deposition following myocardial infarction*. Co-registered LGE images projected onto the segmented blood pool surface (panel A) with infarcted territory (color coded in red), border zone (yellow and blue shades) and remote territories (purple)) with the corresponding bipolar map (panel B, color-coded to indicate low voltage areas) are shown. For reference, an ILP deep within the scar tissue (white arrow) is shown. The voltage traces from V1 and at the coronary sinus, along with bipolar and unipolar mapping traces are also shown. Note the presence of an isolated low-voltage sharp late potential in the bipolar and unipolar traces following the local ventricular activation (yellow arrow) in panel C. The activation map (panel D), a map of the ILPs (panel E), and iron containing regions (in red, panel F) are also shown for reference. Note that iron-containing regions have a greater incidence of ILPs and slow activation regions.

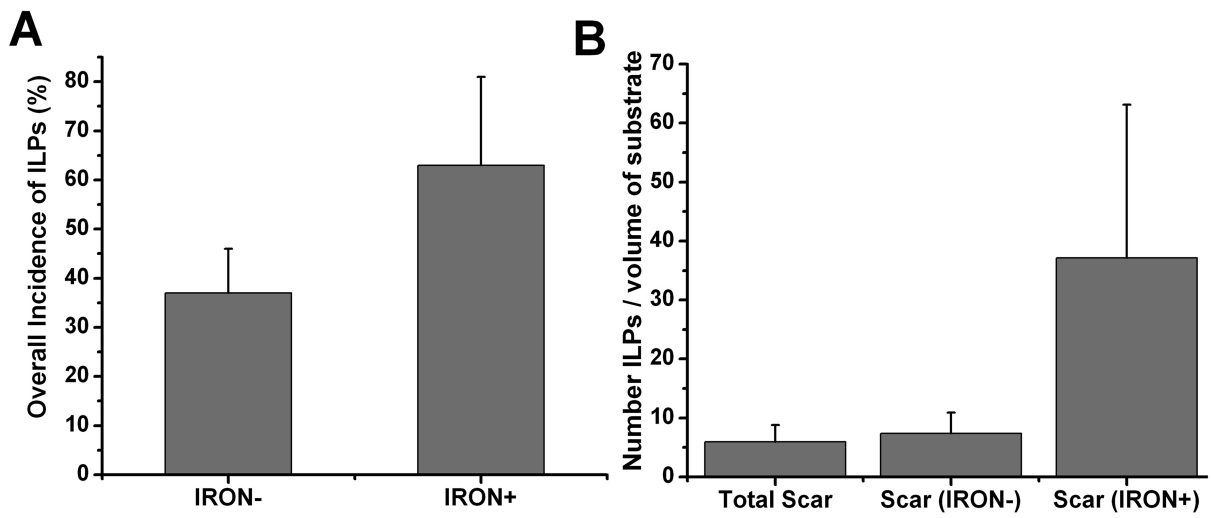

Figure 8.9: *Dependence on the probability of observing ILPs based on substrate type and number of ILPS relative to substrate burden visualized on the basis of co-registered EAM and MR images (LGE and T_2*).* Panel A shows the overall incidence of ILPs (fraction of the total) that were coincident with regions containing iron (IRON+) and regions without iron (IRON-). Panel B shows the mean number of ILPs per volume of substrate, with the substrate being the total scar (i.e., scar with and without iron), scarred regions with iron (IRON+) and scarred regions without iron (IRON-).

8.5. Discussion

In this work, the effect of chronic iron deposition within infarcted myocardium on the electrical behavior of the heart was investigated. From ex-vivo electrical measurements in canine myocardium, this study has shown that one of the consequences of chronic iron deposition within the infarcted zones is the elevation in electrical permittivity ($\bar{\varepsilon}$) of the infarcted myocardium, which is commensurate with the extent of iron deposition. The bulk electrical measurements have also shown that the iron deposition within the infarcted tissue leads to an elevation in electrical permittivity, without a concomitant change in electrical conductivity ($\bar{\sigma}$). From surface ECG recordings of animals with different Iron Volume but similar Scar Volume,

QT and QTc interval have been found to be consistently longer in the Iron(>1.5%) group compared to the Iron(<1.5%) group during the 24-hour period, day, and night; but QTcd was reduced during day, night and the 24-hour period in the Iron(>1.5%) group compared to the Iron(<1.5%) group. Ultra-high resolution LV endocardial EAMs, co-registered with MR images, showed a greater incidence of ILPs in regions of scar with iron accumulation than those without iron accumulation. Moreover, the mean number the ILPs observed per unit volume of scar with iron showed a tendency to be greater than those observed per unit volume of scar without iron or total scar burden.

Biogenic magnetite (hemosiderin) is known to have the highest electrical conductivity of any cellular material (499). Thus, based on previous reports on composite material properties (484), scar tissue with iron deposits is expected to have a greater $\bar{\varepsilon}$ compared to scar tissue without iron (a dielectric). Since the observed changes in $\bar{\varepsilon}$ were not accompanied by changes in $\bar{\sigma}$, it appears that the effect of iron deposition is to transform the infarcted territory into a capacitor (500). Currently it is unclear how these alterations in electrical tissue properties mediate the observed changes in surface ECG parameters and EAMs. In this regard, theoretical modeling may be valuable in gathering mechanistic insight into how or whether these tissue-specific electrical changes mediate alterations in electrical activity in-vivo. Such models need to take into account that the iron deposits following MI are found in the interstitial space, and measurements of $\bar{\varepsilon}$ and $\bar{\sigma}$ that are reported here were collected in ex-vivo preparations. Moreover since iron has been known to induce an inflammatory burden on the surrounding myocardium as demonstrated in the previous chapter, factors other than changes in $\bar{\varepsilon}$ may also explain the electrical changes observed in vivo. Additional studies are needed to explore the mechanism by which iron mediates electrical anomalies in vivo.

The rise in HR during the early morning hours has been found to be slower in Iron(>1.5%) dogs than in Iron(<1.5%) dogs (Figure 8.6A). In addition, a marked prolongation in QT and QTc among Iron(>1.5%) dogs hearts has been found during the day, night and 24 hours compared to Iron(<1.5%) dogs. These differences may be examined in the context of previous studies that attempted to discriminate between SCD victims and MI survivors in the post infarction period. First, the slow rate of increase in HR in SCD victims compared to MI survivors has been reported in the waking hours (501). Second, marked changes in QT patterns have been observed during the day between SCD victims and MI survivors. Prolongation in QTc has been strongly associated with SCD (502). These collective observations suggest that hearts with significant iron deposition (Iron(>1.5%)) may be more susceptible to arrhythmias than hearts with minimal or no iron (Iron(<1.5%)).

ILPs have been shown to be substrates for ventricular arrhythmias in the post-infarction phase (503-505). In particular, ILPs are known to emerge from gray-zones and within the dense scar (506,507). The source of these ILPs has been associated with surviving myocardial bundles within the infarct region, but whether these bundles are indeed the only source of arrhythmias is unclear. In this study, based on MRI and EAM, dense scar regions with iron deposits have been shown to have a greater prevalence of ILPs than scarred regions without iron. In addition, this study showed that the number of ILPs per percentage volume of substrate (total scar, scar without iron and scar with iron) is greatest when the substrate is scar with iron. The mechanistic underpinnings contributing to the association between iron accumulations and ILPs in dense scar is not clear. While the changes in electrical capacitance may explain the isolated potential in the repolarization phase of the cardiac cycle, further studies are necessary to understand how the iron deposits couple with the endogenous electrical activity of the heart to mediate the observed

electrical anomalies.

Finally, recent studies have shown that although infarct volume is a predictor of arrhythmias, the incidence of arrhythmias measured as percentage of arrhythmia-related deaths or ICD discharge, plateaus beyond a particular scar volume (96,497,498,508). Specifically, these studies have shown that the incidence of arrhythmias at a Scar Volume of less than 5% to be small, increasing rapidly between 5-10% and then plateauing above 10%. Importantly, these studies have shown that the risk of developing arrhythmias increases from 10% (for Scar Volume < 5%) to approximately 40-50% (for Scar Volume 5-10%). The current study has shown that for animals within this domain (i.e., 5% < Scar Volume <10%), it is possible to resolve two groups of dogs with similar scar volumes but with markedly different iron volumes. In fact, this study has shown that when animals are dichotomized on the basis of Iron Volume within this range of Scar Volumes, the critical ECG parameters of repolarization in animals with markedly higher iron content has shown significant prolongation of QT and QTc, as well as shortening of QTcd. Notably, such directional changes, particularly in QT and QTc, have been previously associated with increased risk of ventricular arrhythmias in humans (501,502). In addition, it is has been shown that arrhythmogenic substrate is typically found between the subendocardium and the mid-wall (509,510), an observation that is consistent with the spatial distribution of iron deposits in the CMI. These observations suggest that the extent of iron deposition may be a better predictor of arrhythmias. However, further studies are necessary to translate these findings to the clinical arena.

Collectively taken, the findings from this study showed that the electrical behavior of infarcts with iron is different from infarcts without iron. These observations point to the plausibility that iron within myocardial scar may serve as a substrate for cardiac ventricular

arrhythmias in the chronic phase of MI. Additional studies are warranted to understand the mechanism by which iron can potentially mediate arrhythmias. In this respect, it would be of significant interest to understand whether and/or how the iron deposits within the infarcted zones can electrically interact with the surrounding healthy myocardium.

8.5.1. Study Limitations

This is the first study to evaluate the effects of iron in the post-MI scar using ex-vivo measurements, surface ECG recordings, and EAM. However, this study has some limitations. First, given the lack of a better method, electrical measurements of the tissue samples isolated from the same slice were weight averaged in order to examine relationships between $\bar{\varepsilon}$ and $\bar{\sigma}$ with iron. Implicit in these estimated relationships are that the iron is uniformly deposited within IRON+ infarcts, which may not be accurate. To what extent the heterogeneity of iron deposition affects the local electrical measures remains to be investigated. Topographic current density images of infarcted tissues would be ideally suited to such an investigation. However, the standard conductive atomic force microscopy typically used for generating current density maps in spatially extended media has practical limitations for use with fragile biological tissues such as the myocardium. Moreover, measurements of $\bar{\varepsilon}$ and $\bar{\sigma}$ in tissue with and without iron were made from ex-vivo sections, which only account for the extracellular characteristics. Further studies are needed to address the in-vivo effect of iron burden on electrical impedance. Third, this study did not explore mechanistic insight into how the iron deposition in the post infarction period mediates electrical anomalies. Additional studies are needed to explore this limitation. Second, the surface ECG recordings were limited to a 24-hour period but longer recordings have the potential to further confirm the 24-hour observations. Finally, while the metrics used to evaluate

the mean difference in the overall incidence of ILPs and ILP count relative to substrate burden tended to be greatly influenced by the presence and extent of iron, they did not reach statistical significance, likely because of small sample size. Studies with larger sample size may establish statistical significance. While this study demonstrated the possibility that iron depositions in the CMI induce electrical anomalies in dogs, its effect on the electrical behavior in humans following MI remains to be investigated. However, if these findings can be extended to humans, iron may evolve as a novel arrhythmogenic substrate and T_2*-based MRI can be used to noninvasively guide appropriate patient selection for ICD placements.

8.6. Conclusion

The electrical behavior of CMIs with iron appears to be different from those without iron. Chronic iron, detected using T_2*-based MRI, within infarcted zones may evolve as an arrhythmogenic substrate in the post-MI period.

CHAPTER 9

Utility of Balanced SSFP Imaging for Detecting Chronic Iron Deposition and Predicting Ventricular Arrhythmia Risk in Patients with Chronic Myocardial Infarction

9.1. Abstract

The previous chapter has shown that iron deposition within CMI of a canine model influences the electrical behavior of the heart. The purpose of this study is to investigate the association between the iron deposition, identified on the basis of non-contrast enhanced balanced SSFP (bSSFP) imaging, and malignant ventricular arrhythmias (mVAs) in humans with CMI. Ninety-four CMI patients who underwent LGE imaging prior to ICD implantation for primary and secondary prevention were retrospectively analyzed. The predictive values of hypointense cores (HIC) in bSSFP images, conventional MRI parameters, and ECG mVA parameters were evaluated for the prediction of primary combined outcome (appropriate ICD therapy, survived cardiac arrest or sudden cardiac death). The use of HIC within CMI on bSSFP as a marker of iron deposition was validated in a canine MI model. Nineteen patients met the study criteria with events occurring 343±269 days after ICD placement. Of the 19 patients having a primary endpoint, 18 were classified as HIC+ while only 1 was HIC-. Among the cohort in whom the primary endpoint was not met there were 28 HIC+ and 47 HIC- patients. ROC analysis demonstrated an additive predictive value of HIC for mVAs by increasing the AUC to 0.87 when added to EF (AUC with EF alone was 0.68). Both T_2*-based MRI and histological validation studies performed in canines demonstrated that HIC regions in bSSFP images within CMI likely

result from iron depositions. In conclusion, hypointense cores within CMI on bSSFP MRI can be used as a marker of iron deposition and yields incremental information toward the accurate prediction of mVA.

9.2. Introduction

SCD is a major public health problem in the United States accounting for 50% of all deaths due to cardiovascular conditions (511-515). Approximately 80% of patients dying of SCD have underlying coronary heart disease and CMI is present in >50% of the cases (64). In the majority of cases, SCD in patients with CMI is triggered by the onset of malignant ventricular arrhythmias (mVA) (65,516). The implantable cardioverter-defibrillator (ICD) has been instrumental in the primary prevention of SCD (517-519), however, accurate identification of patients at greatest risk for SCD remains challenging (520-522).

Current guidelines for the primary prevention of SCD recommend the prescription of ICDs for patients with severely reduced LV ejection fraction (EF) of <35% (523). However, only 20-30% of these patients have been shown to benefit from this therapy, with the remaining 70-80% not experiencing mVA (524,525). Moreover, of those experiencing SCD, at least 65% were not eligible for primary prevention ICD, as they did not have a conventional risk predictor (EF<35%) (526,527). Hence there is a critical need to develop and validate novel approaches for mVA risk prediction incremental to the assessment of LV function. To date, a number of risk predictors have been explored; namely, infarct size, type of infarction, infarct transmurality, gray-zone signal, surviving bundles, and surface ECG parameters. While these have demonstrated value for the prediction of mVA over conventional EF-based stratification, it is

also apparent that arrhythmia substrate is complex and is not adequately characterized by the markers explored to date.

There is growing evidence in the literature that post-MI iron deposition in the myocardium may be arrhythmogenic. Even though it has been long known that abnormal accumulation of iron in the heart has been associated with cardiac conduction abnormalities (459,461,480), only recently has its relevance come to light in the post-MI setting. Eitel et al have shown that patients with hemorrhagic MI have an increased risk for experiencing major adverse cardiac events, including death (141). Mather et al have shown that patients with hemorrhagic MI have prolonged filtered QRS duration, which has been associated with increased late-arrhythmogenic risk (198). In this regard, the previous chapters have demonstrated that iron deposition can occur in CMIs secondary to post-reperfusion intramyocardial hemorrhage, and such deposits can alter the electrical characteristics of the scar tissue. Moreover, forensic studies utilizing clinical cardiac MRI have shown that SCD victims with CMI consistently have hypointense zones in the scarred myocardium in T_2-weighted MRI (482,483), which is consistent with iron accumulation. To date however, there has been no direct evidence for an association between post-MI iron accumulation and mVAs.

Guided by previous theoretical and experimental observations (528-530), this study hypothesized that hypointense cores (HIC) within CMI detected using balanced SSFP (bSSFP) MRI at 3T can be used as a marker for chronic iron deposition, and when used in conjunction with EF can markedly improve the prediction of SCD or appropriate ICD therapy. This hypothesis was examined through a retrospective analysis of a CMI patient population undergoing MRI prior to ICD implantation. The ability of bSSFP imaging to detect iron deposition within CMI at 3T was validated using T_2*-based MRI in a canine model of CMI.

9.3. Methods

9.3.1. Patient Studies

9.3.1.1. Patient Population

This retrospective cohort study was conducted at a large, tertiary care referral center (London Health Sciences Centre, London, Ontario, Canada), between October 2008 and May 2012. The study population consisted of only those patients (n=94) in whom MRI protocol was prescribed and were subsequently instrumented with ICD. MRI was performed in all consenting patients, with the EF provided to assist in clinical decision-making. Inclusion criteria for the ICD placement were EF≤35% estimated by echocardiography, history of prior MI, and appropriate heart failure (HF) therapy for ≥3 months. Patients with standard contraindications to LGE imaging, inclusive of GFR ≤ 30 mL/min/1.73m^2, were excluded. Both verbal and written informed consent was obtained from patients prior to being studied according to the protocols approved by the Institutional Research Ethics Board.

9.3.1.2. MRI Studies in Patients

Prior to ICD implantation all patients underwent MRI in a 3T MRI system (MAGNETOM Trio, Siemens Healthcare, Erlangen, Germany) equipped with a 32-channel cardiac receive coil. Cine-bSSFP images (TR/TE = 2.6/1.3 ms; $\alpha = 10^o$; voxel size = 2x2x10 mm^3; BW = 930 Hz/pixel; and temporal resolution = 28-38 ms) were acquired in sequential short-axis views covering the entire LV. LGE imaging was performed 10 to 15 minutes following intravenous infusion of gadobutrol (0.15–0.2 mmol/kg, Gadovist, Bayer Inc., Toronto, Canada) with segmented IR-FLASH

sequence matched to the cine imaging slices (optimal TI to null the remote myocardium; TR/TE = 7.8/3.9 ms; $\alpha = 20^{o}$; voxel size = 1.5x1.5x10 mm^3; BW=1500 Hz/pixel).

9.3.1.3. Image Analyses

All quantitative image analyses were performed using the cmr[42] (Circle Cardiovascular Imaging Inc., Calgary, AB, Canada). All qualitative image analyses including contouring the myocardium were performed in consensus by two blinded reviewers with >3 years of experience in reading cardiac MRI images on Osirix (version 4.1.2, Pixmeo, Geneva, Switzerland). Remote myocardium was defined as the region showing no hyperintensity on LGE images, and a reference ROI was drawn in it. Infarcted myocardium was defined using the Mean+5SD criterion relative to the reference ROI (414-416). Infarct gray-zone was defined as areas with signal intensity between Mean+2SD and Mean+3SD cut-offs relative to the reference ROI (282). LV mass, EDV, ESV, and EF were calculated from the cine images and normalized to the body surface area. Scar size and gray-zone size were calculated by normalizing total scar and gray-zone volumes respectively with the total LV myocardial volume.

The presence of infarcted myocardial regions with hypointense cores in bSSFP images (HIC+) were identified qualitatively using a binary scoring scheme (present or absent). All of the HIC determinations were blinded to the clinical outcomes. The image analysis for the identification of patients with HIC+ involved (a) displaying the cine-bSSFP and LGE images side by side in bi-panel views in Osirix; (b) identifying the infarct territory on LGE image and visually mapping it to bSSFP images; and (c) manually windowing when necessary to discriminate the presence of hypointense core within the LGE positive territory on bSSFP images. HIC+ subjects were identified as those with eight or more contiguous nearest-neighbor

hypointense pixels in the infarct territory that are present in every frame of a given short-axis set of cine-bSSFP images. All other subjects that did not have hypointense regions or those that did not conform to the identification criterion (i.e. those resembling 'india-ink' artifacts (531), bSSFP banding artifacts (532), and hyperintense regions enclosed by fine hypointense lines (531)) were identified as HIC-. The 8-pixel approach adapted here was similar to that used in previous publications to visually guide the detection of a desired image contrast (116,533).

9.3.1.4. ICD Implantation and Clinical Follow-Up

ICDs were implanted by the local clinical electrophysiology service in a standard fashion within 71±104 days (1 to 391) of the date of MRI. ICD devices were programmed to detect ventricular fibrillation (VF) if 18 of 24 R-R intervals were ≤240 ms. Fast ventricular tachyarrhythmias (VT) was defined as 18 of 24 consecutive R-R intervals ≤320 ms and slow VT as 16 consecutive R-R intervals ≤400 ms. In patients receiving primary prevention, ICDs were routinely programmed to deliver anti-tachycardia pacing, shock therapy for VF or fast VT, and to monitor (not deliver therapy) for slow VT. For patients receiving secondary prevention, ICD programming was altered to treat slow VT using both anti-tachycardia pacing and shock therapies.

Clinical follow-up and device interrogations at 1, 3, 6 months, and every 6 months thereafter were initiated from the time of MRI. The primary composite endpoint was defined as the occurrence of appropriate ICD therapy, survived cardiac arrest (SCA), or sudden cardiac death (SCD). In patients having ≥2 registered clinical events during follow-up, the time to first clinical event was used for analysis of event-free survival.

At study closure all device interrogations were de-identified and adjudicated by 2 local electrophysiologists blinded to MR image analysis. ICD therapy was classified as appropriate

when anti-tachycardia pacing, or shock for fast VT (R-R<320 ms) or VF was delivered. ICD therapy was defined as inappropriate when delivered for non-target arrhythmias (e.g., sinus or supraventricular tachycardia), T-wave oversensing, or for any device system malfunction (e.g, lead conductor wire fracture).

All study subjects were evaluated for the incidence of SCA or SCD at 12-month intervals and at study closure during a mean follow-up period of 632±262 days. This was performed by telephone interview and a review of all medical records. SCD was defined as death occurring within 1 hour of symptom onset.

9.3.2. Validation of Imaging Findings in Canines

9.3.2.1. Animal preparation and MRI Protocol

To ascertain the tissue composition of the MI territories that appear as HIC+ in bSSFP MRI, studies were performed in a canine model of CMI. Canines (n=19, 20-25kg) were enrolled and studied according to the protocols approved by the Institutional Animal Care and Use Committee. Left lateral thoracotomies were performed on canines, and MI was induced by occluding the LAD for 3 hours followed by reperfusion. Following the surgeries, the canines were allowed to recover for 12 weeks prior to MRI studies.

9.3.2.2. MRI Studies in Canines

All canine MRI studies were performed on a clinical 3T MRI system (MAGNETOM Verio, Siemens Medical Solutions, Erlangen, Germany). Multiple ECG-gated, breath-held, 2D images of contiguous short-axis sections covering the entire left-ventricle (LV) were acquired using cine-bSSFP (TR/TE = 3.5/1.75ms; α = 70°; 20-25 cardiac phases; BW = 930 Hz/pixel), T_2*-

weighted imaging (multi-echo GRE; TR = 12ms; 6 TEs = 2.0–9.5 ms with ΔTE = 1.5 ms; α = 10°; BW = 930Hz/pixel), and LGE imaging (IR-FLASH acquired 10-15 minutes following intravenous infusion of gadopentetate dimeglumine (Magnevist, Bayer Healthcare Pharmaceuticals Inc., Wayne, NJ); optimal TI to null remote myocardium; TR/TE = 3.0/1.5 ms, α = 25°; BW = 586 Hz/pixel). To minimize off-resonance artifacts, volume-selective shim covering the entire heart was performed prior to start of data acquisition. Commonly used imaging parameters for all the scans were in-plane resolution = 1.4x1.4 mm^2, slice thickness = 6 mm, and number of averages = 1.

9.3.2.3. Image Analyses

MRI data from canines were analyzed in cvi[42] (Circle Cardiovascular Imaging Inc., Calgary, AB, Canada). Infarcted, remote and gray-zone myocardial territories were identified on LGE images as described in section 9.3.1.3. Similarly, HIC+ and HIC- short-axis slices were visually identified on bSSFP images as described earlier for patients. First, remote regions identified on LGE images were copied on to T_2* maps, and T_2* of remote myocardium was measured. Next, HIC+ and HIC- territories visually identified on bSSFP images that were positive for LGE were manually traced and copied on to T_2* images (matched to slice positions and trigger time) to allow T_2* values of both territories to be quantified. T_2* values of the remote, HIC+ and HIC- regions were averaged across all animals.

9.3.2.4. Histopathology

Animals were euthanized immediately after the MRI studies and their hearts were excised. Each heart was manually sliced into 5 mm thick slices along the LV short-axis, and ex-vivo TTC

staining was performed. The ex-vivo slices were carefully matched to the in-vivo MR images based on the location of the papillary muscles and infarct morphology, and categorized as HIC+ and HIC-. Three ex-vivo slices each from the HIC+ and HIC- categories were embedded in a paraffin block, sliced into 5μm contiguous sections and stained with EMT (for collagen deposition) and Perl's stains (for iron depositions) using standard techniques. The sections were mounted on glass slides and scanned at 100X magnification using an ACIS II technology based ChromaVision digital slide scanner (Clarient Inc., Aliso Viejo, CA).

9.3.3. Statistical Analyses

All statistical analyses were performed on R statistical software (version 2.15). Categorical variables are expressed as number (and percentage) of patients. Normality of continuous data was evaluated using Shapiro-Wilk test and quantile-quantile plots. Continuous variables with normal distribution are expressed as Mean±SD, while those with non-normal distribution are expressed as median with interquartile range. Depending on the normality of the data, ANOVA or Kruskal-Wallis test was performed with post-hoc analysis to evaluate the differences in EF, scar size, gray-zone size, QRS interval, and QT_C duration among three different groups: 1) HIC+/ICD+, 2) HIC+/ICD-, and 3) HIC-/ICD-. Fisher's exact test was used to compare groups for categorical variables. Univariate logistic regression was used to identify the significant predictors of appropriate ICD therapy. Multivariate logistic regression was performed using only the significant univariate predictors. Odds ratios were computed for the different predictors from the univariate and multivariate regression. ROC analysis was performed to determine the predictive capability of significant univariate and multivariate predictors. Statistical significance was set at $p<0.05$ for all analyses.

Statistical tools used to assess findings in canines were similar to that used to examine patient data. Depending on the normality of the data, ANOVA or Kruskal-Wallis test was used to compare the T_2* values among remote myocardium, HIC+ scarred myocardium, and HIC- scarred myocardium. Statistical significance was set at $p<0.05$.

9.4. Results

9.4.1. Patient Studies

9.4.1.1. Baseline characteristics

The present retrospective cohort study enrolled 94 patients with prior MI, where every patient was positive for LGE. Their baseline characteristics are shown in Table 9.1. Basic risk factors and medical therapies at baseline, except mean New York Heart Association (NYHA) functional class, did not differ between patients who did or did not have the HIC present in bSSFP images (Table 9.1). The baseline MRI values of the study population were as follows: mean LV mass index = 93.0±23.2 g/m^2; EDV = 118.9±35.3 ml/m^2; ESV = 83.3±33.6 ml/m^2; EF = 31.7±11%; mean gray-zone size = 8.0±3.0%. LGE was observed in all patients included in the study with a mean scar volume (%LV) of 23.3±15.9. There was no difference in EF, EDV, ESV, scar size, and gray-zone size between the two study groups.

9.4.1.2. Clinical Follow-Up

All patients were followed for occurrence of primary endpoint for 632±262 days. Device interrogations occurred on months 1, 3, 6, and every 6 months thereafter from the day of MRI.

Endpoint criteria (appropriate ICD therapy, SCA, SCD) were met in 19 patients with events occurring 343±269 days after ICD placement. Of these, 11 patients received an appropriate shock, 3 patients received appropriate anti-tachycardia pacing for sustained VT (1 out of 3 with advanced HF), and 5 patients died due to SCD (1 out of 5 with advanced HF). In addition, 3 patients suffered a non-SCD due to progressive HF and 4 patients with progressive HF died of non-cardiac cause.

Characteristic	All Patients (n=94)	HIC - (n=48)	HIC + (n=46)	p- Value
Age, y (mean ± SD)	62.6 ± 10.5	63.0 ± 11.6	62.2 ± 9.2	0.710
Male sex (%)	90 (96)	46 (96)	44 (96)	0.939
Clinical history				
Hypertension (%)	62 (66)	33 (69)	29 (63)	0.523
Diabetes (%)	38 (40)	21 (44)	17 (37)	0.286
Hyperlipidemia (%)	79 (84)	41 (85)	38 (82)	0.868
Smoking (%)	55 (59)	25 (52)	30 (65)	0.219
History of revascularization (%)	49 (52)	24 (50)	25 (54)	0.666
NYHA functional class (mean ± SD)	2.4 ± 0.8	2.6 ± 0.7	2.2 ± 0.7	0.013*
Systolic BP (mm Hg)	124.1 ± 19.5	122.6 ± 21.3	125.7 ± 17.4	0.492
Diastolic BP (mm Hg)	72.7 ± 11.3	71.5 ± 11.9	73.9 ± 10.7	0.353
History of ventricular arrhythmias (%)	13 (14)	6 (12)	7 (15)	0.714
Medications				
ACE inhibitor (%)	67 (71)	53 (71)	14 (72)	0.946
Amiodarone (%)	7 (7)	6 (8)	1 (6)	0.758
ARB (%)	24 (25)	20 (27)	3 (17)	0.332
ASA (%)	64 (68)	51 (68)	13 (67)	0.874

Beta blocker (%)	75 (80)	61 (81)	14 (72)	0.342
Digoxin (%)	22 (23)	18 (24)	4 (22)	0.885
Diuretic (%)	55 (59)	44 (58)	12 (61)	0.871
Plavix (%)	10 (11)	9 (12)	1 (6)	0.404
Statin (%)	50 (53)	39 (52)	12 (61)	0.497
ECG Parameters				
Heart Rate (beats/minute, Mean ± SD)	70.5 ± 13.7	68.7 ± 11.7	72.5 ± 15.5	0.196
QRS, ms (Mean ± SD)	129.8 ± 29.6	131.4 ± 30.9	127.6 ± 28.5	0.526
QTc, ms (Mean ± SD)	456.4 ± 39.9	459.1 ± 41.7	453.8 ± 38.9	0.523
LBBB (%)	32 (34)	14 (27)	18 (39)	0.313
MRI Parameters				
LV mass index, g/m^2 (Mean ± SD)	93.0 ± 23.2	92.6 ± 23.2	93.5 ± 23.7	0.854
LV EDV index, ml/m^2 (Mean ± SD)	118.9 ± 35.3	116.0 ± 33.1	121.0 ± 37.3	0.472
LV ESV index, ml/m^2 (Mean ± SD)	83.3 ± 33.6	79.9 ± 28.9	85.9 ± 37.7	0.368
LVEF, % (Mean ± SD)	31.7 ± 11	32.3 ± 10.1	31.2 ± 11.8	0.591
Scar volume, %LV (Mean ± SD)	23.3 ± 15.9	22.0 ± 16.6	24.2 ± 14.9	0.473
Gray-zone (2-3SD), % (Mean ± SD)	8.0 ± 3.0	7.9 ± 3.1	8.0 ± 2.9	0.876

NYHA, New York Heart Association; BP, blood pressure; ACE, angiotensin-converting enzyme; ARB, angiotensin receptor blocker; ASA, acetylsalacylic acid; LBBB, left bundle-branch block; ICD, implantable cardiac defibrillator; LV, left ventricle; EDV, end-diastolic volume; ESV, end-systolic volume; EF, ejection fraction. *Statistically significant ($p<0.05$).

Table 9.1: Baseline patient characteristics based on presence of HIC in bSSFP images

9.4.1.3. Hypointense MI Territories on bSSFP Images vs. Primary Endpoint

Analysis of the MRI data showed that of the 19 patients having a primary endpoint 18 were classified as HIC+ while only 1 subject was classified as HIC- (Table 9.2). Figure 9.1 shows representative MRI findings in patients experiencing the primary endpoint who were HIC+ and a

patient who was HIC- who did not experience the primary endpoint. In the group of patients in whom the primary endpoint was not met, there were 28 HIC+ and 47 HIC- patients.

Variable	With Primary Outcome (n=19)		Without Primary Outcome (n=75)		Univariate OR	Multivariate OR
HIC	HIC+ (n=18)	HIC- (n=1)	HIC+ (n=28)	HIC- (n=47)	30.21 p=0.001*	33.29 p=0.001*
LVEF, % (Mean ± SD)	27.4 ± 10.8	21.3	33.0 ± 10.8	32.4 ± 10.4	0.95 p=0.03*	0.95 p=0.04*
Scar size, %LV (Mean ± SD)	25.7 ± 14.8	22.0	26.3 ± 14.7	22.9 ± 16.9	1.01 p=0.728	-
Gray-zone size, %LV (Mean ± SD)	7.9 ± 2.8	12.1	8.0 ± 3.1	7.8 ± 3.0	1.03 p=0.74	-
QRS, ms (Mean ± SD)	126.9 ± 28.7	156.0	130.6 ± 29.8	132.0 ± 31.4	1.00 p=0.695	-
QTc, ms (Mean ± SD)	455.1 ± 33.9	422.0	450.7 ± 42.9	459.3 ± 42.4	1.00 p=0.790	-

HIC+: hypointense core present; HIC-: hypointense core absent; OR: odds ratio; *Statistically significant ($p<0.05$).

Table 9.2: Hypointense core (HIC) versus frequency of primary outcome

Univariate regression analysis showed that only EF (β = –0.06; Odds ratio (OR) = 0.95; 95% CI = 0.94–0.98; p = 0.03) and the presence of HIC (β = 3.41; OR = 30.21; 95% CI = 3.82–238.77; p = 0.001) were significant predictors of primary endpoint (Table 9.2). Multivariate regression analysis showed that both EF (β = –0.06; OR = 0.95; 95% CI = 0.89–0.94; p = 0.04) and the presence of HIC (β = 3.50; OR = 33.29; 95% CI = 4.16–265.6; p = 0.001) were independent predictors of primary endpoint (Table 9.2). ROC analysis showed that the addition

of scar size to EF did not change the AUC, but the addition of HIC to EF and scar size increased the AUC from 0.68 to 0.87, demonstrating an additive prognostic value of HIC (Figure 9.2). In addition, there was no statistically significant difference between the ICD+/HIC+ and ICD-/HIC+ groups with respect to %HIC (53.3±13.9% vs. 51.4±20.5%, p=0.80).

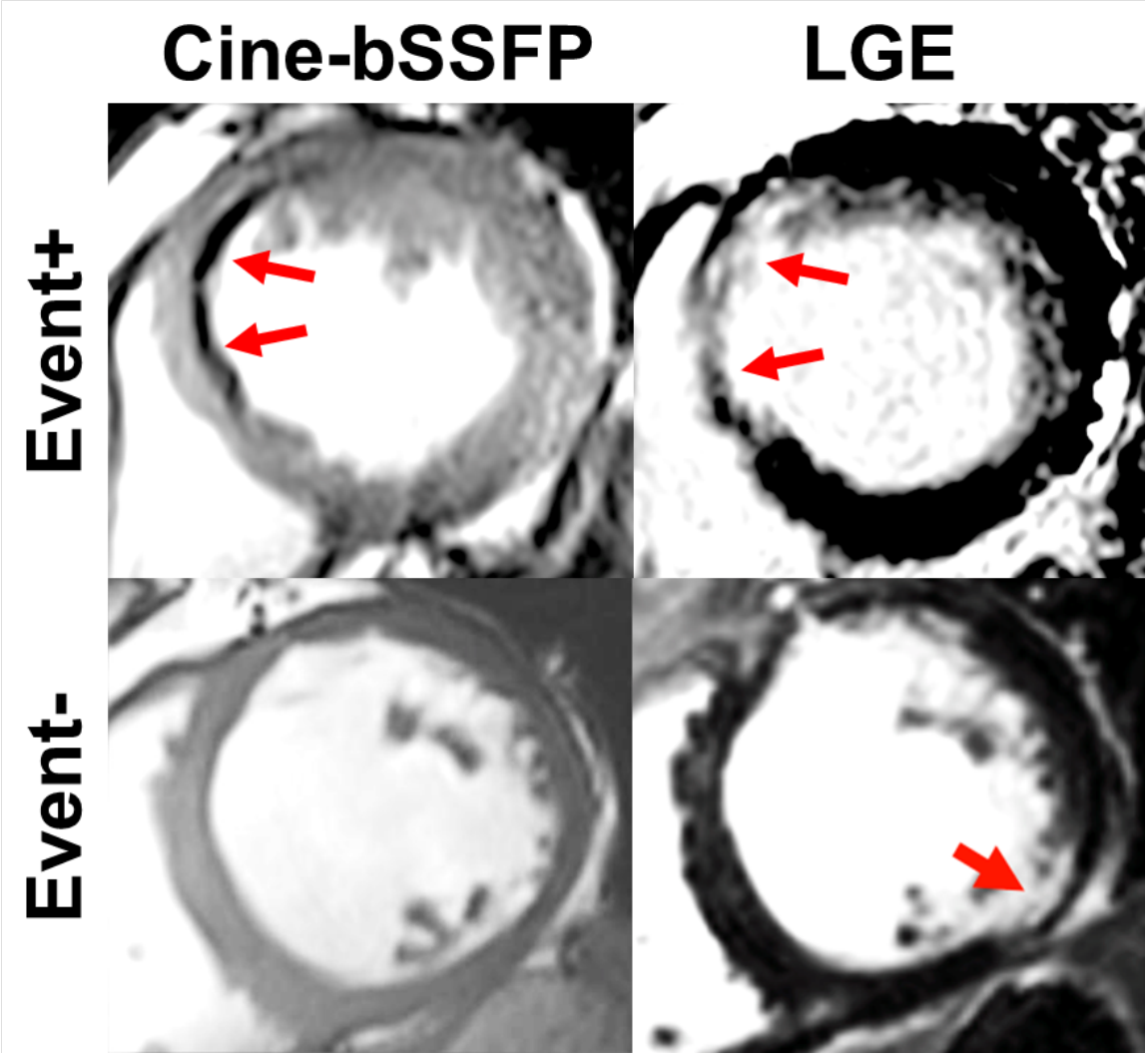

Figure 9.1: *Presence of HIC within MI territories on bSSFP images.* Representative bSSFP and LGE images are shown from two patients receiving ICD therapy; one who met the primary endpoint (Event+) and one who did not meet the primary endpoint (Event-). For the Event+ patient, red arrows denote the MI region on LGE imaging and the Hypointense Core (HIC) region on bSSFP imaging. In the Event- patient, no HIC were observed by bSSFP within the MI region, indicated by the red arrow on LGE imaging.

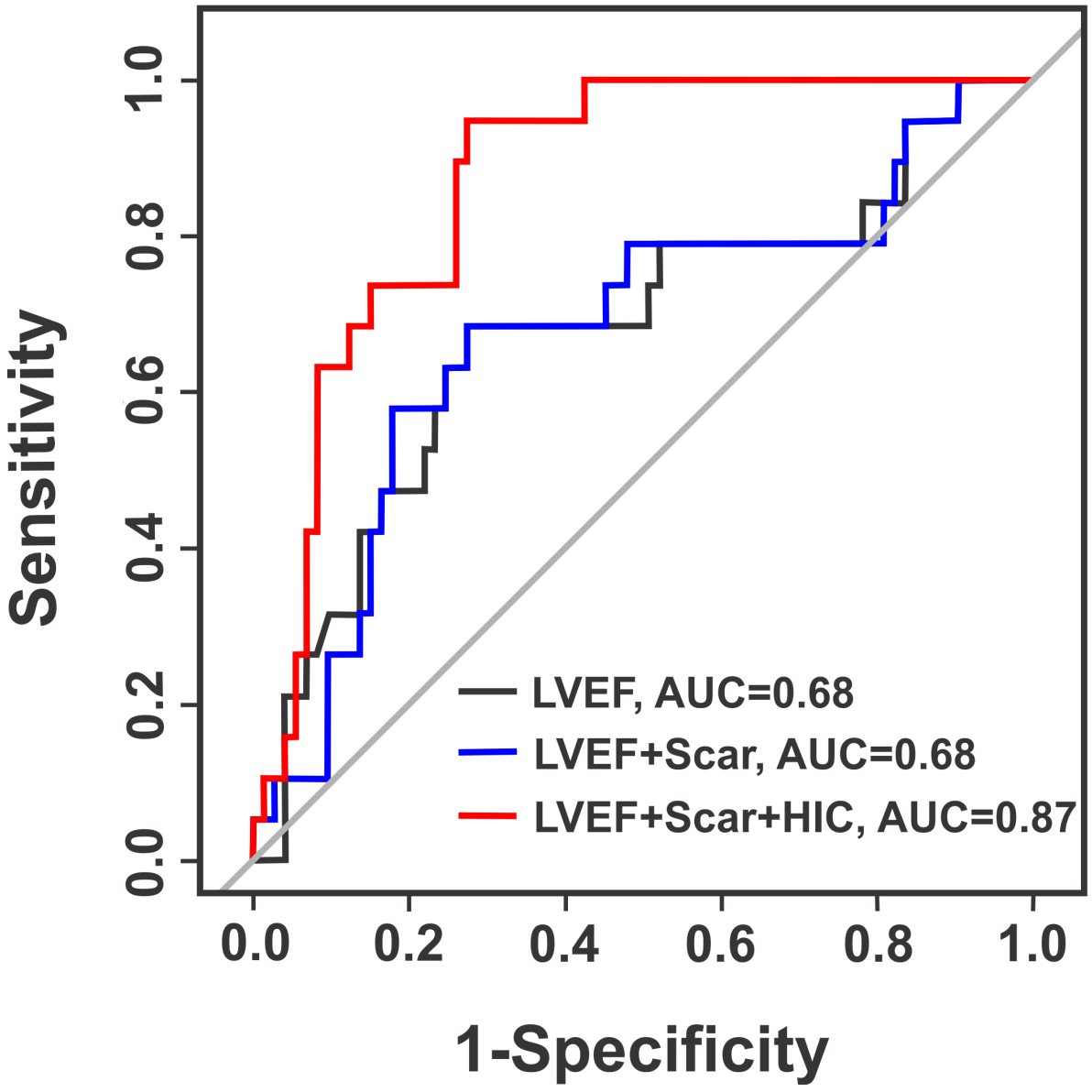

Figure 9.2: *Predictive value of HIC on bSSFP images for primary endpoint*. Corresponding ROC curves for LVEF, LVEF + Scar Size, and LVEF + Scar Size + HIC for the prediction of the primary endpoint. While the addition of total Scar Size alone did not improve the predictive accuracy over LVEF, the addition of HIC improved the AUC from 0.69 to 0.87, suggesting additional prognostic value of HIC.

9.4.2. Canine Studies

9.4.2.1. MRI Findings

Out of 19 animals studied, all animals demonstrated visual LGE evidence for MI. Nine animals were scored as HIC+, and the remainders were scored as HIC-. For each animal, 10-14 spatially matched cine, T_2*-weighted, and LGE image slices were available for analysis. A total of 94 slices (out of 232) demonstrated MI by LGE imaging. Of these, 32 were classified as HIC+ and 62 as HIC- on bSSFP images. T_2*-weighted imaging confirmed the visual presence of distinct hypo-intense regions on all HIC+ slices while HIC- slices failed to show this finding.

Representative LGE, bSSFP, and T_2*-weighted images acquired 12 weeks post-MI are shown from HIC+ and HIC- canines are shown in Figures 9.3 (A-C) and 9.4 (A-C), respectively. Panels 9.3A and 9.3B together show visually evident HIC+ regions within the region of MI. Spatial concordance of HIC+ in bSSFP images (Figure 9.3B) with T_2*-weighted images (Figure 9.3C), a validated approach for detecting iron deposits, was visually evident, suggesting that the HIC+ regions in bSSFP images are likely from iron. In contrast, note that in Figure 9.4, while an MI is evident (Figure 9.4A), there are no hypointense regions within the corresponding MI territories in bSSFP (Figure 9.4B) and T_2*-weighted (Figure 9.4C) images.

Individual and mean cohort T_2* values for remote, HIC+, and HIC- tissue are shown in Figure 9.5. The mean T_2* of HIC+ territories (21±5 ms) were significantly lower than those of remote myocardium (32±3 ms, $p<0.001$) and HIC- territories (30±4 ms, $p<0.001$). The mild difference in T_2* (~2ms) observed between remote tissue and HIC- territories was found to be statistically significant ($p = 0.05$).

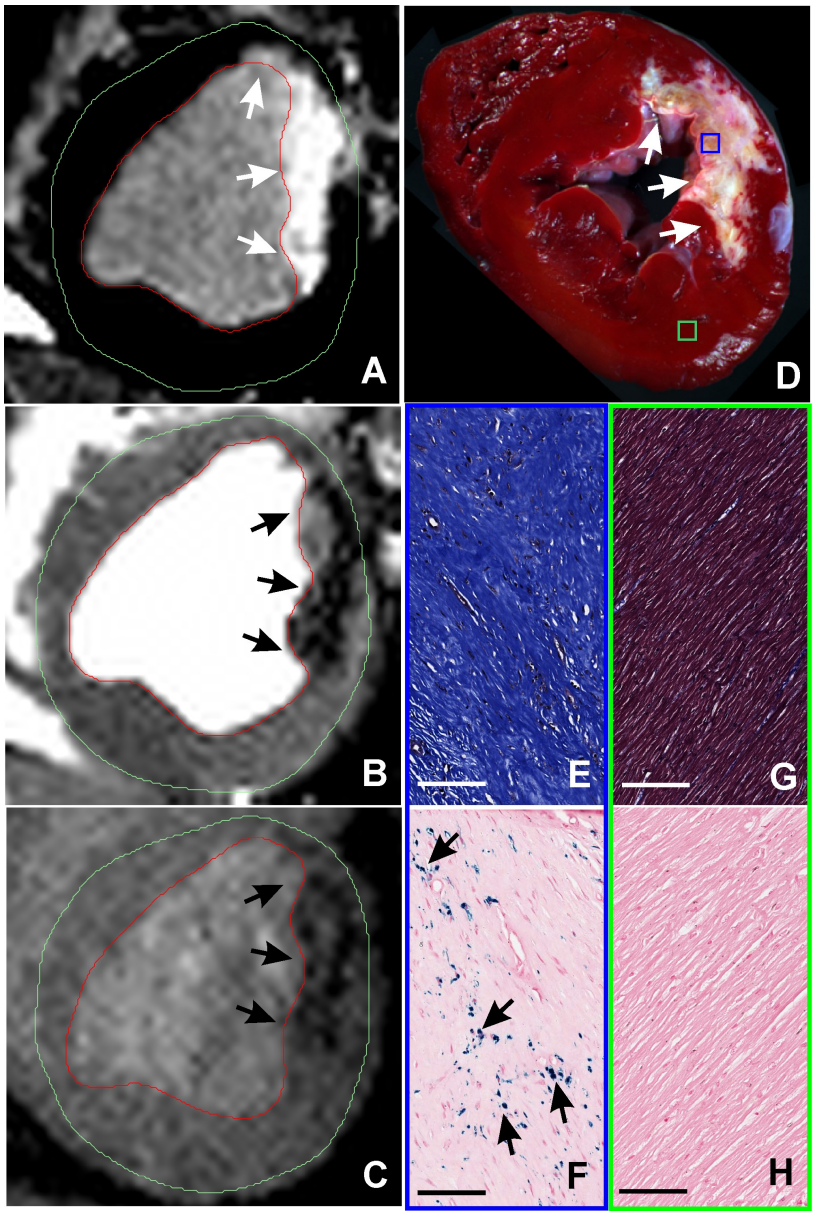

Figure 9.3: *Histological canine validation of HIC on bSSFP images as regions with focal iron deposition.* Representative in-vivo LGE (panel A), bSSFP (panel B), and T_2*-weighted (panel C) images acquired 12 weeks post-MI from a canine classified as HIC+. Hypointense cores could be observed on both bSSFP and T_2*-weighted images (arrows) within the corresponding infarct regions shown on LGE images. Ex-vivo slice-matched TTC image (panel D), EMT staining (panel E: MI territories; panel G: remote territories), and Perl's staining (panel F: MI territories; panel H: remote territories) from the same canine are also shown. Scale bars in EMT and Perl's stained images are 100 microns. EMT staining of MI territories showed extensive collagen deposition (deep blue staining), while Perl's staining showed significant chronic iron depositions (blue deposits pointed at by arrows).

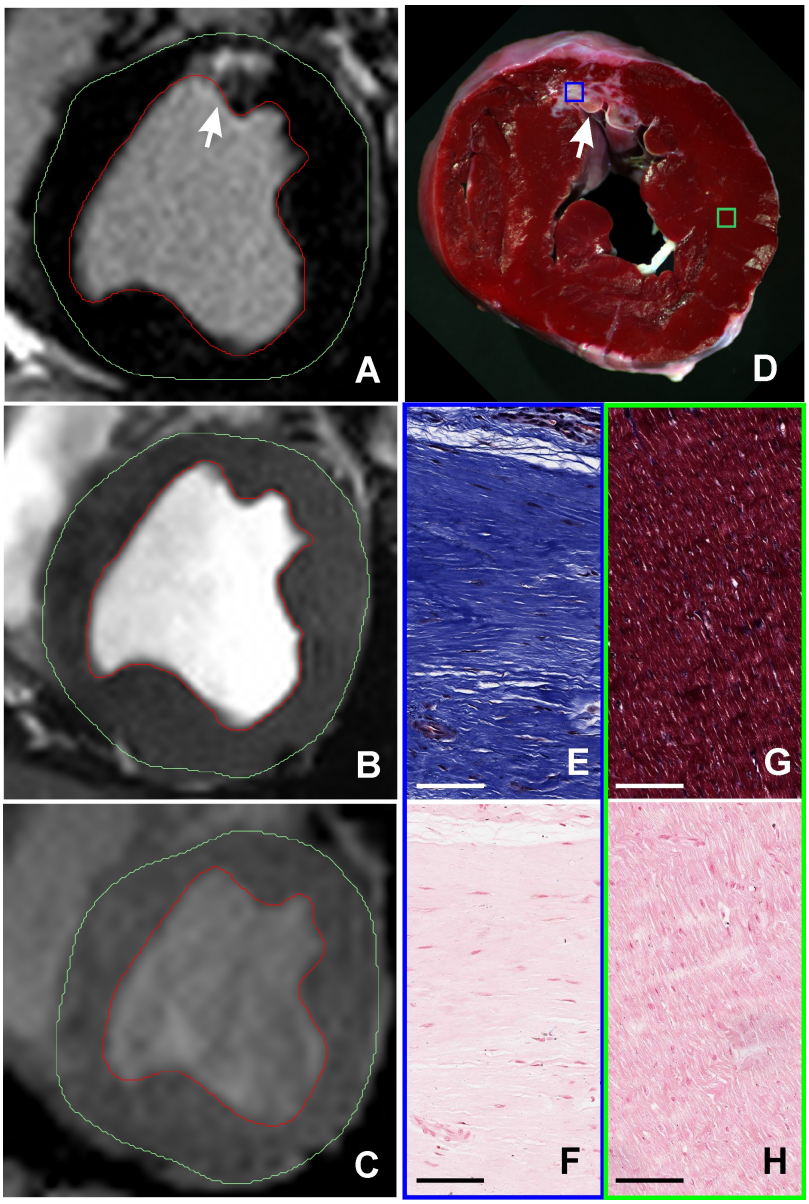

Figure 9.4: *Histological canine validation of the absence of focal iron deposition in HIC- regions*. Representative in-vivo LGE (panel A), bSSFP (panel B), and T_2*-weighted (panel C) images acquired 12 weeks post-MI from a canine at classified as HIC- are shown. No hypointense cores could be observed on either bSSFP or T_2*-weighted images (arrows) within the corresponding infarct regions shown by LGE images. Ex-vivo slice-matched TTC image (panel D), EMT staining (panel E: MI territories; panel G: remote territories), and Perl's staining (panel F: MI territories; H: remote territories) from the same canine are also shown. Scale bars in EMT and Perl's stained images are 100 microns. EMT staining of MI territories showed extensive collagen deposition (deep blue staining), but Perl's staining did not show any chronic iron deposition.

9.4.2.2. Histological Findings

Ex-vivo TTC staining confirmed the presence of MI in both HIC+ (Figure 9.3D) and HIC- (Figure 9.4D) canines. A brown discoloration consistent with chronic iron deposition was observed within the core of MI territories among HIC+ canines, but not HIC- canines. EMT staining showed extensive collagen deposition within the MI territories in both HIC+ (Figure 9.3E) and HIC- slices (Figure 9.4E). Perl's staining confirmed significant chronic iron deposition was only present within the MI territories of HIC+ slices (Figure 9.3F), and not of HIC- slices (Figure 9.4F). EMT and Perl's staining of remote myocardium showed no abnormal pathologies in either canine group (Figures 9.3G-H and 9.4G-H).

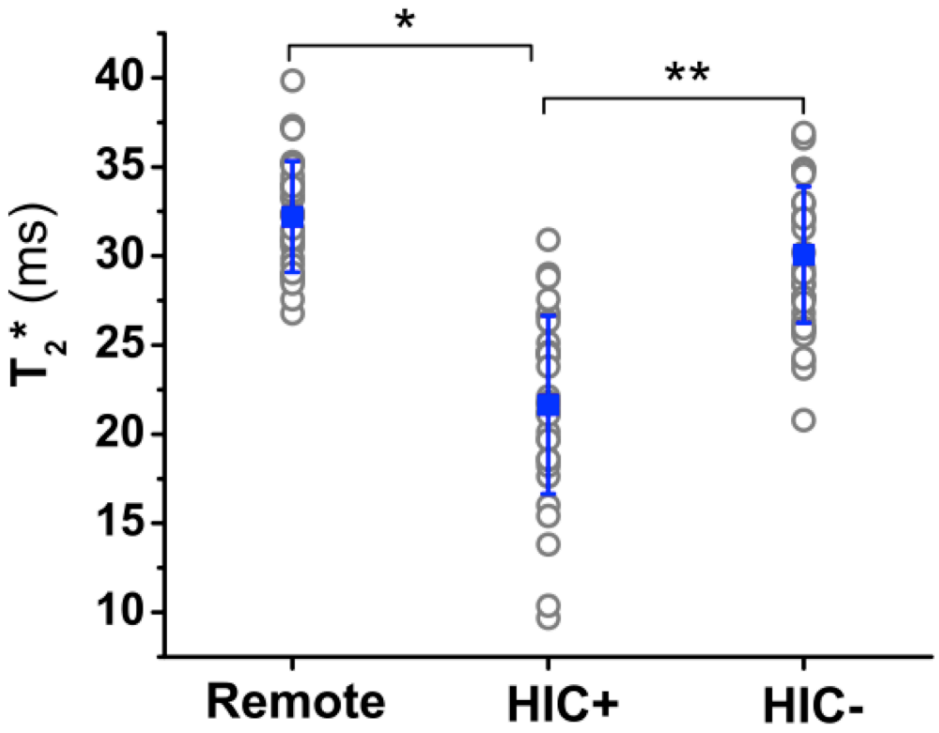

Figure 9.5: *In-vivo T_2* measures from Remote, HIC+, and HIC- segments of the canine myocardium.* Mean T_2* values measured across all animals from Remote myocardial territories was 32.3±-3.1 ms; from HIC+ territories was 21.6.3±5.0 ms and from HIC- territories was 30.1±-3.8 ms. Mean T_2* of HIC+ territories was significantly lower than for Remote territories (*, $p<0.01$) and HIC- territories (**, $p<0.01$).

9.5. Discussion

SCD, typically culminating from mVA, is the leading cause of death in the United States. More than 40% of patients dying of SCD have CMIs. While the ICD is a highly effective tool for the primary prevention of SCD, current guideline recommendations (EF < 35%) inadequately identify those patients at greatest risk, resulting in an undesirably high number needed to treat in order to save one life (520,521,523-527). Accordingly, improved methods for the prediction of mVAs are in critical need.

Multiple studies examining mechanisms of arrhythmogenesis in CMI over the past decade have identified fibrosis as the primary structural substrate associated with mVA (475). It is believed that the presence of collagen fibers acts as a barrier against electrophysiological propagation, facilitating a re-entry circuit. However, not all patients with CMI develop mVA despite the presence of intramyocardial collagen. While scar size has emerged as an important parameter associated with mVA, the exact association of scar size and mVA remains unclear. Klem et al have shown that while there is a sharp increase in SCD incidence (from 10% to 45%) as scar volume increases from 0-5% to 5-10%, the incidence does not appear to be influenced by scar volume beyond this range (349). In contrast, Kwon et al have shown that scar size > 30% is a key risk factor for adverse events (534), and Yan et al have shown that every 10% increase in scar size increases the risk of developing SCD by 50% (282). These observations suggest that other factors in addition to scar size, such as tissue composition, may play an important role. To date, however, only a few studies have examined tissue composition of CMI beyond that of fibrosis.

A number of mechanisms by which heart function may decline and predispose patients to mVA in acute and chronic post-MI settings have been investigated. Among these, it has long

been suspected that iron composites within the AMI region is pro-arrhythmic and has the potential to promote early adverse remodeling and mVAs. This notion inspired the use of chelation therapies to decrease oxidative stress from iron within AMI territories with the goal of decreasing acute injury and marginalizing electrical anomalies (535); however the results have been mixed. Notably, all studies to date examining this therapy were confined to the acute setting (i.e. not more than 1-2 days following an event), and did not randomize subjects (animals or patients) to chelation therapy on the basis of imaging evidence for iron deposition.

MRI has been instrumental in demonstrating that intramyocardial hemorrhage is frequently present in reperfused AMI. However, until recently the fate of extravasated red blood cells within the infarct territory was not known. Chapters 7 and 8 of this thesis has shown that hemorrhagic MIs can lead to chronic iron deposition with a characteristic subendocardial location identified using T_2* MRI. In addition, to demonstrating its actual presence in the chronic setting, these chapter have also shown that such infarcts with iron deposition are associated with worse remodeling, are subjected to prolonged iron-driven inflammation, and exhibit altered electrophysiological parameters (QTc, presence of isolated late potentials, etc.) compared to infarcts without iron deposition. Most notably in-situ forensic pathology studies have consistently noted visually evident hypointense T_2-weighted MRI signals, consistent with iron deposition, among SCD victims with CMIs (482,483). These findings suggest that hemorrhagic AMI may have a significant influence on the development of mVA in the chronic setting. Given that myocarditis represents a frequent cause of life-threatening mVAs and SCD (536-538), a possible mechanism by which iron deposits could influence the arrhythmogenesis is via prolonged iron-driven inflammation in the chronic phase of MI. Additional studies are required

to elucidate the pro-arrhythmic effects of cytokines and inflammatory mediators within iron-laden chronic infarctions.

The loss of bSSFP MRI signal in the presence of π phase shifts induced bulk magnetic susceptibility differences is well known (530). Exploiting this feature, this study performed a retrospective analysis of CMI patients undergoing ICD therapy to assess the incremental predictive value of HIC observed on bSSFP imaging as a marker of iron deposition, over previously explored indices (EF, scar size, gray-zone, QTc and QRS). In univariate analysis using logistic regression, only EF and HIC have been found to be significant predictors, while all other parameters did not reach statistical significance. Using multi-variable logistic regression analysis, only EF and HIC have reached statistical significance. In particular, ROC analysis has shown that when HIC was added to EF, there was a marked increase in the area under the curve compared to EF alone, demonstrating improved predictive accuracy. Moreover, using an established canine model of chronic reperfused MI, this study confirmed the theoretical predictions that iron deposition will appear hypointense on bSSFP-based imaging and that these HIC+ regions have a marked decrease in T_2* by quantitative mapping. In addition, histological observations definitively established that HIC+ regions within MI territories are indeed related to local iron deposition.

In this study, the predictive utility of previously explored indices on the primary outcome was also explored. Among these, only EF was predictive. Total scar size, expressed as a continuous variable, showed a trend towards greater size in those with events, but this was not significant. However, the incidence of primary endpoint was nearly 7 fold higher in patients with a scar size > 10% compared to those with scar size <5%. This is consistent with the previous observations that the risk of developing mVA appears to be low in patients with small

infarcts, and significantly elevated among those with large MIs (349). Based on the canine studies, the source of HIC+ in the patient population is speculated to be due to iron deposition related to a prior hemorrhagic AMI. It is reasonable to expect that HIC+ infarcts are less likely to occur in the setting of small infarcts, and may provide a rational explanation for an observed "threshold phenomenon" relating infarct size to future arrhythmic risk.

While this study showed that the hypointense regions in CMI are likely related to iron deposition, several other sources can mimic hypointensities on bSSFP imaging of the myocardium. First, the well-known banding artifacts can be a source of these artifacts (532). However, such bands tend to be continuous across adjacent organs and are also known to impart flow artifacts. When such banding artifacts were identified to be present in this study, data from those imaging slices were not included in the analysis. Another source of hypointensity in bSSFP images is motion artifact, which is typically observed only in imaging frames when the cardiac motion is severe. Since the current analysis conditioned that the hypointense regions be present throughout the cardiac cycle (i.e. in all frames), motion artifacts were limited from being incorrectly identified as HIC+. Third, although it is possible that calcification may also contribute to hypointensity within the infarct core, iron deposits are more readily visible as hypointense regions since the magnetic susceptibility shift arising from calcium deposits is at least two orders of magnitude weaker than with iron (539). Moreover the arrhythmogenic capacity of calcium deposits within MI is weak (540). Finally, the presence of fat may also appear as hypointense lines ('india-ink' artifact) or hypointense lines enclosing hyperintense territories in SSFP images (531). Based on the definition that HIC+ regions need to have at least eight contiguous nearest neighbor pixels, fatty infarcts were limited from being counted as HIC+.

9.5.1. Study Limitations

This study has several limitations. First, this is a retrospective observational study from a single-center with limited sample size. Thus, the findings from this study need to be confirmed in a larger, multicenter setting with adequate power to examine all relevant indices on the primary outcome. Second, histologic confirmation of iron deposition was not available in the patient cohort due to its retrospective study design and inability to obtain post-mortem tissue for iron-sensitive staining. Further, while every effort was made to remove potential confounders in the image analysis, the scoring of hypointense cores (HIC) in clinical cohorts may be improved using T_2* mapping sequences. Given the retrospective nature of this study, T_2* acquisitions were not routinely performed as part of the MRI examination, and were therefore not available for analysis. However, the ability to categorize HIC using routine bSSFP imaging offers greater generalizability to routine clinical practice. Finally, only MI patients who were considered eligible for ICD therapy (i.e. EF < 35%) were recruited. Of great interest is the prognostic utility of this technique among those currently not meeting eligibility criteria for ICD therapy. Accordingly, further studies are needed to examine the relation between post-MI iron and mVA in patients with EF > 35%.

9.6. Conclusion

This study provides sentinel evidence that hypointense cores (HIC) on bSSFP imaging may be a powerful predictor of mVA in patients with CMIs. Further prospective studies sufficiently powered to evaluate the incremental utility of HIC versus contemporary risk prediction markers are warranted.

CHAPTER 10

Persistent Microvascular Obstruction as a Source for Iron Deposition in Chronic Myocardial Infarctions

10.1. Abstract

Persistent microvascular obstruction (PMO) is an important predictor of long-term adverse LV remodeling and adverse cardiac outcomes. However, the exact mechanism by which PMO, which typically resolves within a few weeks, can exert adverse effects throughout the post-MI period is not well understood. The purpose of this study is to investigate whether PMO, with or without reperfusion hemorrhage, can resolve into localized iron deposition within CMI territories, and thereby lead to adverse pathological effects as elucidated in the previous chapters.

Seventeen canines were subjected to I-R injury (Reperfused group), while another 16 canines were subjected to permanent ligation of LAD (Non-Reperfused group). T_2*-weighted and LGE images were acquired from the canines on a 3T clinical system at 7 days (acute) and 56 days (chronic) post-MI.. The presence and extent of infarct and PMO were evaluated from LGE images, while the presence and extent of iron deposition within MI territories were evaluated using T_2*-weighted images. LV remodeling parameters including EDV, ESV, EF, and EDSI were measured. Following the chronic MRI study, canines were euthanized and ex-vivo gross and microscopic histochemical staining was performed using TTC, EMT, and Perls stains. Inflammatory activity associated with iron deposition was studied using immunohistochemical staining with monoclonal antibodies for Mac387, TNF-α, and MMP-9.

Nine canines from the Reperfused group had PMO and acute reperfusion hemorrhage as evidenced by day 7 LGE and T_2*-weighted images, and all the canines subsequently chronic iron deposition within MI territories on day 56 (PMO^+/T_2*^+). Four canines from the Reperfused group had PMO as observed on day 7 LGE images, but did not sustain acute reperfusion hemorrhage as observed on day 7 T_2*-weighted images (PMO^+/T_2*^- group). All the canines in the PMO^+/T_2*^- group had chronic iron deposition within MI territories on day 56. The remaining four canines in the Repefused group did not sustain PMO on day 7, acute reperfusion hemorrhage on day 7, or chronic iron deposition on day 56 (PMO^-/T_2*^- group). Canines in the PMO^+/T_2*^+ group had the worst LV remodeling between the acute and chronic phases, followed by the PMO^+/T_2*^- and PMO^-/T_2*^- groups respectively.

Sixteen canines from the Non-reperfused group had PMO and acute iron deposition as evidenced by day 7 LGE and T_2*-weighted images, and all the canines subsequently chronic iron deposition within MI territories on day 56 (NR-PMO^+/T_2*^+). Only one canine from the Non-reperfused group did not sustain PMO on day 7, and acute or chronic iron deposition on day 56 (NR-PMO^-/T_2*^- group). Canines in the NR-PMO^+/T_2*^+ group had the poorer LV remodeling relative to the canine in the NR-PMO^-/T_2*^- group.

In both Reperfused and Non-reperfused groups, the extent of infarct and iron deposition measured in both acute and chronic phases were independent and significant predictors of the change in EDSI between the acute and chronic phases. Perls staining confirmed the presence of chronic iron deposition in PMO^+/T_2*^+, PMO^+/T_2*^-, and NR-PMO^+/T_2*^+ groups, but not in PMO^-/T_2*^- and NR-PMO^-/T_2*^- groups. The extent of chronic iron deposition seen on Perls staining was directly related to the extent of Mac387, TNF-α, and MMP-9 activities.

In conclusion, PMO, with or without reperfusion hemorrhage, can lead to iron deposition within CMIs. Such chronic iron deposition is associated with adverse LV remodeling and significant pro-inflammatory burden.

10.2. Introduction

Infarct size is long known to be an independent predictor of adverse LV remodeling (92,107,347,405-407,541) and large reperfused AMIs have been known to be commonly accompanied by MO (20,135). Several clinical and pre-clinical studies now support the notion that in addition to infarct size, the extent of MO is also an important independent predictor of adverse LV remodeling (136,137,139,143,149,178,180,198,241,265). Recent studies have shown that persistent MO (PMO), defined as hypointense cores on LGE images at 7-10 days post-reperfusion, is a stronger predictor of adverse cardiac outcomes than early MO (138,140,142,145-147,179). However, how PMO, a phenomenon limited to the acute/sub-acute period of MI, imparts adverse remodeling throughout the post-MI period is incompletely understood.

MO is frequently associated with intramyocardial hemorrhage in reperfused MIs (167,173,185,291), which in turn can lead to localized iron deposition within infarcted territories in the chronic phase as shown in the previous chapters. Hemorrhage itself has been implicated in adverse cardiac outcomes (141,196-199,463), and recent studies have further shown that chronic iron deposition secondary to reperfusion hemorrhage is associated with prolonged inflammatory activity and long-term adverse LV remodeling (430,542). The hemorrhage/chronic iron-mediated pathway could potentially explain the mechanism by which MO can lead to long-term adverse effects. However, MO is not always accompanied with acute reperfusion hemorrhage (141),

which further poses the question of how MO in the absence of hemorrhage can still lead to adverse cardiac outcomes. Recent studies have shown that MO delays the recruitment of monocytes to the MO territories in the acute and sub-acute period post-reperfusion, which could potentially delay the healing process and lead to adverse functional outcomes (542).

This study investigated whether PMO even in the absence of acute reperfusion hemorrhage can resolve into iron deposition or promote prolonged inflammation in CMIs, which can potentially unravel how MO imparts adverse long-term effects on the infarcted heart and underscore iron as a therapeutic target post-MI. Specifically, this study hypothesized that (a) every PMO (with or without reperfusion hemorrhage) can lead to prolonged accumulation of iron, the extent of which is determined by the size of PMO; (b) extent of iron deposition within the CMI territories is a reflection of ongoing inflammatory activity; and (c) iron deposits post-PMO resolution is a potent, independent, predictor of adverse LV remodeling. To systematically examine this hypothesis, established canine models that are known to lead to MO with (late reperfusion) and without (no reperfusion) hemorrhage were used. Cardiac MRI was used to characterize the spatiotemporal relationships between PMO, iron deposits, and LV remodeling indices, while histopathological studies were performed to microscopically map and quantify the relation between iron-rich CMI regions and pro-inflammatory burden.

10.3. Methods

10.3.1. Animal Preparation and MRI Protocol

Canines (n=40) were studied according to the protocols approved by the Institutional Animal Care and Use Committee. Twenty canines were subjected to I-R injury by occluding the LAD

artery for 3 hours followed by reperfusion (Reperfused Group). The remaining 20 canines were subjected to permanent ligation of the LAD (Non-Reperfused Group). All canines underwent cardiac MRI at 7 days (acute) and 56 days (chronic) post-MI on a 3T clinical MRI system (MAGNETOM Verio, Siemens Healthcare, Erlangen, Germany). ECG-triggered breath-held 2D cine-SSFP images (20-25 cardiac phases; TR/TE = 3.5/1.75 ms; α = 70°; BW=930 Hz/pixel), T_2*-weighted images (multi-echo GRE; TR=12 ms; 6 TEs = 2.0–9.5ms with ΔTE=1.5ms; α = 10° and BW = 930 Hz/pixel), and LGE images (IR-prepared FLASH acquired 10-15 minutes following intravenous infusion of gadopentetate dimeglumine (Magnevist, Bayer Healthcare Pharmaceuticals Inc., Wayne, NJ); optimal TI to null remote myocardium; TR/TE = 3.0/1.5 ms, α = 25°; BW = 586 Hz/pixel) were acquired along the short-axis direction covering the entire LV. Commonly used imaging parameters for all the scans were in-plane resolution = 1.4x1.4 mm^2, slice thickness = 6 mm, and number of averages = 1. Animals were euthanized following the day 56 MRI scan and their hearts were excised for histological examination.

10.3.2. Image Analyses

All MR image analyses were performed on cvi[42] image processing software (Circle Cardiovascular Imaging Inc., Calgary, AB, Canada). LV function parameters such as EDV, ESV, EF, and EDSI were calculated from the cine-SSFP images and normalized to the body surface area using standard methods. Percentage change in the LV function parameters (ΔEDV, ΔESV, ΔEF, and ΔEDSI) between the acute and chronic phases post-MI were also calculated.

Remote myocardium was identified on LGE images as the region showing no hyperintensity and reference ROI was drawn in it. Infarcted myocardium was then defined on LGE images using the Mean+5SD technique relative to the reference ROI (414-416). Persistent

microvascular obstruction (PMO) was defined as the hypointense core within the hyperintense infracted myocardium identified on LGE images using the Mean+5SD criterion. For the sake of simplicity, the classic PMO arising from the no-reflow phenomenon in reperfused MIs is henceforth referred to as just PMO, while the PMO observed on the day 7 LGE images in non-reperfused MIs is referred to as NR-PMO (non-reperfused persistent microvascular obstruction). Infarct size was calculated by summing the volumes of the hyperintense regions on LGE images identified using the Mean+5SD criterion and the hypointense PMO cores.

The presence of iron arising from blood degradation within infarcted myocardium were identified as hypointense regions on T_2*-weighted images confined to the hyperintense LGE territory. The reference ROIs drawn on LGE images were copied on to the corresponding T_2*-weighted images and the spatial extent of the hypointense regions on T_2*-weighted images were identified using the Mean-2SD criterion relative to the reference ROI (199,293). Off-resonance artifacts arising due to susceptibility differences at the heart-lung interface were manually excluded.

Based on the presence or absence of PMO and iron within the MI territories at 7 days post-MI, canines from the Reperfused group were classified as PMO^{+}/T_2*^{+} (both PMO and T_2* loss are present), PMO^{+}/T_2*^{-} (PMO is present but T_2* loss is absent), PMO^{-}/T_2*^{+} (PMO is absent but T_2* loss is present), and PMO^{-}/T_2*^{-} (both PMO and T_2* loss are absent). Similarly, based on the presence or absence of NR-PMO and iron within the infarcted territories on day 7 post-MI, canines from the Non-Reperfused group were classified as NR-PMO^{+}/T_2*^{+}, NR-PMO^{+}/T_2*^{-}, NR-PMO^{-}/T_2*^{+}, and NR-PMO^{-}/T_2*^{-}. Infarct and iron volumes were calculated at both acute and chronic phases across all the groups as the percentage of total LV myocardial

volume. T_2* values of the remote myocardium, entire infarcted myocardium, and the iron deposits within the infarcted myocardium were measured.

10.3.3. Histopathology

Freshly explanted hearts from the canines were sectioned along the short-axis direction from base to apex into 1 cm thick slices. Infarcted and remote territories were identified on the basis of TTC staining. Ex-vivo 2D T_2*-weighted images (same parameters were used as those for the in-vivo images) were subsequently acquired from the slices positive for MI on TTC staining. Based on the presence of hypointense cores within the infarcted territories on the ex-vivo T_2*-weighted images, slices were classified as those with and without iron deposition (T_2*+ and T_2*− respectively). Paraffin-embeded serial sections (5 μm) from representative segments of infarcted and remote areas were stained with H&E stain for necrosis, EMT stain for fibrosis, and Perl's stain for iron deposition. For immunostaining, sections were probed with antibodies against the following markers of inflammatory activity: Mac387 (Abcam, ab22506, Cambridge, MA), TNF-α (Abcam, ab6671, Cambridge, MA), and MMP-9 (Abcam, ab38898, Cambridge, MA).

All histological analyses were performed at the Translational Pathology Core Laboratory, David Geffen School of Medicine, University of California, Los Angeles. Slides were digitized on a ScanScope AT (Aperio Technologies, Vista, CA) instrument and morphimetric analysis was performed using Definiens Tissue Studio (Definiens, Parsippany, NJ) software. Predefined stain specific algorithms and classification tools were created utilizing Definiens eCognitionNetwork Language™ to identify positive and negative stained area under the marker (μm²) within each tissue region in a non-biased method. Thresholds were set to classify the following: blue for iron, and DAB stain for Mac387, TNF-α, and MMP-9 positive cells.

10.3.4. Statistical Analyses

All statistical analyses were performed using IBM SPSS Statistics (version 21.0, IBM Corporation, Armonk, NY). Shapiro-Wilk test and quantile-quantile plots were used to test the normality of the data. Depending on the normality of the data, analysis of variance or Kruskal-Wallis test along with post-hoc analyses were used to compare measurements among the different canine groups. Bonferroni correction was used for multiple comparisons. Univariate and multivariate linear regression analyses were performed to determine the associations among different measurement variables. Statistical significance was set at $p<0.05$. Normal data is expressed as Mean ±SD, while non-normal data is expressed as Median with interquartile range.

10.4. Results

Three canines within the Reperfused group and four canines from the Non-Reperfused group died within the first week post-MI. The remaining 17 canines from the Reperfused group and 16 canines from the Non-Reperfused group sustained MIs as confirmed by LGE images on day 7.

10.4.1. Chronic Iron Deposition in Reperfused Myocardial Infarctions

Within the Reperfused group, 9 canines were classified as $PMO^{+}/T_2{*}^{+}$, 4 canines were classified as $PMO^{+}/T_2{*}^{-}$, and 4 canines were classified as $PMO^{-}/T_2{*}^{-}$ at 7 days post-MI. None of the reperfused canines showed iron deposition within the infarcted territories in the absence of PMO on day 7 post-MI. Representative T_2*-weighted and LGE images from the $PMO^{+}/T2{*}^{+}$, $PMO^{+}/T_2{*}^{-}$, and $PMO^{-}/T_2{*}^{-}$ groups in both acute and chronic phases are shown in Figure 10.1, along with corresponding ex-vivo histology sections stained with TTC, EMT, and Perl's stains.

No PMO could be observed on LGE images in all the 3 groups in the chronic phase. In the $PMO^{+}/T_2{*}^{+}$ group, significant T_2* losses indicative of iron deposition could be visually observed in all the canines within the infarcted territories in both acute and chronic phases.

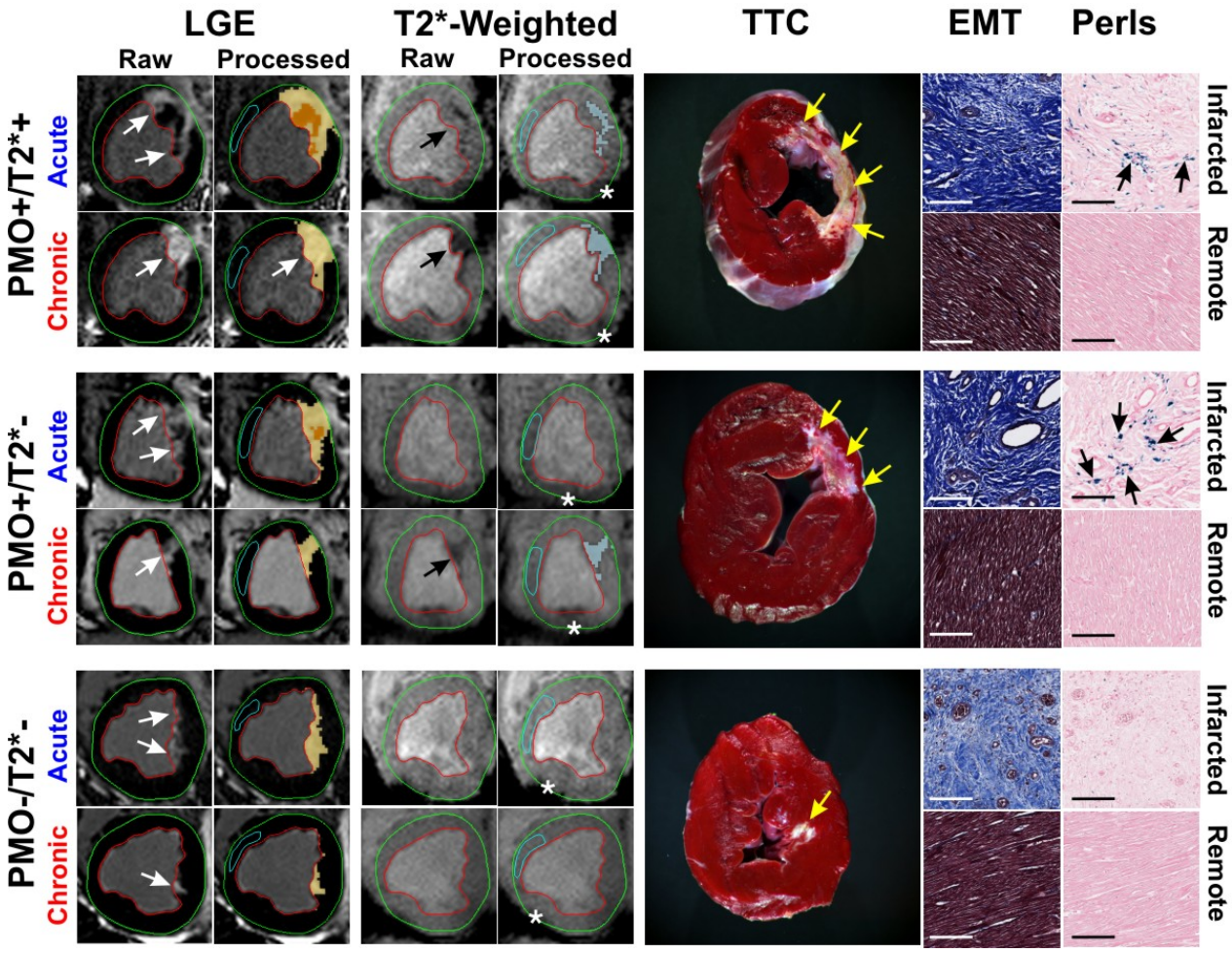

Figure 10.1: *Chronic iron deposition in reperfused myocardial infarctions.* Representative in-vivo raw and processed LGE and T_2*-weighted images from Reperfused canines acquired in both acute and chronic phases post-MI are shown. Arrows point to the sites of MI and iron deposition on LGE and T_2*-weighted images respectively. Corresponding ex-vivo histological sections stained with TTC, EMT and Perls stain are also shown. Note the significant chronic iron deposition in the $PMO^{+}/T_2{*}^{-}$ group, despite the absence of acute reperfusion hemorrhage. Perls stain confirmed the presence of chronic iron deposition (blue deposits pointed at by the arrows) in the $PMO^{+}/T_2{*}^{+}$ and $PMO^{+}/T_2{*}^{-}$ groups, but not in the $PMO^{-}/T_2{*}^{-}$ group. Asterisks in the T_2*-weighted images point to the sites of off-resonance artifacts that were manually excluded in the final analysis.

While none of the canines in the PMO^{+}/T_2*^{-} showed T_2* losses within the infarct in the acute phase, all the canines subsequently showed significant T_2* losses within the infarct in the chronic phase. None of canines in the PMO^{-}/T_2*^{-} group showed any T_2* losses within the infarct in both acute and chronic phases.

TTC images confirmed the presence of MI in all the groups (Figure 10.1). EMT staining showed extensive collagen deposition within the infarcted territories, but not in the remote myocardium (Figure 10.1). Perls staining further confirmed the presence of iron deposition in the chronic phase in the PMO^{+}/T_2*^{+} and PMO^{+}/T_2*^{-} groups, and the absence of iron deposition in the PMO^{-}/T_2*^{-} group (Figure 10.1).

In the acute phase, mean infarct volume in the PMO^{+}/T_2*^{+} group (33.9±15.1%) was significantly higher than that of PMO^{+}/T_2*^{-} group (17.6±6.6%, $p<0.001$) and the $PMO^{-}/T2*^{-}$ group (12.2±8.1%; Figure 10.2A). Mean PMO volume in the PMO^{+}/T_2*^{+} group (6.1±6.6%) was also significantly higher than that of the PMO^{+}/T_2*^{-} group (2.4±1.1%, $p<0.001$; Figure 10.2B). In the chronic phase, mean infarct volume in the PMO^{+}/T_2*^{+} group (20.9±15.6%; Figure 10.2A) was significantly higher than that of PMO^{+}/T_2*^{-} group (10.2±3.8%, $p<0.001$) and the PMO^{-}/T_2*^{-} group (5.6±4.9%, $p<0.001$). Mean chronic iron volume in the PMO^{+}/T_2*^{+} group (5.3±3.7%) was also significantly higher than that of the PMO^{+}/T_2*^{-} group (2.6±1.6%, $p<0.001$; Figure 10.2C).

Relative to the acute phase, mean iron volume in the chronic phase decreased significantly in the PMO^{+}/T_2*^{+} group (9.3±6.6% vs. 5.3±3.7%, $p = 0.02$; Figure 10.2C). In contrast, mean iron volume in the PMO^{+}/T_2*^{-} group increased from 0 in the acute phase to 2.6±1.6% ($p = 0.01$; Figure 10.2C). When calculated as a percentage of the total infarct volume, mean iron volume significantly increased between acute and chronic phases in both PMO^{+}/T_2*^{+} (26.3±15.6% vs. 33.8±15.5%, $p = 0.003$) and PMO^{+}/T_2*^{-} groups (0 vs. 26.7±12.5%, $p<0.001$;

Figure 10.2D). Significant linear relationships were observed between the PMO volume and acute iron volume (R^2 = 0.40, p<0.001; Figure 10.2E), and PMO volume and chronic iron volume (R^2 = 0.72, p<0.001; Figure 10.2F).

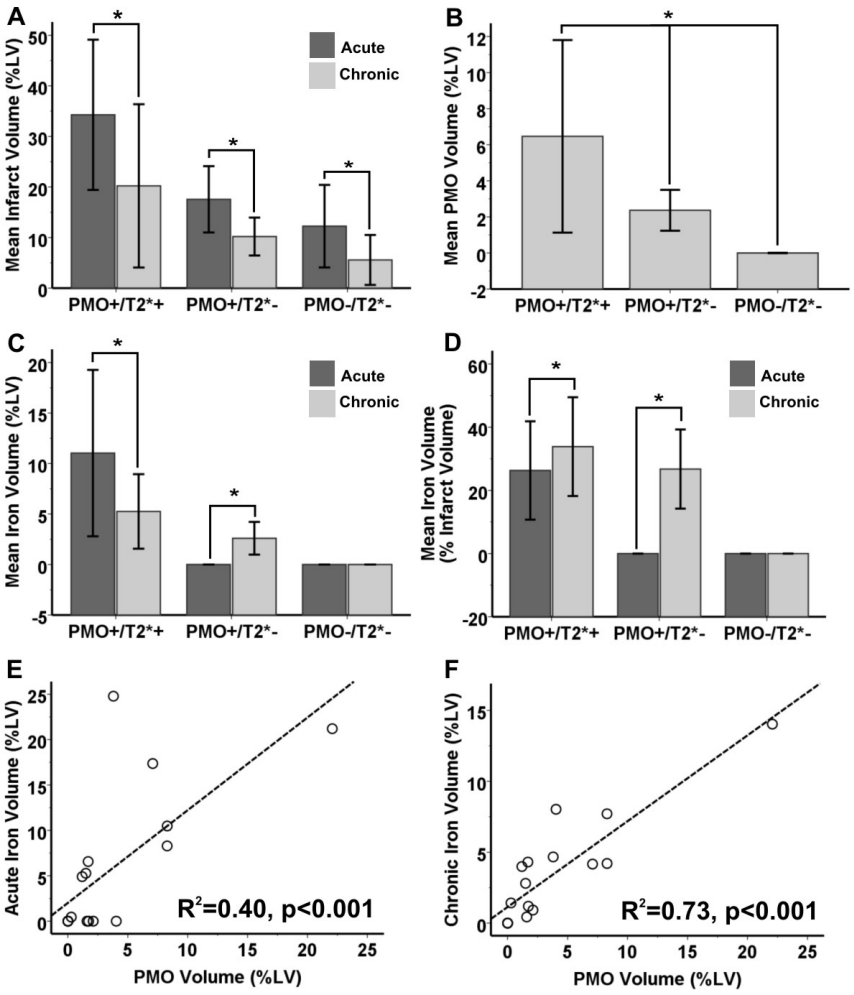

Figure 10.2: *Infarct, PMO, and iron volumes in reperfused myocardial infarctions.* Mean infarct volume (%LV, panel A), PMO volume (%LV, panel B), iron volume (%LV, panel C), and iron volume as percentage of infarct volume (panel C) measured from reperfused canines are shown. Note that, while infarct volume, iron volume, and iron volume as percentage of infarct volume are reported for both acute and chronic phases, PMO volume is only reported for acute phase as PMO completely resolved in the chronic phases. Strong linear relationships of PMO volume with acute iron volume (R^2 = 0.40, p<0.001, panel E) and chronic iron volume (R^2 = 0.73, p<0.001, panel F) were observed. *Statistically significant difference (p<0.05).

10.4.2. Chronic Iron Deposition in Non-Reperfused Myocardial Infarctions

Within the Non-Reperfused group, 15 canines were classified as NR-PMO^{+}/T_2*$^{+}$, and 1 canine was classified as NR-PMO^{-}/T_2*$^{-}$. No canine was classified as either NR-PMO^{+}/T_2*$^{+}$ or NR-PMO^{-}/T_2*$^{-}$. Representative T_2*-weighted and LGE images from the NR-PMO^{+}/T_2*$^{+}$ and NR-PMO^{-}/T_2*$^{-}$ groups in both acute and chronic phases are shown in Figure 10.3, along with corresponding ex-vivo histology sections stained with TTC, EMT, and Perl's stains. No PMO could be observed on LGE images in both the groups in the chronic phase. In the NR-PMO^{+}/T_2*$^{+}$ group, significant T_2* losses indicative of iron deposition could be visually observed in all the canines within the infarcted territories in both acute and chronic phases. The only canine in the NR-PMO^{-}/T_2*$^{-}$ group did not show any T_2* losses within the infarct in both acute and chronic phases. Perls staining further confirmed the presence of iron deposition in the chronic phase in the NR-PMO^{+}/T_2*$^{+}$ group, but not in the NR-PMO^{-}/T_2*$^{-}$ group.

TTC images confirmed the presence of MI in all the groups (Figure 10.3). EMT staining showed extensive collagen deposition within the infarcted territories, but not in the remote myocardium (Figure 10.3). Perls staining further confirmed the presence of iron deposition in the chronic phase in the PMO^{+}/T_2*$^{+}$ and PMO^{+}/T_2*$^{-}$ groups, and the absence of iron deposition in the PMO^{-}/T_2*$^{-}$ group (Figure 10.3).

Mean infarct volume in the NR-PMO^{+}/T_2*$^{+}$ group was significantly higher than that of NR-PMO^{-}/T_2*$^{-}$ group in both acute (15.4±8.7% vs. 3.9%, $p<0.001$) and chronic phases (7.6±5.9% vs. 2.6%, $p<0.001$; Figure 10.4A). Relative to the acute phase, mean iron volume in the chronic phase decreased significantly in the NR-PMO^{+}/T_2*$^{+}$ group (2.7±2.5% vs. 2.2±1.7%, $p = 0.02$; Figure 10.4C). When calculated as a percentage of the total infarct volume, mean iron volume significantly increased between acute and chronic phases in the NR-PMO^{+}/T_2*$^{+}$ group

(17.7±10.5% vs. 33.2±15.1%, p = 0.01; Figure 10.4D). Significant linear relationships were observed between the NR-PMO volume and acute iron volume (R^2 = 0.87, p<0.001; Figure 10.4E), and NR-PMO volume and chronic iron volume (R^2 = 0.65, p<0.001; Figure 10.4F).

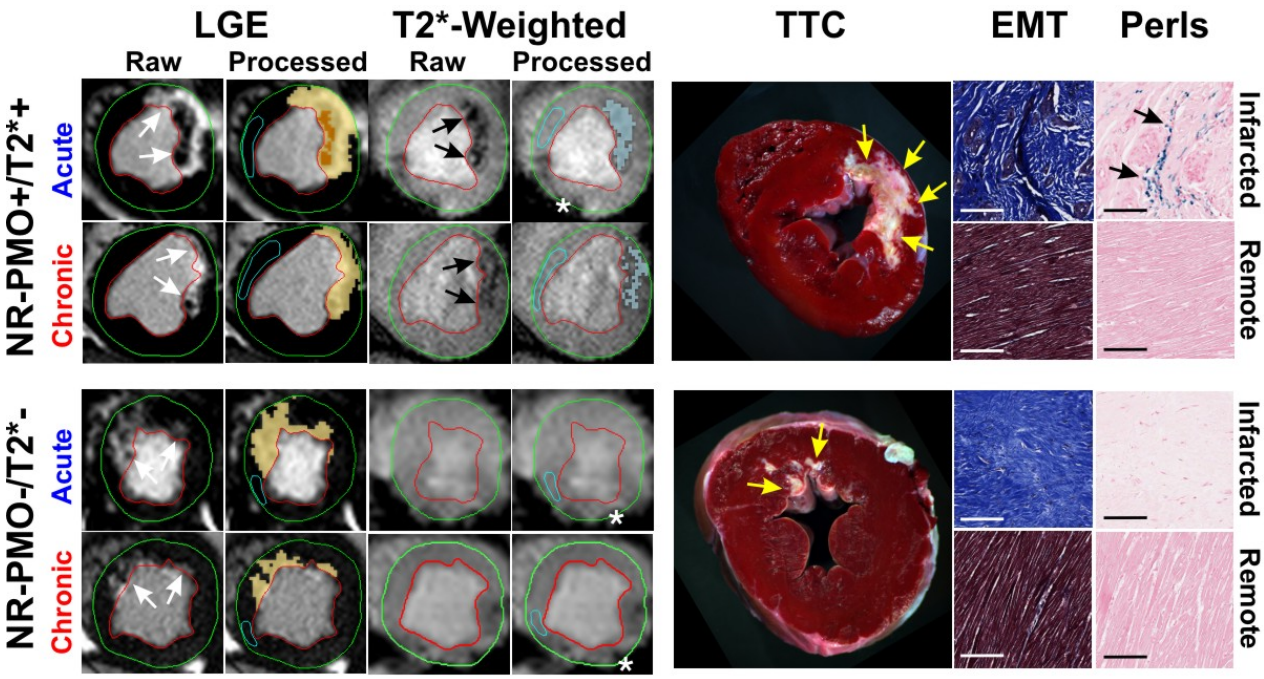

Figure 10.3: *Chronic iron deposition in non-reperfused myocardial infarctions.* Representative in-vivo raw and processed LGE and T_2*-weighted images from Non-reperfused canines acquired in both acute and chronic phases post-MI are shown. Arrows point to the sites of MI and iron deposition on LGE and T_2*-weighted images respectively. Corresponding ex-vivo histological sections stained with TTC, EMT and Perls stain are also shown. Note the significant chronic iron deposition in the NR-PMO$^+$/T_2*$^+$ group as observed on the in-vivo T_2*-weighted images. Perls stain confirmed the presence of chronic iron deposition (blue deposits pointed at by the arrows) in the NR-PMO$^+$/T_2*$^+$ group, but not in the NR-PMO$^-$/T_2*$^-$ group. Asterisks in the T_2*-weighted images point to the sites of off-resonance artifacts that were manually excluded in the final analysis.

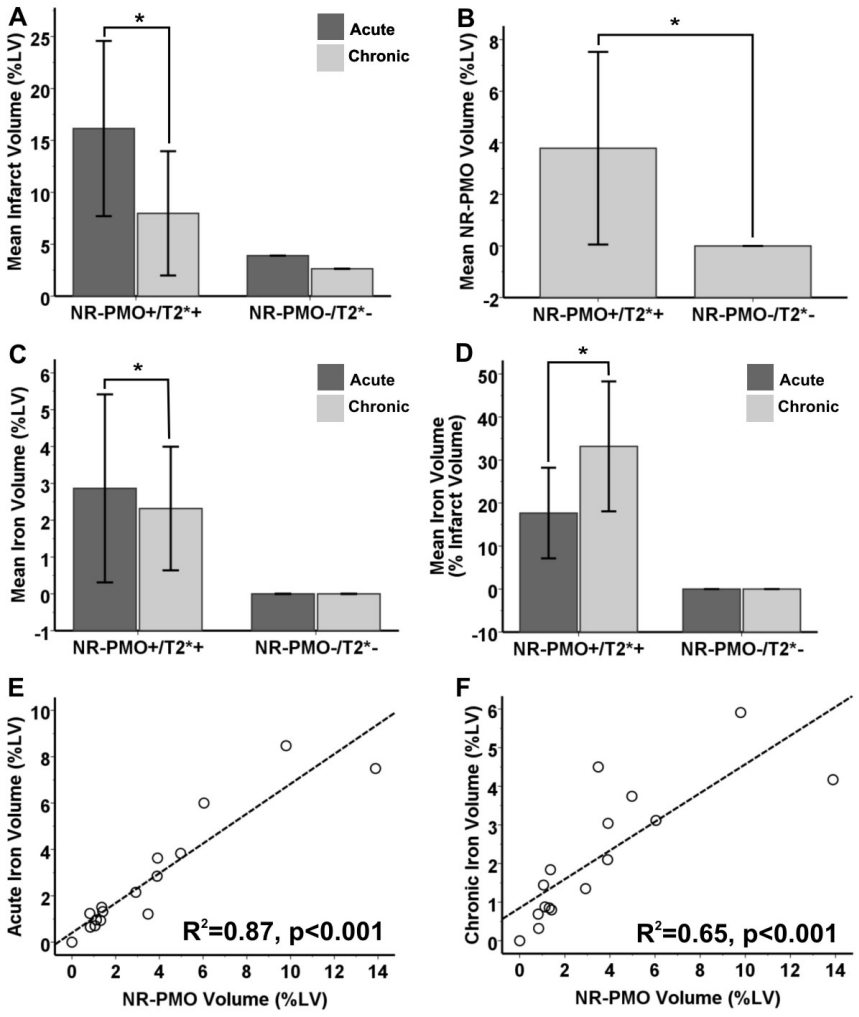

Figure 10.4: *Infarct, PMO, and iron volumes in non-reperfused myocardial infarctions.* Mean infarct volume (%LV, panel A), NR-PMO volume (%LV, panel B), iron volume (%LV, panel C), and iron volume as percentage of infarct volume (panel C) measured from non-reperfused canines are shown. Note that, while infarct volume, iron volume, and iron volume as percentage of infarct volume are reported for both acute and chronic phases, NR-PMO volume is only reported for acute phase as NR-PMO completely resolved in the chronic phases. Strong linear relationships of NR-PMO volume with both acute iron volume (R^2 = 0.87, p<0.001, panel E) and chronic iron volume (R^2 = 0.65, p<0.001, panel F) were observed. *Statistically significant difference (p<0.05).

10.4.3. Left-Ventricle Remodeling in Reperfused Myocardial Infarctions

Canines in the $PMO^{+}/T_2{*}^{+}$ group had significantly larger EDV (Figure 10.5A), larger ESV (Figure 10.5B), lower EF (Figure 10.5C), and larger EDSI (Figure 10.5D) compared to the canines in the $PMO^{+}/T_2{*}^{-}$ and $PMO^{-}/T_2{*}^{-}$ groups in both acute and chronic phases (EDV and ESV: $p<0.001$ for all comparisons in both acute and chronic phases; EF: $p<0.001$ for all comparisons in the acute and chronic phases, except $p = 0.03$ for chronic EF between $PMO^{+}/T_2{*}^{-}$ and $PMO^{-}/T_2{*}^{-}$; EDSI: $p = 0.001$ for acute EDSI between $PMO^{+}/T_2{*}^{+}$ and $PMO^{+}/T_2{*}^{-}$, $p = 0.01$ for acute EDSI between $PMO^{+}/T_2{*}^{-}$ and $PMO^{-}/T_2{*}^{-}$, $p<0.001$ for acute EDSI between $PMO^{+}/T_2{*}^{+}$ and $PMO^{-}/T_2{*}^{-}$, and $p<0.001$ for all comparisons in the chronic phase; Figure 10.5). The $PMO^{+}/T_2{*}^{+}$ group also had significantly larger EDV ($p=0.04$), larger ESV ($p=0.03$), lower EF ($p=0.03$), and larger EDSI ($p=0.02$) in the chronic phase compared to the acute phase (Figure 5). However, there was no significant difference in the LV remodeling parameters between the acute and chronic phases in the $PMO^{+}/T_2{*}^{-}$ (EDV: $p = 0.30$, ESV: $p = 0.87$, EF: $p = 0.81$, EDSI: $p = 0.39$) and $PMO^{-}/T_2{*}^{-}$ (EDV: $p = 0.11$, ESV: $p = 0.57$, EF: $p = 0.98$, EDSI: $p = 0.65$) groups. Compared to the canines in the $PMO^{+}/T_2{*}^{-}$ and $PMO^{-}/T_2{*}^{-}$ groups, canines in the $PMO^{+}/T_2{*}^{+}$ group had significantly higher ΔEDV (Figure 10.5E), ΔESV (Figure 10.5F), ΔEF (Figure 10.5G), and ΔEDSI (Figure 10.5H) between the acute and chronic phases (ΔEDV, ΔESV, ΔEDSI: $p<0.001$ for all comparisons; ΔEF: $p<0.001$ for $PMO^{+}/T_2{*}^{+}$ vs. $PMO^{+}/T_2{*}^{-}$ and $PMO^{+}/T_2{*}^{+}$ vs. $PMO^{-}/T_2{*}^{-}$, $p = 0.98$ for $PMO^{+}/T_2{*}^{-}$ vs. $PMO^{-}/T_2{*}^{-}$; Figure 10.5).

Linear regression analyses showed significant associations of ΔEDSI with both infarct and iron volumes measured at both acute (infarct: $R^2 = 0.46$, $p<0.001$, Figure 10.5I; iron: $R^2 = 0.29$, $p<0.001$, Figure 10.5K) and chronic (infarct: $R^2 = 0.28$, $p<0.001$, Figure 10.5J; iron: $R^2 = 0.42$, $p<0.001$, Figure 10.5L) phases. Multivariate regression analyses showed that both infarct

and scar volumes measured at both acute (infarct: $\beta = 2.02$, $p = 0.002$; iron: $\beta = 1.57$, $p = 0.02$) and chronic phases (infarct: $\beta = 3.46$, $p = 0.003$; iron: $\beta = 4.12$, $p<0.001$) were significant and independent predictors of ΔEDSI. Neither infarct volume nor iron volume measured at either acute or chronic phases could significantly predict ΔEDV, ΔESV, or ΔEF.

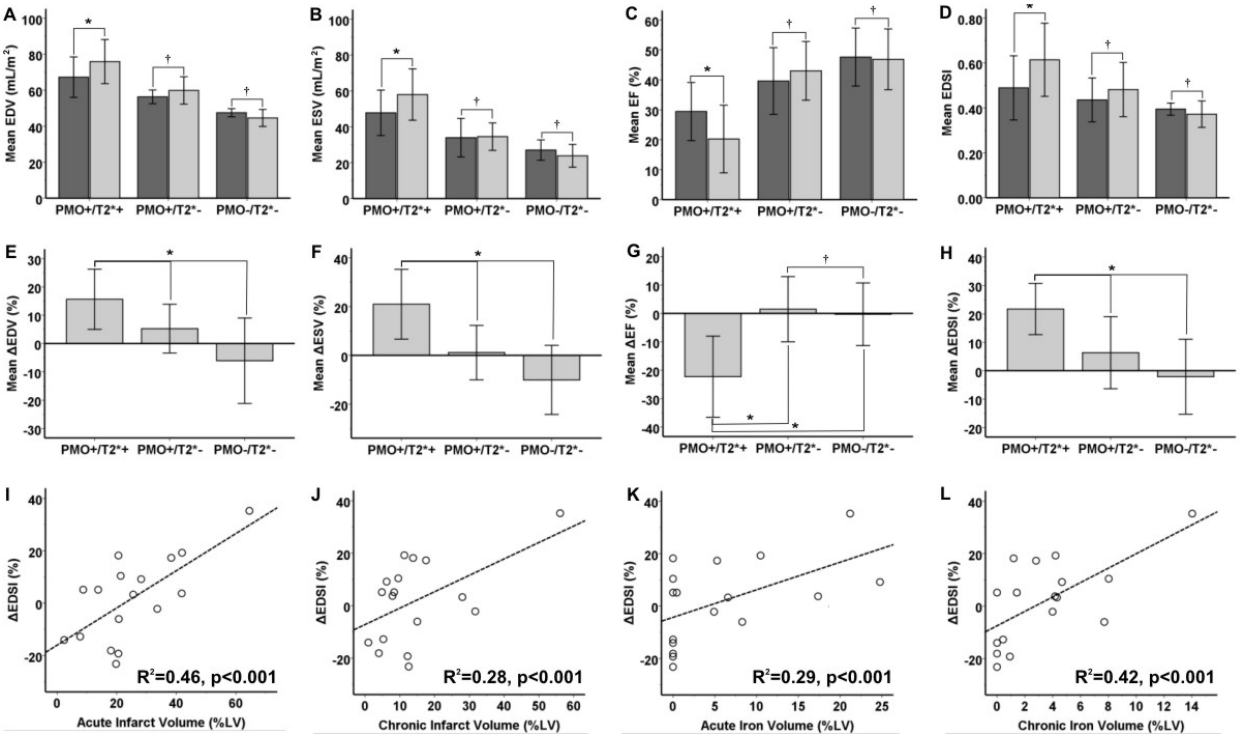

Figure 10.5: *LV remodeling in reperfused myocardial infarctions.* Mean EDV (panel A), ESV (panel B), EF (panel C), and EDSI (panel D) measures from reperfused canines are shown. ΔEDV (panel E), ΔESV (panel F), ΔEF (panel G), and ΔEDSI (panel H) between acute and chronic phases are also shown. Significant linear relationships of ΔEDSI with acute infarct volume ($R^2 = 0.46$, $p<0.001$, panel I), chronic infarct volume ($R^2 = 0.28$, $p<0.001$, panel J), acute iron volume ($R^2 = 0.29$, $p<0.001$, panel K), and chronic iron volume ($R^2 = 0.42$, $p<0.001$, panel L) were also found. *Statistically significant difference ($p<0.05$). †No statistically significant difference ($p>0.05$).

10.4.4. Left-Ventricle Remodeling in Non-Reperfused Myocardial Infarctions

Canines in the PMO^{+}/T_2*^{+} group had significantly larger EDV ($p = 0.002$) and lower EF ($p<0.001$) to the PMO^{-}/T_2*^{-} canine in the acute phase (Figure 10.6). However, there was no significant difference in ESV ($p = 0.21$) and EDSI ($p = 0.56$) between the two groups in the acute phase (Figure 6). In the chronic phase, canines in the PMO^{+}/T_2*^{+} group had significantly larger EDV ($p<0.001$), larger ESV ($p = 0.01$), lower EF ($p = 0.002$), and larger EDSI ($p<0.001$) compared to the control canine. The PMO^{+}/T_2*^{+} canines also had significantly larger EDV ($p<0.001$), larger ESV ($p = 0.001$), and larger EDSI ($p = 0.001$) in the chronic phase compared to the acute phase (Figure 10.6). However, there was no significant difference in EF between the acute and chronic phases in the PMO^{+}/T_2*^{+} canines (EF: $p=0.17$; Figure 10.6). Compared to the PMO^{-}/T_2*^{-} canine, canines in the PMO^{+}/T_2*^{+} group had significantly higher ΔEDV, ΔESV, and ΔEDSI between the acute and chronic phases (ΔEDV: $p<0.001$; ΔESV: $p = 0.001$; ΔEDSI: $p = 0.01$; Figure 10.6). However, ΔEF in the PMO^{+}/T_2*^{+} group was not significantly different than that of the control canine ($p = 0.60$; Figure 10.6).

Linear regression analyses showed significant associations of ΔEDSI with both infarct and iron volumes measured at both acute (infarct: $R^2 = 0.52$, $p<0.001$; iron: $R^2 = 0.40$, $p<0.001$; Figure 10.6) and chronic (infarct: $R^2 = 0.44$, $p<0.001$; iron: $R^2 = 0.43$, $p<0.001$; Figure 10.6) phases. Multivariate regression analyses showed that both infarct and scar volumes measured at both acute (infarct: $\beta = 2.75$, $p = 0.006$; iron: $\beta = 1.64$, $p = 0.01$) and chronic phases (infarct: $\beta = 4.16$, $p = 0.002$; iron: $\beta = 4.81$, $p<0.001$) were significant and independent predictors of ΔEDSI. Neither infarct volume nor iron volume measured at either acute or chronic phases could significantly predict ΔEDV, ΔESV, or ΔEF.

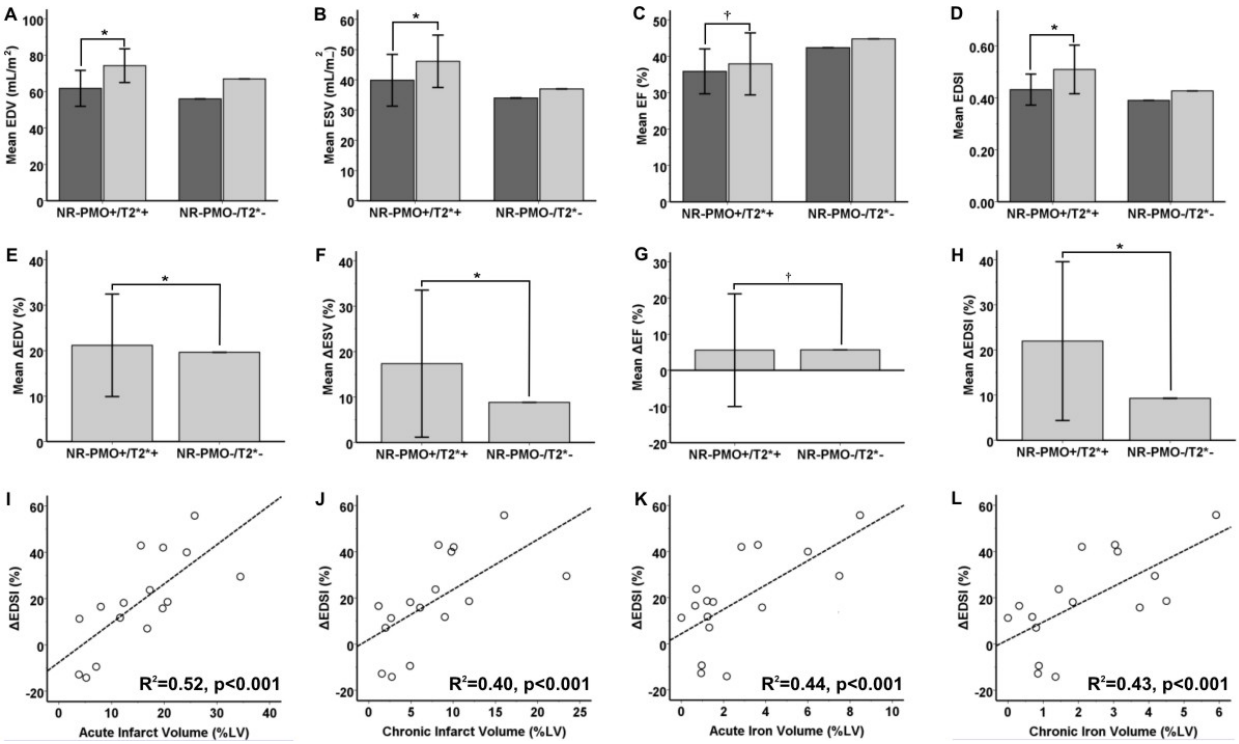

Figure 10.6: *LV remodeling in non-reperfused myocardial infarctions.* Mean EDV (panel A), ESV (panel B), EF (panel C), and EDSI (panel D) measures from non-reperfused canines are shown. ΔEDV (panel E), ΔESV (panel F), ΔEF (panel G), and ΔEDSI (panel H) between acute and chronic phases are also shown. Significant linear relationships of ΔEDSI with acute infarct volume (R^2 = 0.52, p<0.001, panel I), chronic infarct volume (R^2 = 0.40, p<0.001, panel J), acute iron volume (R^2 = 0.44, p<0.001, panel K), and chronic iron volume (R^2 = 0.43, p<0.001, panel L) were also found. *Statistically significant difference (p<0.05). †No statistically significant difference (p>0.05).

10.4.5. Immunohistological Analyses

Representative microscopic immunohistological sections of reperfused and non-reperfused MIs obtained from canines with and without T_2* losses (T_2*+ and T_2*− respectively) as observed on ex-vivo T_2*-weighted images are shown in Figure 10.7. Significant collagen deposition within the infarcted territories could be observed in all cases, while Perl's stain confirmed the presence of iron deposition only in the T_2*+ cases. Significant co-localization of Mac387+ cells with iron

deposits was observed in both reperfused and non-reperfused MIs. There was intense TNF-α immunoreactivity associated with Mac387+ cells. Linear regression analyses showed strong associations of area of iron (Perl's stain) with area of Mac387+ cells ($R^2 = 0.87$, $p<0.001$; Figure 10.8A), area of TNF-α activity ($R^2 = 0.73$, $p<0.001$; Figure 10.8B), and area of MMP-9 activity ($R^2 = 0.85$, $p<0.001$; Figure 10.8C).

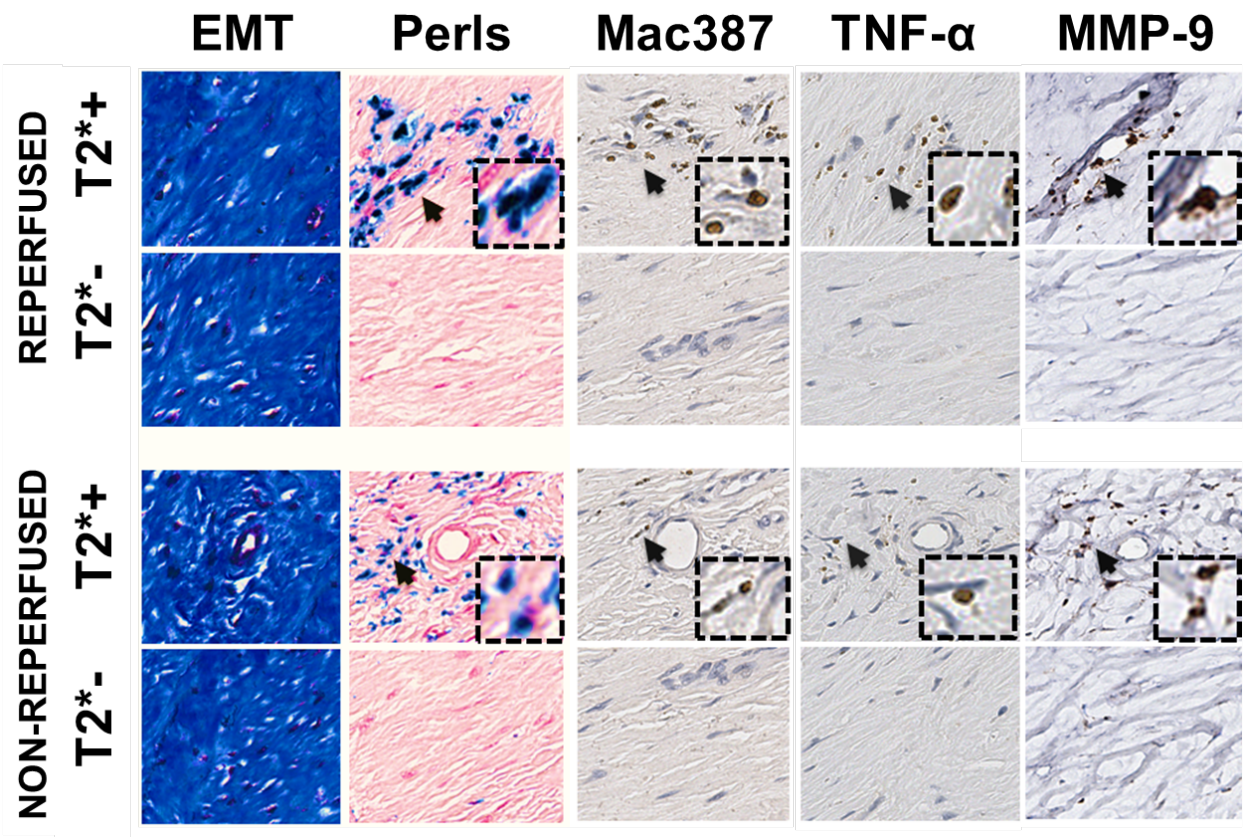

Figure 10.7: *Co-localization of pro-inflammatory burden with chronic iron deposition.* Representative contiguous ex-vivo histology sections stained with EMT, Perls, and monoclonal antibodies for Mac387, TNF-α, and MMP-9 are shown from reperfused and non-reperfused canines with and without T_2* losses (T_2*+ and T_2*- respectively) as observed in ex-vivo T_2*-weighted images. Note significant co-localization of Mac387+ cells, TNF-α activity, and MMP-9 activity with chronic iron deposits.

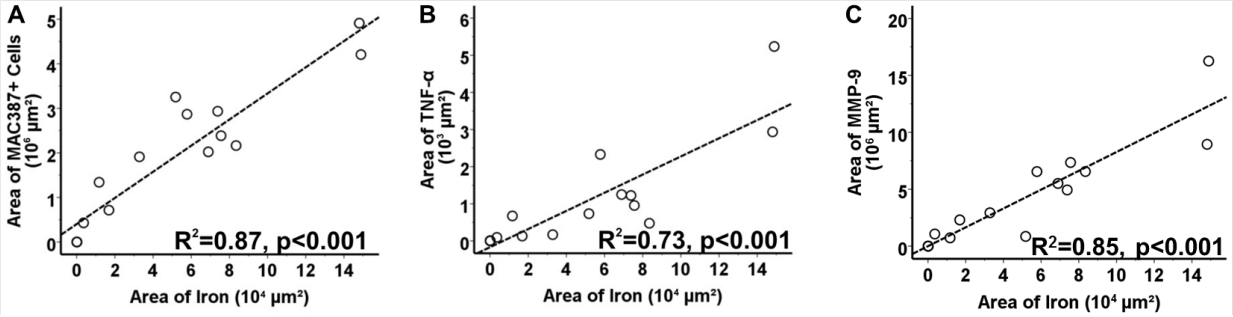

Figure 10.8: *Relationship between chronic iron deposition and pro-inflammatory burden*. Strong linear relationships of the area of iron (measured from Perls stain) were observed with area of Mac387+ cells (R^2 = 0.87, p<0.001, panel A), area of TNF-α activity (R^2 = 0.73, p<0.001, panel B), and area of MMP-9 activity (R^2 = 0.85, p<0.001, panel C).

10.5. Discussion

MO is a well-known marker of I-R injury, but the underlying mechanisms by which it leads to adverse effects in the long-term well beyond its resolution are not well understood. This study has shown that PMO, with or without reperfusion hemorrhage can lead to significant chronic iron deposition within the infarcted territories, and the extent of chronic iron deposition is strongly related to the extent of PMO observed in the acute phase. In canines with reperfused MIs, this study shown that, although PMO may not always be associated with reperfusion hemorrhage as seen on T_2*-weighted images in the acute phase, it can still resolve into iron deposition within the infarcted territories in the chronic phase. This was further validated by the occurrence of significant chronic iron deposition within non-reperfused MIs, which are classically known to not have any reperfusion hemorrhage. The chronic iron deposition post-PMO resolution has been also found to be a significant and independent predictor of adverse LV remodeling on the basis of sphericity index in the chronic phase. Significant pro-inflammatory burden was also found to be associated with the chronic iron deposition.

While the previous chapters have identified acute reperfusion intramyocardial hemorrhage as an etiology for iron deposition within CMIs, this study extends the findings to the presence of PMO alone without any concurrent reperfusion hemorrhage has not been explored previously. However, the exact mechanisms by which PMO leads to chronic iron deposition remain to be investigated. One possible mechanism could be that the stagnant blood within the blocked 'no-reflow' microvasculature could gradually degrade. The eventual breakdown of the no-reflow microvasculature can externalize the degraded stagnant blood into the scar tissue and manifest itself as iron deposits.

The occurrence of chronic iron deposition within non-reperfused MIs has also not been shown previously in the literature. Khan et al have shown that PMO, defined as hypointense cores on LGE images, is equally prevalent in patients with non-reperfused MIs as in reperfused MIs (543). While the PMO observed in reperfused MIs is attributed to plugging of microvasculature by inflammatory cells, erythrocytes and other microembolic debris (171), the pathological mechanism of PMO observed in non-reperfused MIs could be due to permanently occluded coronary artery that has not been reperfused. However, the mechanism of iron deposition in non-reperfused MIs could be still similar to that observed in reperfused MIs. The permanently ligated vasculature will eventually degrade and the stagnant blood and blood-degradation products within can be externalized into the scar tissue, which further manifest as chronic iron deposits. These results suggest that chronic iron deposition is a fingerprint of PMO observed in the acute phase, and could be a potential mechanism through which PMO exerts adverse effects in the long-term.

In the previous chapters, chronic iron deposition within reperfused MIs has been implicated in adverse LV remodeling and arrhythmogenesis in healed MIs. In line with previous

observations, this study has shown that iron deposition post-PMO resolution is a strong predictor of LV structural remodeling. The role of iron in the onset of adverse LV remodeling and heart failure remains is well documented in non-ischemic iron-overload cardiomyopathies (461,544-546). While the exact mechanism by which iron post-PMO resolution in MIs mediates adverse LV remodeling remains to be investigated, active and prolonged pro-inflammatory activity co-localized with iron deposits with CMIs observed in this study seems to be one potential mechanism. In this study, significant co-localization of Mac387+ cells has been observed with post-PMO iron deposition in the chronic MI territories, which is similar to earlier observations in chapter 7 in chronic reperfused MIs with a history of acute reperfusion hemorrhage (430). Moreover, the extent of iron deposition has been found to be directly proportional to the extent of Mac387+ co-localization. The monoclonal antibody Mac387 is specific to calgranulin, a protein expressed by newly recruited monocytes, and is significantly downregulated when they mature to macrophages (466,467). Frangogiannis et al have shown that the number of Mac387+ cells in the infarcted myocardium was significantly reduced at 7 days post-reperfusion, and this marker can be used an index for new recruitment of leukocytes in the heart (468). The presence of Mac387+ cells highly co-localized with iron in this study shows an active and prolonged inflammatory process within CMIs that extends well beyond the acute inflammatory stage. The interaction of Mac387+ cells with post-PMO iron remains to be investigated, but iron phagocytosis and clearance seem to be the plausible explanations. Terrovitis et al have previously shown that iron-oxide particles from ferumoxide labeled stem cells are internalized by macrophages. The role of monocyte-derived macrophages in iron phagocytosis is also well known in other pathologies such as atherosclerotic plaques (547,548) and in the liver (549).

A number of pro-inflammatory cytokines, which have been implicated in the development of LV dysfunction and LV remodeling dysfunction, are released when monocytes mature into macrophages. This study has shown that Mac387+ cells are associated with significant TNF-α and MMP-9 activities. TNF-α is a well-known potent pro-inflammatory cytokine implicated in development of LV dysfunction, LV remodeling and endothelial dysfunction (550-552). MMP-9 activity is well known to be associated with extracellular matrix degradation and modulating mechanical architecture of the scar (553,554). These results suggest that the macrophages derived from Mac387+ cells are in an unrestrained pro-inflammatory M1 activation state that can potentially worsen LV remodeling.

Recent studies have been instrumental in shedding light on the relation between MO and inflammation. These studies have shown that in cases of reperfused MIs with MO, monocyte recruitment is delayed in the acute and sub-acute period; and, in cases where erythrocyte extravasation (hemorrhage) accompanies MO, iron accumulates within the MI territories in the chronic phase and is site of intense macrophage recruitment (542). Although adequate inflammatory activity is necessary for wound healing, long-term persistence of inflammation is detrimental to the reparative effects. Mechanistically, the extent of LV remodeling in the post-MI period is related to the timely inhibition and resolution of the inflammatory activity (555-558). In particular, prolonged inflammation has been shown to impair collagen deposition and scar formation resulting in reduced tensile strength and LV dilatation (556). Early studies suggest that ineffective suppression of inflammation post-MI is associated with adverse LV remodeling of the heart (559-561). The finding that iron deposits within CMI plays an intermediary role in wound healing may be of substantial clinical relevance as it can unravel how PMO imparts adverse

long-term effects on the infarcted heart and underscore iron as a therapeutic target in post-MI HF.

Supported by extensive histopathology, T_2*-weighted MRI was used in this study to validate the occurrence of acute reperfusion hemorrhage and chronic iron deposition within infarcted tissue. In the previous chapters, T_2*-based MRI has been validated to be a highly sensitive technique for the detection of both acute hemorrhage and chronic iron deposition in MIs. However, T_2*-weighted MRI is also susceptible to off-resonance artifacts in the infero-lateral LV wall, which become highly pronounced as higher magnetic field strengths, such as in this study, are used. These off-resonance artifacts can be potentially misinterpreted as hemorrhage or chronic iron. For this reason, we have limited our analysis to LAD infarctions, as the antero-septal LV wall is less prone to off-resonance artifacts. To minimize the off-resonance artifacts, we have further used careful volume-selective shimming and short TEs. With the aid of LGE imaging, hemorrhage and chronic iron can still be adequately differentiated from off-resonance artifacts, as these two pathological features are always confined to the infarcted territories. Moreover, blooming effect from hemorrhage and chronic iron originate from the endocardium, while off-resonance artifacts originate from epicardium.

10.5.1. Study Limitations

This study has few limitations. First, the sample size of our study is small, which may have precluded us from observing modest differences. This could partly be the reason why we could not significant associations of LV remodeling parameters such as EDV, ESV, and EF with infarct and iron volumes. Nevertheless, we could still observe a clear relationship of EDSI with infarct and iron volumes. Second, we have limited our analysis to LAD infarctions. While we

expect the observations to be valid regardless of the culprit artery, further studies are needed to extend the observations other types of infarctions. Third, our observations were made only in a canine model of MI. Future studies in patients with different types of MIs are warranted.

10.6. Conclusion

PMO, with or without reperfusion hemorrhage, can lead to chronic iron deposition within CMI territories, the extent of which is directly related to the extent of PMO in the acute phase. The chronic iron post-PMO resolution is an independent predictor of adverse LV remodeling, and is associated with a prolonged pro-inflammatory activity within the infarct, the extent of which is directly related to the extent of iron. Chronic iron post-PMO resolution could be a potential mechanism by which PMO imparts adverse long-term effects.

CHAPTER 11

Summary and Future Directions

11.1 Native T_1 Mapping at 3T for Characterizing Chronic Myocardial Infarctions

LGE MRI is a robust non-invasive imaging technique for characterizing CMIs with excellent diagnostic accuracy and prognostic significance. However, this technique requires administration of a Gadolinium chelate, which is contraindicated in patients with chronic end-stage kidney disease. In this dissertation, native T_1 mapping using MOLLI-bSSFP at 3T, which does not require exogenous contrast agents, has been shown to determine the location, extent, and transmurality of CMIs in a canine model with a diagnostic performance comparable to that of LGE imaging. Mean native T_1 of CMI was elevated by ~20% relative to that of remote myocardium at 3T. The absence of any residual myocardial edema in the CMI territories as confirmed by T_2 mapping, suggest that these T_1 elongations are predominantly arising from replacement fibrosis in CMIs. Apart from the biophysical differences between CMI and remote myocardium, magnetic field strength dependent native T_1 elongations seem to be an important mechanism that facilitates CMI detection by native T_1 mapping at 3T. This is explained by the findings that infarcted to remote myocardium T_1 contrast is 1.5-fold higher at 3T relative to 1.5T. This study suggests that native T_1 mapping at 3T can be a reliable alternative to LGE for characterizing CMI with the potential for clinical translation. This work, titled "Determination of location, size, and transmurality of chronic myocardial infarction without exogenous contrast

media by using cardiac magnetic resonance imaging at 3T", has been published in Circulation: Cardiovascular Imaging, 2014; 7(3): 471-81.

While the feasibility of using native T_1 mapping at 3T for detecting CMIs has been demonstrated, an optimal approach for objectively characterizing CMIs using the proposed approach is needed. Comparison of different semi-automatic, automatic, and visual techniques has shown that the Mean+5SD criterion is the most robust technique for characterizing CMIs on native T_1 maps at 3T. The diagnostic performances of other semi-automatic and automatic detection techniques were also comparable. However, the visual delineation of CMIs showed moderate sensitivity, despite high specificity. Therefore, visual identification may not be feasible approach for clinical application. This could be a perceived weakness of native T_1 maps for characterizing CMIs among cardiac MRI readers who solely rely on visual analysis for detection and characterization of CMI. The semi-automatic Mean+5SD technique still requires the reader to visually identify remote myocardium to draw the reference ROI. Since the specificity (i.e., the ability to identify remote myocardium) of visual delineation of CMIs on native T_1 maps in this study is 99%, the remote myocardium is expected to be reliably identified based on visual analysis, and Mean+5SD criterion can still be practically implemented for identifying CMIs. Of particular note is the strong diagnostic performance of the automatic Otsu's technique, which does not require any user interference. Therefore, this method can be a promising alternative to visual identification of the remote and infarcted territories on native T_1 maps. This work, titled "Accuracy and precision of chronic myocardial infarct characterization with native T_1 mapping at 3T", has been published in an abstract form in the Journal of Cardiovascular Magnetic Resonance, 2015; 17(Suppl 1): P166.

Using the Mean+5SD criterion validated in the canine studies, native T_1 mapping at 3T showed high sensitivity and specificity for detecting CMIs in a patient cohort with healed STEMIs and NSTEMIs. However, similar to the observations from the canine model, the sensitivity for visually detecting CMIs on native T_1 maps at 3T remained moderate, albeit high specificity. This may be limiting in some patients if visual analysis is the only mode used for CMI characterization. This work, titled "Native T_1 mapping at 3T can characterize chronic myocardial infarctions in patients", has been accepted for publication in JACC Cardiovascular Imaging, 2015.

Future studies should investigate the biophysical mechanisms responsible for native T_1 contrast in CMIs and its dependence on field strength. Based on previous observations, field-strength dependent native T_1 elongations, increased diffusion coefficient of protons, and reduced MT effects in CMIs relative to remote myocardium seem to be the plausible explanations. The low sensitivity of visual detection of CMIs native T_1 maps is also a significant concern. Further increases in image contrast on the basis of native T_1 characteristics at 3T remains to be investigated. Possible techniques to improve CMI visualization using native T_1 contrast include use of IR preparation to null the remote myocardium (analogous to IR preparation used for LGE) and optimization of the MT effects. High-resolution 3D native T_1 mapping approaches with free breathing will further boost widespread clinical adoption of this technique for characterizing CMIs. The ability of native T_1 maps to detect other pathologies typically detected in CMIs using LGE imaging such as the gray-zones also remains to be investigated.

11.2. Iron Deposition within CMIs as a Potential Substrate for Adverse LV Remodeling and Malignant Ventricular Arrhythmias: Utility of T_2*-based and bSSFP MRI

Intramyocardial hemorrhage is a frequent hallmark of large reperfused MIs. To understand the effects of reperfusion hemorrhage on acute tissue damage and post-MI remodeling, it is imperative to ensure that the most optimal imaging strategy is employed. A direct comparison of T_2*-based and T_2-based MRI techniques has shown that acute reperfusion myocardial hemorrhage is better characterized by T_2* than T_2-based MRI. Owing to its inherent sensitivity to myocardial edema in AMIs, the sensitivity of T_2-based techniques to intramyocardial hemorrhage can be diminished due to the counteracting T_2 effects of edema and hemorrhage. The relative insensitivity of T_2*-based MRI to edema, make it a more suitable approach for accurate characterization of hemorrhage. This work, titled "Detecting acute reperfusion myocardial hemorrhage with CMR: T_2 vs. T_2*", has been published in Radiology, 2013; 269(2): 387-395.

While intramyocardial hemorrhage has been well studied in the setting of AMI, its influence on the make-up and the ensuing effect on the infarcted tissue during the chronic phase of MI are not well studied. This dissertation has shown that intramyocardial hemorrhage resolves into localized iron deposits within CMIs, which can persist for many months post-reperfusion. Supported by extensive histopathological and mass-spectrometric findings, T_2*-based MRI has been shown to reliably characterize such chronic iron depositions. Volumetric MRI data from both patients and canines has shown that both relative infarct and hemorrhage volume in the acute phase were significant predictors of LV remodeling on the basis of sphericity index in the chronic period following MI. In addition, immunohistological staining for newly recruited

monocytes has shown prolonged inflammatory response in the infarct tissue with iron deposits in the chronic phase of hemorrhagic MIs. This work, titled "Chronic manifestation of post-reperfusion intramyocardial hemorrhage as regional iron deposition – A cardiovascular MR study with ex-vivo validation", has been published in Circulation: Cardiovascular Imaging, 2013; 6(2): 218-228.

Iron deposition in non-ischemic cardiomyopathies has been long documented to induce cardiac electrical conduction anomalies. While scarred myocardium is generally believed to be electrically inert, this dissertation has shown that localized iron deposition within CMIs can alter the electrical characteristics of the myocardial scar. Ex-vivo bulk electrical impedance measurements have shown nearly 25% increase in electrical permittivity, but no change in electrical conductivity, of scarred myocardium with iron relative to that without iron. Since the observed changes in permittivity were not accompanied by changes in electrical conductivity, it appears that the effect of iron deposition is to transform the infarcted territory into a capacitor. ECG measurements from scarred myocardium with iron showed significant prolongation of QT and QTc intervals, which have been traditionally associated with SCD. Co-registration of in-vivo T_2*-weighted images with high-resolution EAMs have shown a trend towards higher incidence of ILPs, a well-known pathological substrate of SCD, in scarred myocardium laden with iron deposits relative to myocardial scar without iron. Collectively these findings indicate that iron deposition within CMIs may evolve into a pathological substrate for mVAs, and underscore the utility of T_2*-based MRI for risk-stratification of CMI patients. This work, titled "Iron deposition following chronic myocardial infarction as a substrate for cardiac electrical anomalies: Initial findings in a canine model", has been published in PLoS One, 2013; 8(9): e73193.

ICD is a highly effective tool for the primary prevention of SCD in CMI patients, but the

current guideline recommendations based on EF thresholds are inadequate to identify those patients at greatest risk for SCD. Myocardial scarring determined using LGE MRI has been instrumental in better risk stratification of patients indicated for ICD therapy. This dissertation has shown that hypointense cores identified on non-contrast enhanced bSSFP images within CMI territories is a much stronger independent predictor of mVA risk in CMI patients implanted with ICDs than myocardial scarring evaluated using LGE imaging. Using extensive histopathological and T_2*-based MRI validation in canine model of CMI, hypointense cores identified on bSSFP images have been found to be indicative of chronic iron deposition. Collectively these findings have established the utility of bSSFP imaging for detecting chronic iron deposition as hypointense cores, and the predictive value of bSSFP imaging for risk-stratifying ICD patients. bSSFP imaging is also commonly used for evaluating LV function; therefore, in addition to the hypointense cores, the technique can simultaneously provide EF information, which is a traditional risk-stratification marker for patients indicated for ICD therapy. Since T_2* acquisitions are currently not routinely performed as part of a standard MRI examination, the ability to categorize iron depositions within CMIs using routine bSSFP imaging offers greater generalizability to routine clinical practice. This work, titled "Iron-sensitive cardiac magnetic resonance imaging for improved prediction of malignant ventricular arrhythmias in patients with chronic myocardial infarctions", has been published in an abstract form in the Journal of the American College of Cardiology. 2015; 65(10S): A1084.

Persistent microvascular obstruction (PMO) is an important predictor of long-term adverse LV remodeling and adverse cardiac outcomes. However, the exact mechanism by which PMO, which typically resolves within a few weeks, can exert adverse effects throughout the post-MI period is not well understood. Using extensive histopathology and T_2*-based MRI, this

dissertation has shown that PMO, with or without reperfusion hemorrhage, can resolve into localized within CMI territories, and such iron deposits are associated with adverse LV remodeling. This dissertation has also shown for the first time that non-reperfused MIs, which are classically known not to sustain intramyocardial hemorrhage, can still have significant iron depositions in the chronic phase of MI. More importantly, chronic iron deposition post-PMO resolution was found to be associated with significant pro-inflammatory burden in the form of significant TNF-α and MMP-9 activities, which have been well implicated in adverse LV remodeling and LV dysfunction. These findings potentially unravel how MO imparts adverse long-term effects on the infarcted heart and underscore iron as a potential therapeutic target post-MI. Given these findings, T_2*-based MRI is expected to have widespread applications for monitoring post-MI healing and making informed therapeutic decisions. A portion of this work, titled "Localized chronic iron deposition within non-reperfused myocardial infarctions", has been published in an abstract form in the Journal of Cardiovascular Magnetic Resonance, 2015; 17(Suppl 1): O13.

Preliminary observations in this dissertation have shown that prolonged inflammatory burden and alterations in the bulk electrical characteristics of infarcted myocardium could be the implicit mechanisms by which chronic iron deposition leads to adverse LV remodeling and mVAs. Nevertheless, additional studies are still needed to fully elucidate the underlying pathophysiological mechanisms linking chronic iron deposition with cardiac remodeling and electrical anomalies, and translate these findings to clinical arena. Given that iron within the CMI zones can evolve as a therapeutic target in the management of MI patients who may be at risk for HF and SCD in the post-MI period, the role of iron chelation therapies to improve prognosis in these patients needs to be investigated.

In this dissertation, 2D T_2*-based MRI techniques have shown to be robust for characterizing chronic iron depositions. However, widespread clinical application of this technique can significantly benefit from further technical developments including whole-heart 3D coverage with free breathing. High-resolution 3D imaging can obviate the partial volume effects and improve the conspicuity of minute hemorrhages. Free breathing approaches are of particular importance in CMI patients who generally have difficulties in holding the breath for long times during the scans. Bright blood T_2* techniques, such as those used in this dissertation, also suffer from significant flow artifacts (such as ghosting and smearing) at long TEs. Dark blood T_2* techniques can potentially overcome these limitations of bright blood T_2* techniques. bSSFP imaging appears to be another promising technique for evaluating chronic iron depositions. Future studies also need to fully evaluate the diagnostic performance of this technique for characterizing iron depositions within CMIs.

In conclusion, this dissertation lays extensive groundwork for the widespread clinical adoption of native T_1 mapping at 3T, T_2*-based MRI, and bSSFP MRI as potential non-contrast enhanced MRI techniques for robustly characterizing CMI morphology and pathological substrates of adverse cardiac outcomes within CMIs.

REFERENCES

1. Mozaffarian D, Benjamin EJ, Go AS et al. Heart disease and stroke statistics--2015 update: a report from the American Heart Association. Circulation 2015;131:e29-322.
2. Braunwald E. Heart Disease: A textbook of Cardiovascular Medicine. 5 ed. Philadelphia, 1997.
3. Avkiran M, Marber MS. Na(+)/H(+) exchange inhibitors for cardioprotective therapy: progress, problems and prospects. Journal of the American College of Cardiology 2002;39:747-53.
4. Buja LM. Modulation of the myocardial response to ischemia. Laboratory investigation; a journal of technical methods and pathology 1998;78:1345-73.
5. Buja LM. Myocardial ischemia and reperfusion injury. Cardiovascular pathology : the official journal of the Society for Cardiovascular Pathology 2005;14:170-5.
6. Reimer KA, Ideker RE. Myocardial ischemia and infarction: anatomic and biochemical substrates for ischemic cell death and ventricular arrhythmias. Human pathology 1987;18:462-75.
7. Thandroyen FT, Bellotto D, Katayama A, Hagler HK, Willerson JT, Buja LM. Subcellular electrolyte alterations during progressive hypoxia and following reoxygenation in isolated neonatal rat ventricular myocytes. Circulation research 1992;71:106-19.
8. Reimer KA, Jennings RB. The "wavefront phenomenon" of myocardial ischemic cell death. II. Transmural progression of necrosis within the framework of ischemic bed size

(myocardium at risk) and collateral flow. Laboratory investigation; a journal of technical methods and pathology 1979;40:633-44.

9. Boersma E, Maas AC, Deckers JW, Simoons ML. Early thrombolytic treatment in acute myocardial infarction: reappraisal of the golden hour. Lancet 1996;348:771-5.

10. Schaper J, Schaper W. Time course of myocardial necrosis. Cardiovascular drugs and therapy / sponsored by the International Society of Cardiovascular Pharmacotherapy 1988;2:17-25.

11. Effectiveness of intravenous thrombolytic treatment in acute myocardial infarction. Gruppo Italiano per lo Studio della Streptochinasi nell'Infarto Miocardico (GISSI). Lancet 1986;1:397-402.

12. Randomised trial of intravenous streptokinase, oral aspirin, both, or neither among 17,187 cases of suspected acute myocardial infarction: ISIS-2. ISIS-2 (Second International Study of Infarct Survival) Collaborative Group. Lancet 1988;2:349-60.

13. An international randomized trial comparing four thrombolytic strategies for acute myocardial infarction. The GUSTO investigators. The New England journal of medicine 1993;329:673-82.

14. Indications for fibrinolytic therapy in suspected acute myocardial infarction: collaborative overview of early mortality and major morbidity results from all randomised trials of more than 1000 patients. Fibrinolytic Therapy Trialists' (FTT) Collaborative Group. Lancet 1994;343:311-22.

15. Berger PB, Ellis SG, Holmes DR, Jr. et al. Relationship between delay in performing direct coronary angioplasty and early clinical outcome in patients with acute myocardial

infarction: results from the global use of strategies to open occluded arteries in Acute Coronary Syndromes (GUSTO-IIb) trial. Circulation 1999;100:14-20.

16. Weaver WD, Cerqueira M, Hallstrom AP et al. Prehospital-initiated vs hospital-initiated thrombolytic therapy. The Myocardial Infarction Triage and Intervention Trial. Jama 1993;270:1211-6.

17. Kloner RA. Does reperfusion injury exist in humans? Journal of the American College of Cardiology 1993;21:537-45.

18. Yellon DM, Hausenloy DJ. Myocardial reperfusion injury. The New England journal of medicine 2007;357:1121-35.

19. Jennings RB, Sommers HM, Smyth GA, Flack HA, Linn H. Myocardial necrosis induced by temporary occlusion of a coronary artery in the dog. Archives of pathology 1960;70:68-78.

20. Kloner RA, Ganote CE, Jennings RB. The "no-reflow" phenomenon after temporary coronary occlusion in the dog. J Clin Invest 1974;54:1496-508.

21. Braunwald E, Kloner RA. The stunned myocardium: prolonged, postischemic ventricular dysfunction. Circulation 1982;66:1146-9.

22. Manning AS, Hearse DJ. Reperfusion-induced arrhythmias: mechanisms and prevention. Journal of molecular and cellular cardiology 1984;16:497-518.

23. Piper HM, Garcia-Dorado D, Ovize M. A fresh look at reperfusion injury. Cardiovascular research 1998;38:291-300.

24. Ito H. No-reflow phenomenon and prognosis in patients with acute myocardial infarction. Nature clinical practice Cardiovascular medicine 2006;3:499-506.

25. Hausenloy DJ, Yellon DM. Myocardial ischemia-reperfusion injury: a neglected therapeutic target. The Journal of clinical investigation 2013;123:92-100.

26. Hearse DJ, Tosaki A. Reperfusion-induced arrhythmias and free radicals: studies in the rat heart with DMPO. Journal of cardiovascular pharmacology 1987;9:641-50.

27. Hearse DJ, Tosaki A. Free radicals and reperfusion-induced arrhythmias: protection by spin trap agent PBN in the rat heart. Circulation research 1987;60:375-83.

28. Hearse DJ, Humphrey SM, Chain EB. Abrupt reoxygenation of the anoxic potassium-arrested perfused rat heart: a study of myocardial enzyme release. Journal of molecular and cellular cardiology 1973;5:395-407.

29. Zweier JL, Flaherty JT, Weisfeldt ML. Direct measurement of free radical generation following reperfusion of ischemic myocardium. Proceedings of the National Academy of Sciences of the United States of America 1987;84:1404-7.

30. Herzog WR, Vogel RA, Schlossberg ML, Edenbaum LR, Scott HJ, Serebruany VL. Short-term low dose intracoronary diltiazem administered at the onset of reperfusion reduces myocardial infarct size. International journal of cardiology 1997;59:21-7.

31. Miyamae M, Camacho SA, Weiner MW, Figueredo VM. Attenuation of postischemic reperfusion injury is related to prevention of [Ca2+]m overload in rat hearts. The American journal of physiology 1996;271:H2145-53.

32. Lemasters JJ, Bond JM, Chacon E et al. The pH paradox in ischemia-reperfusion injury to cardiac myocytes. Exs 1996;76:99-114.

33. Vinten-Johansen J. Involvement of neutrophils in the pathogenesis of lethal myocardial reperfusion injury. Cardiovascular research 2004;61:481-97.

34. Griffiths EJ, Halestrap AP. Mitochondrial non-specific pores remain closed during cardiac ischaemia, but open upon reperfusion. The Biochemical journal 1995;307 (Pt 1):93-8.

35. Ertl G, Frantz S. Healing after myocardial infarction. Cardiovascular research 2005;66:22-32.

36. Frangogiannis NG, Smith CW, Entman ML. The inflammatory response in myocardial infarction. Cardiovascular research 2002;53:31-47.

37. Holmes JW, Yamashita H, Waldman LK, Covell JW. Scar remodeling and transmural deformation after infarction in the pig. Circulation 1994;90:411-20.

38. Lewis RP. The ACC at 50: a giant grew in Bethesda. The impact of the ACC on cardiovascular medicine. American College of Cardiology. Journal of the American College of Cardiology 2000;35:60B-65B.

39. Hunink MG, Goldman L, Tosteson AN et al. The recent decline in mortality from coronary heart disease, 1980-1990. The effect of secular trends in risk factors and treatment. Jama 1997;277:535-42.

40. Levy D, Thom TJ. Death rates from coronary disease--progress and a puzzling paradox. The New England journal of medicine 1998;339:915-7.

41. Beller GA. Coronary heart disease in the first 30 years of the 21st century: challenges and opportunities: The 33rd Annual James B. Herrick Lecture of the Council on Clinical Cardiology of the American Heart Association. Circulation 2001;103:2428-35.

42. Velagaleti RS, Pencina MJ, Murabito JM et al. Long-term trends in the incidence of heart failure after myocardial infarction. Circulation 2008;118:2057-62.

43. Go AS, Mozaffarian D, Roger VL et al. Heart disease and stroke statistics--2014 update: a report from the American Heart Association. Circulation 2014;129:e28-e292.

44. Levy D, Kenchaiah S, Larson MG et al. Long-term trends in the incidence of and survival with heart failure. The New England journal of medicine 2002;347:1397-402.

45. Roger VL, Weston SA, Redfield MM et al. Trends in heart failure incidence and survival in a community-based population. Jama 2004;292:344-50.

46. Allman KC, Shaw LJ, Hachamovitch R, Udelson JE. Myocardial viability testing and impact of revascularization on prognosis in patients with coronary artery disease and left ventricular dysfunction: a meta-analysis. Journal of the American College of Cardiology 2002;39:1151-8.

47. Ho KK, Pinsky JL, Kannel WB, Levy D. The epidemiology of heart failure: the Framingham Study. Journal of the American College of Cardiology 1993;22:6A-13A.

48. He J, Ogden LG, Bazzano LA, Vupputuri S, Loria C, Whelton PK. Risk factors for congestive heart failure in US men and women: NHANES I epidemiologic follow-up study. Archives of internal medicine 2001;161:996-1002.

49. Kalogeropoulos A, Georgiopoulou V, Psaty BM et al. Inflammatory markers and incident heart failure risk in older adults: the Health ABC (Health, Aging, and Body Composition) study. Journal of the American College of Cardiology 2010;55:2129-37.

50. Effect of enalapril on survival in patients with reduced left ventricular ejection fractions and congestive heart failure. The SOLVD Investigators. The New England journal of medicine 1991;325:293-302.

51. Digitalis Investigation G. The effect of digoxin on mortality and morbidity in patients with heart failure. The New England journal of medicine 1997;336:525-33.

52. Effect of metoprolol CR/XL in chronic heart failure: Metoprolol CR/XL Randomised Intervention Trial in Congestive Heart Failure (MERIT-HF). Lancet 1999;353:2001-7.

53. Bart BA, Ertl G, Held P et al. Contemporary management of patients with left ventricular systolic dysfunction. Results from the Study of Patients Intolerant of Converting Enzyme Inhibitors (SPICE) Registry. European heart journal 1999;20:1182-90.

54. Packer M, Poole-Wilson PA, Armstrong PW et al. Comparative effects of low and high doses of the angiotensin-converting enzyme inhibitor, lisinopril, on morbidity and mortality in chronic heart failure. ATLAS Study Group. Circulation 1999;100:2312-8.

55. Pitt B, Zannad F, Remme WJ et al. The effect of spironolactone on morbidity and mortality in patients with severe heart failure. Randomized Aldactone Evaluation Study Investigators. The New England journal of medicine 1999;341:709-17.

56. McDonagh TA, Morrison CE, Lawrence A et al. Symptomatic and asymptomatic left-ventricular systolic dysfunction in an urban population. Lancet 1997;350:829-33.

57. Baldasseroni S, Opasich C, Gorini M et al. Left bundle-branch block is associated with increased 1-year sudden and total mortality rate in 5517 outpatients with congestive heart failure: a report from the Italian network on congestive heart failure. American heart journal 2002;143:398-405.

58. Solomon SD, St John Sutton M, Lamas GA et al. Ventricular remodeling does not accompany the development of heart failure in diabetic patients after myocardial infarction. Circulation 2002;106:1251-5.

59. Lavine SJ. Prediction of heart failure post myocardial infarction: comparison of ejection fraction, transmitral filling parameters, and the index of myocardial performance. Echocardiography 2003;20:691-701.

60. Hellermann JP, Goraya TY, Jacobsen SJ et al. Incidence of heart failure after myocardial infarction: is it changing over time? American journal of epidemiology 2003;157:1101-7.

61. Hellermann JP, Jacobsen SJ, Redfield MM, Reeder GS, Weston SA, Roger VL. Heart failure after myocardial infarction: clinical presentation and survival. European journal of heart failure 2005;7:119-25.

62. Lewis EF, Moye LA, Rouleau JL et al. Predictors of late development of heart failure in stable survivors of myocardial infarction: the CARE study. Journal of the American College of Cardiology 2003;42:1446-53.

63. Suleiman M, Khatib R, Agmon Y et al. Early inflammation and risk of long-term development of heart failure and mortality in survivors of acute myocardial infarction predictive role of C-reactive protein. Journal of the American College of Cardiology 2006;47:962-8.

64. Zipes DP, Wellens HJ. Sudden cardiac death. Circulation 1998;98:2334-51.

65. Huikuri HV, Castellanos A, Myerburg RJ. Sudden death due to cardiac arrhythmias. The New England journal of medicine 2001;345:1473-82.

66. Rubart M, Zipes DP. Mechanisms of sudden cardiac death. The Journal of clinical investigation 2005;115:2305-15.

67. Soejima K, Stevenson WG, Maisel WH, Sapp JL, Epstein LM. Electrically unexcitable scar mapping based on pacing threshold for identification of the reentry circuit isthmus: feasibility for guiding ventricular tachycardia ablation. Circulation 2002;106:1678-83.

68. Sharir T, Germano G, Kang X et al. Prediction of myocardial infarction versus cardiac death by gated myocardial perfusion SPECT: risk stratification by the amount of stress-

induced ischemia and the poststress ejection fraction. Journal of nuclear medicine : official publication, Society of Nuclear Medicine 2001;42:831-7.

69. St John Sutton M, Pfeffer MA, Plappert T et al. Quantitative two-dimensional echocardiographic measurements are major predictors of adverse cardiovascular events after acute myocardial infarction. The protective effects of captopril. Circulation 1994;89:68-75.

70. White HD, Norris RM, Brown MA, Brandt PW, Whitlock RM, Wild CJ. Left ventricular end-systolic volume as the major determinant of survival after recovery from myocardial infarction. Circulation 1987;76:44-51.

71. Braunwald E, Rutherford JD. Reversible ischemic left ventricular dysfunction: evidence for the "hibernating myocardium". Journal of the American College of Cardiology 1986;8:1467-70.

72. Diamond GA, Forrester JS, deLuz PL, Wyatt HL, Swan HJ. Post-extrasystolic potentiation of ischemic myocardium by atrial stimulation. American heart journal 1978;95:204-9.

73. Dyke SH, Cohn PF, Gorlin R, Sonnenblick EH. Detection of residual myocardial function in coronary artery disease using post-extra systolic potentiation. Circulation 1974;50:694-9.

74. Helfant RH, Pine R, Meister SG, Feldman MS, Trout RG, Banka VS. Nitroglycerin to unmask reversible asynergy. Correlation with post coronary bypass ventriculography. Circulation 1974;50:108-13.

75. Horn HR, Teichholz LE, Cohn PF, Herman MV, Gorlin R. Augmentation of left ventricular contraction pattern in coronary artery disease by an inotropic catecholamine. The epinephrine ventriculogram. Circulation 1974;49:1063-71.

76. Popio KA, Gorlin R, Bechtel D, Levine JA. Postextrasystolic potentiation as a predictor of potential myocardial viability: preoperative analyses compared with studies after coronary bypass surgery. The American journal of cardiology 1977;39:944-53.

77. Rahimtoola SH. A perspective on the three large multicenter randomized clinical trials of coronary bypass surgery for chronic stable angina. Circulation 1985;72:V123-35.

78. Depre C, Vatner SF. Cardioprotection in stunned and hibernating myocardium. Heart failure reviews 2007;12:307-17.

79. Page B, Young R, Iyer V et al. Persistent regional downregulation in mitochondrial enzymes and upregulation of stress proteins in swine with chronic hibernating myocardium. Circulation research 2008;102:103-12.

80. Depre C, Kim SJ, John AS et al. Program of cell survival underlying human and experimental hibernating myocardium. Circulation research 2004;95:433-40.

81. Ambrosio G, Betocchi S, Pace L et al. Prolonged impairment of regional contractile function after resolution of exercise-induced angina. Evidence of myocardial stunning in patients with coronary artery disease. Circulation 1996;94:2455-64.

82. Barnes E, Hall RJ, Dutka DP, Camici PG. Absolute blood flow and oxygen consumption in stunned myocardium in patients with coronary artery disease. Journal of the American College of Cardiology 2002;39:420-7.

83. Heyndrickx GR, Millard RW, McRitchie RJ, Maroko PR, Vatner SF. Regional myocardial functional and electrophysiological alterations after brief coronary artery occlusion in conscious dogs. The Journal of clinical investigation 1975;56:978-85.

84. Caner B, Beller GA. Are technetium-99m-labeled myocardial perfusion agents adequate for detection of myocardial viability? Clinical cardiology 1998;21:235-42.

85. Bourque JM, Hasselblad V, Velazquez EJ, Borges-Neto S, O'Connor C M. Revascularization in patients with coronary artery disease, left ventricular dysfunction, and viability: a meta-analysis. American heart journal 2003;146:621-7.

86. Ong AT, Serruys PW. Complete revascularization: coronary artery bypass graft surgery versus percutaneous coronary intervention. Circulation 2006;114:249-55.

87. Desideri A, Cortigiani L, Christen AI et al. The extent of perfusion-F18-fluorodeoxyglucose positron emission tomography mismatch determines mortality in medically treated patients with chronic ischemic left ventricular dysfunction. Journal of the American College of Cardiology 2005;46:1264-9.

88. Bonow RO, Maurer G, Lee KL et al. Myocardial viability and survival in ischemic left ventricular dysfunction. The New England journal of medicine 2011;364:1617-25.

89. Gerber BL, Rousseau MF, Ahn SA et al. Prognostic value of myocardial viability by delayed-enhanced magnetic resonance in patients with coronary artery disease and low ejection fraction: impact of revascularization therapy. Journal of the American College of Cardiology 2012;59:825-35.

90. Masci PG, Ganame J, Francone M et al. Relationship between location and size of myocardial infarction and their reciprocal influences on post-infarction left ventricular remodelling. European heart journal 2011;32:1640-8.

91. Kelle S, Roes SD, Klein C et al. Prognostic value of myocardial infarct size and contractile reserve using magnetic resonance imaging. Journal of the American College of Cardiology 2009;54:1770-7.

92. Kwon DH, Halley CM, Carrigan TP et al. Extent of left ventricular scar predicts outcomes in ischemic cardiomyopathy patients with significantly reduced systolic function: a delayed hyperenhancement cardiac magnetic resonance study. JACC Cardiovascular imaging 2009;2:34-44.

93. Di Carli MF, Maddahi J, Rokhsar S et al. Long-term survival of patients with coronary artery disease and left ventricular dysfunction: implications for the role of myocardial viability assessment in management decisions. The Journal of thoracic and cardiovascular surgery 1998;116:997-1004.

94. Lonborg J, Vejlstrup N, Kelbaek H et al. Final infarct size measured by cardiovascular magnetic resonance in patients with ST elevation myocardial infarction predicts long-term clinical outcome: an observational study. European heart journal cardiovascular Imaging 2013;14:387-95.

95. Mauri F, Gasparini M, Barbonaglia L et al. Prognostic significance of the extent of myocardial injury in acute myocardial infarction treated by streptokinase (the GISSI trial). The American journal of cardiology 1989;63:1291-5.

96. Klem I, Weinsaft JW, Bahnson TD et al. Assessment of myocardial scarring improves risk stratification in patients evaluated for cardiac defibrillator implantation. Journal of the American College of Cardiology 2012;60:408-20.

97. McClements BM, Weyman AE, Newell JB, Picard MH. Echocardiographic determinants of left ventricular ejection fraction after acute myocardial infarction. American heart journal 2000;140:284-9.

98. Weisman HF, Healy B. Myocardial infarct expansion, infarct extension, and reinfarction: pathophysiologic concepts. Progress in cardiovascular diseases 1987;30:73-110.

99. Pirolo JS, Hutchins GM, Moore GW. Infarct expansion: pathologic analysis of 204 patients with a single myocardial infarct. Journal of the American College of Cardiology 1986;7:349-54.

100. Picard MH, Wilkins GT, Gillam LD, Thomas JD, Weyman AE. Immediate regional endocardial surface expansion following coronary occlusion in the canine left ventricle: disproportionate effects of anterior versus inferior ischemia. American heart journal 1991;121:753-62.

101. Thanavaro S, Kleiger RE, Province MA et al. Effect of infarct location on the in-hospital prognosis of patients with first transmural myocardial infarction. Circulation 1982;66:742-7.

102. Hands ME, Lloyd BL, Robinson JS, de Klerk N, Thompson PL. Prognostic significance of electrocardiographic site of infarction after correction for enzymatic size of infarction. Circulation 1986;73:885-91.

103. Bourke S, Conroy RM, Mulcahy R, Robinson K. Aetiological and prognostic correlates of site of myocardial infarction. European heart journal 1988;9:734-9.

104. Stone PH, Raabe DS, Jaffe AS et al. Prognostic significance of location and type of myocardial infarction: independent adverse outcome associated with anterior location. Journal of the American College of Cardiology 1988;11:453-63.

105. Morrow DA, Antman EM, Charlesworth A et al. TIMI risk score for ST-elevation myocardial infarction: A convenient, bedside, clinical score for risk assessment at presentation: An intravenous nPA for treatment of infarcting myocardium early II trial substudy. Circulation 2000;102:2031-7.

106. Lee KL, Woodlief LH, Topol EJ et al. Predictors of 30-day mortality in the era of reperfusion for acute myocardial infarction. Results from an international trial of 41,021 patients. GUSTO-I Investigators. Circulation 1995;91:1659-68.

107. Orn S, Manhenke C, Anand IS et al. Effect of left ventricular scar size, location, and transmurality on left ventricular remodeling with healed myocardial infarction. The American journal of cardiology 2007;99:1109-14.

108. Garcia-Dorado D, Oliveras J. Myocardial oedema: a preventable cause of reperfusion injury? Cardiovascular research 1993;27:1555-63.

109. Follette DM, Fey K, Buckberg GD et al. Reducing postischemic damage by temporary modification of reperfusate calcium, potassium, pH, and osmolarity. The Journal of thoracic and cardiovascular surgery 1981;82:221-38.

110. Garcia-Dorado D, Theroux P, Munoz R et al. Favorable effects of hyperosmotic reperfusion on myocardial edema and infarct size. The American journal of physiology 1992;262:H17-22.

111. Kloner RA, Reimer KA, Willerson JT, Jennings RB. Reduction of experimental myocardial infarct size with hyperosmolar mannitol. Proceedings of the Society for Experimental Biology and Medicine Society for Experimental Biology and Medicine 1976;151:677-83.

112. Tranum-Jensen J, Janse MJ, Fiolet WT, Krieger WJ, D'Alnoncourt CN, Durrer D. Tissue osmolality, cell swelling, and reperfusion in acute regional myocardial ischemia in the isolated porcine heart. Circulation research 1981;49:364-81.

113. Starling EH. On the Absorption of Fluids from the Connective Tissue Spaces. The Journal of physiology 1896;19:312-26.

114. Mehlhorn U, Allen SJ, Adams DL et al. Normothermic continuous antegrade blood cardioplegia does not prevent myocardial edema and cardiac dysfunction. Circulation 1995;92:1940-6.

115. Aletras AH, Tilak GS, Natanzon A et al. Retrospective determination of the area at risk for reperfused acute myocardial infarction with T2-weighted cardiac magnetic resonance imaging: histopathological and displacement encoding with stimulated echoes (DENSE) functional validations. Circulation 2006;113:1865-70.

116. Friedrich MG, Abdel-Aty H, Taylor A, Schulz-Menger J, Messroghli D, Dietz R. The salvaged area at risk in reperfused acute myocardial infarction as visualized by cardiovascular magnetic resonance. Journal of the American College of Cardiology 2008;51:1581-7.

117. Abdel-Aty H, Cocker M, Meek C, Tyberg JV, Friedrich MG. Edema as a very early marker for acute myocardial ischemia: a cardiovascular magnetic resonance study. Journal of the American College of Cardiology 2009;53:1194-201.

118. Abdel-Aty H, Zagrosek A, Schulz-Menger J et al. Delayed enhancement and T2-weighted cardiovascular magnetic resonance imaging differentiate acute from chronic myocardial infarction. Circulation 2004;109:2411-6.

119. Davis KL, Mehlhorn U, Laine GA, Allen SJ. Myocardial edema, left ventricular function, and pulmonary hypertension. Journal of applied physiology 1995;78:132-7.

120. Mehlhorn U, Davis KL, Burke EJ, Adams D, Laine GA, Allen SJ. Impact of cardiopulmonary bypass and cardioplegic arrest on myocardial lymphatic function. The American journal of physiology 1995;268:H178-83.

121. Pratt JW, Schertel ER, Schaefer SL et al. Acute transient coronary sinus hypertension impairs left ventricular function and induces myocardial edema. The American journal of physiology 1996;271:H834-41.

122. Mehlhorn U, Allen SJ, Adams DL, Davis KL, Gogola GR, Warters RD. Cardiac surgical conditions induced by beta-blockade: effect on myocardial fluid balance. The Annals of thoracic surgery 1996;62:143-50.

123. Laine GA, Allen SJ. Left ventricular myocardial edema. Lymph flow, interstitial fibrosis, and cardiac function. Circulation research 1991;68:1713-21.

124. Miyamoto M, McClure DE, Schertel ER et al. Effects of hypoproteinemia-induced myocardial edema on left ventricular function. The American journal of physiology 1998;274:H937-44.

125. Rubboli A, Sobotka PA, Euler DE. Effect of acute edema on left ventricular function and coronary vascular resistance in the isolated rat heart. The American journal of physiology 1994;267:H1054-61.

126. Weng ZC, Nicolosi AC, Detwiler PW et al. Effects of crystalloid, blood, and University of Wisconsin perfusates on weight, water content, and left ventricular compliance in an edema-prone, isolated porcine heart model. The Journal of thoracic and cardiovascular surgery 1992;103:504-13.

127. Pogatsa G, Dubecz E, Gabor G. The role of myocardial edema in the left ventricular diastolic stiffness. Basic research in cardiology 1976;71:263-9.

128. Spotnitz HM, Hsu DT. Myocardial edema: importance in the study of left ventricular function. Advances in cardiac surgery 1994;5:1-25.

129. Kahles H, Mezger VA, Hellige G, Spieckermann PG, Bretschneider HJ. The influence of myocardial edema formation on the energy consumption of the heart during aerobiosis and hypoxia. Basic research in cardiology 1982;77:158-69.

130. Ziegler WH, Goresky CA. Transcapillary exchange in the working left ventricle of the dog. Circulation research 1971;29:181-207.

131. Davis KL, Laine GA, Geissler HJ, Mehlhorn U, Brennan M, Allen SJ. Effects of myocardial edema on the development of myocardial interstitial fibrosis. Microcirculation 2000;7:269-80.

132. Payne AR, Berry C, Doolin O et al. Microvascular Resistance Predicts Myocardial Salvage and Infarct Characteristics in ST-Elevation Myocardial Infarction. Journal of the American Heart Association 2012;1:e002246.

133. Berry C, Kellman P, Mancini C et al. Magnetic resonance imaging delineates the ischemic area at risk and myocardial salvage in patients with acute myocardial infarction. Circulation Cardiovascular imaging 2010;3:527-35.

134. Eitel I, Desch S, Fuernau G et al. Prognostic significance and determinants of myocardial salvage assessed by cardiovascular magnetic resonance in acute reperfused myocardial infarction. Journal of the American College of Cardiology 2010;55:2470-9.

135. Krug A, Du Mesnil de R, Korb G. Blood supply of the myocardium after temporary coronary occlusion. Circulation research 1966;19:57-62.

136. Bodi V, Sanchis J, Nunez J et al. Prognostic value of a comprehensive cardiac magnetic resonance assessment soon after a first ST-segment elevation myocardial infarction. JACC Cardiovascular imaging 2009;2:835-42.

137. Bruder O, Breuckmann F, Jensen C et al. Prognostic impact of contrast-enhanced CMR early after acute ST segment elevation myocardial infarction (STEMI) in a regional STEMI network: results of the "Herzinfarktverbund Essen". Herz 2008;33:136-42.

138. Cochet AA, Lorgis L, Lalande A et al. Major prognostic impact of persistent microvascular obstruction as assessed by contrast-enhanced cardiac magnetic resonance in reperfused acute myocardial infarction. European radiology 2009;19:2117-26.

139. de Waha S, Desch S, Eitel I et al. Relationship and prognostic value of microvascular obstruction and infarct size in ST-elevation myocardial infarction as visualized by magnetic resonance imaging. Clinical research in cardiology : official journal of the German Cardiac Society 2012;101:487-95.

140. de Waha S, Desch S, Eitel I et al. Impact of early vs. late microvascular obstruction assessed by magnetic resonance imaging on long-term outcome after ST-elevation myocardial infarction: a comparison with traditional prognostic markers. European heart journal 2010;31:2660-8.

141. Eitel I, Kubusch K, Strohm O et al. Prognostic value and determinants of a hypointense infarct core in T2-weighted cardiac magnetic resonance in acute reperfused ST-elevation-myocardial infarction. Circulation Cardiovascular imaging 2011;4:354-62.

142. Hombach V, Grebe O, Merkle N et al. Sequelae of acute myocardial infarction regarding cardiac structure and function and their prognostic significance as assessed by magnetic resonance imaging. European heart journal 2005;26:549-57.

143. Mather AN, Fairbairn TA, Artis NJ, Greenwood JP, Plein S. Timing of cardiovascular MR imaging after acute myocardial infarction: effect on estimates of infarct characteristics and prediction of late ventricular remodeling. Radiology 2011;261:116-26.

144. Mather AN, Lockie T, Nagel E et al. Appearance of microvascular obstruction on high resolution first-pass perfusion, early and late gadolinium enhancement CMR in patients with acute myocardial infarction. Journal of cardiovascular magnetic resonance : official journal of the Society for Cardiovascular Magnetic Resonance 2009;11:33.

145. Nijveldt R, Beek AM, Hirsch A et al. Functional recovery after acute myocardial infarction: comparison between angiography, electrocardiography, and cardiovascular magnetic resonance measures of microvascular injury. Journal of the American College of Cardiology 2008;52:181-9.

146. Orn S, Manhenke C, Greve OJ et al. Microvascular obstruction is a major determinant of infarct healing and subsequent left ventricular remodelling following primary percutaneous coronary intervention. European heart journal 2009;30:1978-85.

147. Weir RA, Murphy CA, Petrie CJ et al. Microvascular obstruction remains a portent of adverse remodeling in optimally treated patients with left ventricular systolic dysfunction after acute myocardial infarction. Circulation Cardiovascular imaging 2010;3:360-7.

148. Wu KC, Kim RJ, Bluemke DA et al. Quantification and time course of microvascular obstruction by contrast-enhanced echocardiography and magnetic resonance imaging following acute myocardial infarction and reperfusion. Journal of the American College of Cardiology 1998;32:1756-64.

149. Wu KC, Zerhouni EA, Judd RM et al. Prognostic significance of microvascular obstruction by magnetic resonance imaging in patients with acute myocardial infarction. Circulation 1998;97:765-72.

150. Engler RL, Schmid-Schonbein GW, Pavelec RS. Leukocyte capillary plugging in myocardial ischemia and reperfusion in the dog. The American journal of pathology 1983;111:98-111.

151. Galinanes M, Lawson CS, Ferrari R, Limb GA, Derias NW, Hearse DJ. Early and late effects of leukopenic reperfusion on the recovery of cardiac contractile function. Studies in the transplanted and isolated blood-perfused rat heart. Circulation 1993;88:673-83.

152. Kolodgie FD, Virmani R, Farb A. Limitation of no reflow injury by blood-free reperfusion with oxygenated perfluorochemical (Fluosol-DA 20%). Journal of the American College of Cardiology 1991;18:215-23.

153. Lindal S, Sorlie D, Jorgensen L. Endothelial cells of the cardiac microvasculature during and after cold cardioplegic ischaemia. Comparison of endothelial and myocyte damage. Scandinavian journal of thoracic and cardiovascular surgery 1988;22:257-65.

154. Reynolds JM, McDonagh PF. Early in reperfusion, leukocytes alter perfused coronary capillarity and vascular resistance. The American journal of physiology 1989;256:H982-9.

155. Hale SL, Hammerman H, Kloner RA. Effect of two perfluorocarbon emulsions on reperfusion injury after coronary artery occlusion in rabbits. Basic research in cardiology 1995;90:404-9.

156. Manciet LH, Poole DC, McDonagh PF, Copeland JG, Mathieu-Costello O. Microvascular compression during myocardial ischemia: mechanistic basis for no-reflow phenomenon. The American journal of physiology 1994;266:H1541-50.

157. Golino P, Maroko PR, Carew TE. Efficacy of platelet depletion in counteracting the detrimental effect of acute hypercholesterolemia on infarct size and the no-reflow phenomenon in rabbits undergoing coronary artery occlusion-reperfusion. Circulation 1987;76:173-80.

158. Golino P, Ragni M, Cirillo P et al. Effects of tissue factor induced by oxygen free radicals on coronary flow during reperfusion. Nature medicine 1996;2:35-40.

159. Golino P, Ragni M, Cirillo P et al. Recombinant human, active site-blocked factor VIIa reduces infarct size and no-reflow phenomenon in rabbits. American journal of physiology Heart and circulatory physiology 2000;278:H1507-16.

160. Ambrosio G, Becker LC, Hutchins GM, Weisman HF, Weisfeldt ML. Reduction in experimental infarct size by recombinant human superoxide dismutase: insights into the pathophysiology of reperfusion injury. Circulation 1986;74:1424-33.

161. Przyklenk K, Kloner RA. "Reperfusion injury" by oxygen-derived free radicals? Effect of superoxide dismutase plus catalase, given at the time of reperfusion, on myocardial infarct size, contractile function, coronary microvasculature, and regional myocardial blood flow. Circulation research 1989;64:86-96.

162. Villari B, Ambrosio G, Golino P et al. The effects of calcium channel antagonist treatment and oxygen radical scavenging on infarct size and the no-reflow phenomenon in reperfused hearts. American heart journal 1993;125:11-23.

163. Aiello EA, Jabr RI, Cole WC. Arrhythmia and delayed recovery of cardiac action potential during reperfusion after ischemia. Role of oxygen radical-induced no-reflow phenomenon. Circulation research 1995;77:153-62.

164. Sakuma T, Leong-Poi H, Fisher NG, Goodman NC, Kaul S. Further insights into the no-reflow phenomenon after primary angioplasty in acute myocardial infarction: the role of microthromboemboli. Journal of the American Society of Echocardiography : official publication of the American Society of Echocardiography 2003;16:15-21.

165. Kloner RA, Rude RE, Carlson N, Maroko PR, DeBoer LW, Braunwald E. Ultrastructural evidence of microvascular damage and myocardial cell injury after coronary artery occlusion: which comes first? Circulation 1980;62:945-52.

166. Ambrosio G, Weisman HF, Mannisi JA, Becker LC. Progressive impairment of regional myocardial perfusion after initial restoration of postischemic blood flow. Circulation 1989;80:1846-61.

167. Reffelmann T, Kloner RA. Microvascular reperfusion injury: rapid expansion of anatomic no reflow during reperfusion in the rabbit. American journal of physiology Heart and circulatory physiology 2002;283:H1099-107.

168. Rochitte CE, Lima JA, Bluemke DA et al. Magnitude and time course of microvascular obstruction and tissue injury after acute myocardial infarction. Circulation 1998;98:1006-14.

169. Gerber BL, Rochitte CE, Melin JA et al. Microvascular obstruction and left ventricular remodeling early after acute myocardial infarction. Circulation 2000;101:2734-41.

170. Ghugre NR, Ramanan V, Pop M et al. Quantitative tracking of edema, hemorrhage, and microvascular obstruction in subacute myocardial infarction in a porcine model by MRI.

Magnetic resonance in medicine : official journal of the Society of Magnetic Resonance in Medicine / Society of Magnetic Resonance in Medicine 2011;66:1129-41.

171. Wu KC. CMR of microvascular obstruction and hemorrhage in myocardial infarction. Journal of cardiovascular magnetic resonance : official journal of the Society for Cardiovascular Magnetic Resonance 2012;14:68.

172. Kleinbongard P, Konorza T, Bose D et al. Lessons from human coronary aspirate. Journal of molecular and cellular cardiology 2012;52:890-6.

173. Asanuma T, Tanabe K, Ochiai K et al. Relationship between progressive microvascular damage and intramyocardial hemorrhage in patients with reperfused anterior myocardial infarction: myocardial contrast echocardiographic study. Circulation 1997;96:448-53.

174. Sakuma T, Hayashi Y, Shimohara A, Shindo T, Maeda K. Usefulness of myocardial contrast echocardiography for the assessment of serial changes in risk area in patients with acute myocardial infarction. The American journal of cardiology 1996;78:1273-7.

175. Reffelmann T, Hale SL, Dow JS, Kloner RA. No-reflow phenomenon persists long-term after ischemia/reperfusion in the rat and predicts infarct expansion. Circulation 2003;108:2911-7.

176. Ito H, Iwakura K, Oh H et al. Temporal changes in myocardial perfusion patterns in patients with reperfused anterior wall myocardial infarction. Their relation to myocardial viability. Circulation 1995;91:656-62.

177. Funaro S, Galiuto L, Boccalini F et al. Determinants of microvascular damage recovery after acute myocardial infarction: results from the acute myocardial infarction contrast imaging (AMICI) multi-centre study. European journal of echocardiography : the journal

of the Working Group on Echocardiography of the European Society of Cardiology 2011;12:306-12.

178. Larose E, Rodes-Cabau J, Pibarot P et al. Predicting late myocardial recovery and outcomes in the early hours of ST-segment elevation myocardial infarction traditional measures compared with microvascular obstruction, salvaged myocardium, and necrosis characteristics by cardiovascular magnetic resonance. Journal of the American College of Cardiology 2010;55:2459-69.

179. Wong DT, Leung MC, Richardson JD et al. Cardiac magnetic resonance derived late microvascular obstruction assessment post ST-segment elevation myocardial infarction is the best predictor of left ventricular function: a comparison of angiographic and cardiac magnetic resonance derived measurements. The international journal of cardiovascular imaging 2012;28:1971-81.

180. Limalanathan S, Eritsland J, Andersen GO, Klow NE, Abdelnoor M, Hoffmann P. Myocardial salvage is reduced in primary PCI-treated STEMI patients with microvascular obstruction, demonstrated by early and late CMR. PloS one 2013;8:e71780.

181. Kloner RA. No-reflow phenomenon: maintaining vascular integrity. Journal of cardiovascular pharmacology and therapeutics 2011;16:244-50.

182. Bresnahan GF, Roberts R, Shell WE, Ross J, Jr., Sobel BE. Deleterious effects due to hemorrhage after myocardial reperfusion. The American journal of cardiology 1974;33:82-6.

183. Capone RJ, Most AS. Myocardial hemorrhage after coronary reperfusion in pigs. The American journal of cardiology 1978;41:259-66.

184. Fishbein MC, J YR, Lando U, Kanmatsuse K, Mercier JC, Ganz W. The relationship of vascular injury and myocardial hemorrhage to necrosis after reperfusion. Circulation 1980;62:1274-9.

185. Garcia-Dorado D, Theroux P, Solares J et al. Determinants of hemorrhagic infarcts. Histologic observations from experiments involving coronary occlusion, coronary reperfusion, and reocclusion. The American journal of pathology 1990;137:301-11.

186. Higginson LA, Beanlands DS, Nair RC, Temple V, Sheldrick K. The time course and characterization of myocardial hemorrhage after coronary reperfusion in the anesthetized dog. Circulation 1983;67:1024-31.

187. Pislaru SV, Barrios L, Stassen T, Jun L, Pislaru C, Van de Werf F. Infarct size, myocardial hemorrhage, and recovery of function after mechanical versus pharmacological reperfusion: effects of lytic state and occlusion time. Circulation 1997;96:659-66.

188. Beek AM, Nijveldt R, van Rossum AC. Intramyocardial hemorrhage and microvascular obstruction after primary percutaneous coronary intervention. The international journal of cardiovascular imaging 2010;26:49-55.

189. Waller BF, Rothbaum DA, Pinkerton CA et al. Status of the myocardium and infarct-related coronary artery in 19 necropsy patients with acute recanalization using pharmacologic (streptokinase, r-tissue plasminogen activator), mechanical (percutaneous transluminal coronary angioplasty) or combined types of reperfusion therapy. Journal of the American College of Cardiology 1987;9:785-801.

190. Lie JT, Lawrie GM, Morris GC, Jr., Winters WL. Hemorrhagic myocardial infarction associated with aortocoronary bypass revascularization. American heart journal 1978;96:295-302.

191. Fujiwara H, Onodera T, Tanaka M et al. A clinicopathologic study of patients with hemorrhagic myocardial infarction treated with selective coronary thrombolysis with urokinase. Circulation 1986;73:749-57.

192. Topol EJ, Herskowitz A, Hutchins GM. Massive hemorrhagic myocardial infarction after coronary thrombolysis. The American journal of medicine 1986;81:339-43.

193. Kloner RA, Ellis SG, Lange R, Braunwald E. Studies of experimental coronary artery reperfusion. Effects on infarct size, myocardial function, biochemistry, ultrastructure and microvascular damage. Circulation 1983;68:I8-15.

194. Higginson LA, White F, Heggtveit HA, Sanders TM, Bloor CM, Covell JW. Determinants of myocardial hemorrhage after coronary reperfusion in the anesthetized dog. Circulation 1982;65:62-9.

195. Roberts CS, Schoen FJ, Kloner RA. Effect of coronary reperfusion on myocardial hemorrhage and infarct healing. The American journal of cardiology 1983;52:610-4.

196. Ganame J, Messalli G, Dymarkowski S et al. Impact of myocardial haemorrhage on left ventricular function and remodelling in patients with reperfused acute myocardial infarction. European heart journal 2009;30:1440-9.

197. Husser O, Monmeneu JV, Sanchis J et al. Cardiovascular magnetic resonance-derived intramyocardial hemorrhage after STEMI: Influence on long-term prognosis, adverse left ventricular remodeling and relationship with microvascular obstruction. International journal of cardiology 2013;167:2047-54.

198. Mather AN, Fairbairn TA, Ball SG, Greenwood JP, Plein S. Reperfusion haemorrhage as determined by cardiovascular MRI is a predictor of adverse left ventricular remodelling and markers of late arrhythmic risk. Heart 2011;97:453-9.

199. O'Regan DP, Ariff B, Neuwirth C, Tan Y, Durighel G, Cook SA. Assessment of severe reperfusion injury with T2* cardiac MRI in patients with acute myocardial infarction. Heart 2010;96:1885-91.

200. Rother RP, Bell L, Hillmen P, Gladwin MT. The clinical sequelae of intravascular hemolysis and extracellular plasma hemoglobin: a novel mechanism of human disease. Jama 2005;293:1653-62.

201. Pierard LA, Lancellotti P, Kulbertus HE. ST-segment elevation during dobutamine stress testing predicts functional recovery after acute myocardial infarction. American heart journal 1999;137:500-11.

202. Margonato A, Chierchia SL, Xuereb RG et al. Specificity and sensitivity of exercise-induced ST segment elevation for detection of residual viability: comparison with fluorodeoxyglucose and positron emission tomography. Journal of the American College of Cardiology 1995;25:1032-8.

203. Nakano A, Lee JD, Shimizu H et al. Reciprocal ST-segment depression associated with exercise-induced ST-segment elevation indicates residual viability after myocardial infarction. Journal of the American College of Cardiology 1999;33:620-6.

204. Schneider CA, Helmig AK, Baer FM, Horst M, Erdmann E, Sechtem U. Significance of exercise-induced ST-segment elevation and T-wave pseudonormalization for improvement of function in healed Q-wave myocardial infarction. The American journal of cardiology 1998;82:148-53.

205. Schneider CA, Voth E, Baer FM, Horst M, Wagner R, Sechtem U. QT dispersion is determined by the extent of viable myocardium in patients with chronic Q-wave myocardial infarction. Circulation 1997;96:3913-20.

206. Chikamori T, Hirose K, Hamada T et al. Functional recovery after coronary artery bypass grafting in patients with severe left ventricular dysfunction and preserved myocardial viability in the left anterior descending arterial territory as assessed by thallium-201 myocardial perfusion imaging. Japanese circulation journal 1999;63:752-8.

207. Pagley PR, Beller GA, Watson DD, Gimple LW, Ragosta M. Improved outcome after coronary bypass surgery in patients with ischemic cardiomyopathy and residual myocardial viability. Circulation 1997;96:793-800.

208. Brown KA, Heller GV, Landin RS et al. Early dipyridamole (99m)Tc-sestamibi single photon emission computed tomographic imaging 2 to 4 days after acute myocardial infarction predicts in-hospital and postdischarge cardiac events: comparison with submaximal exercise imaging. Circulation 1999;100:2060-6.

209. Mahmarian JJ, Pratt CM, Nishimura S, Abreu A, Verani MS. Quantitative adenosine 201Tl single-photon emission computed tomography for the early assessment of patients surviving acute myocardial infarction. Circulation 1993;87:1197-210.

210. Bax JJ, Wijns W, Cornel JH, Visser FC, Boersma E, Fioretti PM. Accuracy of currently available techniques for prediction of functional recovery after revascularization in patients with left ventricular dysfunction due to chronic coronary artery disease: comparison of pooled data. Journal of the American College of Cardiology 1997;30:1451-60.

211. Wagner A, Mahrholdt H, Holly TA et al. Contrast-enhanced MRI and routine single photon emission computed tomography (SPECT) perfusion imaging for detection of subendocardial myocardial infarcts: an imaging study. Lancet 2003;361:374-9.

212. Pakkal M, Raj V, McCann GP. Non-invasive imaging in coronary artery disease including anatomical and functional evaluation of ischaemia and viability assessment. The British journal of radiology 2011;84 Spec No 3:S280-95.

213. Allman KC. Noninvasive assessment myocardial viability: current status and future directions. Journal of nuclear cardiology : official publication of the American Society of Nuclear Cardiology 2013;20:618-37; quiz 638-9.

214. Thornhill RE, Prato FS, Wisenberg G. The assessment of myocardial viability: a review of current diagnostic imaging approaches. Journal of cardiovascular magnetic resonance : official journal of the Society for Cardiovascular Magnetic Resonance 2002;4:381-410.

215. Gerber BL, Ordoubadi FF, Wijns W et al. Positron emission tomography using(18)F-fluoro-deoxyglucose and euglycaemic hyperinsulinaemic glucose clamp: optimal criteria for the prediction of recovery of post-ischaemic left ventricular dysfunction. Results from the European Community Concerted Action Multicenter study on use of(18)F-fluoro-deoxyglucose Positron Emission Tomography for the Detection of Myocardial Viability. European heart journal 2001;22:1691-701.

216. Pagano D, Bonser RS, Townend JN, Ordoubadi F, Lorenzoni R, Camici PG. Predictive value of dobutamine echocardiography and positron emission tomography in identifying hibernating myocardium in patients with postischaemic heart failure. Heart 1998;79:281-8.

217. Wiggers H, Nielsen TT, Bottcher M, Egeblad H, Botker HE. Positron emission tomography and low-dose dobutamine echocardiography in the prediction of postrevascularization improvement in left ventricular function and exercise parameters. American heart journal 2000;140:928-36.

218. Rahimtoola SH. Hibernating myocardium has reduced blood flow at rest that increases with low-dose dobutamine. Circulation 1996;94:3055-61.

219. Schinkel AF, Bax JJ, Geleijnse ML et al. Noninvasive evaluation of ischaemic heart disease: myocardial perfusion imaging or stress echocardiography? European heart journal 2003;24:789-800.

220. Hoffmann R, Lethen H, Marwick T et al. Analysis of interinstitutional observer agreement in interpretation of dobutamine stress echocardiograms. Journal of the American College of Cardiology 1996;27:330-6.

221. Hundley WG, Hamilton CA, Thomas MS et al. Utility of fast cine magnetic resonance imaging and display for the detection of myocardial ischemia in patients not well suited for second harmonic stress echocardiography. Circulation 1999;100:1697-702.

222. Lepper W, Hoffmann R, Kamp O et al. Assessment of myocardial reperfusion by intravenous myocardial contrast echocardiography and coronary flow reserve after primary percutaneous transluminal coronary angioplasty [correction of angiography] in patients with acute myocardial infarction. Circulation 2000;101:2368-74.

223. Brochet E, Czitrom D, Karila-Cohen D et al. Early changes in myocardial perfusion patterns after myocardial infarction: relation with contractile reserve and functional recovery. Journal of the American College of Cardiology 1998;32:2011-7.

224. Meza MF, Kates MA, Barbee RW et al. Combination of dobutamine and myocardial contrast echocardiography to differentiate postischemic from infarcted myocardium. Journal of the American College of Cardiology 1997;29:974-84.

225. Choi KM, Kim RJ, Gubernikoff G, Vargas JD, Parker M, Judd RM. Transmural extent of acute myocardial infarction predicts long-term improvement in contractile function. Circulation 2001;104:1101-7.

226. Kim RJ, Wu E, Rafael A et al. The use of contrast-enhanced magnetic resonance imaging to identify reversible myocardial dysfunction. The New England journal of medicine 2000;343:1445-53.

227. Selvanayagam JB, Kardos A, Francis JM et al. Value of delayed-enhancement cardiovascular magnetic resonance imaging in predicting myocardial viability after surgical revascularization. Circulation 2004;110:1535-41.

228. Tarantini G, Razzolini R, Cacciavillani L et al. Influence of transmurality, infarct size, and severe microvascular obstruction on left ventricular remodeling and function after primary coronary angioplasty. The American journal of cardiology 2006;98:1033-40.

229. Klein C, Nekolla SG, Bengel FM et al. Assessment of myocardial viability with contrast-enhanced magnetic resonance imaging: comparison with positron emission tomography. Circulation 2002;105:162-7.

230. Tomlinson DR, Becher H, Selvanayagam JB. Assessment of myocardial viability: comparison of echocardiography versus cardiac magnetic resonance imaging in the current era. Heart, lung & circulation 2008;17:173-85.

231. Powell WJ, Jr., wittenberg J, Maturi RA, Dinsmore RE, Miller SW. Detection of edema associated with myocardial ischemia by computerized tomography in isolated, arrested canine hearts. Circulation 1977;55:99-108.

232. Haasler GB, Rodigas PC, Collins RH et al. Two-dimensional echocardiography in dogs. Variation of left ventricular mass, geometry, volume, and ejection fraction on cardiopulmonary bypass. The Journal of thoracic and cardiovascular surgery 1985;90:430-40.

233. Brown JJ, Peterson TM, Slutsky RA. Regional myocardial blood flow, edema formation, and magnetic relaxation times during acute myocardial ischemia in the canine. Investigative radiology 1985;20:465-71.

234. Garcia-Dorado D, Oliveras J, Gili J et al. Analysis of myocardial oedema by magnetic resonance imaging early after coronary artery occlusion with or without reperfusion. Cardiovascular research 1993;27:1462-9.

235. Karolle BL, Carlson RE, Aisen AM, Buda AJ. Transmural distribution of myocardial edema by NMR relaxometry following myocardial ischemia and reperfusion. American heart journal 1991;122:655-64.

236. McNamara MT, Higgins CB, Schechtmann N et al. Detection and characterization of acute myocardial infarction in man with use of gated magnetic resonance. Circulation 1985;71:717-24.

237. Wisenberg G, Prato FS, Carroll SE, Turner KL, Marshall T. Serial nuclear magnetic resonance imaging of acute myocardial infarction with and without reperfusion. American heart journal 1988;115:510-8.

238. Morishima I, Sone T, Okumura K et al. Angiographic no-reflow phenomenon as a predictor of adverse long-term outcome in patients treated with percutaneous transluminal coronary angioplasty for first acute myocardial infarction. Journal of the American College of Cardiology 2000;36:1202-9.

239. Gibson CM, Murphy SA, Rizzo MJ et al. Relationship between TIMI frame count and clinical outcomes after thrombolytic administration. Thrombolysis In Myocardial Infarction (TIMI) Study Group. Circulation 1999;99:1945-50.

240. Henriques JP, Zijlstra F, van 't Hof AW et al. Angiographic assessment of reperfusion in acute myocardial infarction by myocardial blush grade. Circulation 2003;107:2115-9.

241. Ito H, Tomooka T, Sakai N et al. Lack of myocardial perfusion immediately after successful thrombolysis. A predictor of poor recovery of left ventricular function in anterior myocardial infarction. Circulation 1992;85:1699-705.

242. de Lemos JA, Antman EM, Giugliano RP et al. ST-segment resolution and infarct-related artery patency and flow after thrombolytic therapy. Thrombolysis in Myocardial Infarction (TIMI) 14 investigators. The American journal of cardiology 2000;85:299-304.

243. de Lemos JA, Braunwald E. ST segment resolution as a tool for assessing the efficacy of reperfusion therapy. Journal of the American College of Cardiology 2001;38:1283-94.

244. Feldman LJ, Coste P, Furber A et al. Incomplete resolution of ST-segment elevation is a marker of transient microcirculatory dysfunction after stenting for acute myocardial infarction. Circulation 2003;107:2684-9.

245. Kim JS, Ko YG, Yoon SJ et al. Correlation of serial cardiac magnetic resonance imaging parameters with early resolution of ST-segment elevation after primary percutaneous

coronary intervention. Circulation journal : official journal of the Japanese Circulation Society 2008;72:1621-6.

246. Santoro GM, Valenti R, Buonamici P et al. Relation between ST-segment changes and myocardial perfusion evaluated by myocardial contrast echocardiography in patients with acute myocardial infarction treated with direct angioplasty. The American journal of cardiology 1998;82:932-7.

247. van 't Hof AW, Liem A, de Boer MJ, Zijlstra F. Clinical value of 12-lead electrocardiogram after successful reperfusion therapy for acute myocardial infarction. Zwolle Myocardial infarction Study Group. Lancet 1997;350:615-9.

248. Appelbaum E, Kirtane AJ, Clark A et al. Association of TIMI myocardial perfusion grade and ST-segment resolution with cardiovascular magnetic resonance measures of microvascular obstruction and infarct size following ST-segment elevation myocardial infarction. Journal of thrombosis and thrombolysis 2009;27:123-9.

249. Weaver JC, Ramsay DD, Rees D, Binnekamp MF, Prasan AM, McCrohon JA. Dynamic Changes in ST Segment Resolution After Myocardial Infarction and the Association with Microvascular Injury on Cardiac Magnetic Resonance Imaging. Heart, lung & circulation 2011;20:111-8.

250. Wong DT, Leung MC, Das R et al. Intracoronary ECG ST-segment recovery during primary percutaneous intervention for ST-segment myocardial infarction: insights from a cardiac MRI study. Catheterization and cardiovascular interventions : official journal of the Society for Cardiac Angiography & Interventions 2012;80:746-53.

251. Cooper HA, de Lemos JA, Morrow DA et al. Minimal ST-segment deviation: a simple, noninvasive method for identifying patients with a patent infarction-related artery after fibrinolytic administration. American heart journal 2002;144:790-5.

252. Syed MA, Borzak S, Asfour A et al. Single lead ST-segment recovery: a simple, reliable measure of successful fibrinolysis after acute myocardial infarction. American heart journal 2004;147:275-80.

253. Zeymer U, Schroder R, Tebbe U, Molhoek GP, Wegscheider K, Neuhaus KL. Non-invasive detection of early infarct vessel patency by resolution of ST-segment elevation in patients with thrombolysis for acute myocardial infarction; results of the angiographic substudy of the Hirudin for Improvement of Thrombolysis (HIT)-4 trial. European heart journal 2001;22:769-75.

254. Gorgels AP, Vos MA, Letsch IS et al. Usefulness of the accelerated idioventricular rhythm as a marker for myocardial necrosis and reperfusion during thrombolytic therapy in acute myocardial infarction. The American journal of cardiology 1988;61:231-5.

255. Gressin V, Gorgels A, Louvard Y, Lardoux H, Bigelow R. ST-segment normalization time and ventricular arrhythmias as electrocardiographic markers of reperfusion during intravenous thrombolysis for acute myocardial infarction. The American journal of cardiology 1993;71:1436-9.

256. Wehrens XH, Doevendans PA, Ophuis TJ, Wellens HJ. A comparison of electrocardiographic changes during reperfusion of acute myocardial infarction by thrombolysis or percutaneous transluminal coronary angioplasty. American heart journal 2000;139:430-6.

257. Krucoff MW, Johanson P, Baeza R, Crater SW, Dellborg M. Clinical utility of serial and continuous ST-segment recovery assessment in patients with acute ST-elevation myocardial infarction: assessing the dynamics of epicardial and myocardial reperfusion. Circulation 2004;110:e533-9.

258. Onishi T, Kobayashi I, Onishi Y et al. Evaluating microvascular obstruction after acute myocardial infarction using cardiac magnetic resonance imaging and 201-thallium and 99m-technetium pyrophosphate scintigraphy. Circulation journal : official journal of the Japanese Circulation Society 2010;74:2633-40.

259. Schofer J, Montz R, Mathey DG. Scintigraphic evidence of the "no reflow" phenomenon in human beings after coronary thrombolysis. Journal of the American College of Cardiology 1985;5:593-8.

260. Gerber BL, Belge B, Legros GJ et al. Characterization of acute and chronic myocardial infarcts by multidetector computed tomography: comparison with contrast-enhanced magnetic resonance. Circulation 2006;113:823-33.

261. Lardo AC, Cordeiro MA, Silva C et al. Contrast-enhanced multidetector computed tomography viability imaging after myocardial infarction: characterization of myocyte death, microvascular obstruction, and chronic scar. Circulation 2006;113:394-404.

262. Nieman K, Shapiro MD, Ferencik M et al. Reperfused myocardial infarction: contrast-enhanced 64-Section CT in comparison to MR imaging. Radiology 2008;247:49-56.

263. Akasaka T, Yoshida K, Kawamoto T et al. Relation of phasic coronary flow velocity characteristics with TIMI perfusion grade and myocardial recovery after primary percutaneous transluminal coronary angioplasty and rescue stenting. Circulation 2000;101:2361-7.

264. Furber AP, Prunier F, Nguyen HC, Boulet S, Delepine S, Geslin P. Coronary blood flow assessment after successful angioplasty for acute myocardial infarction predicts the risk of long-term cardiac events. Circulation 2004;110:3527-33.

265. Ito H, Maruyama A, Iwakura K et al. Clinical implications of the 'no reflow' phenomenon. A predictor of complications and left ventricular remodeling in reperfused anterior wall myocardial infarction. Circulation 1996;93:223-8.

266. Iwakura K, Ito H, Nishikawa N et al. Early temporal changes in coronary flow velocity patterns in patients with acute myocardial infarction demonstrating the "no-reflow" phenomenon. The American journal of cardiology 1999;84:415-9.

267. Iwakura K, Ito H, Takiuchi S et al. Alternation in the coronary blood flow velocity pattern in patients with no reflow and reperfused acute myocardial infarction. Circulation 1996;94:1269-75.

268. Kawamoto T, Yoshida K, Akasaka T et al. Can coronary blood flow velocity pattern after primary percutaneous transluminal coronary angioplasty [correction of angiography] predict recovery of regional left ventricular function in patients with acute myocardial infarction? Circulation 1999;100:339-45.

269. Yamamuro A, Akasaka T, Tamita K et al. Coronary flow velocity pattern immediately after percutaneous coronary intervention as a predictor of complications and in-hospital survival after acute myocardial infarction. Circulation 2002;106:3051-6.

270. Greaves K, Dixon SR, Fejka M et al. Myocardial contrast echocardiography is superior to other known modalities for assessing myocardial reperfusion after acute myocardial infarction. Heart 2003;89:139-44.

271. Ito H, Okamura A, Iwakura K et al. Myocardial perfusion patterns related to thrombolysis in myocardial infarction perfusion grades after coronary angioplasty in patients with acute anterior wall myocardial infarction. Circulation 1996;93:1993-9.

272. Porter TR, Li S, Oster R, Deligonul U. The clinical implications of no reflow demonstrated with intravenous perfluorocarbon containing microbubbles following restoration of Thrombolysis In Myocardial Infarction (TIMI) 3 flow in patients with acute myocardial infarction. The American journal of cardiology 1998;82:1173-7.

273. Villanueva FS, Glasheen WP, Sklenar J, Kaul S. Assessment of risk area during coronary occlusion and infarct size after reperfusion with myocardial contrast echocardiography using left and right atrial injections of contrast. Circulation 1993;88:596-604.

274. Manning WJ, Atkinson DJ, Grossman W, Paulin S, Edelman RR. First-pass nuclear magnetic resonance imaging studies using gadolinium-DTPA in patients with coronary artery disease. Journal of the American College of Cardiology 1991;18:959-65.

275. van Rugge FP, van der Wall EE, van Dijkman PR, Louwerenburg HW, de Roos A, Bruschke AV. Usefulness of ultrafast magnetic resonance imaging in healed myocardial infarction. The American journal of cardiology 1992;70:1233-7.

276. Wilke N, Simm C, Zhang J et al. Contrast-enhanced first pass myocardial perfusion imaging: correlation between myocardial blood flow in dogs at rest and during hyperemia. Magnetic resonance in medicine : official journal of the Society of Magnetic Resonance in Medicine / Society of Magnetic Resonance in Medicine 1993;29:485-97.

277. Judd RM, Lugo-Olivieri CH, Arai M et al. Physiological basis of myocardial contrast enhancement in fast magnetic resonance images of 2-day-old reperfused canine infarcts. Circulation 1995;92:1902-10.

278. Lima JA, Judd RM, Bazille A, Schulman SP, Atalar E, Zerhouni EA. Regional heterogeneity of human myocardial infarcts demonstrated by contrast-enhanced MRI. Potential mechanisms. Circulation 1995;92:1117-25.

279. Lund GK, Stork A, Saeed M et al. Acute myocardial infarction: evaluation with first-pass enhancement and delayed enhancement MR imaging compared with 201Tl SPECT imaging. Radiology 2004;232:49-57.

280. Rogers WJ, Jr., Kramer CM, Geskin G et al. Early contrast-enhanced MRI predicts late functional recovery after reperfused myocardial infarction. Circulation 1999;99:744-50.

281. Taylor AJ, Al-Saadi N, Abdel-Aty H, Schulz-Menger J, Messroghli DR, Friedrich MG. Detection of acutely impaired microvascular reperfusion after infarct angioplasty with magnetic resonance imaging. Circulation 2004;109:2080-5.

282. Yan AT, Gibson CM, Larose E et al. Characterization of microvascular dysfunction after acute myocardial infarction by cardiovascular magnetic resonance first-pass perfusion and late gadolinium enhancement imaging. Journal of cardiovascular magnetic resonance : official journal of the Society for Cardiovascular Magnetic Resonance 2006;8:831-7.

283. Kao KJ, Hackel DB, Kong Y. Hemorrhagic myocardial infarction after streptokinase treatment for acute coronary thrombosis. Archives of pathology & laboratory medicine 1984;108:121-4.

284. Smith DF, Higginson LA, Walley VM. Reperfusion hemorrhage following PTCA and thrombolysis for left main coronary artery occlusion. The Canadian journal of cardiology 1988;4:33-6.

285. Bradley WG, Jr. MR appearance of hemorrhage in the brain. Radiology 1993;189:15-26.

286. Gomori JM, Grossman RI, Goldberg HI, Zimmerman RA, Bilaniuk LT. Intracranial hematomas: imaging by high-field MR. Radiology 1985;157:87-93.

287. van den Bos EJ, Baks T, Moelker AD et al. Magnetic resonance imaging of haemorrhage within reperfused myocardial infarcts: possible interference with iron oxide-labelled cell tracking? European heart journal 2006;27:1620-6.

288. Basso C, Corbetti F, Silva C et al. Morphologic validation of reperfused hemorrhagic myocardial infarction by cardiovascular magnetic resonance. The American journal of cardiology 2007;100:1322-7.

289. Lotan CS, Miller SK, Cranney GB, Pohost GM, Elgavish GA. The effect of postinfarction intramyocardial hemorrhage on transverse relaxation time. Magnetic resonance in medicine : official journal of the Society of Magnetic Resonance in Medicine / Society of Magnetic Resonance in Medicine 1992;23:346-55.

290. Payne AR, Berry C, Kellman P et al. Bright-blood T(2)-weighted MRI has high diagnostic accuracy for myocardial hemorrhage in myocardial infarction: a preclinical validation study in swine. Circulation Cardiovascular imaging 2011;4:738-45.

291. Ochiai K, Shimada T, Murakami Y et al. Hemorrhagic myocardial infarction after coronary reperfusion detected in vivo by magnetic resonance imaging in humans: prevalence and clinical implications. Journal of cardiovascular magnetic resonance : official journal of the Society for Cardiovascular Magnetic Resonance 1999;1:247-56.

292. O'Regan DP, Ahmed R, Karunanithy N et al. Reperfusion hemorrhage following acute myocardial infarction: assessment with T2* mapping and effect on measuring the area at risk. Radiology 2009;250:916-22.

293. Kumar A, Green JD, Sykes JM et al. Detection and quantification of myocardial reperfusion hemorrhage using T2*-weighted CMR. JACC Cardiovasc Imaging 2011;4:1274-83.

294. Linfante I, Llinas RH, Caplan LR, Warach S. MRI features of intracerebral hemorrhage within 2 hours from symptom onset. Stroke; a journal of cerebral circulation 1999;30:2263-7.

295. Hermier M, Nighoghossian N. Contribution of susceptibility-weighted imaging to acute stroke assessment. Stroke; a journal of cerebral circulation 2004;35:1989-94.

296. Abragam A. The principles of nuclear magnetism. Oxford: Clarendon Press, 1961.

297. Haacke EM. Magnetic resonance imaging : physical principles and sequence design. New York: Wiley, 1999.

298. Levitt MH. Spin dynamics : basics of nuclear magnetic resonance. 2nd ed. Chichester, England ; Hoboken, NJ: John Wiley & Sons, 2008.

299. Nishimura DG. Principles of magnetic resonance imaging. Ed. 1.1. ed. S.l.: D. Nishimura, 2010.

300. Slichter CP. Principles of magnetic resonance. 3rd ed. Berlin ; New York: Springer-Verlag, 1990.

301. Guyton AC, Hall JE. Textbook of medical physiology. 11th ed. Philadelphia: Elsevier Saunders, 2006.

302. Bloembergen N, Purcell EM, Pound RV. Relaxation effects in nuclear magnetic resonance absorption. Physical Review 1948;73:679-712.

303. Brown JJ, Peck WW, Gerber KH, Higgins CB, Strich G, Slutsky RA. Nuclear magnetic resonance analysis of acute and chronic myocardial infarction in dogs: alterations in spin-lattice relaxation times. American heart journal 1984;108:1292-7.

304. Higgins CB, Herfkens R, Lipton MJ et al. Nuclear magnetic resonance imaging of acute myocardial infarction in dogs: alterations in magnetic relaxation times. The American journal of cardiology 1983;52:184-8.

305. Williams ES, Kaplan JI, Thatcher F, Zimmerman G, Knoebel SB. Prolongation of proton spin lattice relaxation times in regionally ischemic tissue from dog hearts. Journal of nuclear medicine : official publication, Society of Nuclear Medicine 1980;21:449-53.

306. Goldfarb JW, Arnold S, Han J. Recent myocardial infarction: assessment with unenhanced T1-weighted MR imaging. Radiology 2007;245:245-50.

307. Pedersen SF, Thrysoe SA, Robich MP et al. Assessment of intramyocardial hemorrhage by T1-weighted cardiovascular magnetic resonance in reperfused acute myocardial infarction. Journal of cardiovascular magnetic resonance : official journal of the Society for Cardiovascular Magnetic Resonance 2012;14:59.

308. Kim RJ, Fieno DS, Parrish TB et al. Relationship of MRI delayed contrast enhancement to irreversible injury, infarct age, and contractile function. Circulation 1999;100:1992-2002.

309. Kim RJ, Shah DJ, Judd RM. How we perform delayed enhancement imaging. Journal of cardiovascular magnetic resonance : official journal of the Society for Cardiovascular Magnetic Resonance 2003;5:505-14.

310. Messroghli DR, Radjenovic A, Kozerke S, Higgins DM, Sivananthan MU, Ridgway JP. Modified Look-Locker inversion recovery (MOLLI) for high-resolution T1 mapping of

the heart. Magnetic resonance in medicine : official journal of the Society of Magnetic Resonance in Medicine / Society of Magnetic Resonance in Medicine 2004;52:141-6.

311. Messroghli DR, Greiser A, Frohlich M, Dietz R, Schulz-Menger J. Optimization and validation of a fully-integrated pulse sequence for modified look-locker inversion-recovery (MOLLI) T1 mapping of the heart. Journal of magnetic resonance imaging : JMRI 2007;26:1081-6.

312. Gai ND, Stehning C, Nacif M, Bluemke DA. Modified Look-Locker T1 evaluation using Bloch simulations: human and phantom validation. Magnetic resonance in medicine : official journal of the Society of Magnetic Resonance in Medicine / Society of Magnetic Resonance in Medicine 2013;69:329-36.

313. Piechnik SK, Ferreira VM, Dall'Armellina E et al. Shortened Modified Look-Locker Inversion recovery (ShMOLLI) for clinical myocardial T1-mapping at 1.5 and 3 T within a 9 heartbeat breathhold. Journal of cardiovascular magnetic resonance : official journal of the Society for Cardiovascular Magnetic Resonance 2010;12:69.

314. Chow K, Flewitt JA, Green JD, Pagano JJ, Friedrich MG, Thompson RB. Saturation recovery single-shot acquisition (SASHA) for myocardial T(1) mapping. Magnetic resonance in medicine : official journal of the Society of Magnetic Resonance in Medicine / Society of Magnetic Resonance in Medicine 2014;71:2082-95.

315. Dall'Armellina E, Piechnik SK, Ferreira VM et al. Cardiovascular magnetic resonance by non contrast T1-mapping allows assessment of severity of injury in acute myocardial infarction. Journal of cardiovascular magnetic resonance : official journal of the Society for Cardiovascular Magnetic Resonance 2012;14:15.

316. Ferreira VM, Piechnik SK, Dall'Armellina E et al. Non-contrast T1-mapping detects acute myocardial edema with high diagnostic accuracy: a comparison to T2-weighted cardiovascular magnetic resonance. Journal of cardiovascular magnetic resonance : official journal of the Society for Cardiovascular Magnetic Resonance 2012;14:42.

317. Messroghli DR, Walters K, Plein S et al. Myocardial T1 mapping: application to patients with acute and chronic myocardial infarction. Magnetic resonance in medicine : official journal of the Society of Magnetic Resonance in Medicine / Society of Magnetic Resonance in Medicine 2007;58:34-40.

318. Ugander M, Bagi PS, Oki AJ et al. Myocardial edema as detected by pre-contrast T1 and T2 CMR delineates area at risk associated with acute myocardial infarction. JACC Cardiovascular imaging 2012;5:596-603.

319. Bauner KU, Biffar A, Theisen D et al. Extracellular volume fractions in chronic myocardial infarction. Investigative radiology 2012;47:538-45.

320. Lee JJ, Liu S, Nacif MS et al. Myocardial T1 and extracellular volume fraction mapping at 3 tesla. Journal of cardiovascular magnetic resonance : official journal of the Society for Cardiovascular Magnetic Resonance 2011;13:75.

321. Cury RC, Shash K, Nagurney JT et al. Cardiac magnetic resonance with T2-weighted imaging improves detection of patients with acute coronary syndrome in the emergency department. Circulation 2008;118:837-44.

322. Arai AE. Using magnetic resonance imaging to characterize recent myocardial injury: utility in acute coronary syndrome and other clinical scenarios. Circulation 2008;118:795-6.

323. Raman SV, Simonetti OP, Winner MW, 3rd et al. Cardiac magnetic resonance with edema imaging identifies myocardium at risk and predicts worse outcome in patients with non-ST-segment elevation acute coronary syndrome. Journal of the American College of Cardiology 2010;55:2480-8.

324. Masci PG, Ganame J, Strata E et al. Myocardial salvage by CMR correlates with LV remodeling and early ST-segment resolution in acute myocardial infarction. JACC Cardiovascular imaging 2010;3:45-51.

325. Tilak GS, Hsu LY, Hoyt RF, Jr., Arai AE, Aletras AH. In vivo T2-weighted magnetic resonance imaging can accurately determine the ischemic area at risk for 2-day-old nonreperfused myocardial infarction. Investigative radiology 2008;43:7-15.

326. Francone M, Bucciarelli-Ducci C, Carbone I et al. Impact of primary coronary angioplasty delay on myocardial salvage, infarct size, and microvascular damage in patients with ST-segment elevation myocardial infarction: insight from cardiovascular magnetic resonance. Journal of the American College of Cardiology 2009;54:2145-53.

327. Wright J, Adriaenssens T, Dymarkowski S, Desmet W, Bogaert J. Quantification of myocardial area at risk with T2-weighted CMR: comparison with contrast-enhanced CMR and coronary angiography. JACC Cardiovascular imaging 2009;2:825-31.

328. Carlsson M, Ubachs JF, Hedstrom E, Heiberg E, Jovinge S, Arheden H. Myocardium at risk after acute infarction in humans on cardiac magnetic resonance: quantitative assessment during follow-up and validation with single-photon emission computed tomography. JACC Cardiovascular imaging 2009;2:569-76.

329. Sorensson P, Heiberg E, Saleh N et al. Assessment of myocardium at risk with contrast enhanced steady-state free precession cine cardiovascular magnetic resonance compared

to single-photon emission computed tomography. Journal of cardiovascular magnetic resonance : official journal of the Society for Cardiovascular Magnetic Resonance 2010;12:25.

330. Bekkers SC, Backes WH, Kim RJ et al. Detection and characteristics of microvascular obstruction in reperfused acute myocardial infarction using an optimized protocol for contrast-enhanced cardiovascular magnetic resonance imaging. European radiology 2009;19:2904-12.

331. Simonetti OP, Finn JP, White RD, Laub G, Henry DA. "Black blood" T2-weighted inversion-recovery MR imaging of the heart. Radiology 1996;199:49-57.

332. Huang TY, Liu YJ, Stemmer A, Poncelet BP. T2 measurement of the human myocardium using a T2-prepared transient-state TrueFISP sequence. Magnetic resonance in medicine : official journal of the Society of Magnetic Resonance in Medicine / Society of Magnetic Resonance in Medicine 2007;57:960-6.

333. Kellman P, Aletras AH, Mancini C, McVeigh ER, Arai AE. T2-prepared SSFP improves diagnostic confidence in edema imaging in acute myocardial infarction compared to turbo spin echo. Magnetic resonance in medicine : official journal of the Society of Magnetic Resonance in Medicine / Society of Magnetic Resonance in Medicine 2007;57:891-7.

334. Giri S, Chung YC, Merchant A et al. T2 quantification for improved detection of myocardial edema. Journal of cardiovascular magnetic resonance : official journal of the Society for Cardiovascular Magnetic Resonance 2009;11:56.

335. Verhaert D, Thavendiranathan P, Giri S et al. Direct T2 quantification of myocardial edema in acute ischemic injury. JACC Cardiovascular imaging 2011;4:269-78.

336. Wood JC, Enriquez C, Ghugre N et al. MRI R2 and R2* mapping accurately estimates hepatic iron concentration in transfusion-dependent thalassemia and sickle cell disease patients. Blood 2005;106:1460-5.

337. Carpenter JP, He T, Kirk P et al. On T2* magnetic resonance and cardiac iron. Circulation 2011;123:1519-28.

338. Di Tucci AA, Matta G, Deplano S et al. Myocardial iron overload assessment by T2* magnetic resonance imaging in adult transfusion dependent patients with acquired anemias. Haematologica 2008;93:1385-8.

339. He T, Gatehouse PD, Smith GC, Mohiaddin RH, Pennell DJ, Firmin DN. Myocardial T2* measurements in iron-overloaded thalassemia: An in vivo study to investigate optimal methods of quantification. Magnetic resonance in medicine : official journal of the Society of Magnetic Resonance in Medicine / Society of Magnetic Resonance in Medicine 2008;60:1082-9.

340. Kondur AK, Li T, Vaitkevicius P, Afonso L. Quantification of myocardial iron overload by cardiovascular magnetic resonance imaging T2* and review of the literature. Clinical cardiology 2009;32:E55-9.

341. Ghugre NR, Enriquez CM, Gonzalez I, Nelson MD, Jr., Coates TD, Wood JC. MRI detects myocardial iron in the human heart. Magnetic resonance in medicine : official journal of the Society of Magnetic Resonance in Medicine / Society of Magnetic Resonance in Medicine 2006;56:681-6.

342. Ghugre NR, Enriquez CM, Coates TD, Nelson MD, Jr., Wood JC. Improved R2* measurements in myocardial iron overload. Journal of magnetic resonance imaging : JMRI 2006;23:9-16.

343. Fieno DS, Kim RJ, Chen EL, Lomasney JW, Klocke FJ, Judd RM. Contrast-enhanced magnetic resonance imaging of myocardium at risk: distinction between reversible and irreversible injury throughout infarct healing. Journal of the American College of Cardiology 2000;36:1985-91.

344. Kramer CM, Rogers WJ, Jr., Mankad S, Theobald TM, Pakstis DL, Hu YL. Contractile reserve and contrast uptake pattern by magnetic resonance imaging and functional recovery after reperfused myocardial infarction. Journal of the American College of Cardiology 2000;36:1835-40.

345. Ramani K, Judd RM, Holly TA et al. Contrast magnetic resonance imaging in the assessment of myocardial viability in patients with stable coronary artery disease and left ventricular dysfunction. Circulation 1998;98:2687-94.

346. Ibrahim T, Bulow HP, Hackl T et al. Diagnostic value of contrast-enhanced magnetic resonance imaging and single-photon emission computed tomography for detection of myocardial necrosis early after acute myocardial infarction. Journal of the American College of Cardiology 2007;49:208-16.

347. Ingkanisorn WP, Rhoads KL, Aletras AH, Kellman P, Arai AE. Gadolinium delayed enhancement cardiovascular magnetic resonance correlates with clinical measures of myocardial infarction. Journal of the American College of Cardiology 2004;43:2253-9.

348. Bello D, Shah DJ, Farah GM et al. Gadolinium cardiovascular magnetic resonance predicts reversible myocardial dysfunction and remodeling in patients with heart failure undergoing beta-blocker therapy. Circulation 2003;108:1945-53.

349. Klem I, Heitner JF, Shah DJ et al. Improved detection of coronary artery disease by stress perfusion cardiovascular magnetic resonance with the use of delayed enhancement infarction imaging. Journal of the American College of Cardiology 2006;47:1630-8.

350. Ansari M, Araoz PA, Gerard SK et al. Comparison of late enhancement cardiovascular magnetic resonance and thallium SPECT in patients with coronary disease and left ventricular dysfunction. Journal of cardiovascular magnetic resonance : official journal of the Society for Cardiovascular Magnetic Resonance 2004;6:549-56.

351. Ichikawa Y, Sakuma H, Suzawa N et al. Late gadolinium-enhanced magnetic resonance imaging in acute and chronic myocardial infarction. Improved prediction of regional myocardial contraction in the chronic state by measuring thickness of nonenhanced myocardium. Journal of the American College of Cardiology 2005;45:901-9.

352. Arheden H, Saeed M, Higgins CB et al. Measurement of the distribution volume of gadopentetate dimeglumine at echo-planar MR imaging to quantify myocardial infarction: comparison with 99mTc-DTPA autoradiography in rats. Radiology 1999;211:698-708.

353. Arheden H, Saeed M, Higgins CB et al. Reperfused rat myocardium subjected to various durations of ischemia: estimation of the distribution volume of contrast material with echo-planar MR imaging. Radiology 2000;215:520-8.

354. Wendland MF, Saeed M, Arheden H et al. Toward necrotic cell fraction measurement by contrast-enhanced MRI of reperfused ischemically injured myocardium. Academic radiology 1998;5 Suppl 1:S42-4; discussion S45-6.

355. Knowles BR, Batchelor PG, Parish V et al. Pharmacokinetic modeling of delayed gadolinium enhancement in the myocardium. Magnetic resonance in medicine : official

journal of the Society of Magnetic Resonance in Medicine / Society of Magnetic Resonance in Medicine 2008;60:1524-30.

356. Simonetti OP, Kim RJ, Fieno DS et al. An improved MR imaging technique for the visualization of myocardial infarction. Radiology 2001;218:215-23.

357. Kim RJ, Albert TS, Wible JH et al. Performance of delayed-enhancement magnetic resonance imaging with gadoversetamide contrast for the detection and assessment of myocardial infarction: an international, multicenter, double-blinded, randomized trial. Circulation 2008;117:629-37.

358. Moon JC, De Arenaza DP, Elkington AG et al. The pathologic basis of Q-wave and non-Q-wave myocardial infarction: a cardiovascular magnetic resonance study. Journal of the American College of Cardiology 2004;44:554-60.

359. Wu E, Judd RM, Vargas JD, Klocke FJ, Bonow RO, Kim RJ. Visualisation of presence, location, and transmural extent of healed Q-wave and non-Q-wave myocardial infarction. Lancet 2001;357:21-8.

360. Wellnhofer E, Olariu A, Klein C et al. Magnetic resonance low-dose dobutamine test is superior to SCAR quantification for the prediction of functional recovery. Circulation 2004;109:2172-4.

361. Knuesel PR, Nanz D, Wyss C et al. Characterization of dysfunctional myocardium by positron emission tomography and magnetic resonance: relation to functional outcome after revascularization. Circulation 2003;108:1095-100.

362. Makkar RR, Smith RR, Cheng K et al. Intracoronary cardiosphere-derived cells for heart regeneration after myocardial infarction (CADUCEUS): a prospective, randomised phase 1 trial. Lancet 2012;379:895-904.

363. Malliaras K, Smith RR, Kanazawa H et al. Validation of contrast-enhanced magnetic resonance imaging to monitor regenerative efficacy after cell therapy in a porcine model of convalescent myocardial infarction. Circulation 2013;128:2764-75.

364. Bello D, Fieno DS, Kim RJ et al. Infarct morphology identifies patients with substrate for sustained ventricular tachycardia. Journal of the American College of Cardiology 2005;45:1104-8.

365. Schmidt A, Azevedo CF, Cheng A et al. Infarct tissue heterogeneity by magnetic resonance imaging identifies enhanced cardiac arrhythmia susceptibility in patients with left ventricular dysfunction. Circulation 2007;115:2006-14.

366. Yan AT, Shayne AJ, Brown KA et al. Characterization of the peri-infarct zone by contrast-enhanced cardiac magnetic resonance imaging is a powerful predictor of post-myocardial infarction mortality. Circulation 2006;114:32-9.

367. Watanabe E, Abbasi SA, Heydari B et al. Infarct tissue heterogeneity by contrast-enhanced magnetic resonance imaging is a novel predictor of mortality in patients with chronic coronary artery disease and left ventricular dysfunction. Circulation Cardiovascular imaging 2014;7:887-94.

368. Ledneva E, Karie S, Launay-Vacher V, Janus N, Deray G. Renal safety of gadolinium-based contrast media in patients with chronic renal insufficiency. Radiology 2009;250:618-28.

369. Puntmann VO, Gebker R, Duckett S et al. Left ventricular chamber dimensions and wall thickness by cardiovascular magnetic resonance: comparison with transthoracic echocardiography. European heart journal cardiovascular Imaging 2013;14:240-6.

370. Akgun H, Gonlusen G, Cartwright J, Jr., Suki WN, Truong LD. Are gadolinium-based contrast media nephrotoxic? A renal biopsy study. Archives of pathology & laboratory medicine 2006;130:1354-7.

371. Briguori C, Colombo A, Airoldi F et al. Gadolinium-based contrast agents and nephrotoxicity in patients undergoing coronary artery procedures. Catheterization and cardiovascular interventions : official journal of the Society for Cardiac Angiography & Interventions 2006;67:175-80.

372. Ergun I, Keven K, Uruc I et al. The safety of gadolinium in patients with stage 3 and 4 renal failure. Nephrology, dialysis, transplantation : official publication of the European Dialysis and Transplant Association - European Renal Association 2006;21:697-700.

373. Gemery J, Idelson B, Reid S et al. Acute renal failure after arteriography with a gadolinium-based contrast agent. AJR American journal of roentgenology 1998;171:1277-8.

374. Nyman U, Elmstahl B, Leander P, Nilsson M, Golman K, Almen T. Are gadolinium-based contrast media really safer than iodinated media for digital subtraction angiography in patients with azotemia? Radiology 2002;223:311-8; discussion 328-9.

375. Reed PS, Dixon SR, Boura JA, O'Neill WW, Kahn JK. Comparison of the usefulness of gadodiamide and iodine mixture versus iodinated contrast alone for prevention of contrast-induced nephropathy in patients with chronic kidney disease undergoing coronary angiography. The American journal of cardiology 2007;100:1090-3.

376. Thomsen HS. Gadolinium-based contrast media may be nephrotoxic even at approved doses. European radiology 2004;14:1654-6.

377. Boyd AS, Zic JA, Abraham JL. Gadolinium deposition in nephrogenic fibrosing dermopathy. Journal of the American Academy of Dermatology 2007;56:27-30.

378. Grobner T. Gadolinium--a specific trigger for the development of nephrogenic fibrosing dermopathy and nephrogenic systemic fibrosis? Nephrology, dialysis, transplantation : official publication of the European Dialysis and Transplant Association - European Renal Association 2006;21:1104-8.

379. High WA, Ayers RA, Chandler J, Zito G, Cowper SE. Gadolinium is detectable within the tissue of patients with nephrogenic systemic fibrosis. Journal of the American Academy of Dermatology 2007;56:21-6.

380. Sadowski EA, Bennett LK, Chan MR et al. Nephrogenic systemic fibrosis: risk factors and incidence estimation. Radiology 2007;243:148-57.

381. Thomsen HS, Morcos SK, Dawson P. Is there a causal relation between the administration of gadolinium based contrast media and the development of nephrogenic systemic fibrosis (NSF)? Clinical radiology 2006;61:905-6.

382. Marckmann P, Skov L, Rossen K et al. Nephrogenic systemic fibrosis: suspected causative role of gadodiamide used for contrast-enhanced magnetic resonance imaging. Journal of the American Society of Nephrology : JASN 2006;17:2359-62.

383. US Renal Data System. USRDS 2013 Annual Data Report: Atlas of Chronic Kidney Disease and End-Stage Renal Disease in the United States. Bethesda, MD: National Institutes of Health, National Institute of Diabetes and Digestive and Kidney Diseases, 2013.

384. Fox CS, Muntner P, Chen AY et al. Use of evidence-based therapies in short-term outcomes of ST-segment elevation myocardial infarction and non-ST-segment elevation

myocardial infarction in patients with chronic kidney disease: a report from the National Cardiovascular Data Acute Coronary Treatment and Intervention Outcomes Network registry. Circulation 2010;121:357-65.

385. Shroff GR, Frederick PD, Herzog CA. Renal failure and acute myocardial infarction: clinical characteristics in patients with advanced chronic kidney disease, on dialysis, and without chronic kidney disease. A collaborative project of the United States Renal Data System/National Institutes of Health and the National Registry of Myocardial Infarction. American heart journal 2012;163:399-406.

386. Chang CA. Magnetic resonance imaging contrast agents. Design and physicochemical properties of gadodiamide. Investigative radiology 1993;28 Suppl 1:S21-7.

387. Cacheris WP, Quay SC, Rocklage SM. The relationship between thermodynamics and the toxicity of gadolinium complexes. Magnetic resonance imaging 1990;8:467-81.

388. Swan SK, Lambrecht LJ, Townsend R et al. Safety and pharmacokinetic profile of gadobenate dimeglumine in subjects with renal impairment. Investigative radiology 1999;34:443-8.

389. Berg KJ, Lundby B, Reinton V, Nordal KP, Rootwelt K, Smith HJ. Gadodiamide in renal transplant patients: effects on renal function and usefulness as a glomerular filtration rate marker. Nephron 1996;72:212-7.

390. Schuhmann-Giampieri G, Krestin G. Pharmacokinetics of Gd-DTPA in patients with chronic renal failure. Investigative radiology 1991;26:975-9.

391. Swan SK, Baker JF, Free R et al. Pharmacokinetics, safety, and tolerability of gadoversetamide injection (OptiMARK) in subjects with central nervous system or liver

pathology and varying degrees of renal function. Journal of magnetic resonance imaging : JMRI 1999;9:317-21.

392. Joffe P, Thomsen HS, Meusel M. Pharmacokinetics of gadodiamide injection in patients with severe renal insufficiency and patients undergoing hemodialysis or continuous ambulatory peritoneal dialysis. Academic radiology 1998;5:491-502.

393. Idee JM, Port M, Raynal I, Schaefer M, Le Greneur S, Corot C. Clinical and biological consequences of transmetallation induced by contrast agents for magnetic resonance imaging: a review. Fundamental & clinical pharmacology 2006;20:563-76.

394. Morcos SK, Anderson PB. Pediatric bronchography performed through the flexible bronchoscope. European journal of radiology 1993;17:134-6.

395. Port M, Idee JM, Medina C, Robic C, Sabatou M, Corot C. Efficiency, thermodynamic and kinetic stability of marketed gadolinium chelates and their possible clinical consequences: a critical review. Biometals : an international journal on the role of metal ions in biology, biochemistry, and medicine 2008;21:469-90.

396. Puttagunta NR, Gibby WA, Puttagunta VL. Comparative transmetallation kinetics and thermodynamic stability of gadolinium-DTPA bis-glucosamide and other magnetic resonance imaging contrast media. Investigative radiology 1996;31:619-24.

397. Tweedle MF, Wedeking P, Kumar K. Biodistribution of radiolabeled, formulated gadopentetate, gadoteridol, gadoterate, and gadodiamide in mice and rats. Investigative radiology 1995;30:372-80.

398. McDonald RJ, McDonald JS, Kallmes DF et al. Intracranial Gadolinium Deposition after Contrast-enhanced MR Imaging. Radiology 2015:150025.

399. Radbruch A, Weberling LD, Kieslich PJ et al. Gadolinium Retention in the Dentate Nucleus and Globus Pallidus Is Dependent on the Class of Contrast Agent. Radiology 2015:150337.

400. Kanda T, Fukusato T, Matsuda M et al. Gadolinium-based Contrast Agent Accumulates in the Brain Even in Subjects without Severe Renal Dysfunction: Evaluation of Autopsy Brain Specimens with Inductively Coupled Plasma Mass Spectroscopy. Radiology 2015:142690.

401. Kanda T, Osawa M, Oba H et al. High Signal Intensity in Dentate Nucleus on Unenhanced T1-weighted MR Images: Association with Linear versus Macrocyclic Gadolinium Chelate Administration. Radiology 2015:140364.

402. Oshinski JN, Yang Z, Jones JR, Mata JF, French BA. Imaging time after Gd-DTPA injection is critical in using delayed enhancement to determine infarct size accurately with magnetic resonance imaging. Circulation 2001;104:2838-42.

403. Grebe O, Paetsch I, Kestler HA et al. Optimal acquisition parameters for contrast enhanced magnetic resonance imaging after chronic myocardial infarction. Journal of cardiovascular magnetic resonance : official journal of the Society for Cardiovascular Magnetic Resonance 2003;5:575-87.

404. Dall'Armellina E, Karia N, Lindsay AC et al. Dynamic changes of edema and late gadolinium enhancement after acute myocardial infarction and their relationship to functional recovery and salvage index. Circulation Cardiovascular imaging 2011;4:228-36.

405. Pfeffer MA, Braunwald E. Ventricular remodeling after myocardial infarction. Experimental observations and clinical implications. Circulation 1990;81:1161-72.

406. Sutton MG, Sharpe N. Left ventricular remodeling after myocardial infarction: pathophysiology and therapy. Circulation 2000;101:2981-8.

407. Wu E, Ortiz JT, Tejedor P et al. Infarct size by contrast enhanced cardiac magnetic resonance is a stronger predictor of outcomes than left ventricular ejection fraction or end-systolic volume index: prospective cohort study. Heart 2008;94:730-6.

408. Pennell DJ, Sechtem UP, Higgins CB et al. Clinical indications for cardiovascular magnetic resonance (CMR): Consensus Panel report. Journal of cardiovascular magnetic resonance : official journal of the Society for Cardiovascular Magnetic Resonance 2004;6:727-65.

409. Ferreira VM, Piechnik SK, Dall'Armellina E et al. T(1) mapping for the diagnosis of acute myocarditis using CMR: comparison to T2-weighted and late gadolinium enhanced imaging. JACC Cardiovascular imaging 2013;6:1048-58.

410. Grover-McKay M, Scholz TD, Burns TL, Skorton DJ. Myocardial collagen concentration and nuclear magnetic resonance relaxation times in the spontaneously hypertensive rat. Investigative radiology 1991;26:227-32.

411. Bull S, White SK, Piechnik SK et al. Human non-contrast T1 values and correlation with histology in diffuse fibrosis. Heart 2013;99:932-7.

412. Dass S, Suttie JJ, Piechnik SK et al. Myocardial tissue characterization using magnetic resonance noncontrast t1 mapping in hypertrophic and dilated cardiomyopathy. Circulation Cardiovascular imaging 2012;5:726-33.

413. Puntmann VO, Voigt T, Chen Z et al. Native T1 mapping in differentiation of normal myocardium from diffuse disease in hypertrophic and dilated cardiomyopathy. JACC Cardiovascular imaging 2013;6:475-84.

414. Amado LC, Gerber BL, Gupta SN et al. Accurate and objective infarct sizing by contrast-enhanced magnetic resonance imaging in a canine myocardial infarction model. Journal of the American College of Cardiology 2004;44:2383-9.

415. Bondarenko O, Beek AM, Hofman MB et al. Standardizing the definition of hyperenhancement in the quantitative assessment of infarct size and myocardial viability using delayed contrast-enhanced CMR. Journal of cardiovascular magnetic resonance : official journal of the Society for Cardiovascular Magnetic Resonance 2005;7:481-5.

416. Schulz-Menger J, Bluemke DA, Bremerich J et al. Standardized image interpretation and post processing in cardiovascular magnetic resonance: Society for Cardiovascular Magnetic Resonance (SCMR) board of trustees task force on standardized post processing. Journal of cardiovascular magnetic resonance : official journal of the Society for Cardiovascular Magnetic Resonance 2013;15:35.

417. Muthupillai R, Flamm SD, Wilson JM, Pettigrew RI, Dixon WT. Acute myocardial infarction: tissue characterization with T1rho-weighted MR imaging--initial experience. Radiology 2004;232:606-10.

418. Witschey WR, Zsido GA, Koomalsingh K et al. In vivo chronic myocardial infarction characterization by spin locked cardiovascular magnetic resonance. Journal of cardiovascular magnetic resonance : official journal of the Society for Cardiovascular Magnetic Resonance 2012;14:37.

419. Dall'Armellina E, Ferreira VM, Kharbanda RK et al. Diagnostic value of pre-contrast T1 mapping in acute and chronic myocardial infarction. JACC Cardiovascular imaging 2013;6:739-42.

420. Stanisz GJ, Odrobina EE, Pun J et al. T1, T2 relaxation and magnetization transfer in tissue at 3T. Magnetic resonance in medicine : official journal of the Society of Magnetic Resonance in Medicine / Society of Magnetic Resonance in Medicine 2005;54:507-12.

421. Chen J, Song SK, Liu W et al. Remodeling of cardiac fiber structure after infarction in rats quantified with diffusion tensor MRI. American journal of physiology Heart and circulatory physiology 2003;285:H946-54.

422. Pop M, Ghugre NR, Ramanan V et al. Quantification of fibrosis in infarcted swine hearts by ex vivo late gadolinium-enhancement and diffusion-weighted MRI methods. Physics in medicine and biology 2013;58:5009-28.

423. Wu MT, Tseng WY, Su MY et al. Diffusion tensor magnetic resonance imaging mapping the fiber architecture remodeling in human myocardium after infarction: correlation with viability and wall motion. Circulation 2006;114:1036-45.

424. Nguyen C, Fan Z, Xie Y et al. In vivo contrast free chronic myocardial infarction characterization using diffusion-weighted cardiovascular magnetic resonance. Journal of cardiovascular magnetic resonance : official journal of the Society for Cardiovascular Magnetic Resonance 2014;16:68.

425. Simpson JH, Carr HY. Diffusion and nuclear spin relaxation in water. The Physical Review 1958;111:1201-1202.

426. Robson MD, Piechnik SK, Tunnicliffe EM, Neubauer S. T1 measurements in the human myocardium: The effects of magnetization transfer on the SASHA and MOLLI sequences. Magnetic resonance in medicine : official journal of the Society of Magnetic Resonance in Medicine / Society of Magnetic Resonance in Medicine 2013.

427. Scholz TD, Hoyt RF, DeLeonardis JR, Ceckler TL, Balaban RS. Water-macromolecular proton magnetization transfer in infarcted myocardium: a method to enhance magnetic resonance image contrast. Magnetic resonance in medicine : official journal of the Society of Magnetic Resonance in Medicine / Society of Magnetic Resonance in Medicine 1995;33:178-84.

428. Weber OM, Speier P, Scheffler K, Bieri O. Assessment of magnetization transfer effects in myocardial tissue using balanced steady-state free precession (bSSFP) cine MRI. Magnetic resonance in medicine : official journal of the Society of Magnetic Resonance in Medicine / Society of Magnetic Resonance in Medicine 2009;62:699-705.

429. Salerno M, Janardhanan R, Jiji RS et al. Comparison of methods for determining the partition coefficient of gadolinium in the myocardium using T1 mapping. Journal of magnetic resonance imaging : JMRI 2013;38:217-24.

430. Kali A, Kumar A, Cokic I et al. Chronic manifestation of postreperfusion intramyocardial hemorrhage as regional iron deposition: a cardiovascular magnetic resonance study with ex vivo validation. Circulation Cardiovascular imaging 2013;6:218-28.

431. Otsu N. A threshold selection method from gray-level histograms. IEEE Transactions on Systems, Man, and Cybernetics 1979;9:62-66.

432. Kali A, Tang RL, Kumar A, Min JK, Dharmakumar R. Detection of acute reperfusion myocardial hemorrhage with cardiac MR imaging: T2 versus T2. Radiology 2013;269:387-95.

433. Schuijf JD, Kaandorp TA, Lamb HJ et al. Quantification of myocardial infarct size and transmurality by contrast-enhanced magnetic resonance imaging in men. The American journal of cardiology 2004;94:284-8.

434. Xue H, Greiser A, Zuehlsdorff S et al. Phase-sensitive inversion recovery for myocardial T1 mapping with motion correction and parametric fitting. Magnetic resonance in medicine : official journal of the Society of Magnetic Resonance in Medicine / Society of Magnetic Resonance in Medicine 2013;69:1408-20.

435. Kali A, Cokic I, Tang RL et al. Determination of location, size, and transmurality of chronic myocardial infarction without exogenous contrast media by using cardiac magnetic resonance imaging at 3 T. Circulation Cardiovascular imaging 2014;7:471-81.

436. Kali A, Cokic I, Yang HJ, Sharif B, Dharmakumar R. Accuracy and precision of chronic myocardial infarct characterization with native T1 mapping at 3T. Journal of cardiovascular magnetic resonance : official journal of the Society for Cardiovascular Magnetic Resonance 2015;17:P166.

437. Goldfarb JW, Arnold S, Roth M, Han J. T1-weighted magnetic resonance imaging shows fatty deposition after myocardial infarction. Magnetic resonance in medicine : official journal of the Society of Magnetic Resonance in Medicine / Society of Magnetic Resonance in Medicine 2007;57:828-34.

438. Ferreira VM, Holloway CJ, Piechnik SK, Karamitsos TD, Neubauer S. Is it really fat? Ask a T1-map. European heart journal cardiovascular Imaging 2013;14:1060.

439. Martirosian P, Boss A, Deimling M et al. Systematic variation of off-resonance prepulses for clinical magnetization transfer contrast imaging at 0.2, 1.5, and 3.0 tesla. Investigative radiology 2008;43:16-26.

440. Sado DM, Maestrini V, Piechnik SK et al. Noncontrast myocardial T1 mapping using cardiovascular magnetic resonance for iron overload. Journal of magnetic resonance imaging : JMRI 2014.

441. Deshpande VS, Shea SM, Li D. Artifact reduction in true-FISP imaging of the coronary arteries by adjusting imaging frequency. Magnetic resonance in medicine : official journal of the Society of Magnetic Resonance in Medicine / Society of Magnetic Resonance in Medicine 2003;49:803-9.

442. Husser O, Monmeneu JV, Sanchis J et al. Cardiovascular magnetic resonance-derived intramyocardial hemorrhage after STEMI: Influence on long-term prognosis, adverse left ventricular remodeling and relationship with microvascular obstruction. Int J Cardiol 2012.

443. Zia MI, Ghugre NR, Connelly KA et al. Characterizing Myocardial Edema and Hemorrhage Using Quantitative T2 and T2* Mapping at Multiple Time Intervals Post ST-Segment Elevation Myocardial Infarction. Circ Cardiovasc Imaging 2012;5:566-72.

444. Lotan CS, Bouchard A, Cranney GB, Bishop SP, Pohost GM. Assessment of postreperfusion myocardial hemorrhage using proton NMR imaging at 1.5 T. Circulation 1992;86:1018-25.

445. Jensen JH, Chandra R. NMR relaxation in tissues with weak magnetic inhomogeneities. Magn Reson Med 2000;44:144-56.

446. Gillis P, Koenig SH. Transverse relaxation of solvent protons induced by magnetized spheres: application to ferritin, erythrocytes, and magnetite. Magn Reson Med 1987;5:323-45.

447. Wagner KR, Sharp FR, Ardizzone TD, Lu A, Clark JF. Heme and iron metabolism: role in cerebral hemorrhage. J Cereb Blood Flow Metab 2003;23:629-52.

448. McNeill A, Chinnery PF. Neurodegeneration with brain iron accumulation. Handb Clin Neurol 2011;100:161-72.

449. Grace ND, Powell LW. Iron storage disorders of the liver. Gastroenterology 1974;67:1257-83.

450. Ernst O, Sergent G, Bonvarlet P, Canva-Delcambre V, Paris JC, L'Hermine C. Hepatic iron overload: diagnosis and quantification with MR imaging. AJR Am J Roentgenol 1997;168:1205-8.

451. Liu P, Olivieri N. Iron overload cardiomyopathies: new insights into an old disease. Cardiovasc Drugs Ther 1994;8:101-10.

452. Horwitz LD, Rosenthal EA. Iron-mediated cardiovascular injury. Vasc Med 1999;4:93-9.

453. Tucker HS, Jr., Moss LF, Williams JP. Hemochromatosis with death from heart failure. American heart journal 1948;35:993-1000.

454. Buja LM, Roberts WC. Iron in the heart. Etiology and clinical significance. The American journal of medicine 1971;51:209-21.

455. Engle MA. Cardiac Involvement in Cooley's Anemia. Annals of the New York Academy of Sciences 1964;119:694-702.

456. Mavrogeni S, Gotsis E, Verganelakis D et al. Effect of iron overload on exercise capacity in thalassemic patients with heart failure. Int J Cardiovasc Imaging 2009;25:777-83.

457. Patton N, Brown G, Leung M et al. Observational study of iron overload as assessed by magnetic resonance imaging in an adult population of transfusion-dependent patients with beta thalassaemia: significant association between low cardiac T2* < 10 ms and cardiac events. Intern Med J 2010;40:419-26.

458. Pennell DJ. T2* magnetic resonance: iron and gold. JACC Cardiovasc Imaging 2008;1:579-81.

459. Kaye SB, Owen M. Cardiac arrhythmias in thalassaemia major: evaluation of chelation treatment using ambulatory monitoring. British medical journal 1978;1:342.

460. Schwartz KA, Li Z, Schwartz DE, Cooper TG, Braselton WE. Earliest cardiac toxicity induced by iron overload selectively inhibits electrical conduction. J Appl Physiol 2002;93:746-51.

461. Kirk P, Roughton M, Porter JB et al. Cardiac T2* magnetic resonance for prediction of cardiac complications in thalassemia major. Circulation 2009;120:1961-8.

462. Braunwald E. Acute myocardial infarction. Heart disease : a textbook of cardiovascular medicine. 5th ed. Philadelphia ; London: Saunders, 1997:1184-1288.

463. Bekkers SC, Smulders MW, Passos VL et al. Clinical implications of microvascular obstruction and intramyocardial haemorrhage in acute myocardial infarction using cardiovascular magnetic resonance imaging. European radiology 2010;20:2572-8.

464. Reeder SB, Faranesh AZ, Boxerman JL, McVeigh ER. In vivo measurement of T2* and field inhomogeneity maps in the human heart at 1.5 T. Magn Reson Med 1998;39:988-98.

465. Abragam A. The principles of nuclear magnetism. Oxford: Clarendon Press, 1961.

466. Goebeler M, Roth J, Teigelkamp S, Sorg C. The monoclonal antibody MAC387 detects an epitope on the calcium-binding protein MRP14. Journal of leukocyte biology 1994;55:259-61.

467. Rugtveit J, Scott H, Halstensen TS, Norstein J, Brandtzaeg P. Expression of the L1 antigen (calprotectin) by tissue macrophages reflects recent recruitment from peripheral blood rather than upregulation of local synthesis: implications for rejection diagnosis in formalin-fixed kidney specimens. The Journal of pathology 1996;180:194-9.

468. Frangogiannis NG, Shimoni S, Chang SM et al. Evidence for an active inflammatory process in the hibernating human myocardium. The American journal of pathology 2002;160:1425-33.

469. Terrovitis J, Stuber M, Youssef A et al. Magnetic resonance imaging overestimates ferumoxide-labeled stem cell survival after transplantation in the heart. Circulation 2008;117:1555-62.

470. Wang Y, Wang B, Zhu MT et al. Microglial activation, recruitment and phagocytosis as linked phenomena in ferric oxide nanoparticle exposure. Toxicol Lett 2011;205:26-37.

471. Guildford AL, Poletti T, Osbourne LH, Di Cerbo A, Gatti AM, Santin M. Nanoparticles of a different source induce different patterns of activation in key biochemical and cellular components of the host response. J R Soc Interface 2009;6:1213-21.

472. Hooiveld MJ, Roosendaal G, van den Berg HM, Bijlsma JW, Lafeber FP. Haemoglobin-derived iron-dependent hydroxyl radical formation in blood-induced joint damage: an in vitro study. Rheumatology (Oxford) 2003;42:784-90.

473. Issa ZF, Miller JM, Zipes DP. Clinical arrhythmology and electrophysiology a companion to Braunwald's heart disease. 2nd ed. Philadelphia, PA: Elseiver/Saunders, 2012:1 online resource (xiii, 726 p.).

474. Shenasa M, Hindricks G, Borggrefe M. Cardiac Mapping. 3rd ed. Chichester: John Wiley & Sons, 2009:1 online resource (544 p.).

475. de Bakker JM, van Capelle FJ, Janse MJ et al. Reentry as a cause of ventricular tachycardia in patients with chronic ischemic heart disease: electrophysiologic and anatomic correlation. Circulation 1988;77:589-606.

476. de Bakker JM, Coronel R, Tasseron S et al. Ventricular tachycardia in the infarcted, Langendorff-perfused human heart: role of the arrangement of surviving cardiac fibers. Journal of the American College of Cardiology 1990;15:1594-607.

477. Cinca J, Bardaji A, Carreno A et al. ST segment elevation at the surface of a healed transmural myocardial infarction in pigs. Conditions for passive transmission from the ischemic peri-infarction zone. Circulation 1995;91:1552-9.

478. Cinca J, Warren M, Rodriguez-Sinovas A et al. Passive transmission of ischemic ST segment changes in low electrical resistance myocardial infarct scar in the pig. Cardiovascular research 1998;40:103-12.

479. Hildebrand AM, Bhagirath KM, Ariyarajah V et al. Myocardial siderosis due to hemochromatosis in an individual with hypertrophic cardiomyopathy. The Canadian journal of cardiology 2009;25:e424-5.

480. Schwartz KA, Li Z, Schwartz DE, Cooper TG, Braselton WE. Earliest cardiac toxicity induced by iron overload selectively inhibits electrical conduction. Journal of applied physiology 2002;93:746-51.

481. Isma'eel H, Shamseddeen W, Taher A et al. Ventricular late potentials among thalassemia patients. International journal of cardiology 2009;132:453-5.

482. Jackowski C, Schwendener N, Grabherr S, Persson A. Post-mortem cardiac 3-T magnetic resonance imaging: visualization of sudden cardiac death? Journal of the American College of Cardiology 2013;62:617-29.

483. Jackowski C, Christe A, Sonnenschein M, Aghayev E, Thali MJ. Postmortem unenhanced magnetic resonance imaging of myocardial infarction in correlation to histological infarction age characterization. European heart journal 2006;27:2459-67.

484. Tsuda N. Electronic conduction in oxides. 3rd rev. and enl. ed. Berlin ; New York: Springer, 2000.

485. Gabriel C, Peyman A, Grant EH. Electrical conductivity of tissue at frequencies below 1 MHz. Physics in medicine and biology 2009;54:4863-78.

486. Kofod G, Risse S, Stoyanov H, McCarthy DN, Sokolov S, Kraehnert R. Broad-spectrum enhancement of polymer composite dielectric constant at ultralow volume fractions of silica-supported copper nanoparticles. ACS nano 2011;5:1623-9.

487. Wang J, Profitt JA, Pugia MJ, Suni, II. Au nanoparticle conjugation for impedance and capacitance signal amplification in biosensors. Analytical chemistry 2006;78:1769-73.

488. Schwan HP. Determination of biological impedances. In: Nastuk WL, editor Physical techniques in biological research. London: Academic Press, 1963:323-407.

489. Schwartzman D, Chang I, Michele JJ, Mirotznik MS, Foster KR. Electrical impedance properties of normal and chronically infarcted left ventricular myocardium. Journal of interventional cardiac electrophysiology : an international journal of arrhythmias and pacing 1999;3:213-24.

490. Schwan HP, Kay CF. The conductivity of living tissues. Annals of the New York Academy of Sciences 1957;65:1007-13.

491. Grimnes S, Martinsen ØG. Dielectrics. Bioelectricity and bioimpedance basics. London: Academic Press, 2008:57-92.

492. Ahnve S. Correction of the QT interval for heart rate: review of different formulas and the use of Bazett's formula in myocardial infarction. American heart journal 1985;109:568-74.

493. Gupta S, Desjardins B, Baman T et al. Delayed-enhanced MR scar imaging and intraprocedural registration into an electroanatomical mapping system in post-infarction patients. JACC Cardiovascular imaging 2012;5:207-10.

494. Kocovic DZ, Harada T, Friedman PL, Stevenson WG. Characteristics of electrograms recorded at reentry circuit sites and bystanders during ventricular tachycardia after myocardial infarction. Journal of the American College of Cardiology 1999;34:381-8.

495. Saito J, Downar E, Doig JC et al. Characteristics of local electrograms with diastolic potentials: identification of different components of return pathways in ventricular tachycardia. Journal of interventional cardiac electrophysiology : an international journal of arrhythmias and pacing 1998;2:235-45.

496. Cabo C, Schmitt H, Masters G, Coromilas J, Wit AL, Scheinman MM. Location of diastolic potentials in reentrant circuits causing sustained ventricular tachycardia in the infarcted canine heart: relationship to predicted critical ablation sites. Circulation 1998;98:2598-607.

497. Scott PA, Morgan JM, Carroll N et al. The extent of left ventricular scar quantified by late gadolinium enhancement MRI is associated with spontaneous ventricular arrhythmias in patients with coronary artery disease and implantable cardioverter-defibrillators. Circulation Arrhythmia and electrophysiology 2011;4:324-30.

498. Scott PA, Rosengarten JA, Shahed A et al. The relationship between left ventricular scar and ventricular repolarization in patients with coronary artery disease: insights from late gadolinium enhancement magnetic resonance imaging. Europace : European pacing, arrhythmias, and cardiac electrophysiology : journal of the working groups on cardiac

pacing, arrhythmias, and cardiac cellular electrophysiology of the European Society of Cardiology 2013;15:899-906.

499. Kirschvink JL, Kobayashi-Kirschvink A, Diaz-Ricci JC, Kirschvink SJ. Magnetite in human tissues: a mechanism for the biological effects of weak ELF magnetic fields. Bioelectromagnetics 1992;Suppl 1:101-13.

500. Jackson JD. Classical electrodynamics. 3rd ed. New York: Wiley, 1999.

501. Yi G, Guo XH, Reardon M et al. Circadian variation of the QT interval in patients with sudden cardiac death after myocardial infarction. The American journal of cardiology 1998;81:950-6.

502. Straus SM, Kors JA, De Bruin ML et al. Prolonged QTc interval and risk of sudden cardiac death in a population of older adults. Journal of the American College of Cardiology 2006;47:362-7.

503. Fontaine G, Guiraudon G, Frank R. Stimulation studies and epicardial mapping in ventricular tachycardia: Study of mechanism and selections for surgery. In: Kulbertus HE, editor Reentrant Arrhythmias. Baltimore, MD: University Park Press, 1976:334-350.

504. Josephson ME, Horowitz LN, Farshidi A. Continuous local electrical activity. A mechanism of recurrent ventricular tachycardia. Circulation 1978;57:659-65.

505. Simson MB, Euler D, Michelson EL, Falcone RA, Spear JF, Moore EN. Detection of delayed ventricular activation on the body surface in dogs. The American journal of physiology 1981;241:H363-9.

506. el-Sherif N, Gomes JA, Restivo M, Mehra R. Late potentials and arrhythmogenesis. Pacing and clinical electrophysiology : PACE 1985;8:440-62.

507. Nakahara S, Vaseghi M, Ramirez RJ et al. Characterization of myocardial scars: electrophysiological imaging correlates in a porcine infarct model. Heart rhythm : the official journal of the Heart Rhythm Society 2011;8:1060-7.

508. Dawson DK, Hawlisch K, Prescott G et al. Prognostic role of CMR in patients presenting with ventricular arrhythmias. JACC Cardiovascular imaging 2013;6:335-44.

509. Miller JM, Kienzle MG, Harken AH, Josephson ME. Subendocardial resection for ventricular tachycardia: predictors of surgical success. Circulation 1984;70:624-31.

510. Miller JM, Tyson GS, Hargrove WC, 3rd, Vassallo JA, Rosenthal ME, Josephson ME. Effect of subendocardial resection on sinus rhythm endocardial electrogram abnormalities. Circulation 1995;91:2385-91.

511. Zipes DP, Camm AJ, Borggrefe M et al. ACC/AHA/ESC 2006 Guidelines for Management of Patients With Ventricular Arrhythmias and the Prevention of Sudden Cardiac Death: a report of the American College of Cardiology/American Heart Association Task Force and the European Society of Cardiology Committee for Practice Guidelines (writing committee to develop Guidelines for Management of Patients With Ventricular Arrhythmias and the Prevention of Sudden Cardiac Death): developed in collaboration with the European Heart Rhythm Association and the Heart Rhythm Society. Circulation 2006;114:e385-484.

512. Rea TD, Page RL. Community approaches to improve resuscitation after out-of-hospital sudden cardiac arrest. Circulation 2010;121:1134-40.

513. Adabag AS, Luepker RV, Roger VL, Gersh BJ. Sudden cardiac death: epidemiology and risk factors. Nature reviews Cardiology 2010;7:216-25.

514. Myerburg RJ, Reddy V, Castellanos A. Indications for implantable cardioverter-defibrillators based on evidence and judgment. Journal of the American College of Cardiology 2009;54:747-63.

515. Kong MH, Fonarow GC, Peterson ED et al. Systematic review of the incidence of sudden cardiac death in the United States. Journal of the American College of Cardiology 2011;57:794-801.

516. Breithardt G, Borggrefe M, Martinez-Rubio A, Budde T. Pathophysiological mechanisms of ventricular tachyarrhythmias. European heart journal 1989;10 Suppl E:9-18.

517. A comparison of antiarrhythmic-drug therapy with implantable defibrillators in patients resuscitated from near-fatal ventricular arrhythmias. The Antiarrhythmics versus Implantable Defibrillators (AVID) Investigators. The New England journal of medicine 1997;337:1576-83.

518. Bardy GH, Lee KL, Mark DB et al. Amiodarone or an implantable cardioverter-defibrillator for congestive heart failure. The New England journal of medicine 2005;352:225-37.

519. Moss AJ, Zareba W, Hall WJ et al. Prophylactic implantation of a defibrillator in patients with myocardial infarction and reduced ejection fraction. The New England journal of medicine 2002;346:877-83.

520. Fishman GI, Chugh SS, Dimarco JP et al. Sudden cardiac death prediction and prevention: report from a National Heart, Lung, and Blood Institute and Heart Rhythm Society Workshop. Circulation 2010;122:2335-48.

521. Buxton AE, Lee KL, Hafley GE et al. Limitations of ejection fraction for prediction of sudden death risk in patients with coronary artery disease: lessons from the MUSTT study. Journal of the American College of Cardiology 2007;50:1150-7.

522. Chugh SS, Uy-Evanado A, Teodorescu C et al. Women have a lower prevalence of structural heart disease as a precursor to sudden cardiac arrest: The Ore-SUDS (Oregon Sudden Unexpected Death Study). Journal of the American College of Cardiology 2009;54:2006-11.

523. Hunt SA, Abraham WT, Chin MH et al. ACC/AHA 2005 Guideline Update for the Diagnosis and Management of Chronic Heart Failure in the Adult: a report of the American College of Cardiology/American Heart Association Task Force on Practice Guidelines (Writing Committee to Update the 2001 Guidelines for the Evaluation and Management of Heart Failure): developed in collaboration with the American College of Chest Physicians and the International Society for Heart and Lung Transplantation: endorsed by the Heart Rhythm Society. Circulation 2005;112:e154-235.

524. Lloyd-Jones D, Adams R, Carnethon M et al. Heart disease and stroke statistics--2009 update: a report from the American Heart Association Statistics Committee and Stroke Statistics Subcommittee. Circulation 2009;119:480-6.

525. Turakhia MP. Sudden cardiac death and implantable cardioverter-defibrillators. American family physician 2010;82:1357-66.

526. de Vreede-Swagemakers JJ, Gorgels AP, Dubois-Arbouw WI et al. Circumstances and causes of out-of-hospital cardiac arrest in sudden death survivors. Heart 1998;79:356-61.

527. Stecker EC, Vickers C, Waltz J et al. Population-based analysis of sudden cardiac death with and without left ventricular systolic dysfunction: two-year findings from the Oregon

Sudden Unexpected Death Study. Journal of the American College of Cardiology 2006;47:1161-6.

528. Bieri O, Patil S, Quick HH, Scheffler K. Morphing steady-state free precession. Magnetic resonance in medicine : official journal of the Society of Magnetic Resonance in Medicine / Society of Magnetic Resonance in Medicine 2007;58:1242-8.

529. Dharmakumar R, Koktzoglou I, Li D. Factors influencing fast low angle positive contrast steady-state free precession (FLAPS) magnetic resonance imaging. Physics in medicine and biology 2007;52:3261-73.

530. Scheffler K, Seifritz E, Bilecen D et al. Detection of BOLD changes by means of a frequency-sensitive trueFISP technique: preliminary results. NMR in biomedicine 2001;14:490-6.

531. Aquaro GD, Nucifora G, Pederzoli L et al. Fat in left ventricular myocardium assessed by steady-state free precession pulse sequences. The international journal of cardiovascular imaging 2012;28:813-21.

532. Sekihara K. Steady-state magnetizations in rapid NMR imaging using small flip angles and short repetition intervals. IEEE transactions on medical imaging 1987;6:157-64.

533. Matsumoto H, Matsuda T, Miyamoto K, Shimada T, Mikuri M, Hiraoka Y. Peri-infarct zone on early contrast-enhanced CMR imaging in patients with acute myocardial infarction. JACC Cardiovascular imaging 2011;4:610-8.

534. Kwon DH, Smedira NG, Rodriguez ER et al. Cardiac magnetic resonance detection of myocardial scarring in hypertrophic cardiomyopathy: correlation with histopathology and prevalence of ventricular tachycardia. Journal of the American College of Cardiology 2009;54:242-9.

535. Bernier M, Hearse DJ, Manning AS. Reperfusion-induced arrhythmias and oxygen-derived free radicals. Studies with "anti-free radical" interventions and a free radical-generating system in the isolated perfused rat heart. Circulation research 1986;58:331-40.

536. Theleman KP, Kuiper JJ, Roberts WC. Acute myocarditis (predominately lymphocytic) causing sudden death without heart failure. The American journal of cardiology 2001;88:1078-83.

537. Zeppenfeld K, Blom NA, Bootsma M, Schalij MJ. Incessant ventricular tachycardia in fulminant lymphocytic myocarditis: Evidence for origin in the Purkinje system and successful treatment with ablation. Heart rhythm : the official journal of the Heart Rhythm Society 2007;4:88-91.

538. Magnani JW, Danik HJ, Dec GW, Jr., DiSalvo TG. Survival in biopsy-proven myocarditis: a long-term retrospective analysis of the histopathologic, clinical, and hemodynamic predictors. American heart journal 2006;151:463-70.

539. Schenck JF. The role of magnetic susceptibility in magnetic resonance imaging: MRI magnetic compatibility of the first and second kinds. Medical physics 1996;23:815-50.

540. Cameron CS, Roberts WC. Clinical and necropsy findings in patients with calcified myocardial infarcts. Proceedings 2004;17:420-4.

541. Fletcher PJ, Pfeffer JM, Pfeffer MA, Braunwald E. Left ventricular diastolic pressure-volume relations in rats with healed myocardial infarction. Effects on systolic function. Circulation research 1981;49:618-26.

542. Ye YX, Basse-Lusebrink TC, Arias-Loza PA et al. Monitoring of monocyte recruitment in reperfused myocardial infarction with intramyocardial hemorrhage and microvascular

obstruction by combined fluorine 19 and proton cardiac magnetic resonance imaging. Circulation 2013;128:1878-88.

543. Khan JN, Razvi N, Nazir SA et al. Prevalence and extent of infarct and microvascular obstruction following different reperfusion therapies in ST-elevation myocardial infarction. Journal of cardiovascular magnetic resonance : official journal of the Society for Cardiovascular Magnetic Resonance 2014;16:38.

544. Kremastinos DT, Tsetsos GA, Tsiapras DP, Karavolias GK, Ladis VA, Kattamis CA. Heart failure in beta thalassemia: a 5-year follow-up study. The American journal of medicine 2001;111:349-54.

545. Tanner MA, Galanello R, Dessi C et al. Combined chelation therapy in thalassemia major for the treatment of severe myocardial siderosis with left ventricular dysfunction. Journal of cardiovascular magnetic resonance : official journal of the Society for Cardiovascular Magnetic Resonance 2008;10:12.

546. Tanner MA, Galanello R, Dessi C et al. A randomized, placebo-controlled, double-blind trial of the effect of combined therapy with deferoxamine and deferiprone on myocardial iron in thalassemia major using cardiovascular magnetic resonance. Circulation 2007;115:1876-84.

547. Araujo JA, Romano EL, Brito BE et al. Iron overload augments the development of atherosclerotic lesions in rabbits. Arteriosclerosis, thrombosis, and vascular biology 1995;15:1172-80.

548. Wan X, Huo Y, Johns M et al. 5'-AMP-activated protein kinase-activating transcription factor 1 cascade modulates human monocyte-derived macrophages to atheroprotective

functions in response to heme or metformin. Arteriosclerosis, thrombosis, and vascular biology 2013;33:2470-80.

549. Xiong S, She H, Takeuchi H et al. Signaling role of intracellular iron in NF-kappaB activation. The Journal of biological chemistry 2003;278:17646-54.

550. Bolger AP, Anker SD. Tumour necrosis factor in chronic heart failure: a peripheral view on pathogenesis, clinical manifestations and therapeutic implications. Drugs 2000;60:1245-57.

551. Mann DL. Tumor necrosis factor-induced signal transduction and left ventricular remodeling. Journal of cardiac failure 2002;8:S379-86.

552. von Haehling S, Jankowska EA, Anker SD. Tumour necrosis factor-alpha and the failing heart--pathophysiology and therapeutic implications. Basic research in cardiology 2004;99:18-28.

553. Ducharme A, Frantz S, Aikawa M et al. Targeted deletion of matrix metalloproteinase-9 attenuates left ventricular enlargement and collagen accumulation after experimental myocardial infarction. The Journal of clinical investigation 2000;106:55-62.

554. Lindsey M, Wedin K, Brown MD et al. Matrix-dependent mechanism of neutrophil-mediated release and activation of matrix metalloproteinase 9 in myocardial ischemia/reperfusion. Circulation 2001;103:2181-7.

555. Anker SD, von Haehling S. Inflammatory mediators in chronic heart failure: an overview. Heart 2004;90:464-70.

556. Frangogiannis NG. Regulation of the inflammatory response in cardiac repair. Circulation research 2012;110:159-73.

557. Lambert JM, Bongers RS, de Vos WM, Kleerebezem M. Functional analysis of four bile salt hydrolase and penicillin acylase family members in Lactobacillus plantarum WCFS1. Applied and environmental microbiology 2008;74:4719-26.

558. Nahrendorf M, Pittet MJ, Swirski FK. Monocytes: protagonists of infarct inflammation and repair after myocardial infarction. Circulation 2010;121:2437-45.

559. Dobaczewski M, Xia Y, Bujak M, Gonzalez-Quesada C, Frangogiannis NG. CCR5 signaling suppresses inflammation and reduces adverse remodeling of the infarcted heart, mediating recruitment of regulatory T cells. The American journal of pathology 2010;176:2177-87.

560. Huebener P, Abou-Khamis T, Zymek P et al. CD44 is critically involved in infarct healing by regulating the inflammatory and fibrotic response. Journal of immunology 2008;180:2625-33.

561. Kempf T, Zarbock A, Widera C et al. GDF-15 is an inhibitor of leukocyte integrin activation required for survival after myocardial infarction in mice. Nature medicine 2011;17:581-8.